Optimal Configuration of Large Arrays of Floating Bodies for Ocean Wave Energy Extraction

by

Grgur Tokić

Diploma Engineer in Naval Architecture
Faculty of Mechanical Engineering and Naval Architecture
University of Zagreb (2006)

Submitted to the Department of Mechanical Engineering
in partial fulfillment of the requirements for the degree of

Doctor of Philosophy in Mechanical Engineering

at the

MASSACHUSETTS INSTITUTE OF TECHNOLOGY

June 2016

Signature redacted

Author .....
Department of Mechanical Engineering
May 25, 2016

Signature redacted

Certified by.....
Dick K.P. Yue
Philip J. Solondz Professor of Engineering
Thesis Supervisor

Signature redacted

Accepted by .....
Rohan Abeyaratne
Chairman, Department Committee on Graduate Theses

Optimal Configuration of Large Arrays of Floating Bodies for Ocean Wave Energy Extraction

by

Grgur Tokić

Submitted to the Department of Mechanical Engineering
on May 25, 2016, in partial fulfillment of the
requirements for the degree of
Doctor of Philosophy in Mechanical Engineering

Abstract

Ocean wave energy is a large, and mostly untapped potential source of renewable energy worldwide. The scope of engineering solutions for harvesting wave energy is vast, ranging from wave-induced oscillating bodies, to overtopping devices and oscillating water columns. One particularly interesting approach to energy harvesting is to use arrays of oscillating bodies. The advantage of such a solution lies in potential amplification of the wave field through the interactions of waves that are diffracted and radiated by the bodies. Recent examples from other fields of physics (e.g. photonics crystals) show that by carefully engineering the configuration of the array, it is possible to greatly improve its performance. This thesis studies the performance of large arrays of axisymmetric bodies through the use of multiple scattering formulation of wave interactions. The focus is on the energy extraction characteristics in particular, but the effects on mean drift force are also studied.

The multiple scattering (MS) formulation for Wave Energy Converter (WEC) arrays is extended in three areas. First, the dynamical behavior of a body in an array is decoupled from the dynamics of the array as a whole. This allows for the dynamical characteristics of a body to be completely determined in isolation, and then used in an array setting through newly-formed dynamical transfer matrices. This approach is especially beneficial in optimization studies, where the changes in the spatial array configuration do not require the recalculation of the hydrodynamic characteristics of an array. Second, the non-linear mean drift force on an array is expressed in terms of newly-formed non-linear drift transfer matrices. Lastly, a theoretical formulation is developed for periodic arrays with closely-spaced rows of bodies so that they can be analyzed in an exact manner within the MS formulation. Based on these extensions, a fast computational algorithm is developed that is capable of handling large arrays ($O(100)$ bodies) of different configurations (general finite-size arrays, periodic arrays, periodic arrays of subarrays). The algorithm imposes no constraints on the body-size-to-wavelength ratio or on the inter-body spacings.

Using this algorithm, a series of systematic studies of energy extraction characteristics by different array configurations is performed (as a function of wavenumber and wave incoming angle). These array configurations can be described with at most two parameters. In particular, the study of periodic and uniformly spaced line arrays reveals that large gains occur before new scattering orders appear (at Rayleigh wavelength). The gains are particularly large for super-resonant wavenumbers where there is still significant energy extraction. The studies of rectangularly arranged arrays show that, while still related to Rayleigh wavelengths, the optimal spacing is governed by the emergence of higher scatter-

ing orders. In all cases, arrays arranged in the direction of array propagation (attenuator arrays) perform poorly, except for sub-resonant wavenumbers. The effect or spacing irregularity (linear, quadratic and random) is studied on terminator arrays. The performance of irregularly spaced arrays as a function of wavenumber is more uniform, without high peaks in performance, and it indicates that there is a trade-off between high array gain and broad-bandedness of array gain.

Finally, optimization of spatial configuration of a series of large arrays (up to 200 bodies) is performed. The array configuration is parameterized such that it can be described by a small number of variables, but that still allows a large number of different configuration types (irregularities in body spacings). Gradients of objective functions (extracted energy, array gain, drift force) are obtained using the adjoint method that, by also employing matrix-free matrix-vector multiplications, leads to a fast, memory-efficient gradient-based optimization algorithm. The optimization is performed for regular and irregular seas. The optimized rectangular arrays lead to high array gains, especially for mildly super-resonant wavenumbers where it reaches values of over 4. Surprisingly, uniformly spaced rectangular arrays perform better than the irregularly spaced ones in both regular and irregular seas. For many optimized arrays, the array capture width (extraction cross-section) is equal to the geometrical extent (cross-section) of the array, indicating that these arrays harvest all the energy of a particular frequency incoming on the spatial area they occupy. The optimal configurations are analyzed from a physical standpoint and compared to other structured arrays in physics. The results overall provide guidelines on the possible future design of WEC arrays.

Thesis Supervisor: Dick K.P. Yue
Title: Philip J. Solondz Professor of Engineering

Acknowledgments

This is a thesis that took far longer to complete than I ever imagined. But throughout my long journey towards the completion, Professor Yue's support was unquestionable, and his guidance was crucial for not letting me veer off the course too much. Sometimes, however, the appeal was too strong. I have learned a lot from the discussions we have had over the years, about the scientific problems at hand, as well as about the way to approach problems in general. I will cherish these discussions for the rest of my life, and I hope there will still be many more to come.

I am greatly indebted to my committee members — Professor Akylas, Professor Johnson, and Dr. Yuming Liu. Professor Akylas has been a part of my MIT life from the first semester here, as I had the privilege to attend several of his courses and unforgettable lectures. One might argue that I have acquired most of my knowledge on waves and linear and nonlinear dynamics in these classes. Professor Johnson exposed me to the problems in photonics and optical structures, a field similar the one studied in this thesis, and teeming with exciting developments. I have tried to learn and draw parallels between the two fields as much as I could. I believe the thesis that much better for it. Yuming, as a member of our group, was a continuous support in every manner. His deep knowledge on wave hydrodynamics have motivated me to learn more every step of the way. And I could always find wisdom and comfort in his words.

A glass being always half full, my long stay at MIT meant I have met countless amazing people over the years, both at MIT and Boston in general. Many of them I am proud to call my friends for life. And even so, I am bound to forget some in these lines. First, I would like to mention my Croatian friends who have kept me sane all these years — to Vladimir Bosiljevac, Petra Šimić, Joško Silobrčić, Siniša Hrvatin, and Tea Žakula. Our drinking, singing, dancing, hiking outings (to name a few) always left me happy, excited, motivated, and filled with the lust for life in all its glory. Tea, you have been my best friend for more than a decade, and someone who helped me become the person I am today. Getting to meet and know the rest of you was almost worth coming to Boston alone. I would also like to thank Ben Druecke, Alex Kalmikov, Hadi Tavakoli Nia, Wenting Xiao, Bryce Cambpbell and Kirki Kofiani for making the first years at MIT the most exciting and intellectually exciting period of my life. Our late night discussions and banter on any

topic is a memory I often go back to. There are many sports teams I was a part of over the years, but Andrej Košmrlj was always there with me. A more versatile athlete one can rarely meet. As our paths inevitably separated, other people filled my life with joy and excitement. My later years at MIT were marked by many of my Greek friends — Eleni Margariti, Themis Resvanis, and Nina Panagiotidou, to name a few. I loved every moment we spent together, especially outside MIT. I would especially like to thank Nina for her support in the final push towards finishing this thesis. But one person who has been with me from almost the beginning is George Christou. A roommate, comedian, drugar, a late-night connoisseur, and a best friend, he has been an inseparable part of my life in Boston in all its good moments, as well as the bad ones. And now we will walk together in commencement, a fitting end to the MIT episode of our lives.

In the end, I would like to thank my parents and my sister Ivana. Without their endless support in every way imaginable, I would not have made it to MIT in the first place, let alone endured the stresses that MIT inevitably brings. I believe that this thesis means more to them than to me, and I know they will forgive that it does not match the standard it would have to, if it were a direct product of love and nerves that they have invested in it through me. This thesis is dedicated to them.

Contents

List of Figures

List of Tables

Chapter 1

Introduction

Ocean wave energy is a large, and mostly untapped potential source of renewable energy worldwide. The scope of engineering solutions for harvesting wave energy is vast, ranging from wave-induced oscillating bodies, to overtopping devices and oscillating water columns. One particularly interesting approach to energy harvesting is to use arrays of oscillating bodies. The advantage of such a solution lies in potential amplification of the wave field through the interactions of waves that are diffracted and radiated by the bodies. Recent examples from other fields of physics (e.g. photonics crystals) show that by carefully engineering the configuration of the array, it is possible to greatly improve its performance. This thesis studies the performance of large arrays of axisymmetric bodies through the use of multiple scattering formulation of wave interactions. The focus is on the energy extraction characteristics in particular, but the effects on mean drift force are also studied.

The wave energy potential on the US shores in given in Figure 1.1a. The power carried

(a) Wave Energy Flux on continental US

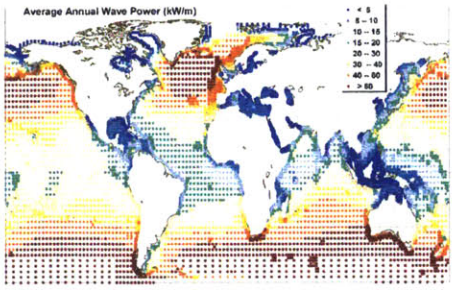

(b) Wave energy flux worldwide (Cruz, 2008)

Figure 1.1: Renewable energy resources.

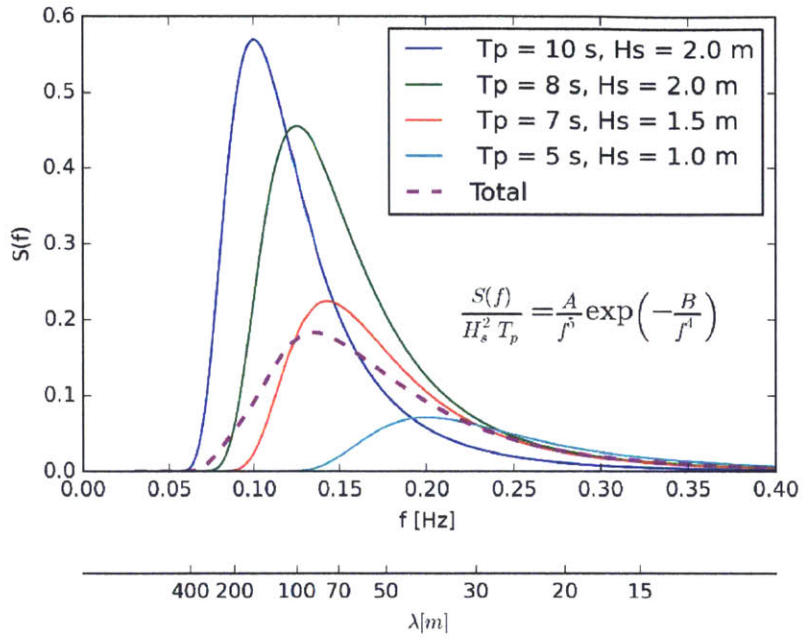

Figure 1.2: Examples of ocean spectra (Brentschneider)

by a monochromatic wave of amplitude A is given by

$$P_w = \frac{1}{2}\rho g c_g A^2 \tag{1.1}$$

where ρ is the fluid density, g the gravitational acceleration and c_g the group velocity of the wave. A quick back of the envelope calculation can give us a look into the orders of magnitude of the wave energy potential. For example, the 30 kW/m power flux could be carried by a wave of amplitude of 1 meter and a period of 10 seconds.

There are several reasons why ocean wave energy is a viable source of renewable energy — it does not depend on diurnal rhythm like solar energy; energy density is rather high (due to water density, as compared to wind); energy put in by distant offshore storms reaches the shores where it can be captured with almost no dissipation. Engineering challenges, however, are also rather big, mainly due to the harsh environment the wave energy converter devices need to operate in — the ocean. Floating devices (more about them in the next section) are exposed to potentially devastating storms that can destroy the entire structure/power plant in a matter of hours. Slowly acting forces are no less destructible. Biological growth and corrosion take place over longer periods of time, but require constant maintenance of the devices, and can cause problems in regular operation.

In comparison, solar power is a well-established source of renewable energy. Commercial power plants have already been built and are connected to the power grid. For example, the world's largest solar power plant, Noor 1, has been put into service recently (2015). It uses concentrated solar power using parabolic trough mirrors to melt salt that can then be used as energy storage even when there is no sun. The expected production is 370 GWh per year, to be sold at \$0.19/kWh.

According to US Energy Information Administration (EIA), the cost of wind energy on land is \$0.07/kWh, while the cost of the offshore wind energy is \$0.20/kWh. (In comparison, EIA also reports that the cost of thermal solar energy is around \$0.24/kWh.) Wave energy technology, although still far from being mature, seems to be competitive with wind and solar — the cost of wave energy in the UK is reported to be \$0.075/kWh.

1.1 State-of-the-Art in Wave Energy Converters

Despite almost forty-year-long research effort in ocean wave energy conversion, it can still be considered a nascent technology. An indication why that might be the case is in the sheer number of completely different wave energy converter (WEC) concepts (some purely theoretical, some operational) that have been developed over the years. Babarit (2015) gave a rather exhaustive review of hundreds of different WECs and their comparison in terms of performance. Some of the different design solutions are shown in Figure 1.3. However, there is still no clear consensus on what the best design(s) for energy harvesting might be. Undoubtedly, given the variety of environmental, operational, governmental conditions that WECs operate in, there does not need to be a single preferred design. The size and the harshness of the environment in which the WECs operate make the real-size tests very costly.

WEC technology can be systematized in many different ways — according to WEC size, principle, proximity to shore etc. Babarit (2015) classifies WEC devices into oscillating water columns (OWCs), overtopping devices, oscillating wave surge converters (OWSC), and heaving devices. Mei, Stiassnie, and Yue (2005) classify WEC devices according to their orientation with respect to the incoming waves. This is the classification that we will mostly use in this thesis because it is also more applicable to different kinds of WEC arrays. According to this classification, floating wave energy converter (WEC) devices can roughly

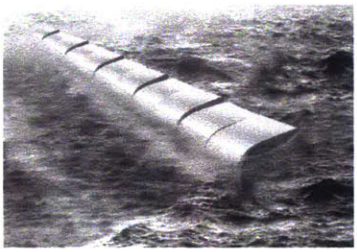

(a) Artist's impression of a row or Salter's ducks (terminator device)

(b) Artist view of a Pelamis farm (attenuator devices) (Drew, Plummer, and Sahinkaya, 2009)

(c) WaveDragon, an overtopping device (Drew, Plummer, and Sahinkaya, 2009)

(d) Oyster (OWSC device)

(e) Wavebob, an omnidirectional device

(f) Array of PowerBuoys, by Ocean Power Technologies (Drew, Plummer, and Sahinkaya, 2009)

Figure 1.3: Different types of wave energy converters.

be separated into three groups: terminators, attenuators, and omnidirectional absorbers. The first designs of how to extract energy from ocean waves were employing terminator devices (or beam-sea absorbers) — devices that oscillate around a horizontal axis that is placed parallel to the incoming wave crest. The device that started it all is Salter's duck (Salter, 1974), Figure 1.3a. The devices can have more than one degree of freedom, and the energy is usually extracted from the relative motion between the different segments of the device. The advantage of these devices is that they can extract a very large portion of the incoming energy at certain frequency. In particular, a submerged horizontal circular cylinder undergoing circular oscillations can be tuned to extract *all* of the incoming energy at a given frequency (Evans, Jeffrey, et al., 1979). Attenuators, on the other hand, are devices oriented such that their characteristic dimension is in the direction of wave propagation, Figure 1.3b.

Omnidirectional absorbers are devices that are axisymmetric around the vertical axis. They have a power-take off (PTO) device connected to them, and they usually extract energy from the heave motion of the body. An appealing feature of omnidirectional absorbers is that they can be placed in proximity to each other and form WEC arrays, thus potentially achieving a multiplication of energy absorption. The position of the devices with respect to each other greatly influences the wave interactions between them, and consequently the actual extracted energy. This question — how to position the devices in order to extract the most energy for a given sea state — is the main subject of this thesis.

Careful hydrodynamic consideration is perhaps nowhere more crucial than in designing WEC arrays. The WEC array performance varies drastically based on the spatial configuration of bodies that form it. If not carefully designed, it can perform several times *worse* than how the same number of bodies would perform in isolation.

However, for many of the proposed designs the hydrodynamic performance almost seems like an afterthought — the performance of the device is analyzed after the device has been designed, rather than designing the device with an optimal performance in mind. More emphasis seems to be directed towards the (optimal) control of a given device, rather than its hydrodynamic design. For example, one is hard-pressed to find the hydrodynamic reasoning behind the array layout in some existing WEC array, Figure 1.4.

A potential indication that arrays could prove to be the method of choice for energy extraction comes via a glaring example from another field of physics — photonic crystals.

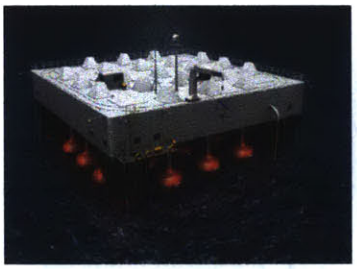

(a) FO3 (Olsen & ABB)

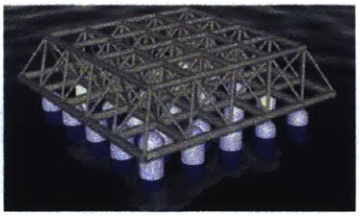

(b) Manchester Bobber (5×5 WEC array) (reuk.co.uk)

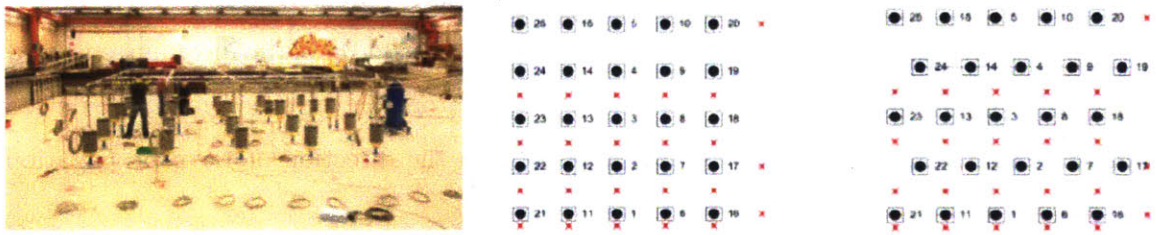

(c) Experimental setup of a 5×5 WEC array (Stratigaki et al., 2014)

Figure 1.4: Some WEC array concepts

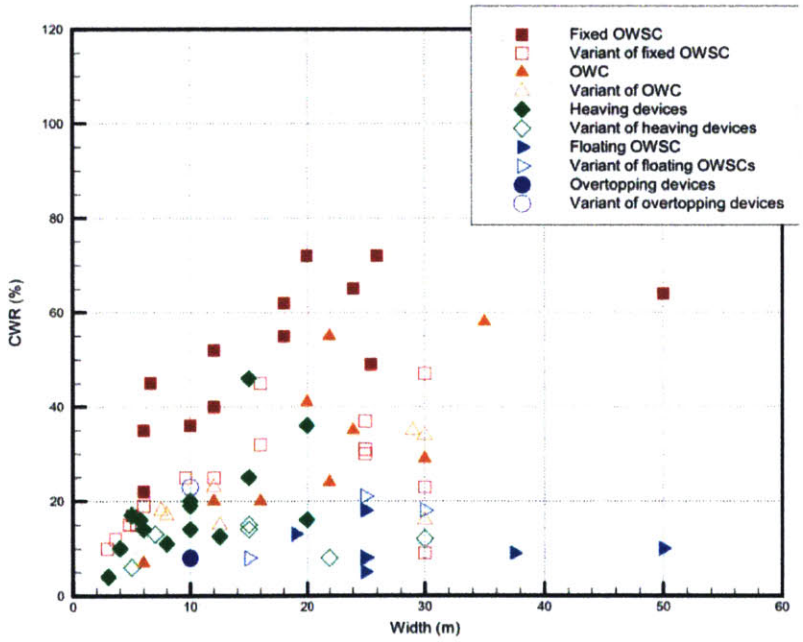

Figure 1.5: Comparison between different WEC concepts (Babarit, 2015)

Photonic crystals are man-made "materials", i.e. carefully designed and engineered patterns in an optical material (Joannopoulos, Villeneuve, and Fan, 1997). The interaction between the electromagnetic waves (light) and the patterns in the material (e.g. large arrays of holes or rods) has been harnessed through the design and utilized to achieve different purposes — selective mirrors (Shen et al., 2014), waveguides (Fan et al., 2001), resonant cavities (Joannopoulos, Villeneuve, and Fan, 1997), energy harvesters (Sheng et al., n.d.) — with a much improved performance over the traditional materials. The governing physics between photonic crystals and WEC arrays is very similar, so one can wonder whether there is room for a greater improvement in ocean wave energy extraction by carefully designing large WEC arrays.

Floating structures, be it WEC arrays or any other large structure, need to be moored to the ocean bottom so that they do not drift away under the action of waves. Mooring lines constraint surge and sway (oscillatory horizontal motion) of the structure that is of the same frequency as the incoming wave, but they are even more crucial for constraining the effect of the mean wave drift force on the array. Mean drift force is a non-linear effect that arises because of the change in the wave momentum caused by the structure, and, unlike the oscillatory character (with zero mean) of the first-order force, it has a constant value (for a wave of particular frequency). (There are other important phenomena regarding mooring lines and wave forcing — such as large second-order non-linear oscillations at the difference (slow) frequency — but these are outside the scope of the thesis.) Mean drift force, thus, has a huge impact on very large floating structures (VFLS), Figure 1.6, due to the expenses related to the mooring systems.

Similar to boosting the performance by designing spatial array configuration, bodies can be placed in an array in a way that would mitigate the effects of the mean drift force. For WEC arrays, maximizing the energy extraction while minimizing the drift force results in conflicting objectives because energy extraction will necessarily change the wave momentum and thus cause an increase in drift force. A solution to this multi-objective problem might lie closer to the maximal-energy-extraction extreme. For structures that are not intended for energy extraction, finding the array configuration that minimizes the drift force is a well-posed problem, and one that has not been thoroughly studied.

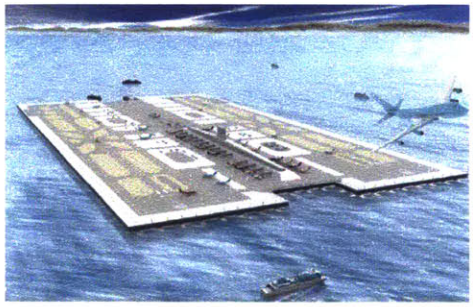

(a) Artist rendering (Euphlotea Inc.) of the proposed floating airport in San Diego, US by Walter Munk

(b) 1000m long Mega-Float in Tokyo Bay (a test for a floating airport) (Wang and Tay, 2011)

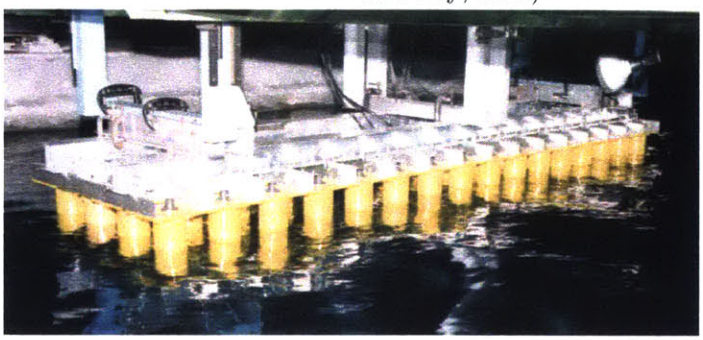

(c) Model testing of a 64-body floating structure (Kashiwagi, 2002)

Figure 1.6: Some examples of Very Large Floating Structures

1.2 Thesis Objectives

Based on the challenges presented in the previous sections, the objective of this thesis is to address a number of scientific and technical challenges. Namely, the objectives of this thesis are:

- Develop a framework that enables the study and optimization of large ($O(100)$-body) arrays in regular and irregular seas, capable of dealing with bodies of any size, and without imposing constraints on body size or body spacings.

- Systematically study the performance of large arrays of simple spatial configurations in order to better understand the underlying physics behind the potential amplifications in extraction performance. Address differences in performance between regularly spaced arrays (e.g. uniformly spaced line arrays), and those where some level of irregularity has been introduced.

- Develop parameterizations such that the number of optimization variables for large arrays can be reduced, while still allowing for a large variation in configuration irregularity.

- Systematically optimize the spatial configuration of large arrays in order to further improve the energy extraction performance. In particular, this refers to arrays that have too many optimization variables to be analyzed directly, i.e. to have their performance mapped out as a function of every variable.

- Provide guidelines for the improved design of WEC arrays, in terms of the number of bodies and their spatial configuration. These guidelines should address both regular and irregular seas. Address how these improvements are achieved, e.g. by increasing the energy extraction bandwidth in irregular seas, or by significantly improving energy extraction at a particular frequency.

- Address the effects of mean drift force on WEC arrays and other Very Large Floating Structures (VLFS). Develop a fast algorithm that enables a fast evaluation and minimization of these forces on an array of bodies.

1.3 Approach

This thesis will consider inviscid, potential flow of the fluid, with linear wave hydrodynamics and linear wave-body interaction. The linearity here implies that wave slopes are small, and that the motion of the body is also small. The problem will be addressed in frequency domain; we will consider monochromatic waves and irregular seas (multiple wave components either all aligned or having a directional spread). We will study axisymmetric bodies only, placed in a fluid of finite depth. The bodies are constrained to move in one degree of freedom only, and a passive power take-off device is connected to it.

The hydrodynamic model of wave interactions that satisfies the requirements laid out in the thesis objective is the multiple scattering theory (Kagemoto and Yue, 1986). It is (in principle) exact, it does not impose constraints on body size, shape, or inter-body spacing, and it has a very attractive feature that the performance of an array is built from the performances of individual bodies in isolation. For an array that is formed from bodies of the same type (or of few types), this means that with the changes in the spatial array configuration the characteristics of individual bodies do not need to be recalculated, but only their mutual interaction is recalculated. This makes it particularly appealing for array configuration optimization. Multiple scattering framework is, thus, a good model to build upon, and it is the main model used in this thesis. This thesis provides some theoretical and computational improvements to the model in order to better meet the objectives laid out in Section 1.2.

The thesis is organized in the following way. Chapter 2 covers the hydrodynamics of wave-body interaction and the dynamics of energy extraction of a single body, which serves as a building block for forming WEC arrays. It also contains a parametric study of energy extraction performance of a truncated vertical cylinder. A novel implementation of the multiple scattering framework for WEC arrays is introduced in Chapter 3. Chapter 4 contains the analyses of large structured arrays, where one or two parameters describing the array configuration have been systematically varied. It gives insights into the phenomena that occur in large WEC arrays, and serves as a motivation and provides explanations for Chapter 5, which contains results of optimized large arrays. These arrays have been optimized based on a larger set of optimization variables that make detailed systematic analysis computationally prohibitively expensive. In a slight departure from WEC arrays,

Chapter 6 covers a novel multiple scattering formulation of mean drift forces on an array, and provides results of an optimized VLFS. Finally, the findings and contributions of the thesis are summarized in Chapter 7, including some suggestions for extending this work in the future.

Chapter 2

An Isolated Body as an Energy Converter

A floating body set in motion by the waves is a fundamental part of many ocean wave energy extraction devices. It is also a basic building block for forming WEC arrays. This chapter reviews the basics of hydrodynamics of wave-body interaction, and describes the describes the performance of an isolated axisymmetric WEC and the optimal extraction conditions. It also contains a systematic study of energy-extraction performance of a truncated vertical cylinder as a function its radius and draft in monochromatic and irregular seas, and the effects of the PTO device. This analysis is the basis for the selection of the WEC device that is used in arrays in the later chapters of the thesis.

The shape of the chosen WEC is not optimized, but it is chosen such that it meets conflicting criteria — ensuring efficient energy extraction with limited body motions.

2.1 An Isolated Body as an Energy Harvester

The hydrodynamics and energetics of energy extraction by a floating body is reviewed here for completeness. These results are well known and can be found in many references, e.g. Mei, Stiassnie, and Yue (2005) and Evans (1981b).

2.1.1 The Hydrodynamics of Wave-Body Interaction

Consider a body floating in a fluid of finite depth h, being set into motion by the incoming monochromatic wave of amplitude A, angular frequency ω, and wavenumber k

$$k = \frac{2\pi}{\lambda},$$

where λ is the wavelength. We focus here on linear (small steepness $kA \ll 1$), time-harmonic waves only. We will use complex notation throughout, with the time-dependent term $e^{-i\omega t}$, unless otherwise stated. This term will be omitted in the text, but is always tacitly present. To get the real-valued physical quantities, the real part of the complex functions is to be taken in the end, unless stated otherwise (e.g. in power calculations).

The motion of water waves can be considered as inviscid, and thus can be modeled to a great degree of accuracy as governed by the potential flow. Under the potential flow assumption, the velocity field can be expressed in terms of a potential ϕ as

So the potential is $\hat{\phi} = \mathrm{Re}\,\phi e^{-i\omega t})$. Note that we will be using complex notation for all time-dependent quantities throughout this thesis, so a complex amplitude A stands for a time-dependent quantity $\hat{A} = \Re(Ae^{-i\omega t})$ is

The governing equation for the inviscid fluid is the Laplace equation

$$\nabla^2\phi = 0\,, \tag{2.1}$$

where ϕ is the velocity potential ($\boldsymbol{v} = \nabla\,\phi$). For the case of uniform depth, the depth dependence can be factored out, and the Laplace equation becomes the Helmholtz equation

$$\nabla_H\phi + k^2\,\phi = 0 \tag{2.2}$$

where k is the wavenumber, and ∇_H is the Laplace operator in the horizontal plane

$$\nabla_H \equiv \frac{\partial^2}{\partial x^2} + \frac{\partial^2}{\partial y^2}\,. \tag{2.3}$$

The potential ϕ needs to satisfy the combined linearized kinematic-dynamic boundary

condition on the free surface

$$-\omega^2\phi + g\frac{\partial\phi}{\partial z} = 0\,, \quad z = 0\,. \tag{2.4}$$

where g is the acceleration of gravity, and the kinematic no-flux condition on the bottom

$$\frac{\partial\phi}{\partial z} = 0\,, \quad z = -h\,. \tag{2.5}$$

Finally, equations (2.2), (2.4), and (2.5) lead to the dispersion relation for a fluid of finite depth

$$\omega^2 = gk\,\tanh kh\,. \tag{2.6}$$

In a non-dimensional form, the dispersion relation reads

$$\frac{\omega^2 h}{g} = kh\,\tanh kh\,. \tag{2.7}$$

For any frequency ω, there is a single k that satisfies the dispersion relation. Due to this relationship, quantities that are a function of frequency (say $f(\omega)$) will regularly be expressed as a function of wavenumber (say $f(kh)$ or $f(ka)$) and vice versa (in a slight abuse of notation), with the mapping between the frequency and the wavenumber according to (2.6) (or (2.7) tacitly implied.

A presence of a body will usually lead to the creation of evanescent waves in its vicinity. Evanescent waves do not propagate into the far field, and are governed by the modified Helmholtz equation

$$\nabla_H\phi - k^2\,\phi = 0\,. \tag{2.8}$$

They also satisfy a modified dispersion relation

$$\omega^2 = gk_i\,\tan k_i h\,, \tag{2.9}$$

which has an infinite number of real solutions k_i.

In general, the motion of a body in waves can lead to geometrical nonlinearities (changing of the body surface and volume, large angles of rotation) due to large motion amplitudes, even under the action of linear water waves. However, if the motion of the body is assumed

small as well, i.e. the amplitude of motion X of any degree of freedom is comparable to the wave amplitude A or smaller

$$|X| = O(A)\,, \tag{2.10}$$

then the general wave-body interaction problem can be broken into two simpler ones — the diffraction problem and the radiation problem (Mei, Stiassnie, and Yue, 2005).

The presence of a body scatters the incoming waves, which sets the body into motion, thus further radiating waves. This coupled wave-body interaction problem can be cleanly decoupled for linear problems, i.e. linear waves and small body motions. The total problem can be then considered by studying separately the diffraction problem, i.e. wave-body interaction for a fixed body, and a radiation problem where a body is oscillating in an otherwise undisturbed fluid. The total potential ϕ can thus be decomposed into

$$\phi = \phi^D + \sum_i U_i\,\phi_i^R = \phi^I + \phi^S + \sum_i U_i\,\phi_i^R \tag{2.11}$$

where ϕ^D is the diffraction potential consisting of the incoming wave potential ϕ^I and the scattered wave potential ϕ^S; $\phi_{,i}^R$ is the radiation potential due to the unit velocity in the i-th degree of freedom, and U_i is the corresponding velocity amplitude.

The diffraction potential ϕ^D needs to satisfy the homogeneous no-penetration condition on the body surface S

$$\frac{\partial \phi^D}{\partial n} = 0 \quad \Rightarrow \quad -\frac{\partial \phi^I}{\partial n} = \frac{\partial \phi^S}{\partial n} \quad @S\,, \tag{2.12}$$

where n is the unit normal of the surface S. The radiation potential ϕ_i^R needs to satisfy the non-homogeneous boundary condition caused by the body motion. For the unit velocity oscillation in direction k, the boundary condition for the radiation potential is

$$\frac{\partial \phi_k^R}{\partial n} = n_k \quad @S\,. \tag{2.13}$$

with n_k being the k-component of the surface normal.

The harmonic forces exerted on the floating body can be decomposed in a similar way. The diffraction force F is caused by the diffraction potential ϕ^D, and its k-th component is

given by

$$F_k = -i\omega\rho \int_S \phi^D \, n_k \, dS \, . \tag{2.14}$$

The radiation force F^R due to body motion can be decomposed into two components — one dependent on body velocity and one on body acceleration. The radiation force in direction k can be written as

$$\begin{aligned} F_k^R &= -i\omega\rho \int_S n_k \sum_j U_j \, \phi_j^R \, dS \\ &= -i\omega\rho \sum_j \left(\int_S \phi_j^R \, n_k \, dS \right) U_j \\ &= -\omega^2\rho \sum_j \left(\int_S \phi_j^R \, n_k \, dS \right) X_j \\ &= \sum_j \left(\omega^2 \mu_{kj}(\omega) + i\omega \, b_{kj}(\omega) \right) X_j \, , \end{aligned} \tag{2.15}$$

where the relationship between the body velocity and body motion

$$U_j = -i\omega X_j \tag{2.16}$$

has been used in the above. Due to their equivalence to the dynamic equation of motion of a body, the frequency-dependent hydrodynamic coefficients in (2.15) are called the added mass coefficient $\mu_{kj}(\omega)$

$$\mu_{kj}(\omega) = -\rho \, \mathrm{Re} \int_S \phi_j^R \, n_k \, dS \, , \tag{2.17}$$

and the radiation damping coefficient $b_{kj}(\omega)$

$$b_{kj}(\omega) = i\omega\rho \, \mathrm{Im} \int_S \phi_j^R \, n_k \, dS \, . \tag{2.18}$$

The added mass and damping coefficient are $N_{DOF} \times N_{DOF}$ matrices, and they are symmetric in terms of j and k

$$\mu_{kj}(\omega) = \mu_{jk}(\omega) \, , \quad b_{kj}(\omega) = b_{jk}(\omega) \, , \tag{2.19}$$

courtesy of Green's theorem (Mei, Stiassnie, and Yue, 2005). They are dependent on the submerged shape of the body and the frequency of the motion, but not on its amplitude. With these basic hydrodynamic concepts of wave-body interaction in place, we turn our

attention to the dynamics of power extraction.

2.1.2 Power Extraction by an Oscillating Body

The energy is extracted from the motion of a floating body by a power take-off (PTO) device that is connected to it. Throughout this thesis we will assume that the PTO device has linear properties, such that the force exerted by it (in the direction opposite to the motion) is

$$F_{PTO}(x) = c_{\mathrm{PTO}}\, x + b_{\mathrm{PTO}}\, \dot{x} \tag{2.20}$$

where x is the time-dependent motion amplitude, c_{PTO} is the elastic spring constant, and b_{PTO} the power extraction constant.

Due to the overall linearity of the problem (linear excitation force, linear restoring and damping forces), the governing equation of body motion simplifies to that for a forced harmonic oscillator. For simplicity, we will consider here motion in one degree of freedom only, so we will drop the subscript denoting the degree of freedom. The equation of motion in the frequency domain for a body oscillating in one degree of freedom is given by

$$\left[-\omega^2(m+\mu(\omega)) - i\omega(b(\omega)+b_{\mathrm{PTO}}) + (c+c_{\mathrm{PTO}})\right] X = F(\omega) \tag{2.21}$$

where X is the complex motion amplitude, $F(\omega)$ the diffraction force, and c is the restoring coefficient due to changes in buoyancy. For a body whose waterplane area is A_w, the restoring coefficient is

$$c = \rho g A_w \tag{2.22}$$

The radiation forces are represented by frequency-depended added mass $\mu(\omega)$ and damping $b(\omega)$ coefficients. All these quantities are for the corresponding degree of freedom. In the case of multiple degrees of freedom, X and F are replaced by their vector representations, and the coefficients by coefficient matrices.

The equation (2.21) for a given frequency ω represents a forced harmonic oscillator (FHO), whose motion amplitude is

$$X = \frac{F(\omega)}{-\omega^2(m+\mu(\omega)) - i\omega(b(\omega)+b_{\mathrm{PTO}}) + (c+c_{\mathrm{PTO}})}\,. \tag{2.23}$$

The behavior differs, however, from the standard FHO because the coefficients are func-

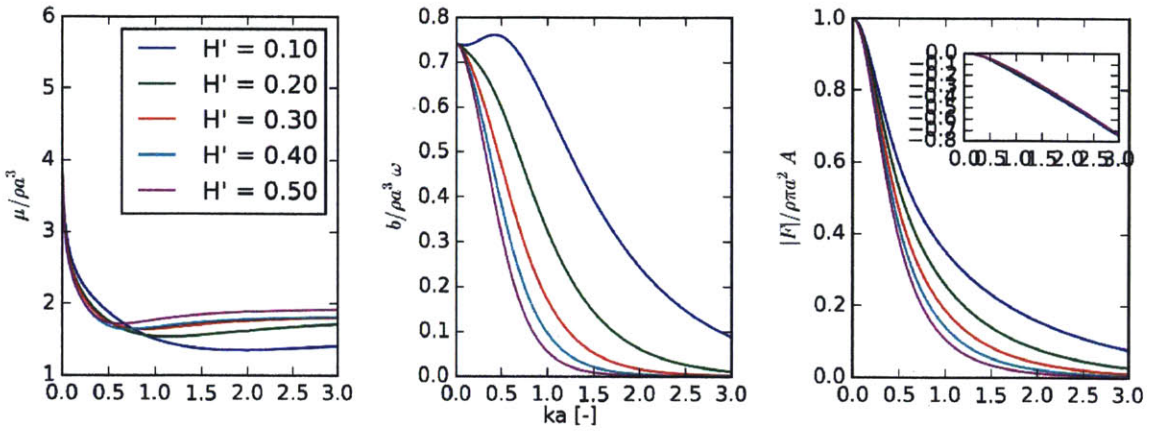

Figure 2.1: Added mass, radiation damping and diffraction force for a series of vertical truncated cylinders.

tions of frequency, not constants. The response is in general very similar qualitatively; the difference in the response would be for impulsive forcing, where in the absence of a PTO device an over-damped response cannot be achieved.

The added mass, damping and the diffraction force depend on the geometry of the body, but some features are similar for all bodies. Figure 2.1 shows added mass, damping and diffraction force for a range of vertical truncated cylinders with different radius-to-draft ratio. For long waves $ka \ll 1$, the diffraction force F tends to Froude-Krylov force where the only excitation is due to buoyancy variation.

The mean power P extracted by a WEC is $P = -\overline{F_{PTO}\,\dot{x}}$, or in the frequency domain

$$P(\omega) = \frac{1}{2} b_{\mathrm{PTO}} \dot{X}^* \dot{X} = \frac{1}{2} \omega^2 b_{\mathrm{PTO}} |X|^2 \tag{2.24}$$

The analysis of the optimality of energy extraction can be approached in two different ways. The first approach is to fix the frequency for which the maximum energy extraction is sought, and look for the device characteristics that would ensure it. This is usually the approach that one takes if the performance of a device at a single frequency, and not over the entire spectrum, is needed. The conditions for optimal energy extraction by an isolated device for a fixed frequency are well known (Mei, Stiassnie, and Yue, 2005), and the most important results are repeated here for completeness.

Consider a WEC operating with one degree of freedom only. We want to find the maximal power that can be extracted from waves for a certain frequency ω. For example,

this frequency could be the peak frequency ω_p of a wave spectrum. The extracted power is

$$P = \frac{1}{2} \frac{\omega^2 |F(\omega)|^2 b}{[c - \omega^2(m + \mu(\omega))]^2 + \omega^2(b + \lambda(\omega))^2} \tag{2.25}$$

The denominator is strictly positive, so making it smaller without influencing the numerator increases the power extraction. This can be achieved by making

$$c - \omega^2(m + \mu(\omega)) = 0\,. \tag{2.26}$$

This means that for optimal power extraction the device has to be tuned in such a way that at the given frequency it is in resonance, i.e. that ω should be equal to resonant frequency ω_0. This can be achieved by modifying the body geometry (affects c and $\mu(\omega)$), or by adding a an elastic restoring element with stiffness c_{PTO} to the PTO system.

Further improvements in extracted power can be made by modifying the extraction rate b. The optimal value of b is found by requiring

$$\frac{\partial P}{\partial b} = 0 \tag{2.27}$$

This leads to the condition at the given frequency $\omega = \omega_0$

$$b_{opt} = \lambda(\omega_0) \tag{2.28}$$

indicating that at the given frequency the optimal extraction rate is equal to the radiation damping coefficient. If these two conditions are satisfied, the power extraction at $\omega = \omega_0$ is

$$P_r = \frac{|F(\omega)|^2}{8b} = \frac{|F(\omega)|^2}{8\lambda(\omega)} \tag{2.29}$$

The conditions (2.26) and (2.28) ensure that the body achieves the highest energy extraction among all bodies.

To get a better scale of the extracted energy, we can normalize it by the energy flux carried by a monochromatic ocean wave of the same frequency. For a wave of unit length along the crest, the energy flux is given by (1.1)

$$P_w = \frac{1}{2}\rho g c_g A^2 \tag{2.30}$$

where c_g is the group velocity of the wave. The ratio of the extracted power and the incoming power flux is called *capture width* W

$$W \equiv \frac{P}{P_w} \tag{2.31}$$

and it corresponds to the (dimensional) width of the incoming wave crest from which all the energy has been extracted by the body. To make W non-dimensional, one can relate it to wavelength λ, or equivalently to wavenumber k, which leads to *non-dimensional capture width* kW.

The capture width of a device optimized according to (2.26) and (2.28) is

$$W_r = \frac{|F(\omega_0)|^2}{4\lambda(\omega_0)\rho g c_g} \tag{2.32}$$

This expression can be simplified by using Haskind relation (Mei, Stiassnie, and Yue, 2005, sec. 8.6.3)

$$b_{ii} = \frac{k}{8\pi\rho g c_g |A|^2} \int_0^{2\pi} |F_i(\omega;\theta)|^2 \, d\theta \tag{2.33}$$

where i is the degree of freedom in question. For an axisymmetric heaving cylinder, the expression (2.33) simplifies to

$$b_{33}(\omega) = \frac{k\,|F_3(\omega)|^2}{4\rho g c_g A^2} \tag{2.34}$$

which simplifies the expression for capture width to

$$W_r = 1/k_r \tag{2.35}$$

where k_r is the wavenumber corresponding to the resonant frequency ω_r. The normalization of W_r with the resonant wavenumber k_r The form of (2.35) begs for a non-dimensionalization of W by k_r, giving

$$(kW)_r = 1\ . \tag{2.36}$$

where $(kW)_r$ is The result (2.36), in addition to its simplicity, has another important consequence.

In addition to considering energy extraction from body dynamics (2.25), we can look at the power extraction and energy conservation from the hydrodynamics side. With the

use of the optical theorem (Mei, Stiassnie, and Yue, 2005, sec. 8.9.3), we find that the maximum value of kW that an axisymmetric device can achieve while oscillating in one degree of freedom is

$$(kW)_{max} = 1 \tag{2.37}$$

Combining (2.36) and (2.37) gives

$$(kW)_r = (kW)_{max} = 1 \ , \tag{2.38}$$

which means that the maximal value of the non-dimensional capture width that any axisymmetric body can achieve is 1, and it occurs at the resonant wavenumber k_r. Without (2.37), (2.36) would not be sufficient to ensure that the value of kW actually achieves an extreme at k_r with respect to the wavenumber.

We will call here the devices that are optimized according to criteria (2.26) and (2.28) (and,thus, achieve (2.36) at the resonant frequency), as *resonance-optimal* devices (or WECs).

Non-dimensional capture width kW is often confused with the efficiency of energy extraction. A clear maximum of kW at the body resonant frequency, however, makes it susceptible to misrepresent the resonant frequency as that where the energy extraction is the largest.

The power extraction is not maximum at the resonant frequency, even for the systems that satisfy (2.26) and (2.28). For such systems, a moment's consideration of (2.25) or (2.29) reveals that $\partial P/\partial\omega$ is not zero at ω_r.

Since the diffraction force F, the added mass $\mu(\omega)$ and the radiation damping are all general functions of frequency and the body shape, we do not have analytical expressions at hand to derive an optimality condition similar to (2.26) or (2.28). We can, however, obtain more knowledge about the location of the maximum of the power extraction of a resonance-optimal device by expanding (2.25) in Taylor series around the resonant frequency.

Going back the the question of the optimality of energy extraction, a second way to look at the problem is to fix the body shape, and look for the frequency (or the wavenumber) and the PTO rate b at which the extraction is maximum.

A different approach to the question of maximum energy extraction is to look for the

frequency at which the extraction is maximum, i.e. look for

$$\frac{\partial P}{\partial \omega} = 0 \, . \tag{2.39}$$

This condition is different than conditions (2.26) and (2.28), so bodies that achieve maximum energy extraction at a given frequency do not actually have a energy extraction peak at that frequency. This fact is not often mentioned in the literature. For example, one might look for the frequency that the body selected according to conditions (2.26) and (2.28)

We can find where the peak of the energy extraction of a body lies with respect to the resonant frequency by Taylor expanding (2.25) around the resonant frequency ω_0.

2.1.3 Power Extraction Characteristics for Irregular Seas

The total power P^S that a device can extract when operating in irregular seas is

$$P^S = \int P(\omega)\, S(\omega)\, d\omega \, , \tag{2.40}$$

where $S(\omega)$ is the ocean wave spectrum. Ocean spectra are usually of the form of a Gamma spectrum **NREL**

$$s(content) \tag{2.41}$$

with the peak frequency The energy flux carried by irregular waves that are impinging on the body is

$$P_w^S = \rho g \int S(\omega) c_g \, d\omega \tag{2.42}$$

The energy period T_e (and the corresponding energy frequency ω_e, wavenumber k_e) is related to the period of waves that have the largest energy flux.

Similar to the approach for monochromatic waves, we define a *spectral capture width* W^s which is the ratio between P^S and the total incoming energy flux

$$W^s \equiv \frac{P^S}{\rho g \int S(\omega) c_g \, d\omega} \tag{2.43}$$

The choice of a non-dimensionalization quantity is not immediately obvious as for the monochromatic waves. Some of the choices for the non-dimensionalization quantity are the spectrum peak wavenumber k_p, spectrum mean wave-number k_1 For example, we can use

We proceed to define *spectral non-dimensional capture width* $k_p W^s$ We further define W^s/D

For a given ocean spectrum, we are free to vary the body geomerty $\mathcal{G}$ and the PTO characteristic b_{PTO} in order to find the maximum extracted energy. This leads to the conditions

$$\begin{aligned} \frac{\partial P^S}{\partial b_{\text{PTO}}} &= \int S(\omega) \frac{\partial P}{\partial b_{\text{PTO}}} \, d\omega \\ \frac{\partial P^S}{\partial \mathcal{G}} &= \int S(\omega) \frac{\partial P}{\partial \mathcal{G}} \, d\omega \end{aligned} \tag{2.44}$$

In this thesis, the PTO characteristics are assumed not to be tunable. They can be set to a optimal value for some frequency based on (2.28), and this value is used for all other frequencies. This makes it crucial to understand the behavior of the WEC away from optimal condition it is tuned for. In particular, it is interesting to compare the bandwidth where the energy extraction is significant to the bandwidth where significant energy exists in the wave spectrum.

For a freely floating body, the mass of the body is not independent from the shape. Once the underwater shape of a WEC is chosen, this fixes the mass of the body by Archimedes principle.

In addition to tuning the PTO extraction rate to optimize the power extraction, could something else be made to improve the performance of the device? This is especially interesting over a larger range of frequencies where the energy carried by the waves is larger. Since the added mass and damping are related to body geometry, they cannot be modified (if we stick with the same body geometry). However, the diffraction force $\mathbf{F}^D$ depends on the environment, and modifying its frequency-dependent behavior could lead to an increased power-absorption bandwidth. One way of modifying the diffraction force is to place many bodies into an array. In that case the interactions between the scattered and radiated waves from many bodies would create a different wave picture around a body, possibly leading the increased performance. This is a problem that we study in the next chapter.

2.2 Vertical Truncated Cylinder as WEC

What do conditions described in the previous section mean for a real power converter? Here we conduct a systematic study of a truncated vertical cylinder heaving in water of finite depth, and study its performance as a function of its radius a and draft H. We are primarily

interested in maximal power extraction, extraction bandwidth, and motion amplitudes of the device.

As shown in the previous section, the maximal non-dimensional capture width kW of an axisymmetric device moving in one degree of freedom is 1, regardless of its shape. The body shape, however, affects the bandwidth of effective power extraction. The capture width kW for truncated cylinders of different radii $a' \equiv a/h$ and drafts $H' \equiv H/h$ are shown in Figure 2.2. Clearly, increasing the cylinder draft H' narrows the extraction bandwidth drastically, while increasing the radius moves the resonant frequency to lower values.

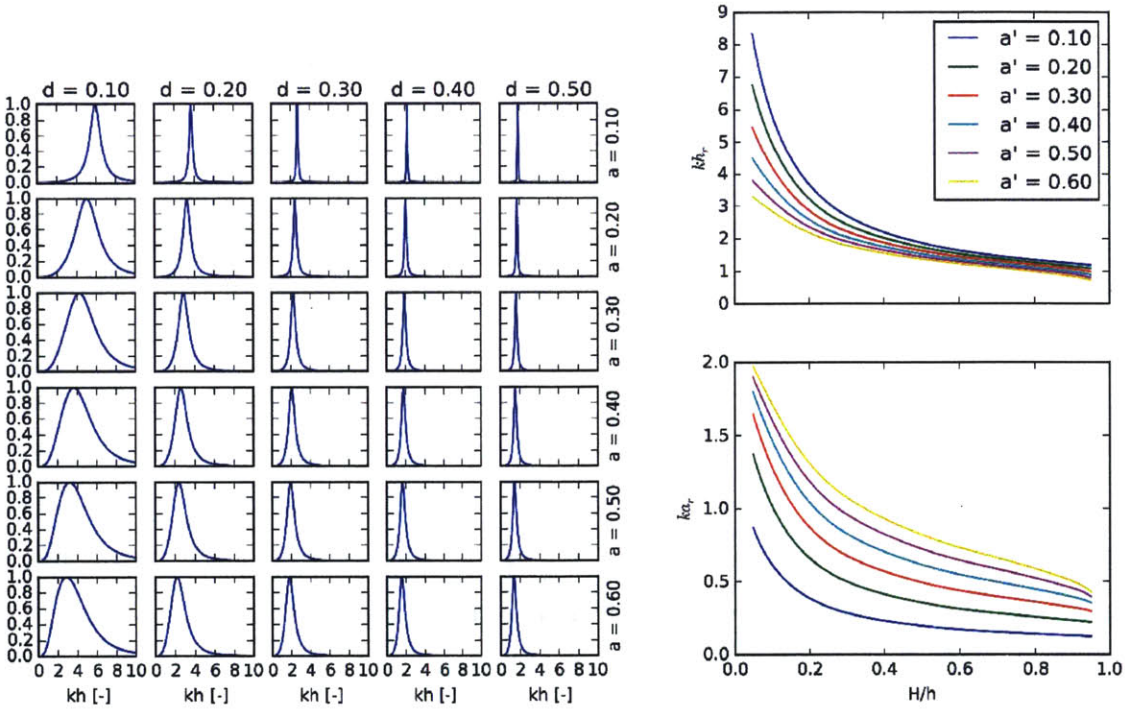

Figure 2.2: Non-dimensional capture width kW for truncated cylinders of different radius $a' = a/h$ and draft $H' = H/h$.

The normalized capture width kW can be somewhat misleading, however. Although it gives a nice theoretical bound $kW_{\max} = 1$, it relates the dimensional capture width W to the incident wavelength λ. One could be inclined to believe that for long waves $kh \ll 1$, a WEC can extract energy from a vast extent of the incoming wave crest. This is better visualized when capture width is normalized by a characteristic body dimension. Figure 2.3 shows that the maximal capture width $W_{\max}$ normalized by body diameter $D = 2a$ is $O(1)$ for a range of different geometries of TVCs in heave. For TVCs with large aspect ratio

H/D, especially those with small radius a/h, the maximal capture width is larger than the body diameter D, i.e. the body extracts the energy

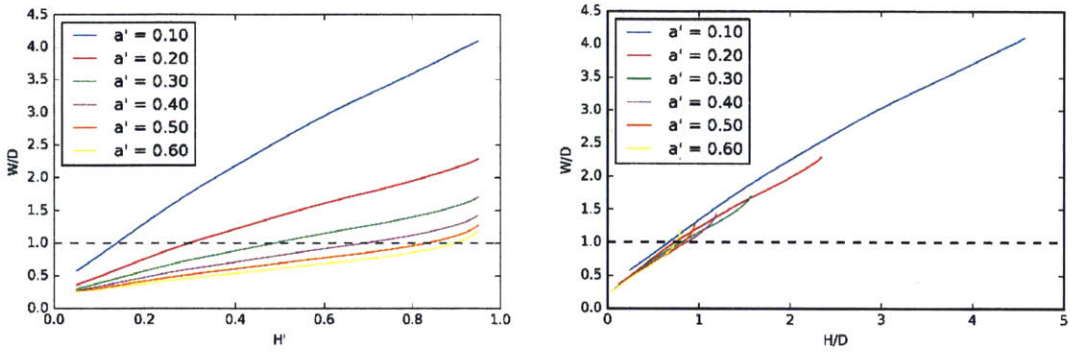

Figure 2.3: Maximal value of capture width ratio $W_{\max}/D$, $D = 2a$ as a function of (a) cylinder draft H/h, and (b) aspect ratio H/D, for different radii a/h. Cylinders of large aspect ratio H/D, the capture width is larger than cylinder diameter D.

The shape of the body greatly affects the motion amplitude as well, which is especially pronounced at resonance. Some characteristic motion amplitudes that correspond to truncated cylinders of different shape are shown in Figure 2.4a. For long waves the motion of the body exactly follows the wave elevation, so $|X/A|$ goes to 1 for $ka \ll 1$. The resonant motion, however, can greatly exceed 1 for some shapes. This is especially pronounced with the increase of body draft H', Figure 2.5a. For "shallow" cylinders, i.e. for those with small values of H/a, the body motion does not exceed 1 even at resonance. In the framework of simple harmonic oscillator, these cylinders can be considered as *over-damped*. The correspondence is not entirely correct, because a heaving cylinder is a harmonic oscillator with variable, frequency dependent coefficients, but the resulting behavior is very similar to constant-coefficient harmonic oscillator, Figure 2.4b.

2.3 Selection of a good WEC(s)

2.3.1 Ocean Spectra

Wave energy converters are usually not exposed to monochromatic waves, but operate in a realistic ocean environment, and are exposed to waves of different frequencies and amplitudes. Typical ocean spectra like Brentschneider or Pierson-Moskowitz carry significant energy at a rather large range of frequencies, i.e. they have a large bandwith. The power spectral density $S(\omega)$ of a standard gamma spectrum in deep water is defined as (Faltinsen,

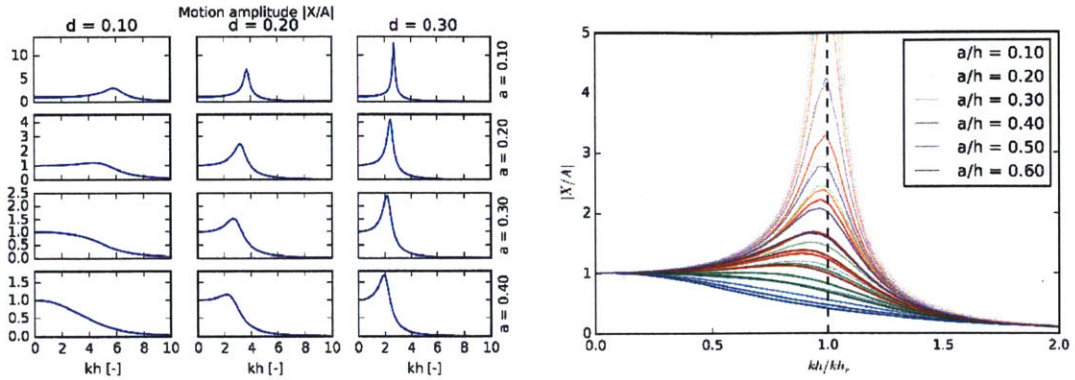

(a) (b)

Figure 2.4: Motion amplitude $|X/A|$ for truncated cylinders of different radius a' and draft H/h, as a function of (a) wavenumber kh, and (b) normalized wavenumber kh/kh_r.

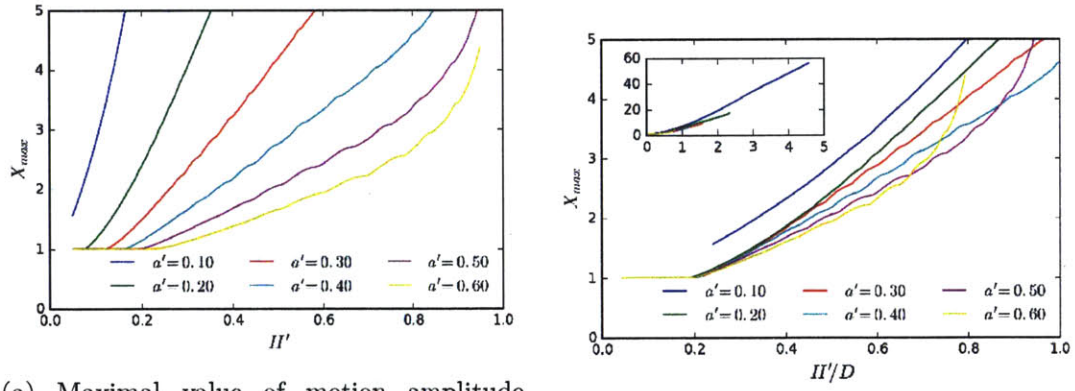

(a) Maximal value of motion amplitude $|X_{\max}/A|$ as a function of cylinder draft H', for different radii a'. The increase in cylinder draft is followed by a more excessive motion at resonance.

(b) Maximal value of motion amplitude $|X_{\max}/A|$ as a function of cylinder aspect ratio H'/D, for different radii a'. .

Figure 2.5: Maximal values of motion amplitude $|X_{\max}/A|$.

1993)

$$S'(\omega') = \frac{S(\omega')}{T_1 H_s^2} = \frac{A}{\omega'^5} e^{-B\omega'^4} \tag{2.45}$$

where T_1 is the mean wave period, H_s the significant wave height, and ω' is the normalized frequency

$$\omega' \equiv \frac{\omega}{\omega_1} = \frac{T_1}{T} \, . \tag{2.46}$$

The parameters A and B depend on fetch etc. For example, for Brentschneider spectrum for fully developed seas, the A and B parameters are

$$A = \frac{1.25}{8\pi}, \quad B = 1.25\,. \tag{2.47}$$

For a Brentschneider spectrum, the maximum value of $S(\omega')$ occurs at $\omega' = 1$. The maximum value of energy flux $S(\omega)\,c_g$, i.e. the energy carried towards an extracting device(s), occurs at a frequency $\omega'_e < 1$.

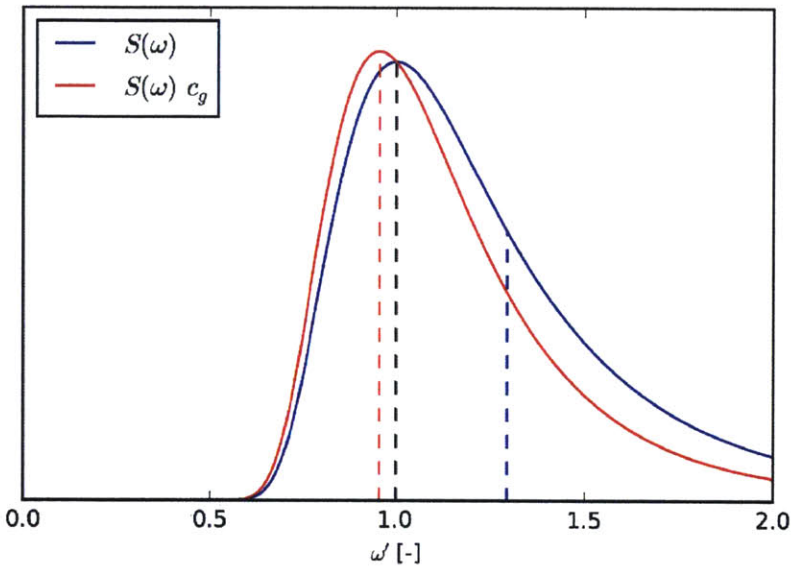

Figure 2.6: Energy density $S(\omega')$ and energy flux $S(\omega')\,c_g$ for Brentschneider spectrum. Characteristic frequencies $\omega'_1 = 1$, ω'_0, and ω'_e are denoted by dashed lines.

One of the main objectives of an effective WEC is to have a energy extraction bandwidth comparable to the energy bandwidth of the wave spectrum the device is operating in. The spectrum definition (2.45) depends on the mean wave period T_1, which is an external variable, so it has to be set before a one-to-one comparison between of energy bandwidths Δkh and $\Delta\omega'$ can be made.

$$\begin{aligned}
\Delta\omega' &= \frac{\omega_b - \omega_a}{\omega_1} \\
&= \frac{g}{h\omega_1}\left(\sqrt{k_b h \tanh k_b h} - \sqrt{k_a h \tanh k_a h}\right) \\
&= \frac{g}{h\omega_1}\, f(k_a h, k_b h)
\end{aligned} \tag{2.48}$$

For truncated vertical cylinders, larger bandwidths occur for small H/h and larger a/h.

Ideally, a WEC should, relative to its size, have large power extraction at resonance with not too excessive motions, and large energy extraction bandwidth. As shown on the example of TVCs (Figures), these requirements cannot be simultaneously achieved. Shallow TVCs, i.e. those with larger a' and small H', have well correlated relatively large bandwidths and moderate motion amplitudes at resonance that makes them a good choice for WECs. Their capture width relative to their diameter is not as good (Figure 2.3), however.

A good way to choose a WEC is to have its resonance frequency match the energy frequency ω_e, i.e. the frequency where energy flux $S(\omega)\, c_g$ is maximum. This depends on the mean wave period and water depth (for finite water depths). Figure 2.8 shows the wavenumber kh_e that corresponds to ω_e' for different peak periods T_p and water depths h.

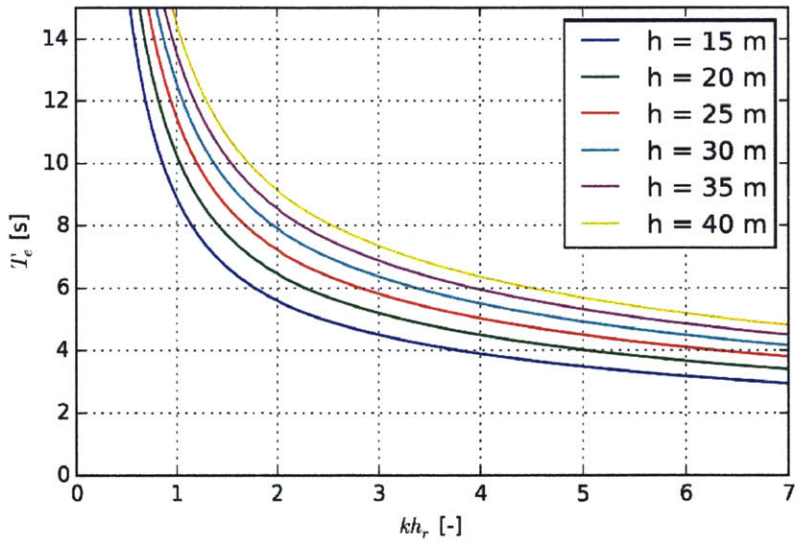

Figure 2.7: Energy period T_e that corresponds to resonant wavelength kh_r for different water depths h.

The PTO device for irregular seas can be selected so that it maximizes the energy extraction at a particular frequency, following the same procedure as for monochromatic waves. The WEC device can be tuned such that the resonance occurs at spectral peak frequency, ensuring large energy extraction

2.3.2 The effect of the PTO device

When it comes to monochromatic seas, tuning the PTO device such that it matches the hydrodynamic damping at resonance leads to high energy extractions. If a WEC with a tunable PTO device is operating in monochromatic waves, it could be set to satisfy the

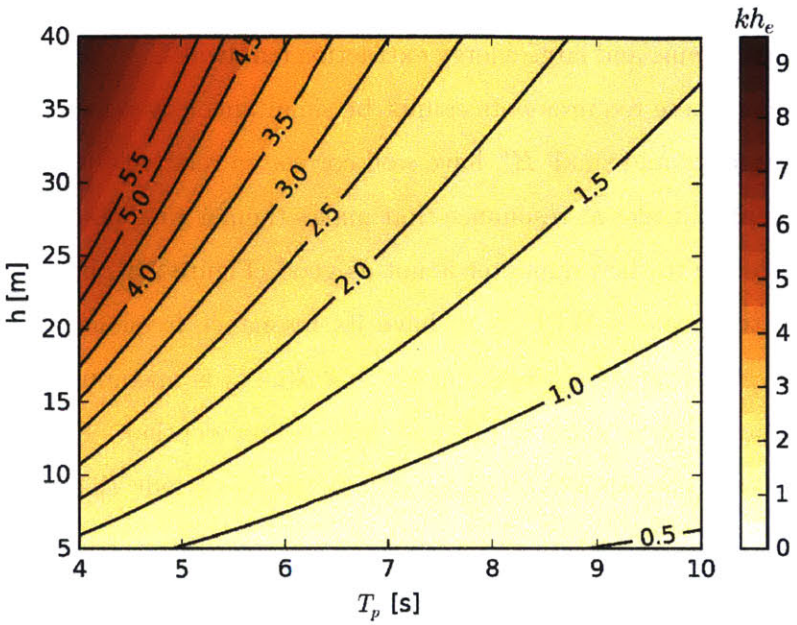

Figure 2.8: Contours of wavenumber kh_e that corresponds to energy frequency ω_e' for different peak periods T_p and water depths h.

conditions (2.26) and (2.28) for optimal energy extraction at any frequency ω (not occurring simultaneously). However, if the device is not tunable, its performance can be significantly diminished away from the resonance frequency. Furthermore, if a WEC is operating in irregular seas where waves of many frequencies are simultaneously present, actively tuning PTO device to resonant conditions for every component is not possible. The PTO device could be tuned according to (2.28) to match the resonant characteristic of the most energetic wave component ω_p in the spectrum, or one might look for PTO characteristics that would give maximal performance in spectral sense, i.e.

$$\frac{\partial P^S}{\partial b} = \int_\omega S(\omega) \frac{\partial P}{\partial b} \, d\omega \, . \tag{2.49}$$

In this case, a simple analytical result like (2.28) does not exist because of the non-trivial frequency-dependent behavior of hydrodynamic quantities.

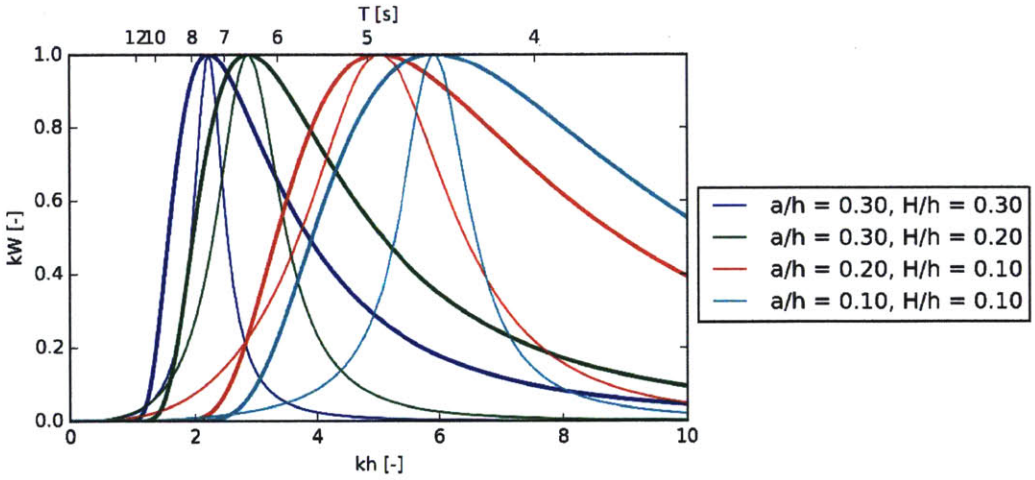

Figure 2.9: Nondimensional capture width kW of several TVCs with spectra that have energy frequency ω_e that matches TVC resonant frequency. Peak periods of these spectra are denoted on the upper border.

Chapter 3

Mathematical Formulation of Array Interactions for Energy Extraction

In this chapter we describe the mathematical framework that is used in the rest of the thesis. The framework is based on the multiple scattering approach, which uses transfer matrices of isolated bodies to obtain in principle an exact solution to the scattering problem.

Section §3.1 reviews some of the present methods for studying the interactions of waves with both finite and infinite arrays of bodies. We then review an existing multiple scattering approach and introduce a novel decomposition of array forces that enables an increase in computational speed, and is more consistent with the overall methodology. We then further extend the multiple scattering framework to allow the calculation of closely spaced group of bodies in a periodic array.

3.1 Literature Review

The multiple scattering approach in ocean waves problems was first studied by Spring and Monkmeyer (1974). They studied the interaction of bottom mounted cylinders, and applied the boundary conditions on all cylinders simultaneously, leading to a linear system for the unknown coefficients. Note that they call this method "direct matrix method", while they reserve the term "multiple scattering" for the method where scattered waves from different

cylinders are sequentially added and approach the "direct" solution. We follow here a slightly different terminology (see e.g. Martin, 2006), where *multiple scattering* refers to the direct method of solving for the unknown scattering coefficients, while *order of scattering* refers to the iterative method like used by Twersky (1952).

Linton and Evans (1990) employed the same multiple scattering approach as Spring & Monkmeyer. The difference between that approach and Kagemoto and Yue (1986) is that the former is only valid for bottom-mounted cylinders.

The hydrodynamic analysis into using arrays of bodies as a means of energy extraction has started with Evans (Evans, 1980) and Falnes (Falnes, 1980), both arriving at the same expression independently. They extended the theory to account for parallel infinite rows of absorbers (Falnes and Budal, 1982; Falnes, 1984).

When dealing with bottom-mounted cylinders in water of constant depth, the depth dependency can be factored out, and the remaining problem is identical to a well-known problem in acoustics of scattering by a sound hard cylinders.

Following an approach similar to Kagemoto & Yue, Linton and Evans (1990) studied the diffraction and drift forces on small arrays of bottom-mounted cylinders (4 bodies in Linton and Evans (1990), 4,5,6 cylinders in Evans and Porter (1997)).

Duclos and Clément (2004) use the multiple scattering formulation of study the influence of near-trapped waves on the diffraction force amplification on arrays of bottom-mounted cylinders (16 and 38 bodies). They also studied the effects of deviation from regular spacing on the average transmission coefficient behind the array.

Periodic arrays of scatterers have been handled with different methods. Linton, McIver and Evans have studied the periodic arrays by placing the body inside an infinite channel and using so-called channel multipoles — eigenfunctions that satisfy the free surface conditions, appropriate radiation conditoin and the boundary conditions on channel walls — for N bodies in a channel of constant depth (Linton and McIver, 1996), radiation and diffraction by a circular cylinder in a channel (Linton and Evans, 1992)

For doubly-periodic arrays, Mei has employed methods of multiple scales for small scatterers $ka \ll 1$ in a series of papers (Li and Mei, 2007b; Li and Mei, 2007a). In particular, he studied the effects of Bragg scattering on energy extraction (Garnaud and Mei, 2010).

The wide-spacing approximation between the infinite rows of scatterers for ocean waves problems has been studied by Dalrymple, Seo, and Martin (1988) where the expressions

for the transmission and reflection coefficients of widely spaced rows of bottom-mounted cylinders are derived. A similar method has been derived by Peter and Meylan (2009).

Doubly-periodic arrays for long waves (wavelength much larger than the spacing) have also been studied by homogenization (Hu, Shen, et al., 2004; Hu and Chan, 2005; Hu, Chan, et al., 2011), and used to study band structure of a dense doubly periodic arrays of bottom-mounted cylinders and resonators. These methods, however, require a doubly periodic array

3.2 Multiple Scattering Formulation for Finite-Size Arrays

We consider a problem of wave-body interaction where an incoming wave is scattered by multiple bodies that may be set into motion by the wave forcing and, thus, further radiate waves. We model the hydrodynamics of the wave-body interaction within the classical multiple scattering framework (Kagemoto and Yue, 1986). This approach is reviewed first and then modified to decouple single body dynamics from the array interactions.

In general, the total potential Φ for N_b oscillating bodies can be written as

$$\Phi = \Phi^I + \sum_{i=1}^{N_b} \left(\Phi^{S,i} + \sum_k V_k^i \, \Phi_k^{R,i} \right) \tag{3.1}$$

where Φ^I represents the incoming planar wave, $\Phi^{S,n}$ the diffraction potential of body n and $\Phi_k^{R,n}$ radiation potential of body n oscillating in mode k with unit velocity amplitude; the actual complex velocity in mode k of body n is V_k^n. Mode k denotes one of six degrees of freedom ($k \in \mathcal{M}$; $\mathcal{M} \subset \mathcal{D} = \{1, 2, \ldots, 6\}$), where directions $1, 2, 3$ correspond to the translation modes of motion (surge, sway, heave) and $4, 5, 6$ to the rotational modes (roll, pitch, yaw).

The incoming field $\Phi^{I,j}$ on body j can be written as

$$\begin{aligned} \Phi^{I,j}(\mathbf{r}_j) &\equiv \Phi - \Phi^{S,j} - \sum_k V_j^k \Phi_k^{R,j} \\ &= \Phi^I + \sum_{i=1, i\neq j}^{N_b} \left(\Phi^{S,i}(\mathbf{r}_i) + \sum_k V_i^k \Phi_k^{R,i}(\mathbf{r}_i) \right) , \end{aligned} \tag{3.2}$$

so that the total potential at body j can also be written as

$$\Phi = \Phi^{I,j} + \Phi^{S,j} + \sum_k V_j^k \Phi_k^{R,j} \ . \tag{3.3}$$

We can expand the potentials near body j in terms of radial incoming and outgoing partial waves, i.e. Hankel functions and modified Bessel functions, which are fundamental solutions of the Helmholtz equation. In the cylindrical coordinate system (r_j, ϑ_j, z) of body j, the general incoming potential can be written as

$$\Phi^{I,j} = \sum_{m,n} d_{nm}^j I_n(k_m r_j) e^{in\vartheta_j} \psi_m(z) \ , \tag{3.4}$$

where $I_n(z)$ is the modified Bessel function of the first kind, d_{nm}^j are the coefficients of the incoming partial waves, and

$$\sum_{m,n} \equiv \sum_{m=0}^{\infty} \sum_{n=-\infty}^{\infty} \ . \tag{3.5}$$

The scattered potential can be written as

$$\Phi^{S,j} = \sum_{m,n} c_{nm}^j K_n(k_m r_j) e^{in\vartheta_j} \psi_m(z) \ , \tag{3.6}$$

where $K_n(z)$ is the modified Bessel function of the second kind, and c_{nm}^j are the coefficients of the scattered, outgoing partial waves. Similarly we can write the radiation potential of body j as

$$\Phi_k^{R,j} = \sum_{m,n} c_{nm}^{R,k,j} K_n(k_m r_j) e^{in\vartheta_j} \psi_m(z) \ , \tag{3.7}$$

where $c_{nm}^{R,k,j}$ are the coefficients of the radiated, outgoing partial waves due to motion of body j in direction k. In the above expressions, we have used the identities between modified Bessel functions and Hankel and Bessel functions

$$K_n(-ix) = \frac{\pi}{2} i^{n+1} H_n^{(1)}(x) \tag{3.8}$$

$$I_n(-ix) = i^{-n} J_n(x) \tag{3.9}$$

to simplify the expressions. Hankel function $H_n^{(1)}(x) = J_n(x) + iY_n(x)$ represents a outward

propagating wave. With that, the propagating mode is $m = 0$, with

$$k_0 = -ik \,, \tag{3.10}$$

while the rest of the evanescent modes are for $m > 0$, with k_m being the solutions of the modified dispersion relation (2.9).

Since the overall problem is linear, there exists a linear mapping between c_{nm}^j and d_{nm}^j. This mapping is determined from the diffraction boundary condition (2.12) on body j, and it is dependent solely on the shape of the body. We can express that in matrix form as

$$c^j = T^j d^j \,, \tag{3.11}$$

where c_j and d_j are vectorized versions of the set of coefficients c_{nm}^j and d_{nm}^j, respectively. The particular order in which the vectorization is conducted is not important, as long as it is consistent.

The most important ingredient of (3.11) is *diffraction transfer matrix* T^j or *T-matrix* of body j. The T-matrix is the basic component of the multiple scattering framework. It is independent of the actual wave field around the body, so it can be calculated for the body in isolation. The T-matrix can be calculated either analytically or numerically, depending on the body shape, but the particular method of calculating it is not a subject of this thesis. (The T-matrix for truncated vertical cylinders used in this thesis can be calculated analytically, and it is given in Appendix B.)

Note that because there are in general infinite number of partial waves (in both radial and angular direction), the vectors of coefficients c^j and d^j are infinitely long, and the T-matrix is doubly-infinite in size. The infinite length ensures that the formulation is still exact, no approximations have been made. However, to make the problem computationally tractable, we truncate the limits of summation of radial modes to M and the number of angular modes to N_p

$$\sum_{m=0}^{\infty} \to \sum_{m=0}^{M}, \quad \sum_{n=-\infty}^{\infty} \to \sum_{n=-N_p}^{N_p} \,. \tag{3.12}$$

This inevitably introduces a truncation error into the calculation results, but the formulation is still generally applicable, and no physical approximations have been made. With such

truncation, c^j and d^j are of the size $1 \times M_t$, where

$$M_t \equiv (2N_p + 1) \times (M + 1)\,, \tag{3.13}$$

while T^j is of the size $M_t \times M_t$.

In order to fully express the potentials on body j in coordinate system of body j so that we can use the (3.11), there are two ingredients missing — (i) scattering potentials in coordinate systems of other bodies from (3.2) need to be expressed in the coordinate system of body j; and (ii) the oscillation velocities V_j^k need to be related to the wave field.

We can transform the partial waves that are in coordinate system i into partial waves in coordinate system j by using Graf's addition theorem for Bessel functions (Abramowitz and Stegun, 1964)

$$K_n(k_m r_i)e^{in\theta_i} = \sum_{l=-\infty}^{\infty} (-1)^l\, K_{n-l}(k_m R_{ij})\, e^{i(n-l)\alpha_{ij}}\, I_l(k_m r_j)\, e^{il\theta_j}, \quad r_j < R_{ij} \tag{3.14}$$

We can express (3.14) in matrix form as a relation between partial wave $K_n(k_m r_i)e^{in\theta_i}$ body-i coordinate system and $I_l(k_m r_j)\, e^{il\theta_j}$ in body-j coordinate system as a matrix S^{ij}, whose elements are

$$(S^{ij})_{n-l,m} = (-1)^l\, K_{n-l}(k_m R_{ij})\, e^{i(n-l)\alpha_{ij}} \tag{3.15}$$

The matrix S^{ij} is called *separation matrix*, and it only depends on the relative position between two bodies. Similar to T-matrix, the ordering of elements in S^{ij} is not important, as long as it is consistent with the ordering of T-matrix. The size of S^{ij} is $M_t \times M_t$, the same as for T^j.

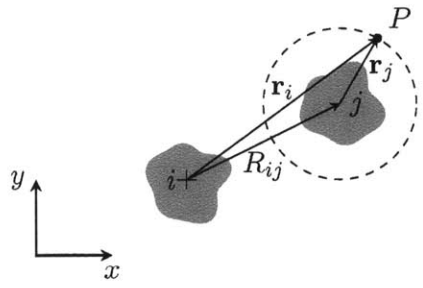

Figure 3.1: Coordinate systems for bodies i and j.

Transfer matrix for body dynamics. The oscillation velocity of body i should be determined from the equation of motion, similar to (2.21) for an isolated body. However, the hydrodynamic forces occurring on the body in an array are different, so the equation of motion needs to change. The standard way how this is done in the literature is to calculate the added mass and radiation damping coefficients for *an array as a whole.* The coefficient matrices then become 4-dimensional, i.e. they are described by four indices (e.g. added mass of body i in direction k due to the motion of body j in direction l). This method has drawbacks in that every time that the configuration of the array is change, all the hydrodynamic coefficients need to be recalculated because they depend on the relative positions between the bodies. Here I introduce a novel way of decomposing forces in an array so that hydrodynamic coefficients remain that of an isolated body, and independent on the spatial array configuration.

The equation of motion for a body j in an array with spatial configuration $\mathcal{C}$ can be written as

$$A^j \cdot X^j = F^j(\omega, \mathcal{C}) \tag{3.16}$$

where A^j is the system matrix from (2.21), X^j the amplitude of motion, and F^j the total diffraction force on body j. Instead of modifying the matrix A^j (i.e the added mass and radiation damping) due to the array effects, we use linearity of the system and modify the diffraction force F. Using the linearity of wave-body interaction, the diffraction force on a body can be related to scattering coefficients of the outgoing partial waves c^j

$$F^j = \hat{F}^{j^T} \cdot c^j \ , \tag{3.17}$$

where $\hat{F}^j$ is the *diffraction force transfer matrix* of body j, which can be calculated for a body in isolation ($\hat{F}$ for a truncated cylinder is given in Appendix B). For a body with N_{DOF} degrees of freedom, the size of $\hat{F}^j$ is $M_t \times N_{DOF}$. By relating the velocity to the motion amplitude

$$V_k^j = -i\omega X_k^j \ , \tag{3.18}$$

we can express velocity of body j completely in terms of the scattering coefficients c^j

$$V^j = \varpi^{j^T} \cdot c^j \tag{3.19}$$

where ϖ^j is the *velocity transfer matrix*

$$\varpi^j = -i\omega \hat{F}^j \cdot (A^j)^{-1} \,. \tag{3.20}$$

In the new formulation, the hydrodynamic coefficients (added mass, damping) remain the same as calculated for an isolated body. The diffraction force is what changes when bodies are in proximity. In the old formulation, the diffraction force on each body would remain the same, but the hydrodynamic coefficients would be altered. This made sense if the scatterers were actually a part of a bigger structure, so that all of them were connected.

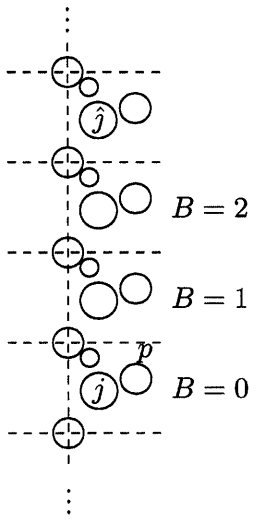

Figure 3.2: Infinite row of periodically repeated configuration of scatterers

3.3 Scattering by an infinite row of periodically placed scatterers

In this section, I present a novel multiple scattering formulation for periodic arrays, formed by cells with multiple closely-spaced bodies. This extends the formulations for periodic arrays with rows that are far apart (Peter, Meylan, and Linton, 2006). For brevity, the exposition here is mostly for fixed bodies. The extension to oscillating (and energy extracting) bodies is equivalent to that in 3.2, and it is made in the end of this section.

Consider an infinite array formed by periodically repeating a configuration $\mathcal{C}$ of N_b bodies along the y-axis, Figure 3.2, with periodicity d. Such an array is often called a diffraction grating The configuration $\mathcal{C}$ consists of a finite number of bodies but is otherwise completely general. Let $\mathbb{B}$ denote the set of all bodies in $\mathcal{C}$.

$$\mathbb{B} = \{\mathcal{B}_i \,|\, i = 1, \ldots, N_b\} \tag{3.21}$$

Each of the bodies $\mathcal{B}_i$ in $\mathbb{B}$ is of arbitrary shape, and the spacing between them (i.e. the configuration $\mathcal{C}$) is arbitrary. The incoming wave is propagating with angle θ_I relative to the positive x-axis.

A periodic array can be viewed as if it is built of identical cells of width d that are stacked in y-direction. We can assign an index B to label each of the cells; $B = 0$ denotes

the cell where the origin is, say. We can also assign an index $\hat{\jmath}$ to each of the bodies in the array. The bodies are labeled in a cell-first manner, i.e. such that we first label all the bodies within cell B before moving to cell $B+1$; the labeling within a cell is always done in the same manner. In that case we can relate a general body index $\hat{\jmath}$ to an index i in the basic cell $B=0$ by

$$\begin{aligned} B &= \left\lfloor \frac{\hat{\jmath}}{N_b} \right\rfloor \\ j &= \hat{\jmath} - B\,N_b\,, \end{aligned} \tag{3.22}$$

where $\lfloor \cdot \rfloor$ denotes the floor function.

The scattering potential of body $\mathcal{B}_p$ is given by

$$\Phi^{S,p} = \sum_{m,n} c_{nm}^{p} K_n(k_m r_p) e^{in\vartheta_p} \psi_m(z) \tag{3.23}$$

where

$$\sum_{m,n} \equiv \sum_{m=0}^{\infty} \sum_{n=-\infty}^{\infty} \tag{3.24}$$

The body $\mathcal{B}_p$ can be in the basic cell $B=0$, without the loss of generality. The incoming wave on $\mathcal{B}_p$ consists of the ambient incoming wave Φ^I, and of the scattered waves from all the other bodies in the array.

$$\begin{aligned} \Phi^{I,p} &= \Phi^I + \sum_{\hat{\jmath}\in\mathbb{Z},\hat{\jmath}\neq p} \Phi^{S,\hat{\jmath}} \\ &= P_p^0 \sum_{n=-\infty}^{\infty} (-1)^n I_n(k_0 r_p) e^{in\vartheta_p} e^{-in\theta} \psi_0(z) + \sum_{\substack{\hat{\jmath}\in\mathbb{Z},\\ \hat{\jmath}\neq p}} \sum_{m,n} c_{nm}^{\hat{\jmath}} K_n(k_m r_{\hat{\jmath}}) e^{in\vartheta_{\hat{\jmath}}} \psi_m(z) \end{aligned} \tag{3.25}$$

where $P_p^0 = e^{i(kx_p\cos\theta + ky_p\sin\theta)}$ is the phase of the incoming wave at body $\mathcal{B}_p$.

Analogous to the approach in Section 3.2, we can transform the body $\mathcal{B}_{\hat{\jmath}}$-based coordinate system into a $\mathcal{B}_j$-based one by using Graf's addition theorem (3.14), giving

$$\Phi^{I,p} = \sum_{m,l} (-1)^l I_l(k_m r_p) e^{il\vartheta_p} \psi_m(z) \left(\delta_{m0} P_p^0 e^{-il\theta} + \sum_{\substack{\hat{\jmath}\in\mathbb{Z},\\ \hat{\jmath}\neq p}} \sum_{n=-\infty}^{\infty} c_{nm}^{\hat{\jmath}} K_{n-l}(k_m R_{\hat{\jmath}p}) e^{i(n-l)\alpha_{\hat{\jmath}p}} \right) \tag{3.26}$$

where $R_{\hat{\jmath}p}$ is the distance between bodies $\hat{\jmath}$ and p, and $\alpha_{\hat{\jmath}p}$ the angle between them. The problem now is how to sum the contributions coming from an infinite number of bodies.

The summation over infinite number of bodies in (3.26) can be simplified by reorganizing the summation itself, and by using Bloch's theorem. First, the summation can be split into two by recognizing

$$\sum_{\substack{\hat{\jmath}\in\mathbb{Z},\\ \hat{\jmath}\neq p}} = \sum_{\substack{B=-\infty,\\ B\neq 0}}^{\infty} \sum_{j\in\mathbb{P}} + \sum_{\substack{j\in\mathbb{P}\setminus\{p\},\\ B=0}} , \tag{3.27}$$

where

$$\mathbb{P} = \{j \ : \ j = 1, \ldots, N_b\} \ . \tag{3.28}$$

Second, we can use the periodic nature of the problem and use Bloch's Theorem. Bloch's Theorem states that in a periodic system, the values of a field in corresponding locations of two different cells differs only in the phase, caused by the incoming wave at the corresponding locations. For a one-dimensional periodic array or a diffraction grating where the periodicity is only in one direction, the Bloch's theorem states

$$\phi(x, y + d) = e^{i\beta d}\phi(x, y) \tag{3.29}$$

where

$$\beta \equiv k \sin\theta_I \tag{3.30}$$

is the component of the wavenumber vector along the array (β is also called *crystal wave vector* in solid state physics).

Using (3.29), the scattering coefficients of body $\hat{\jmath}$ are related to those of body j through

$$c^{\hat{\jmath}}_{nm} = c^{j}_{nm} P_B \ , \tag{3.31}$$

where P_B is a phase difference for cell B

$$P_B \equiv e^{iBkd\sin\theta} \ . \tag{3.32}$$

With (3.31) and (3.27), the second term in parentheses of (3.26) becomes

$$\sum_{\substack{j\in\mathbb{P}\setminus\{p\},\\ B=0}} \sum_{n=-\infty}^{\infty} c^{j}_{nm} K_{n-l}(k_m R_{jp}) e^{i(n-l)\alpha_{jp}} + \sum_{j\in\mathbb{P}} \sum_{n=-\infty}^{\infty} c^{j}_{nm} \sum_{\substack{B=-\infty,\\ B\neq 0}}^{\infty} P_B K_{n-l}(k_m R_{\hat{\jmath}p}) \ , \tag{3.33}$$

where the index $\hat{\jmath}$ in the second summation corresponds to indices j, B according to (3.22).

The first term is the summation over the bodies in the basic cell, and it is identical to (6.30) for scattering by a finite array. The second term needs further treatment.

The summation over all bodies can be considered in two parts — summation within a cell, and summation across the cells. We can take the contributions accounted by $K_{n-l}(k_m R_{\hat{j}p})e^{i(n-l)\alpha_{\hat{j}p}}$ as primary. Contributions from bodies in the other cells can be transformed into contributions by equivalent body in the basic cell using a different version of Graf's Addition Formula.

Consider bodies $\mathcal{B}_p$, $\mathcal{B}_j$, and $\mathcal{B}_{\hat{j}}$ as shown in Figure 3.3. The relationship between their positions is given by

$$\vec{R}_{\hat{j}p} = \vec{R}_{\hat{j}j} + \vec{R}_{jp} \tag{3.34}$$

where $\vec{R}_{\hat{j}j} = -Bd\,\vec{e}_y$. For the case when $|\vec{R}_{\hat{j}j}| > |\vec{R}_{jp}|$, which is for sure valid for large B, the Graf's addition formula (3.14) applied to vectors in Figure 3.3 gives

$$K_\mu(k_m R_{\hat{j}p})e^{i\mu\alpha_{\hat{j}p}} = \sum_{\nu=-\infty}^{\infty} (-1)^\nu\, K_{\mu-\nu}(k_m|B|d)\, e^{i(\mu-\nu)\alpha_B}\, I_\nu(k_m R_{jp})e^{i\nu\alpha_{jp}} \tag{3.35}$$

where

$$\alpha_B = \begin{cases} -\frac{\pi}{2}, & B > 0 \\ \frac{\pi}{2}, & B < 0 \end{cases} . \tag{3.36}$$

Let us assume for now that the maximal distance between the bodies in a cell is smaller than the periodicity d, i.e. $\max\{R_{jp} \;:\; j,p \in \mathbb{P}\} < d$. In that case the expression (3.35) is valid for all cells B, and the second sum in (3.33) (after some straightforward algebra) becomes

$$\sum_{j\in\mathbb{P}} \sum_{n=-\infty}^{\infty} c_{nm}^{j} \sum_{\nu=-\infty}^{\infty} (-i)^{\mu+\nu} I_\nu(k_m R_{jp})e^{i\nu\alpha_{jp}} \sum_{B=1}^{\infty} \left[P_B + P_{-B}(-1)^{\mu-\nu}\right] K_{\mu-\nu}(B\,k_m d) \tag{3.37}$$

where $\mu \equiv n - l$. The last sum is usually in the literature called lattice sum

$$\sigma_{n,m}(\theta, d) = \sum_{B=1}^{\infty} \left[P_B + (-1)^n P_{-B}\right] K_n(B\,k_m d)\,, \tag{3.38}$$

and it only depends on the periodicity of the lattice and the incoming wave angle θ, not on the number of bodies in the basic cell, or on their configuration.

The lattice sums for propagating orders $\sigma_{n,0}$ are extremely slowly convergent, so the

direct application of (3.38) is computationally not feasible. It is possible to accelerate the convergence of the series using Kummer's transformation (Linton, 1998). The transformed series converges to within 10^{-7} usually in less than 10 terms, except for $\sigma_{0,0}$ and $\sigma_{1,0}$ where it might take around 20 terms. The lattice sums for evanescent modes $\sigma_{n,m}$, $m > 0$ converge quickly, so (3.38) can be directly used. In all cases $\sigma_{n,m} = \sigma_{-n,m}$, so only lattice sums for positive $n \geq 0$ need to be calculated.

Finally, with , (3.38), the incoming potential on body p can be written as

$$\Phi^{I,p} = \sum_{m,l} d_{lm}^{p} I_l(k_m r_p) e^{il\vartheta_p} \psi_m(z) \tag{3.39}$$

where

$$\begin{aligned} d_{nm}^{p} &= (-1)^l \delta_{m0} P_p^0 e^{-il\theta} + \\ &+ (-1)^l \sum_{j \in \mathbb{P}} \sum_{n=-\infty}^{\infty} c_{nm}^{j} \left((1-\delta_{jp}) K_\mu(k_m R_{jp}) e^{i\mu\alpha_{jp}} + \sum_{\nu=-\infty}^{\infty} (-i)^{\mu+\nu} I_\nu(k_m R_{jp}) e^{i\nu\,\alpha_{jp}} \sigma_{\mu-\nu,m} \right) \end{aligned} \tag{3.40}$$

The scattering and incoming coefficients c_{nm}^{p}, d_{nm}^{p} are related through the T-matrix of body p. We can thus obtain the same type of linear system as for scattering by a finite array, namely

$$\left(\mathbf{I} - \mathbf{T}(\mathbf{S}+\mathbf{Q})^T\right)\mathbf{c} = \mathbf{T}\mathbf{d}\,, \tag{3.41}$$

where $\mathbf{Q}$ is the global periodicity matrix. Periodicity matrix Q^{jp} for bodies j and p is of size $M_t \times M_t$, and its elements are

$$\left(Q^{jp}\right)_{n,l,m} = \sum_{j \in \mathbb{P}} \sum_{\nu=-\infty}^{\infty} (-i)^{\mu+\nu} I_\nu(k_m R_{jp}) e^{i\nu\alpha_{jp}} \sigma_{\mu-\nu,m}, \quad \mu \equiv n-l\,. \tag{3.42}$$

For a periodic array with a single body ($N_b = 1$), $R_{jp} = 0$, which leads to a well known result (Peter, Meylan, and Linton, 2006)

$$\left(Q^{jp}\right)_{n,l,m} = Q_{n,l,m} = \sigma_{n-l,m} \tag{3.43}$$

Let us return to the case when for some bodies and a range of cells around the basic

cell, the intra-cell spacing is larger than inter-cell spacing, i.e.

$$R_{jp} > R_{\hat{j}j} \ . \tag{3.44}$$

Let $\mathbb{E}$ denote the set of all B for which this condition holds, i.e.

$$\mathbb{E}(j,p) = \{B \ : \ R_{jp} > |B|d, \ B \in \mathbb{Z}\} \ , \tag{3.45}$$

and let B_m denote the largest B for which this condition is valid, i.e.

$$B_m = \max \mathbb{E} \ . \tag{3.46}$$

For bodies $\hat{j}$, j and p for which condition (3.44) does not hold, the set $\mathbb{E}$ is empty, and the previous derivation holds. Otherwise, the Graf's formula for bodies reads

$$K_\mu(k_m R_{\hat{j}p}) e^{i\mu\alpha_{\hat{j}p}} = \sum_{\nu=-\infty}^{\infty} (-1)^{\mu-\nu} \, I_{\mu-\nu}(|B|k_m d) \, e^{i(\mu-\nu)\alpha_B} \, K_\nu(k_m R_{jp}) e^{i\nu\alpha_{jp}} \ , \tag{3.47}$$

and a correction γ needs to be added

$$\gamma = (-1)^l \sum_{\nu=-\infty}^{\infty} \sum_{B=1}^{B_m} \left[P_B + (-1)^{\mu-\nu} P_{-B}\right] \, e^{i\nu\,\alpha_{jp}} \, \left[i^{\mu-\nu} K_\nu(k_m R_{jp}) I_{\mu-\nu}(|B|k_m d) - (-i)^{\mu+\nu} I_\nu(k_m R_{jp}) K_{\mu-\nu}(|B|k_m d)\right] \tag{3.48}$$

If $\mathbb{E}$ is an empty set, $\gamma = 0$. For large orders ν that might arise in the summation, the products of Bessel functions $K_\nu(k_m R_{jp}) I_{\mu-\nu}(|B|k_m d)$ and $I_\nu(k_m R_{jp}) K_{\mu-\nu}(|B|k_m d)$ might lead to overflow errors if not carefully accounted for.

The expression just derived has several appealing properties. It is valid for bodies of general shape that do not need to be all the same. The bodies are allowed to be closely spaced, and the evanescent near-field is taken into account. The bodies do not need to be fixed, and they can also extract energy. The only change in the above derivation is to replace the scattering coefficients c^i_{mn} with those that take into account the radiated waves due to body motion $\tilde{c}^i_{mn}$, where

$$\tilde{c}^i_{mn} = c^i_{mn}(1 + R \cdot \varpi) \ . \tag{3.49}$$

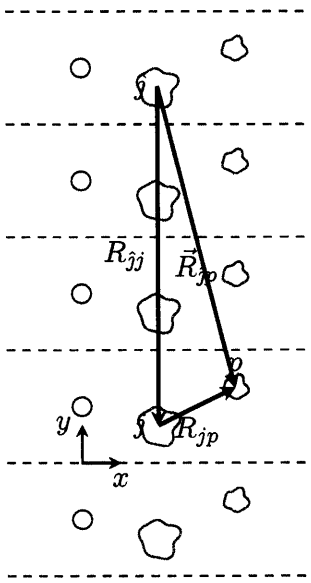

Figure 3.3: Bodies $\hat{j}$, p and j, and distance vector $\vec{R}_{\hat{j}p}$ decomposition.

3.4 Far-Field Structure

The potential describes the full field, but it is not helpful in revealing the wave structure in the far field. The field has to be periodic in y-direction with period d, so the incoming planar wave diffracts into several planar waves whose angles of propagation are such that the periodicity condition on the array is satisfied. The amplitudes of these transmitted and reflected waves are calculated next.

If Bloch' (3.29)theorem is applied on a $x = \text{const.}$ plane far away from the array where evanescent disturbances are no longer present, we get a condition for angles θ_m at which waves are allowed to propagate.

$$\sin\theta_m = \sin\theta_I + \frac{2\pi}{kd}m\,, \quad m = 0, \pm 1, \pm 2, \ldots \tag{3.50}$$

Here the index m denotes the *scattering order*, i.e. a planar wave propagating in direction θ_m in the far field. If we assume that incoming waves are coming from the left half-plane ($-\pi/2 < \theta_I < \pi/2$), then waves propagating in the right half-plane ($-\pi/2 < \theta_m < \pi/2$) are called transmitted waves, and waves propagating in the left half-plane are called reflected waves.

The equation (3.50) also gives the condition for when new scattering modes are to appear. For small values of kd the second term in (3.50) is very large, so the condition

cannot be satisfied except for $m = 0$. Thus, only one transmitted and one reflected wave exist in that case. The transmitted wave is propagating in the same direction as the incoming wave ($\theta_0 = \theta_I$), and the reflected wave is propagating at an angle $\theta_0^R = \pi - \theta_I$, as if reflected by a mirror. (In cases where there confusion or ambiguity might arise, θ_m^T and θ_m^R denote the angles of propagation of transmitted and reflected waves, respectively.)

When kd is increased to a critical value kd_m, a new scattering mode "emerges" at a so-called grazing angle $\theta_m = \pi/2$, i.e. the wave propagates along the grating. Further increase of kd past kd_m the direction of propagation θ_m of the scattered wave with move closer to θ_I. The value of kd_m can easily be obtained from (3.50)

$$kd_m = \pm(2\pi m - kd\sin\theta_I)\,. \tag{3.51}$$

In a βd–kd plane, the equation (3.51) describes two mutually perpendicular families of parallel lines, crossing the ordinate axis at positive multiples of 2π.

When a new scattering order appears, there is a redistribution of amplitudes in the existing scattering orders, resulting in abrupt changes in These "anomalies" were first noticed by Wood (1902) in scattering by optical diffraction gratings and are called Rayleigh's anomalies (Hessel and Oliner, 1965), in tribute to Lord Rayleigh who was the first to give an explanation why they occur. (The original name "Wood's anomalies" is now a larger set that contains Rayleigh anomalies and anomalies occurring due to trapped waves. But, about trapped waves a bit later.) The amplitudes of these scattered waves for a general periodic array are described next.

3.4.1 Transmission and Reflection Coefficients

The total scattering potential of the entire periodic array is

$$\phi^S = \sum_{\hat{\jmath}\in\mathbb{Z}} \sum_{n=-\infty}^{\infty} \sum_{m=0}^{\infty} c_{mn}^{\hat{\jmath}} K_n(k_m r_{\hat{\jmath}}) e^{in\vartheta_{\hat{\jmath}}} \psi_m(z) \tag{3.52}$$

Far away from the array, i.e. $|x| \to \infty$, evanescent waves are absent, and by using (3.8), (3.22), (3.31), (3.32), the equation (3.52) simplifies to

$$\phi^S = \frac{i\pi}{2} \sum_{n=-\infty}^{\infty} \sum_{j\in\mathbb{P}} \sum_{B=-\infty}^{\infty} c_{0n}^{j} P_B H_n(kr_{j,B}) i^n e^{in\vartheta_{j,B}} \psi_0(z) \tag{3.53}$$

where we have retained only propagating $m = 0$ mode and replaced expressed it in terms of Hankel function (we have also used $k = |k_0|$). We can further simplify this expression by using the the Sommerfeld integral representation of Hankel function (Sommerfeld, 1949)

$$H_n(kr_{j,B})e^{in\vartheta_{j,B}}i^{n+1} = \frac{i}{\pi}\int_{-\infty}^{\infty} e^{ik(y_i - Bd)t}e^{ikx_i\sqrt{1-t^2}}\frac{e^{in\arcsin t}}{\sqrt{1-t^2}}\,dt \tag{3.54}$$

and the Poisson summation formula,

$$\sum_{n=-\infty}^{\infty} f(n) = \sum_{k=-\infty}^{\infty}\int_{-\infty}^{\infty} f(x)e^{-i2\pi kx}\,dx \tag{3.55}$$

we can see that

$$\sum_{B=-\infty}^{\infty} P_B H_n(kr)e^{in\vartheta}i^n = \frac{\gamma}{\pi}\sum_{m\in\mathcal{M}}$$

Here we define the set $\mathcal{M}$ of all indices of the propagating modes in the far field

$$\mathcal{M} = \{\mu : \left|\sin\theta + \frac{2\pi m}{kd}\right| < 1\} \tag{3.56}$$

Finally, we get for the scattered potential

$$\phi^S = \frac{\pi i}{kd}\psi_0(z)\sum_{\mu\in\mathcal{M}} e^{ikr\cos(\vartheta-\theta_\mu)}\frac{1}{\cos\theta_\mu}\sum_{i\in\mathbb{P}} e^{ikR_i[\cos(\theta_I-\alpha_i)-\cos(\theta_\mu-\alpha_i)]}\sum_{n=-\infty}^{\infty} c_{0n}^i e^{in\theta_\mu} \tag{3.57}$$

The above expression is a superposition of planar waves propagating in directions θ_μ. The amplitudes of transmitted A_μ^+ and reflected A_μ^- waves in the far field are

$$A_\mu^\pm = \pm\frac{\pi i}{kd}\frac{1}{\cos\theta_\mu}\sum_{p\in\mathbb{P}} e^{\mp ikR_p\cos(\theta_m u\mp\alpha_p)}\sum_{n=-\infty}^{\infty}(\pm 1)^n c_{n0}^i e^{\pm in\theta_\mu}\quad \mu\in\mathcal{M}\,. \tag{3.58}$$

For a single body in the basic cell ($R_i = 0$), these expressions simplify well-known results (Twersky, 1962)

$$A_\mu^+ = \frac{\pi i}{kd}\frac{1}{\cos\theta_\mu}\sum_{n=-\infty}^{\infty} c_{0n}e^{in\theta_\mu}\;;\quad \mu\in\mathcal{M}. \tag{3.59}$$

There is a large redistribution of energy between the scattering modes when the new modes appear (Rayleigh wavelength).

Chapter 4

The Analysis of Energy Extraction by Large WEC Arrays

In this chapter, we perform a series of systematic investigations of different array configurations using the multiple scattering framework introduced in the previous chapter, and study the effects of the configuration parameters on the energy extraction performance. In particular, we study periodic arrays, large arrays with uniform spacings (both line and rectangular types), and large arrays with irregular spacings (systematic and random). Despite the large number of bodies, these arrays can be described with a limited number of configuration parameters, making the visual presentation feasible.

4.1 Literature Review

After the theoretical foundation for energy extraction by isolated bodies was set in the late seventies (Budal and Falnes, 1975; Evans, 1976; Mei, 1976), the analysis of energy extraction by WEC arrays started in the early eighties, most prominently by Evans (Evans, 1980; Evans, 1981a; Evans, 1981b), Falnes (Falnes, 1980; Falnes and Budal, 1982; Falnes, 1984), and Budal (Budal, 1977). In particular Evans (1980) and Falnes (1980) derived an expression for the maximal energy extraction by an array of oscillating and interacting bodies

$$P_{a,\max} = \frac{1}{8}\mathbf{F}^{+}\mathbf{B}^{-1}\mathbf{F} = \frac{1}{2}\mathbf{U}_0^{+}\mathbf{B}^{-1}\mathbf{U}_0 \,, \tag{4.1}$$

where $\mathbf{F}$ is the vector of diffraction forces on the array (for fixed, non-oscillating bodies), $\mathbf{B}$ the hydrodynamic damping matrix of an array as a whole, and $\mathbf{U}_0$ the vector of optimal body velocities

$$\mathbf{U}_0 = \frac{1}{2}\mathbf{B}^{-1}\mathbf{F} \,. \tag{4.2}$$

In this formulation, both $\mathbf{F}$ and $\mathbf{B}$ depend on the actual array configuration. Equation (4.1) provides us with the limit of possible energy extraction for a *given* array. It gives no indication of how $P_{a,\,\max}$ would change with a change in array configuration, either in terms of spatial positioning or in terms of the number of bodies in an array. Furthermore, it gives no indication for how to achieve that the bodies are oscillating with the optimal velocity $\mathbf{U}_0$ at any frequency.

Further advances can be made by assuming that bodies in an array are point absorbers — axisymmetric, heaving devices that are not affected by the radiated waves from other bodies. For that case Evans (1980) derived an expression for the maximal amplification, or gain, q in energy extraction that an array of point absorbers can achieve. The resulting equation is only a function of body locations. Newman (1983) improved the point absorber formulation in the low-frequency limit where the damping matrix $\mathbf{B}$ becomes singular. He also gave theoretical limits for maximum energy extraction by point absorbers in the low-frequency limit. Srokosz (1980) applied point absorber approximation to derive the maximum gain for an infinite row of point absorbers for normal incidence. Falnes and Budal (1982) and Falnes (1984) generalized the result by Srokosz for periodic arrays of multiple bodies and for any incidence angle, and they showed that it is theoretically possible to extract *all* of the energy from an incoming wave if there are four or more rows of bodies. Fitzgerald and Thomas, 2007 derived a useful identity regarding the angular dependency of array gain $q(\theta_I)$ for optimal point absorber arrays — the integral over all possible incoming directions equals 2π

$$\frac{1}{2\pi}\int_0^{2\pi} q(\theta_I)\, d\theta_I = 1 \,. \tag{4.3}$$

The conditions was later generalized for optimal WEC arrays of general axisymmetric bodies by Wolgamot et al. (2011). Here 'ptimal" refers to an array in which all bodies move according to (4.2). If that requirement is not met, the integral (4.3) no longer equals 1 but some other constant c. Child and Venugopal (2010) find c to be close to 1 ($\sim$ 0.9–1) for close-to-optimal arrays.

In addition to point absorber approximation, other approximations have been used to study WEC arrays. Simon (1982) used plane wave approximation (large spacing) to study arrays of up to 9 bodies. McIver and Evans (1984) extended the plane wave theory to include the first-order correction to plane waves, and used it two study arrays of three bodies. Kyllingstad (1984) used a low-scattering approximation to extend the point absorber theory for the large spacing case, and used it to study the performance of two-body WEC array. Unlike the point absorber approximation, in the low-scattering approximation bodies are allowed to oscillate in all three translational modes of motion. A comparison of these approximations to the multiple scattering formulation for a 5-body line array (Mavrakos, 1997) showed that while the point-absorber and plane-wave approximations give good results in their respective region of validity (long waves and large spacings, respectively), only multiple scattering formulation is uniformly valid for all wavenumbers and body spacings.

More recent works studied the performance of small WEC arrays (up to four bodies) based on multiple scattering theory of Kagemoto and Yue (1986) (Child and Venugopal, 2007; Siddorn and Eatock Taylor, 2008). Recently, McNatt, Venugopal, and Forehand (2015) analyzed a single 101-body WEC array, but with no analysis of configuration changes. That simulation is the largest WEC array that has been simulated up to date.

Boundary element method (BEM) was also used to study WEC arrays. Cruz, Sykes, Siddorn, and Eatock Taylor (2009) and Cruz, Sykes, Siddorn, and Taylor (2010) used a commercial BEM code WAMIT to calculate the performance of a 4-body square array. Taghipour and Moan (2008) used WAMIT as well to study a FO^3 Wave Converter, a commercial 21-body square array of small spheres (point absorber like). FO^3 has also been studied by De Backer et al. (2010) using WAMIT. They also performed individual PTO optimization for a 12-body array, keeping the array configuration fixed.

Garnaud and Mei (2009) and Garnaud and Mei (2010) recently studied energy extraction by periodic arrays of small bodies ($ka \ll 1$) by using multiple scales and homogenization theory. The spacing between the bodies is uniform, and assumed to be on the same oder of magnitude as the wavelength ($kd = O(1)$). They found that there is a strong decrease in energy extraction in the vicinity of Bragg resonance, and that there is an advantage of forming a compact array of bodies, compared to having a single body of equal total volume. However, assumption of small, weakly absorbing buoys and strong constraints on spacings make this theory harder to apply for general problems of practical interest.

In summary, our current knowledge on the influence of array configuration on energy extraction is severely lacking. In a problem with (at least) three distinctive length scales — body radius a, inter-body spacing d, wavelength λ — most of the studies have focused on the analysis of performance as a function of a/λ, keeping a/d (and overall configuration) constant. Providing performance maps — performance as a function of wavenumber and array configuration parameters — of different array types would greatly help in designing a better WEC for a realistic utilization. Furthermore, we do not know what are the limits of energy extraction for large arrays, what is their maximal gain, and how do these quantities change with the increase in the number of bodies in an array. Ideally, such questions should be answered in a way that is valid for general array types; approximations that put the regimes of possible strong extraction (closely spaced arrays; strong scattering/absorption) out of reach should ideally be avoided. This chapter attempts to address some of these issues.

4.2 Array Energy Extraction Performance Measures

Let us first define several energetic measures that quantify the energy extraction performance of an array. The total energy extraction rate for a monochromatic wave, or extracted power, P_a of an array is the sum of the extracted power by all the bodies in the array

$$P_a(\omega,\theta) = \sum_{i=1}^{N_b} P_i(\omega,\theta) \tag{4.4}$$

where $P_i(\omega,\theta)$ is the extracted power by body i (operating as a part of the array) at frequency ω and incoming angle θ).

The energy extraction rate for irregular seas, or spectral extracted power, P_a^S is defined as the total extracted power over all wave frequencies

$$P_a^S(\theta) = \int P_a(\omega,\theta)\, S(\omega)\, d\omega\,, \tag{4.5}$$

where $S(\omega)$ is the wave spectrum. The total energy extraction rate P_a^{DS} for a directional sea spectrum $S(\omega)\, f(\theta)$ is defined as the total extracted power over all wave frequencies and

incoming wave angles θ

$$P_a^{DS} = \int_0^{2\pi} P_a^S(\theta) f(\theta)\, d\theta = \int_0^{2\pi} f(\theta)\, d\theta \int P_a(\omega, \theta)\, S(\omega)\, d\omega \tag{4.6}$$

where $f(\theta)$ is the wave direction spectrum, which has to satisfy

$$\int_{-\pi/2}^{\pi/2} f(\theta)\, d\theta = 1\,. \tag{4.7}$$

A very common form of the directional spectrum, which I will also use throughout this thesis, is cosine-based

$$f(\theta) = \alpha\, \cos^{2s}\theta \tag{4.8}$$

where s is a factor that determines the spreading angle, and α is the normalizing constant so that (4.7) holds.

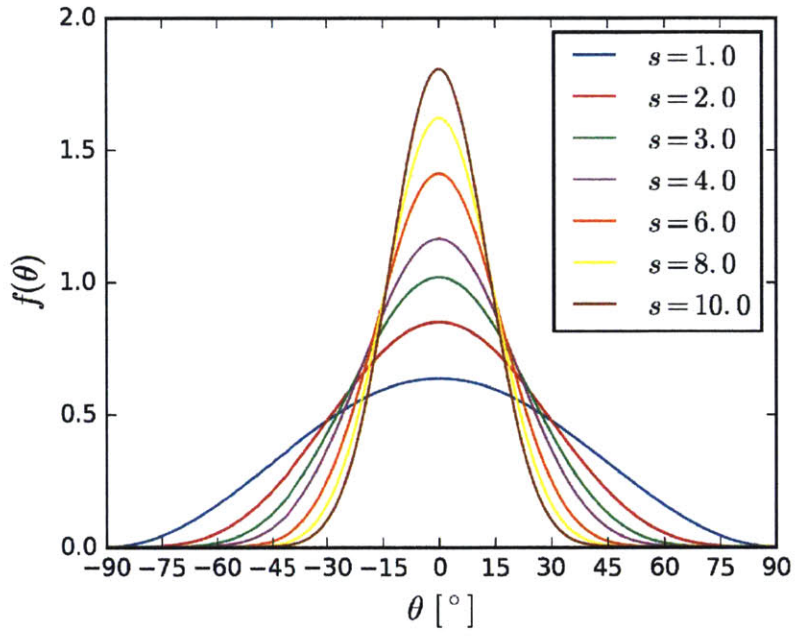

Figure 4.1: Directional spectrum $f(\theta)$ for different values of spreading factor s.

Analogously to the case for an isolated body, we can formulate the capture width for an array. The array capture width W_a is defined as

$$W_a = \frac{P_a}{P_w}\,, \tag{4.9}$$

where P_w is the wave energy flux defined in (1.1). The spectral capture width W_a^S is defined as the ratio of the spectral extracted power P_a^S and the total incoming energy flux P_w^S from a certain direction

$$W_a^S = \frac{P_a^S}{P_w^S} , \tag{4.10}$$

P_w^S is defined in (2.42).

In addition to comparing the energy extraction performance of a WEC array to the incoming wave energy flux, we can compare it to the energy extraction performance of equal number of isolated bodies. This leads to the concept of *array gain* q (or interaction factor), which is the ratio between the energy extracted by an array and the equivalent number of isolated bodies

$$q(\omega, \theta) = \frac{P_a(\omega, \theta)}{P_{\text{iso, tot}}} . \tag{4.11}$$

Here, $P_{\text{iso, tot}}$ is the total energy extracted by the bodies in the array if they were operating as isolated bodies. For an array consisting of N_{typ} types of WECs, and N_i bodies in each type i, the extracted power operating in isolation would be

$$P_{\text{iso, tot}}(\omega) = \sum_{i=1}^{N_{\text{typ}}} N_i \, P_{\text{iso},i}(\omega) , \tag{4.12}$$

with

$$\sum_{i=1}^{N_{\text{typ}}} N_i = N_b . \tag{4.13}$$

WEC devices that belong to the same WEC type need to have identical body geometry, body size, and PTO characteristics. For the most common case of an array consisting of only one WEC type, the equation (4.12) simplifies to

$$P_{\text{iso, tot}}(\omega) = N_b \, P(\omega) , \tag{4.14}$$

leading to

$$q(\omega, \theta) = \frac{P_a(\omega, \theta)}{N_b \, P(\omega)} , \tag{4.15}$$

with $P(\omega)$ defined in (2.24).

The values of array gain q greater than 1 denote WEC arrays which are better (in terms of total extracted power) than N_b isolated (non-interacting) wave energy converters.

Definition (4.15) means that q solely quantifies hydrodynamic interactions within an array, it does not depend on isolated body performance. For example, power extraction peak at resonance does not lead to a similar peak in q; the peaks and troughs in q are all caused by wave interactions. This can be misleading because q can, in principle, obtain large values for wavenumbers where the energy extraction is negligible; in these cases the extracted energy at these wavenumbers is still negligible, despite large q. The goal is, of course, to achieve as high q as possible for a particular frequency, or over a range of frequencies where waves carry a significant amount of energy.

The amplification in energy extraction over a range of frequencies is called spectral gain q^S. It is a measure that quantifies the total benefit of placing wave energy devices in an array for realistic sea state, and it and it is defined as a ratio of spectral performances of array and isolated bodies the array is made out of

$$q^S(\theta) = \frac{P_a^S(\theta)}{P_{\text{iso, tot}}^S} , \tag{4.16}$$

where $P_{\text{iso, tot}}^S$ is the spectrally integrated $P_{\text{iso, tot}}$

$$P_{\text{iso, tot}}^S = \int P_{\text{iso, tot}}(\omega)\, S(\omega)\, d\omega . \tag{4.17}$$

Similarly, the total spectral gain q^{DS} for directional sea spectrum is given by

$$q^{DS} = \frac{P_a^{DS}}{P_{\text{iso, tot}}^S} . \tag{4.18}$$

We have used here the fact that every WEC device is a axisymmetric body ($P(\omega, \beta) = P(\beta)$) so $P_{\text{iso, tot}}^S$ is not a function of the incoming wave angle θ, and we can write the total spectral gain for directional seas as a simple weighted sum of spectral gains over the incoming waves angles

$$q^{DS} = \int_0^{2\pi} f(\theta)\, q^S(\theta)\, d\theta \tag{4.19}$$

As a consequence, we can understand the behavior of a WEC array in directional seas from its behavior in uni-directional seas. In contrast, spectral array gain $q^S(\theta)$ cannot be

expressed in a similar manner from array gains $q(\omega, \theta)$ for monochromatic waves

$$q^S(\theta) \neq \int q(\omega, \theta)\, S(\omega)\, d\omega \,. \tag{4.20}$$

Note that all the definitions of array gain (4.11), (4.16), (4.18) quantify *only* the influence of hydrodynamic interactions between the bodies in the array; all the other WEC properties are the same as if the devices are operating in isolation (e.g. PTO characteristics). Further changes in array performance are possible if, say, PTO characteristics of individual devices are allowed to change. That would lead to another array gain factor, say $\widetilde{q}$, which would include the influence of changing the PTO characteristic of the bodies in the array. In this thesis, we will not be studying the influence of intra-array modification of PTO characteristic, although the framework presented supports such an analysis in a straight-forward manner.

4.3 Performance of Periodic Arrays

We study first periodic arrays as perhaps the simplest of large arrays, even though it is infinite in size. Here "the simplest" refers to the number of parameters needed to describe its configuration, not that its behavior is simple. They also serve as the basis for explaining large but finite arrays of uniform spacing.

Before discussing the arrays performance, let us define the body that will be the building block of all the arrays studied in this chapter, the PTO devices, and the ocean state the arrays are exposed to. We will use a truncated vertical cylinder or radius $a/h = 0.3$ and draft $H/h = 0.2$, oscillating only in heave. Its performance characteristics are described in Chapter 2. This body will also be used for all the simulations in this thesis as a whole, unless otherwise stated. The body is connected to a PTO device that is tuned such that at the body resonant wavenumber ka_r the energy extraction is maximal (i.e. $kW = 1$). The PTO is passive, i.e. there is no real-time tuning, and the extraction rate b_{PTO} is kept constant and equal for all the bodies in the array. We use Brentschneider spectrum to describe the ocean state, selected such that the peak wavenumber k_p matches body resonant wavenumber k_r, Figure 4.2,

$$k_p = k_r \,. \tag{4.21}$$

In addition to a full spectral response, for some analyses we will specifically focus on three wavenumbers — the body resonant wavenumber ka_r, the sub-resonant wavenumber $ka_< = 0.72ka_r$, and the super-resonant wavenumber $ka_> = 1.22ka_r$. These wavenumbers are within the bandwidth where the isolated body extracts significant amount of energy, and an ocean spectrum with a peak matching the resonant wavenumber offers a lot of potential for energy extraction at these wavenumbers, especially at $ka_>$. For directional spectra, we will use a cosine-based spectrum from equation (4.8) with $s = 4.0$. For simplicity, we will only consider directional spectra with the mean incoming angle $\theta_I = 0°$.

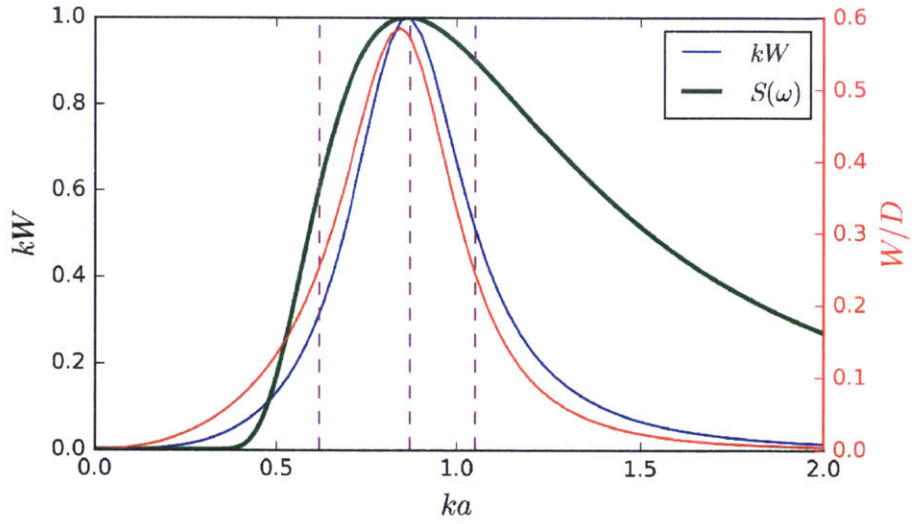

Figure 4.2: Capture widths kW and W/D as a function of ka for a truncated vertical cylinder with $a' = 0.3$, $H' = 0.2$. The Brentschneider spectrum whose peak matches the body resonant wavenumber is shown for comparison (no scale). The dashed magenta lines represent wavenumbers $ka_<$, ka_r and $ka_>$ at which some analyses will be specifically focused.

Consider first a periodic array formed by a single extracting body. Here there is only one parameter that governs the spatial configuration of the array — the periodicity d. In total for frequency-dependent quantities of interest (e.g. array gain q, non-dimensional capture width kW, body motion X), three parameters govern the behavior of the array — wavenumber ka, wave incoming angle θ_I, and the periodicity d.

Based on the Bloch condition (3.50), we can expect that there might be abrupt changes in the features of the observed quantities when new scattering orders appear, because of the redistribution of energy between the scattering orders. Following (3.51), this occurs when

$|\sin\theta_m| = 1$, giving the critical value of periodicity d_m when the m-th order appears to be

$$d_m = m\frac{2\pi}{k\left(\pm 1 - \sin\theta_I\right)} \,. \tag{4.22}$$

We will call here any kd–θ_I combination for which a scattering order of any order appears (i.e. condition (4.22) holds) as a *critical condition.*

The effect of array periodicity d on non-dimensional capture width kW_a is shown in Figure 4.4, for several incoming angles θ_I. The wavenumbers for which the energy extraction is substantial are still strongly centered around the resonant wavenumber ka_r — for $ka \lesssim 0.5$ and $ka \gtrsim 1.5$ the extracted energy is negligible, similar to that for an isolated WEC (c.f. Figure 4.38b). The energy extraction bandwidth is, thus, not increased by the array. The values of kW_a, however, are substantially different than for the isolated body case. The first thing to notice is that the values of kW_a are drastically reduced for critical values where new scattering orders appear. The maximum values of kW_a) are for $ka \approx ka_r$, and for spacings that are between the critical ones. For the $\theta_I = 0°$ case for which the energy extraction is the strongest, the maximal value of $(kW_a)_{\max} = 1.99$ is achieved for $ka = 0.90$ and $d/2a = 2.56$ ($(kW)_{max} = 1$ for an isolated body). The maximal values of kW_a are reduced with the increase of the incoming angle θ_I, and it approaches zero as $\theta_I \to 90°$. This can be explained as a constraint imposed by the Bloch Theorem (3.29), which assumes periodic potential $\phi(x, y)$ along the array, so no reduction in wave amplitude (energy) is possible for $\theta_I = 90°$.

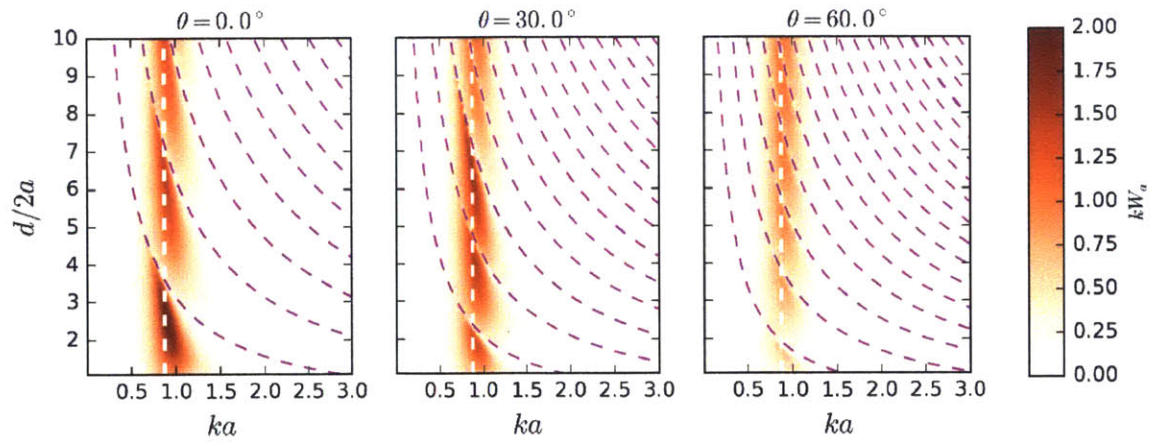

Figure 4.3: Contour plot of the nondimensional capture width kW as a function of wavenumber ka and array periodicity $d/2a$, for (a) $\theta_I = 0.0°$, (b) $\theta_I = 30.0°$, (c) $\theta_I = 60.0°$. The white dashed line denotes the body resonant wavenumber ka_r.

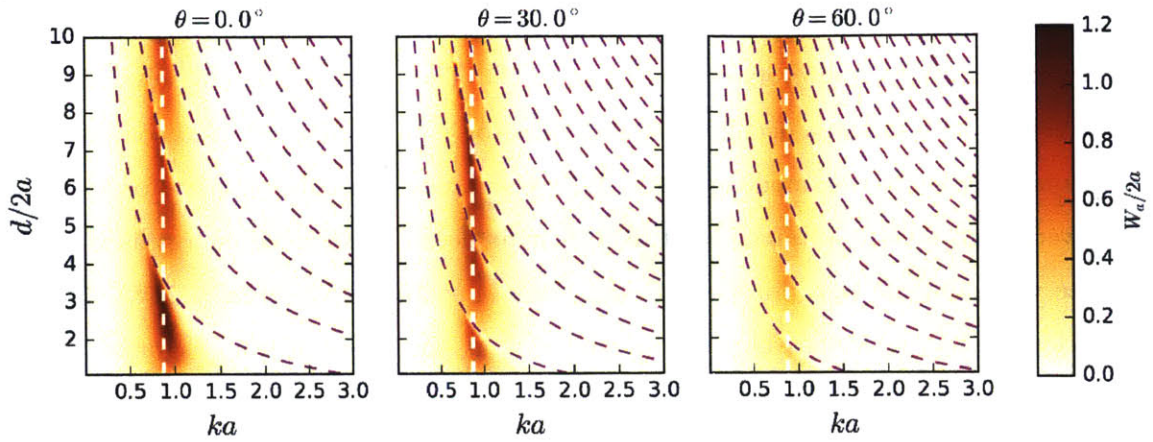

Figure 4.4: Contour plot of the nondimensional capture width $W_a/2a$ as a function of wavenumber ka and array periodicity $d/2a$, for (a) $\theta_I = 0.0°$, (b) $\theta_I = 30.0°$, (c) $\theta_I = 60.0°$. The white dashed line denotes the body resonant wavenumber ka_r.

The exact form of kW_a as a function of wavenumber is better seen on a cross section of Figure 4.3 for a particular spacing and incoming angle. This is shown in Figure 4.5, for $d/2a = 2.0,\ 3.0,\ 3.6$, $\theta_I = 0°$. In all cases, kW_a achieves values larger than 1 for some wavenumbers, but there is also a strong reduction in performance for critical wavenumbers (denoted by arrows). The spacing $d/2a = 3.6$ is chosen specifically so that the body resonance wavenumber ka_r coincides with the wavenumber kd_1 when the first scattering order appears. One might think that matching two "resonances" might lead to substantial amplification of energy extraction. However, the energy extraction is greatly diminished in that case, and it is close to zero at $ka_r = kd_1$, with a very sudden jump in value.

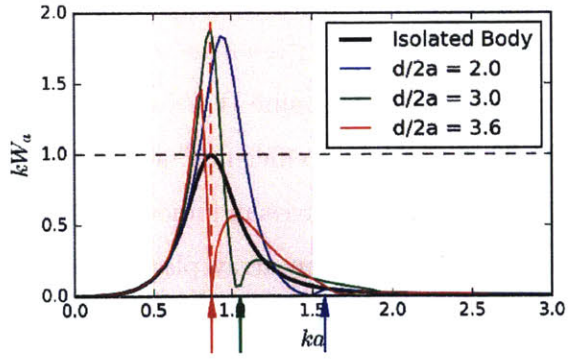

Figure 4.5: Non-dimensional capture width kW_a for three array spacings $d/2a$, $\theta_I = 0°$. The red dashed line denotes the body resonant wavenumber ka_r. Arrows denote critical ka values where the first scattering order appears; arrow color matches the color of kW_a for every spacing. The red region marks an estimate of a standard ocean spectrum bandwidth.

The contour plot of array gain q make the jumps in energy extraction formed by the creation of scattering orders very obvious, Figure 4.6. The ridges of low q closely follow the critical values, with maxima occurring at kd values (or, equivalently, ka–$d/2a$ combination) just below a new scattering mode appears. The overall maximal values of q are for $ka > 1.5$, so the very high q-value attained is of little benefit because extracted energy is very low for these wavenumbers (e.g. for $\theta_I = 0°$, $q_{\max} = 9.14$ at $ka = 2.93$, $d/2a = 2.08$). For the region close to ka_r, maximal value of q is around 2, as was apparent from Figure 4.3.

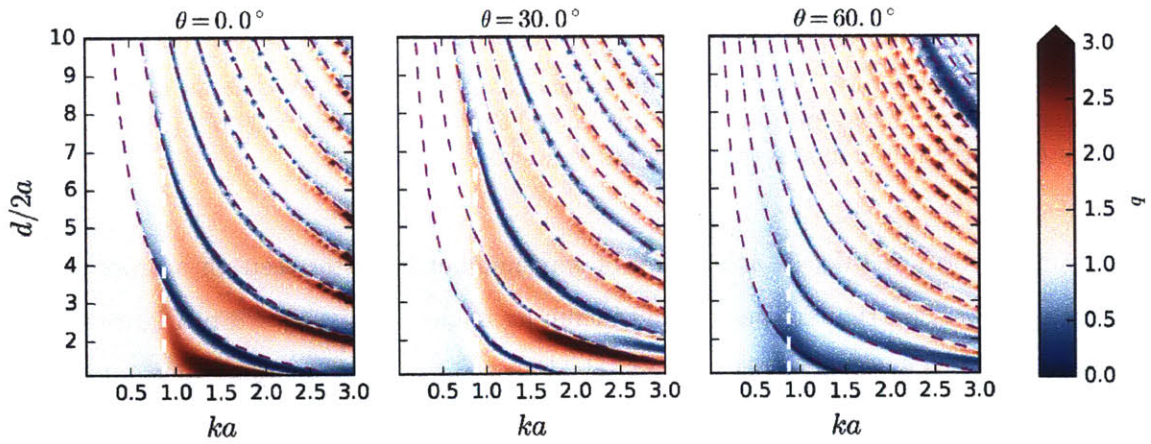

Figure 4.6: Contour plot of array gain q as a function of wavenumber ka and array periodicity $d/2a$, for (a) $\theta_I = 0.0°$, (b) $\theta_I = 30.0°$, (c) $\theta_I = 60.0°$. The white dashed line denotes the body resonant wavenumber ka_r. The color range has been cropped to allow for a better resolution at q values of interest (around 1).

The effect of the array periodicity on the extracted energy is perhaps more pronounced when we have a closer look at the capture width normalized by the periodicity d, rather than normalizing it by wavelength. We call this value W_a/d *capture efficiency* of an array. This normalization is a better indicator of "array efficiency" since it is a ratio of capture width of an array and its spatial extent, and as such gives an indication of the percentage of the power flux incoming on a patch of coastline that an array placed along a coastline has captured. Figure 4.7 shows that W_a/d has a very different character than kW_a (or $W_a/2a$, Figure 4.4). Here there is a clear preference for smaller array spacing, with W_a/d diminishing rapidly for $d/2a \gtrsim 3$. Energy extraction is still the greatest near the resonant wavenumber; the extraction diminishes with the increase in the incoming angle. The maximum value $(W_a/d)_{\max} = 0.50$ occurring for $\theta_I = 0°$ is achieved for $d/2a = 1.76$ and $ka = 0.93$. Thus,

maximum "efficiency" of a periodic array is around 50%.

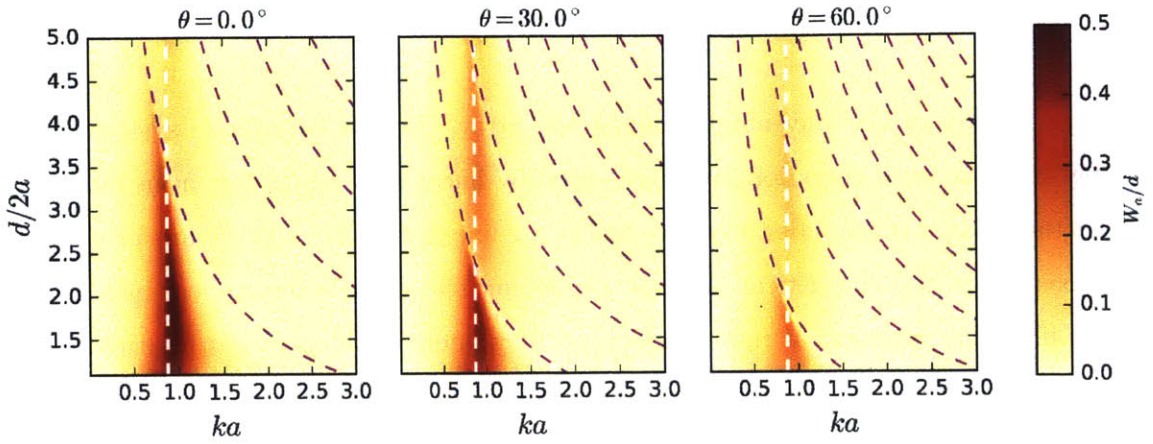

Figure 4.7: Contour plot of the nondimensional capture width W_a/d as a function of wavenumber ka and array periodicity $d/2a$, for (a) $\theta_I = 0.0°$, (b) $\theta_I = 30.0°$, (c) $\theta_I = 60.0°$. The upper y-axis limits are adjusted (c.f. Figure 4.3) so that a large uniform region where $W_a/d \approx 0$ is not shown. The white dashed line denotes the body resonant wavenumber ka_r.

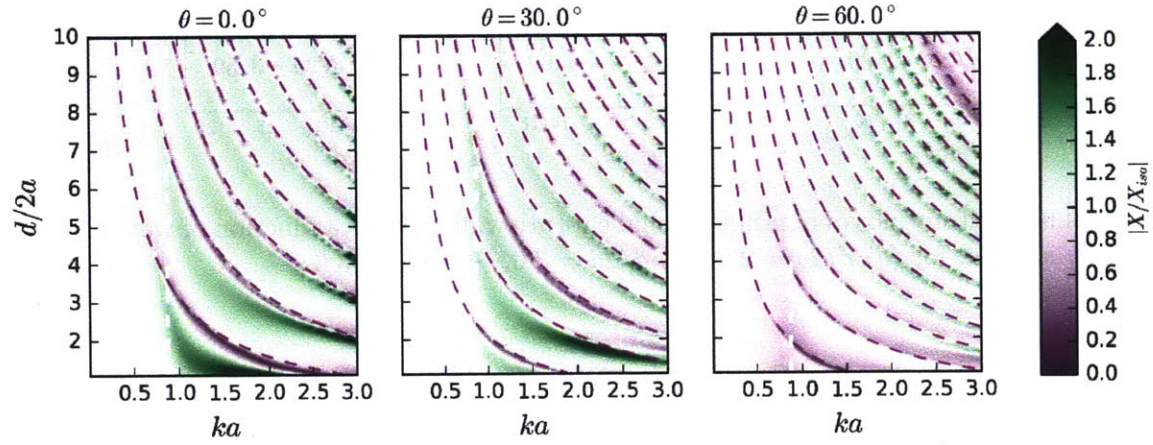

Figure 4.8: Contour plot of motion amplification $|X/X_{iso}|$ as a function of wavenumber ka and array periodicity $d/2a$, for (a) $\theta_I = 0.0°$, (b) $\theta_I = 30.0°$, (c) $\theta_I = 60.0°$. The white dashed line denotes the body resonant wavenumber ka_r.

The incoming angles $\theta_I = 0°$, $30°$, and $60°$ shown in previous figures are show some indication of how the quantities change with respect to the incoming angle. A more detailed picture of that dependency is shown in Figures 4.9–4.11, where the spacing is fixed, and the quantity of interest is shown as a function of the wavenumber and the incoming angle.

Actually, the incoming angle θ_I is only indirectly shown in these figures as $kd \sin\theta_I$, where

$$\beta = k \sin\theta_I \tag{4.23}$$

is the projection of the wavenumber along the array. In this coordinate system, waves coming from the same direction are represented by linear rays emanating from the origin, so that the y-axis corresponds to $\theta_I = 0$, and $y = x$ line to $\theta_I = 90°$. This transformation of the x-axis transforms the critical values at which new scattering orders appear into straight parallel lines that intersect at right angles, and they intersect the y-axis at multiples of 2π. This type of presentation is often used in optics, and it is called *light-cone* because the area above $y = |x|$ lines contains the kd–$kd \sin\theta_I$ values for which light can propagate in free space. This of course holds for water waves as well.

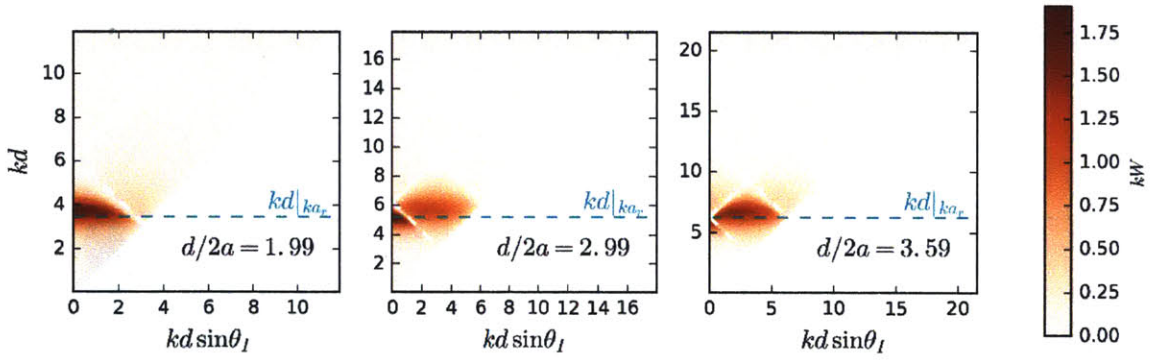

Figure 4.9: Contour plot of nondimensional capture width kW as a function of wavenumbers $kd \sin\theta_I$ and kd, for (a) $d/2a = 2.0$, (b) $d/2a = 3.0$, (c) $d/2a = 3.6$.

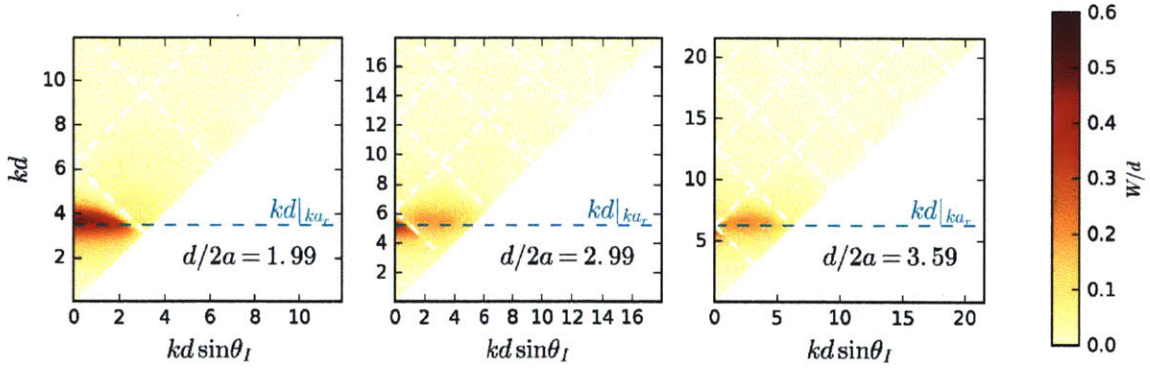

Figure 4.10: Contour plot of nondimensional capture width W/d as a function of wavenumbers $kd \sin\theta_I$ and kd, for (a) $d/2a = 2.0$, (b) $d/2a = 3.0$, (c) $d/2a = 3.6$.

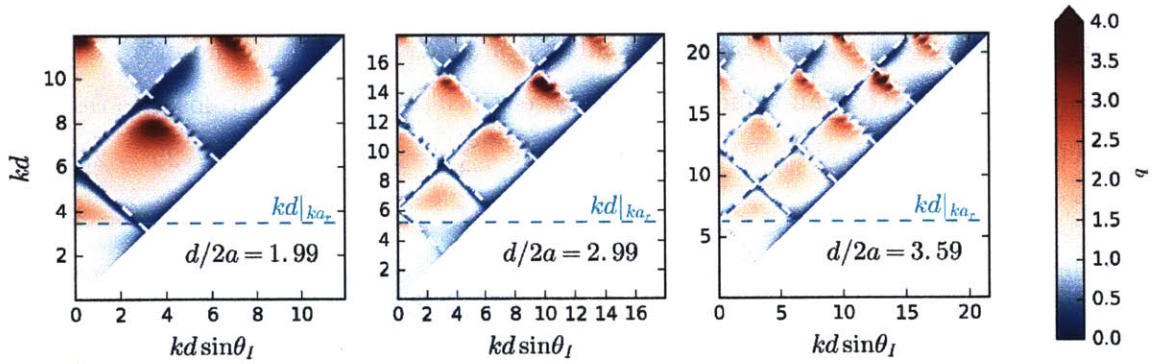

Figure 4.11: Contour plot of array gain q as a function of wavenumbers $kd\sin\theta_I$ and kd, for (a) $d/2a = 2.0$, (b) $d/2a = 3.0$, (c) $d/2a = 3.6$.

The performance of a periodic array for irregular seas loses the features due to scattering modes creation because of the integration over the frequencies (or wavenumbers). The spectral capture width W_a^S/d for irregular seas described by a peak-resonance-matched Brentscheider spectrum we talked about above is shown in Figure 4.12a. The higher values of W_a^S/d are for small spacings and incoming angles, as the maximal value $(W_a^S/d)_{\max} = 0.21$ occurs at $d/2a = 1.19$ and $\theta_I = 0°$. Comparison with the maximal value of $(W_a/d)_{\max} = 0.50$ reveals that for irregular seas described by the given Brentschneider spectrum the array efficiency is .

The spectral gain q^S, which is also equivalent to the ratio of $W^S/2a$ between the array and the isolated case, is shown in Figure 4.12b for a range of periodicity and incoming angles. There is a region of substantial gain for periodicity $1 \lesssim d/2a \lesssim 3$, and for incoming angle $\theta_I \lesssim 20°$. Increasing θ_I beyond these values greatly diminishes q^S to well even below 1. Arrays with large spacing $d/2a$ do not suffer from such an rapid decline in q^S with the increase of θ_I, but the overall values of q^S are lower since those arrays are closer to resemble a collection of isolated bodies. The maximal value $q^S_{\max} = 1.44$ occurs at $d/2a = 2.08$ and $\theta_I = 0°$.

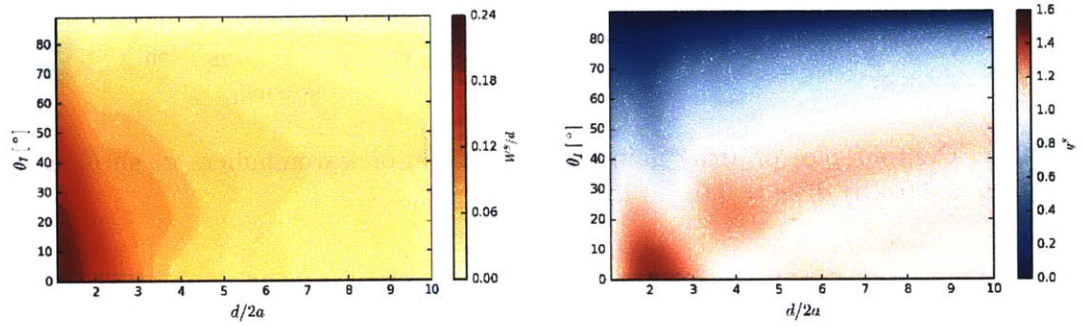

(a) Spectral capture width W_a^S/d (b) Spectral array gain q^S

Figure 4.12: Contour plot of spectral properties as a function of $d/2a$ and θ_I.

We further integrate the spectral performance over the cosine directional spectrum $f(\theta)$ with $s = 4.0$. The capture width W_a^{DS} of periodic arrays in directional seas as a function of array periodicity d is shown in Figure 4.13a. The two normalizations W_a^{DS}/d and $W_a^{DS}/2a$ reveal two different maxima, occurring two different optimal spacings. The maximal value $(W_a^{DS}/d)_{\max} = 0.20$ is achieved when the spacing is $d/2a = 1.17$, while the maximal value $(W_a^{DS}/2a)_{\max} = 0.29$ is achieved when the spacing is $d/2a = 1.83$.

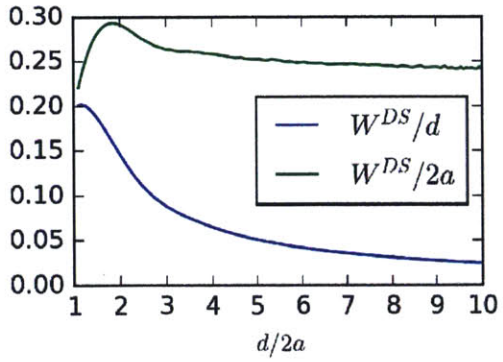

(a) Spectral capture width W_a^{DS}/d.

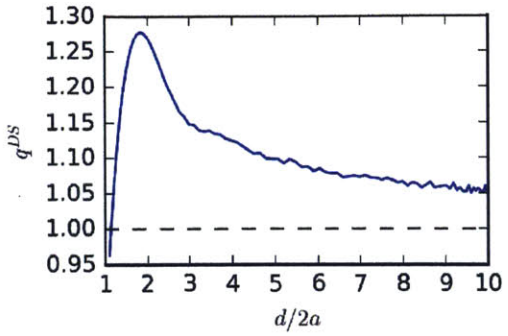

(b) Spectral array gain q^{DS}

Figure 4.13: Total (directional) spectral properties as a function of the periodicity $d/2a$

	Maximal value	$d/2a$	ka
q	9.14	2.08	2.93
q^S	1.44	2.08	—
q^{DS}	1.28	1.83	—
kW_a	1.99	2.56	0.90
W_a/d	0.50	1.76	0.93
$W_a/2a$			
W_a^S/d	0.21	1.19	—
$W_a^S/2a$			
W_a^{DS}/d	0.20	1.17	—
$W_a^{DS}/2a$	0.29	1.83	—

Table 4.1: Maximal performance values and optimal spacings for periodic arrays.

4.4 Performance of Large Uniformly Spaced Line Arrays

As the first example of finite arrays, we look at line arrays with uniform spacing, and study the influence of the number of bodies and spacing d on the array performance. The array geometry is shown in Figure 4.14, where the array extends along the y-axis.

A finite line array with uniform spacing is characterized by two parameters — the number of bodies N_b and spacing d. One can expect that as the number of bodies increases, the performance of a finite array approaches that of a periodic one with the same spacing d. In fact, that number does not need to be very large.

Figure 4.15 shows the maximal attained array gain q over any spacing

$$f(N_b, \theta_I) = \max_{d/2a \in [1.1,6]} q(ka)$$

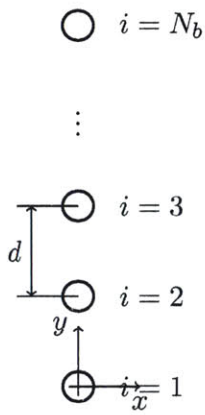

Figure 4.14: Line array with uniformly spaced bodies

where q is evaluated at $ka = ka_r$, $ka_<$, $ka_>$, or at ka that gives maximum value of q . The figure shows that in most cases the q is very close to its asymptotic value for a relatively modest number of bodies (~ 25). Normal incidence leads to maximal gains for resonant and super-resonant wavenumbers, with the maximal q almost monotonically decreasing with the increase in θ_I.

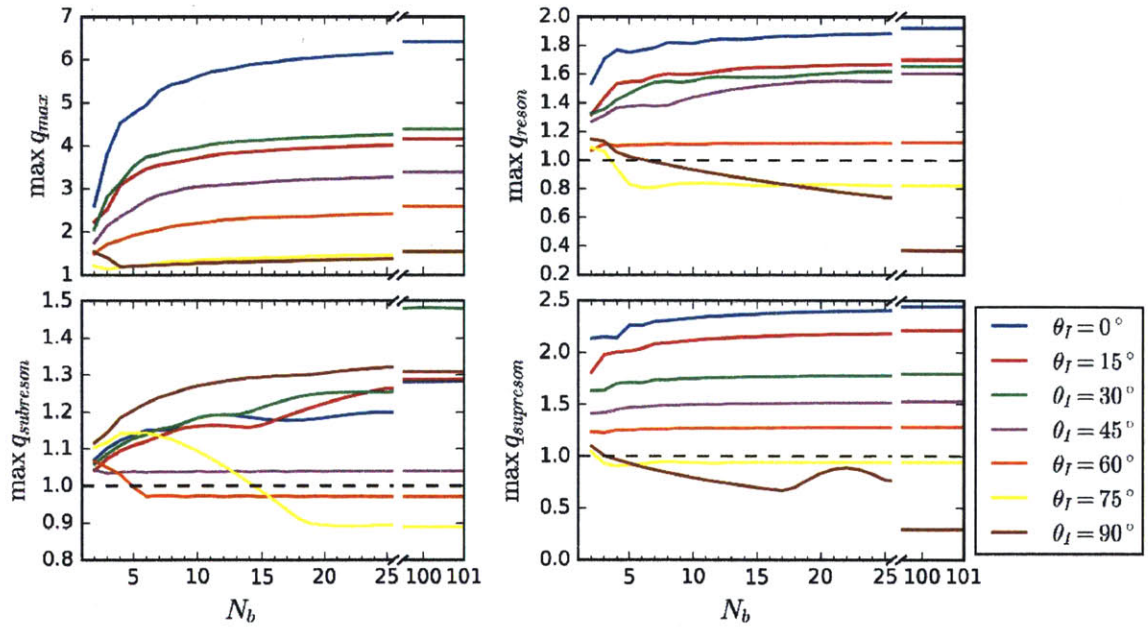

Figure 4.15: Maximal values of array gain q for certain wavenumbers as a function of the number of bodies in an array. Note that for the values that are not close for $N_b = 25$ and $N_b = 100$, the values at $N_b = 100$, 101 are *not* true representatives of the asymptotic values.

A notable exception from the trend is for incidence $\theta_I = 90°$, i.e. when waves are traveling along the array. Arrays of that type (or of that orientation) are called attenuator

arrays. For resonant and super-resonant wavenumbers, the maximal q decreases with the number of bodies. A naïve argument could be framed, stating that only a first few buoys of a terminator arrays ($\theta_I = 90°$) extract energy, regardless of the number of buoys in the array. That would lead array gain to decrease as $q \propto 1/N_b$. The behavior of q at ka_r and $ka_>$ indicates that q tends to zero more slowly than $1/N_b$. Moreover, q for $ka_<$ increases with N_b to an asymptotic value.

The comparison between the array gain q for finite arrays ($N_b = 20$ and 100) and for the periodic array as a function of body spacing is shown in Figure 4.16 for two wavenumbers. For both wavenumbers, the finite arrays perform almost exactly like a periodic array. For the resonant wavenumber ka_r and normal incidence angle $\theta_I = 0°$, this performance can be compared to the theoretical prediction derived by Srokosz (1980) for the maximum extraction by a point absorber in a channel

$$q = \frac{kd}{2}\left\{1 + 2\sum_{n=1}^{p}\left[1 - \left(\frac{2n\pi}{kd}\right)^2\right]^{-\frac{1}{2}}\right\}^{-1} . \tag{4.24}$$

We see that both the periodic arrays and the line arrays with large number of bodies roughly follow the trend set by (4.24), although not quite reaching the peak values. The performance of line arrays closely matches that of periodic arrays for all other wavenumbers and incoming angles until θ reaches the grazing angle $\theta = 90°$ (see Appendix D, Figures 4.2–4.4).

As discussed in the previous section, for $\theta_I = 90°$ the energy extracted by a periodic array is zero ($\theta_I = 89°$ shown in Figure 4.16 to show the trend). On the other hand, the energy extracted by a finite array for $\theta_I = 90°$ is not zero, but it is strongly influenced by the number of bodies N_b, in a negative way — as N_b increases, the overall gain q of the array reduces. For $ka = ka_r$ this trend tends to the periodic array performance; for $ka = ka_{subres}$, the performance of finite arrays is drastically different.

Figures 4.17 and 4.18 further confirm the difference between large line arrays and periodic arrays exists only for angles very close to $\theta_I = 90°$. The difference is only noticeable for angles that are within $\sim 10°$ from θ_I. We will call the range of these angles the *grazing cone.*

These figures also clearly show that for sub-resonant wavenumbers $ka < ka_r$ and non-grazing incoming angles, there is little difference between array performance and isolated

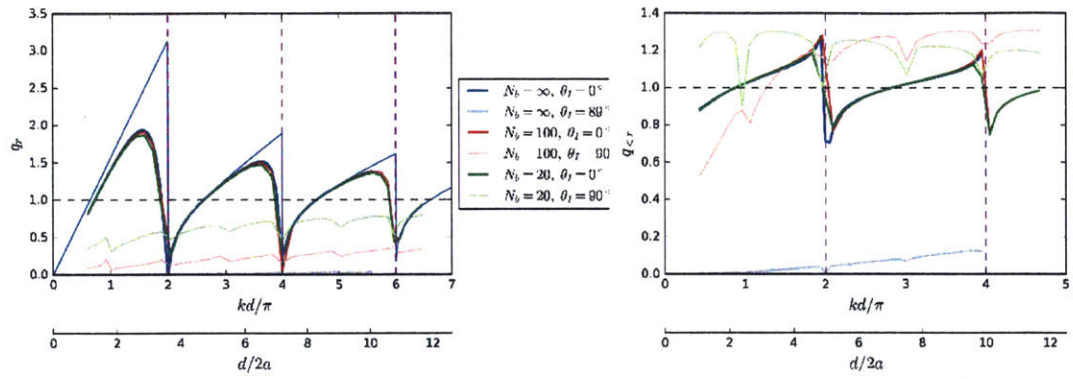

(a) $ka = ka_r$ (b) $ka = ka_<$

Figure 4.16: Comparison of the array gain q between arrays of different size as a function of body spacing for two wavenumbers, (a) resonant, and (b) sub-resonant. Theoretical limit by Srokosz for maximum gain at optimal energy extraction is shown for comparison in (a).

body performance ($q \approx 1$), while for super-resonant wavenumbers $ka > ka_r$ it is possible to achieve high q values. This holds for all angles outside the grazing cone. Within the grazing cone, the situation is reversed. Large array gain $q > 1$ is achieved for sub-resonant frequencies, while for $ka > ka_r$ array gain drops to well below 1 for the entire range (although not zero like for periodic arrays). As these figures show, this overall behavior is independent on spacing $d/2a$ (see also Figure 4.5). More surprisingly, it is also independent on the actual resonant wavenumber (see Figure 4.6 for the results for a larger WEC).

In terms of performance as an efficient WEC array, Figure 4.15 clearly shows it is advantageous to position the array such that it is normal to the incoming wave. Even for broad directional ocean spectra that cover incoming angles from $\pm 70°$ from the mean incoming direction, the performance of a finite line array with uniform spacing is almost identical to a periodic array with the same spacing. Figure 4.19 shows the similarity of q^S and q^{DS} between 25-body line array and a periodic array. (For more comparisons, see Appendix D, Figures 4.10.) Since the performance of all quantities outside the grazing cone is similarly comparable, the analysis and the results presented for periodic arrays in Section 4.3 follows here as well.

The behavior of line arrays at (near) grazing angles deserves a closer look. This array orientation corresponds to attenuator devices, where the main axis of the device is placed inline with the mean direction of wave propagation. Devices like that have been studied (Anaconda, Pelamis), and some have even been deployed in real-scale situation and

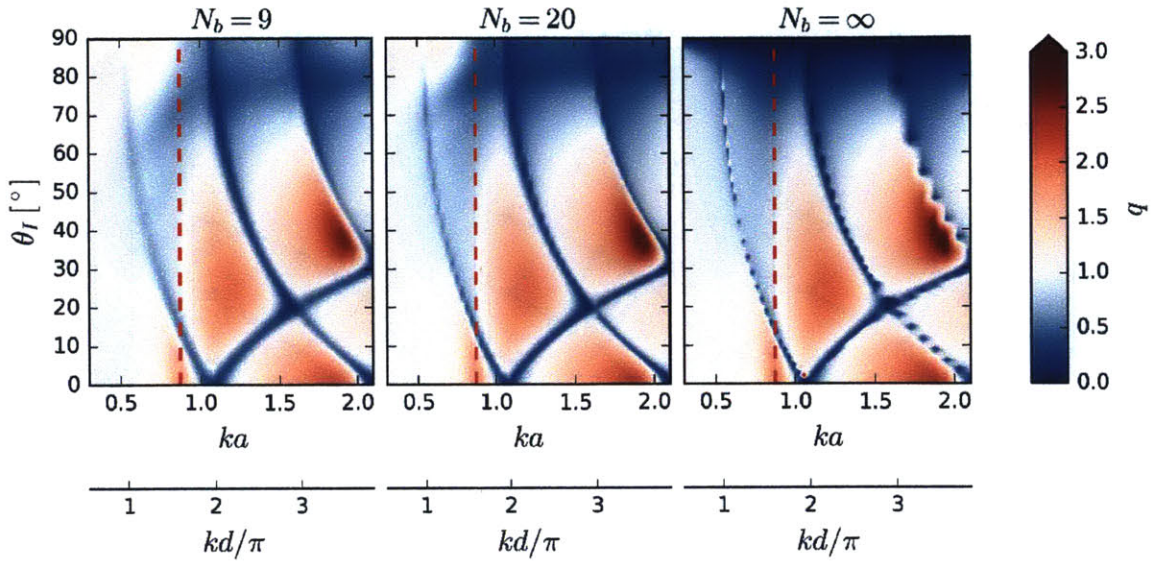

Figure 4.17: The contours of array gain q as a function of wavenumber ka and incoming angle θ_I for arrays with (a) $N_b = 9$ bodies, (b) $N_b = 20$ bodies, and (c) periodic array, all with spacing $d/2a = 2.88$.

connected to an electricity grid (Pelamis).

The array gain q for $\theta_I = 90°$ shows a strong change in behavior around ka_r, Figure 4.20 is a more focused look into the behavior of array gain at $\theta_I = 90°$. It shows that above resonant frequency ka_r, q is always much less than 1, regardless of the number of bodies or array spacing. Below ka_r array gain is larger than 1, and the maximum value of q increases with the number of bodies to an asymptotic value (c.f. Figure 4.15). This indicates that a way to improve the energy extraction at sub-resonant frequency is via an attenuator array. However, we must bear in mind that the energy extracted by a attenuator array (i.e. $\theta_I = 90°$) is much smaller than for terminator arrays ($\theta_I = 0°$), so that even with this improvement it does not compete with the energy extraction at ka_r.

To understand what happens in the points where q drops to close to zero, we plot the forces occurring on the bodies in the array. Figure 4.21 shows the heave and surge (inline) forces on the middle body in a 25-body line array. We see that the heave force for normal incidence $\theta_I = 0°$ exhibits an abrupt jump at every Rayleigh point. For the case of $\theta = 90°$, the peaks occur at wavenumbers that would correspond to trapped waves (Maniar and Newman, 1997), although of much smaller amplitude than for $\theta_I = 0°$ case. The surge (or inline) force for $\theta_I = 0°$ exhibits high large peaks at these trapped wave wavenumbers, increasing the force multi-fold. The peaks are smaller in magnitude than those for fixed,

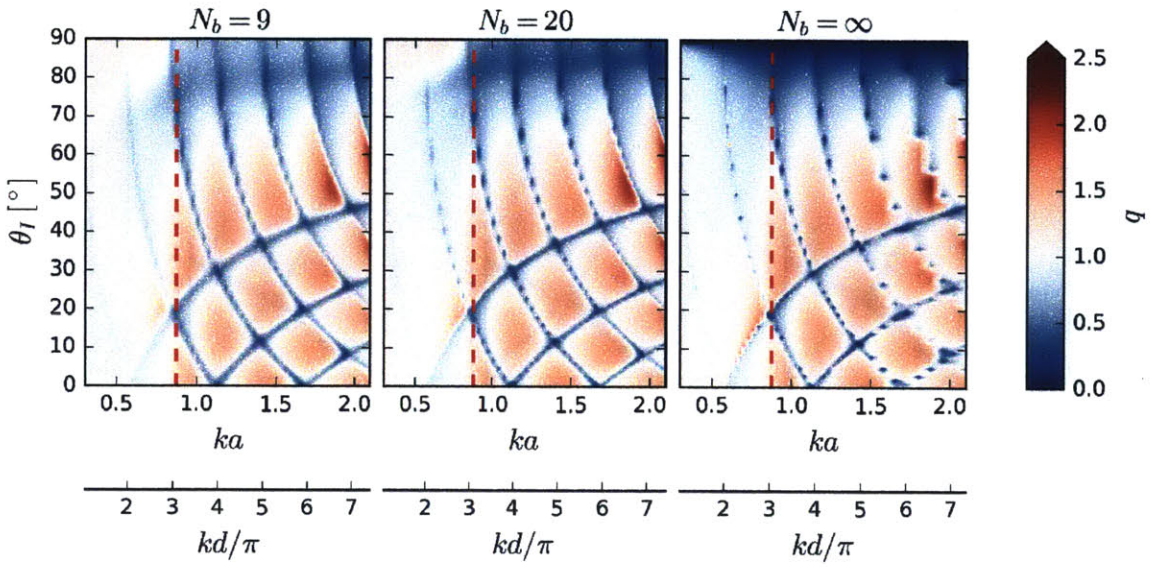

Figure 4.18: The contours of array gain q as a function of wavenumber ka and incoming angle θ_I for arrays with (a) $N_b = 9$ bodies, (b) $N_b = 20$ bodies, and (c) periodic array, all with spacing $d/2a = 2.88$.

bottom mounted cylinders found by Maniar and Newman (1997), because the bodies in our case are of shallow draft, and they are not fixed but radiate waves and extract energy.

The peaks in heave forces translate into peaks in body motion amplitude. Figure 4.22 shows the motion amplitude of the middle body of a 25-body array, where there is a significant reduction in the amplitude at the Rayleigh critical points. The spacing of the array has been chosen such that body resonance occurs at the first, most dominant Rayleigh point, leading to a large reduction in $|X|$ where the body is most capable of extracting energy. This leads to a drastic reduction in array gain q at the resonant wavenumber. The reduction in $|X|$ for $\theta_I = 90°$ due to trapped waves is not that significant, but it still leads to a reduced performance.

Figures 4.23 and 4.24 look beyond the performance of just a single body, and show the performance of every body in the array as a function of wavenumber ka. Figure 4.23 corresponds to the array for which q at resonance is near zero ($d/2a \approx 4.0$, the first Rayleigh point); Figure 4.24 corresponds to the array for which q at resonance is maximum ($d/2a = 2.88$). For the array that leads to near-zero q at resonance, we see that the body resonance wavenumber ka_r aligns with the Rayleigh points, leading to the reduction in motion for all bodies in the array, similar to that shown in Figure 4.22. For the array that has maximum gain at resonance, all the bodies experience an motion amplification at ka_r, leading to large

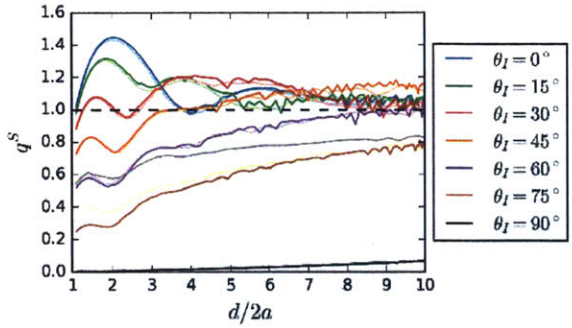

(a) Spectral Array gain q^S. The pair of non-matching lines is for $\theta_I = 90°$ ($\theta_I = 89°$ for periodic array), periodic array being near zero.

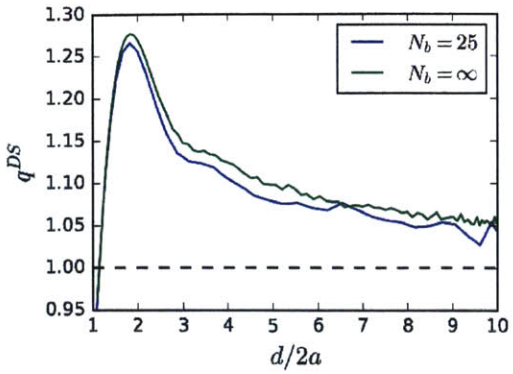

(b) Directional spectral gain

Figure 4.19: Comparison of array gains of 25-body line array with the periodic array, for a range of spacings.

overall gain.

Note that in all the cases the distribution of power extraction per body for angles outside the grazing cone is pretty uniform along the array, except at the resonant frequencies of the array. There the body at the ends of the array extract a much larger portion of the energy than the rest of the array. Recall, the total extracted energy is lower at these resonant wavenumbers. At the grazing angle, the behavior is different. There, for $ka > ka_r$ the first front of the array extracts more energy, with bodies further down the array extracting ever decreasing amount of energy. Correspondingly, the motion amplitudes of the of the first few front bodies are amplified, while all the others are reduced. At critical wavenumbers, however, the energy extraction is far more uniform (although overall smaller).

The inline force for $\theta_I = 90°$ shows large amplification for every wavenumber at which near-trapped waves are present. For higher-order modes, the amplification is reduced for bodies along the array. For normal incidence, Rayleigh points result in inline force amplification, especially for the edge bodies.

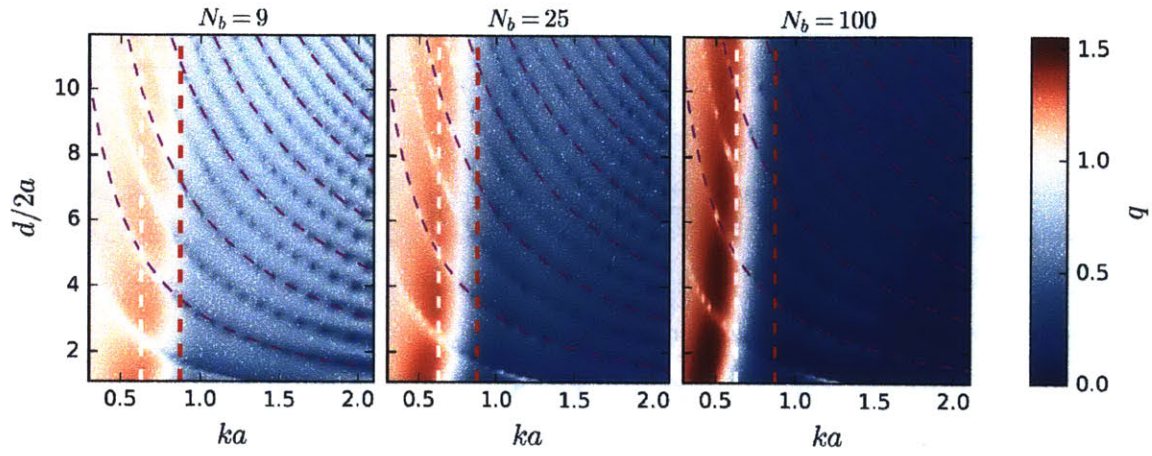

Figure 4.20: The contours of array gain q at $\theta_I = 90°$ as a function of wavenumber ka and spacing $d/2a$ for arrays with (a) $N_b = 9$ bodies, (b) $N_b = 25$ bodies, and (c) $N_b = 100$. The red dashed line marks ka_r; white dashed line for $ka_<$. The dashed magenta lines mark critical values $kd = n\pi$, for integer n.

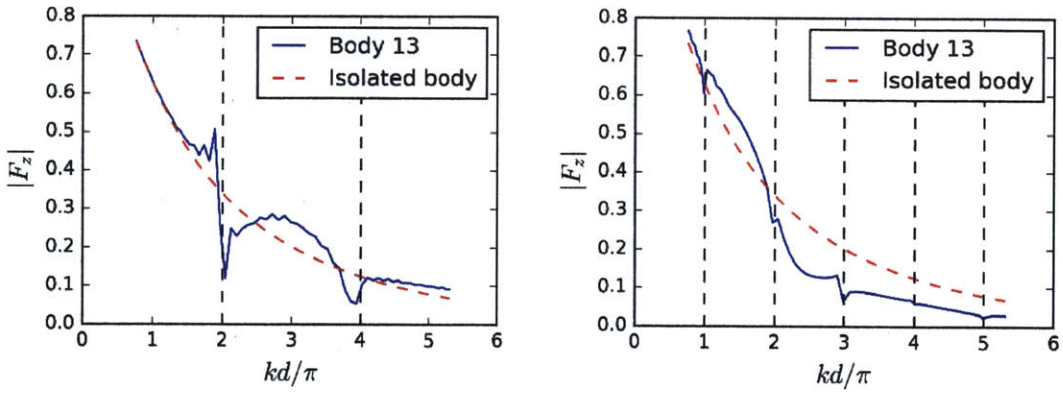

(a) Heave force, $\theta_I = 0°$

(b) Heave force, $\theta_I = 90°$

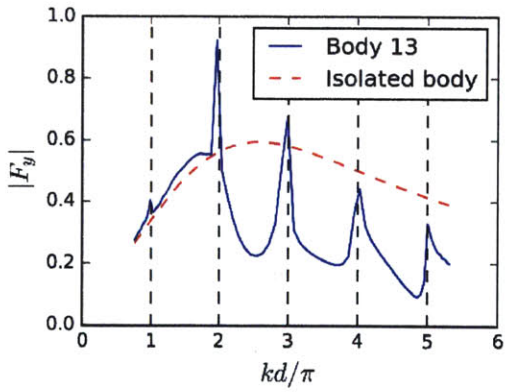

(c) Inline force, $\theta_I = 90°$

Figure 4.21: Force amplitude on the middle body in a 25-body array, $d/2a = 3.97$

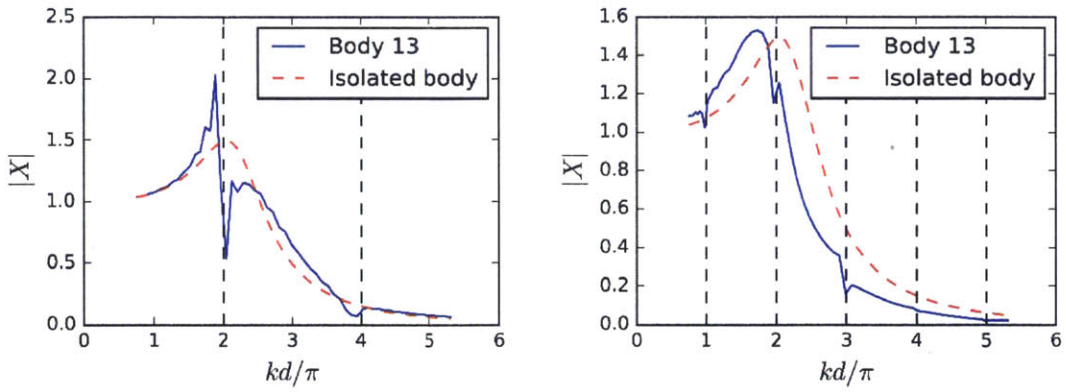

(a) $\theta_I = 0°$ (b) $\theta_I = 90°$

Figure 4.22: Motion amplitude of the middle body in a 25-body array, $d/2a = 3.97$

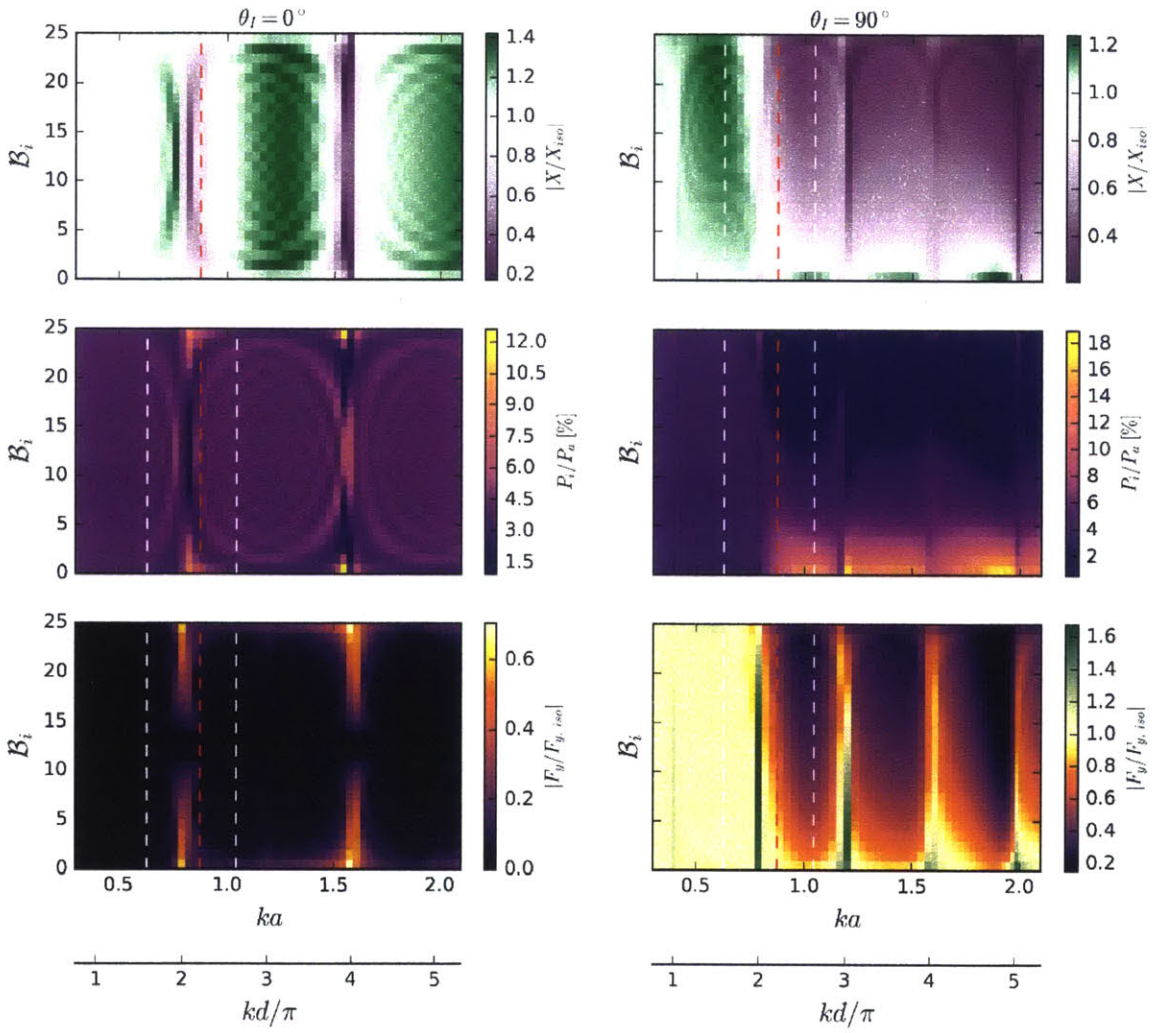

Figure 4.23: Detailed body performance plot for a 25-body array with $d/2a = 4.0$ for $\theta_I = 0°$ (left column) and $\theta_I = 90°$ (right column). For any wavenumber ka, the performance of body $\mathcal{B}_i$ is plotted along the y-axis in color patches according to the corresponding performance colorbar. The first row shows the amplification factor of the body motion amplitude, the second the percentage of the extracted power by a body, and the third row the amplification factor of the inline force. Red dashed line corresponds to the resonant wavenumber ka_r, and the white dashed side-lines to $ka_<$ and $ka_>$.

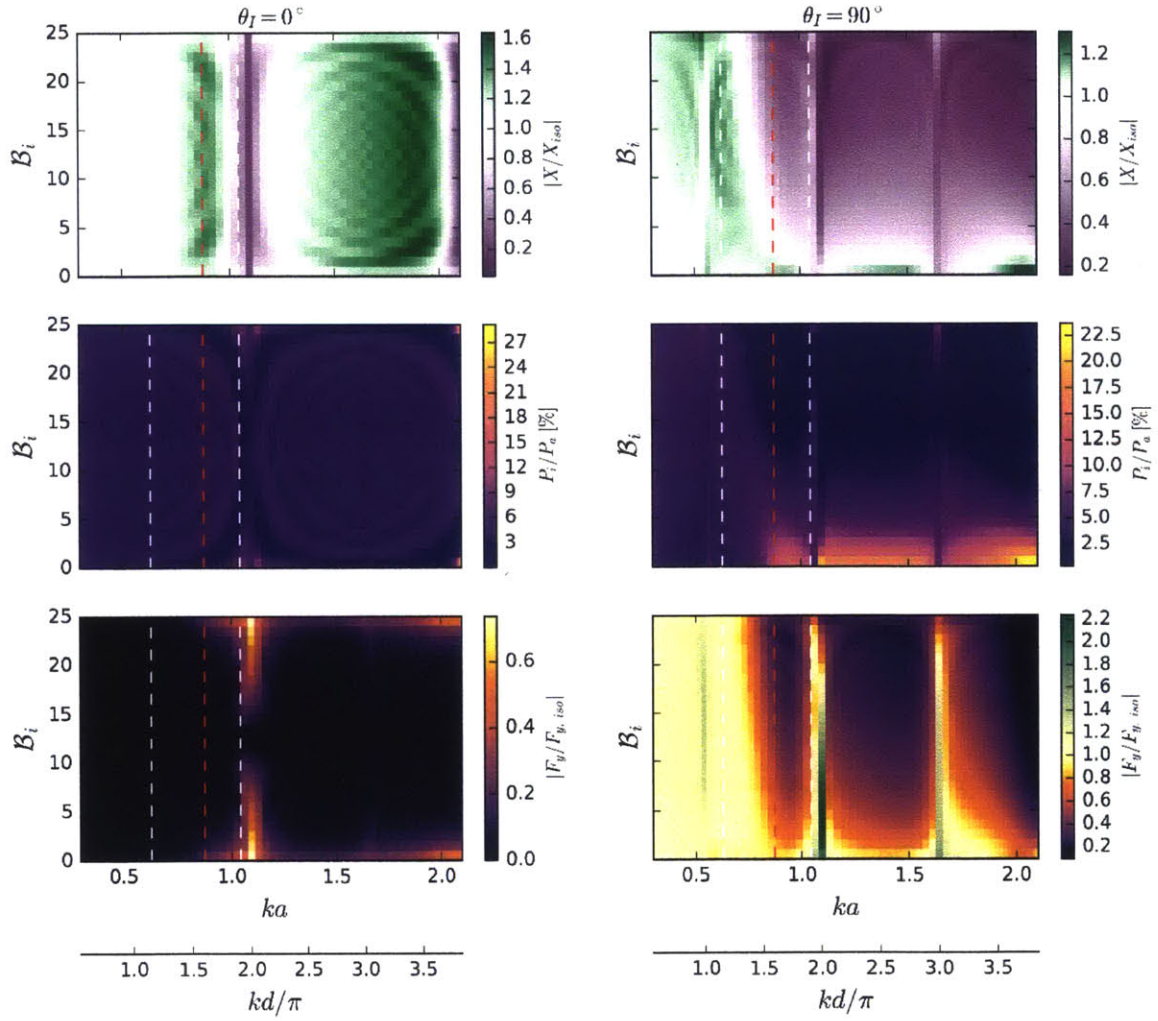

Figure 4.24: Detailed body performance plot for a 25-body array with $d/2a = 2.88$ for $\theta_I = 0°$ (left column) and $\theta_I = 90°$ (right column). See Figure 4.23 for the description of the plots.

4.5 Performance of Large Irregularly Spaced Line Arrays

In this section we relax the requirement that the spacing between the bodies in a line array is uniform, and introduce a random or a systematic variation. For the non-random configurations, the spacing d_i between bodies i and $i+1$ can be expressed in general as

$$d_i = d_0 + c\,\psi(\tau_i)\ , \tag{4.25}$$

where $\psi(\tau_i)$ is the functional dependency of the spacing variation, and c a coefficient that determines the strength of the variation. Here, τ_i represents a point on a $[0,1]$ interval spacing

$$\tau_i = \frac{i-1}{N_b-2}\ , \quad i = 1,\ldots,N_b-1;, \tag{4.26}$$

at which the spacing function for bodies i and $i+1$ is to be evaluated. The grid points τ_i depend only on the number of bodies in the array, not on the particular spacing distribution between them. In this section, we will be studying linear and quadratic variation in spacing.

For the configurations where we study the functional dependence on two geometrical parameters (d and c), we will again focus on three discrete wavenumbers — $ka_<$, ka_r, and $ka_>$ — to make the data easier to visualize. For the randomly spaced arrays, the entire range of ka values of interest is analyzed.

4.5.1 Line Arrays with Linear Spacing

We focus here on a 20-body line array, and we let the spacing to vary linearly along the array. The spacing between bodies i and $i+1$ is

$$d_i = d + c_1(2\tau_i - 1) \tag{4.27}$$

where d is the average spacing between the bodies, and τ_i is determined according to (4.26). The linear function is chosen such that at $\tau_i = 0$ and $\tau_i = 1$ its absolute value is 1, i.e. the spacing between two end buoys will achieve the extreme values of $d \pm |c_1|$. The sign of c_1 determines whether the array is denser at one or the other and of the array, Figure 4.25. Clearly, switching the sign of c_1 merely mirrors the array about the axis that is going through the center of the array and that is parallel to x-axis.

In the analyses below, the constraints are imposed on the minimal and maximal spacing

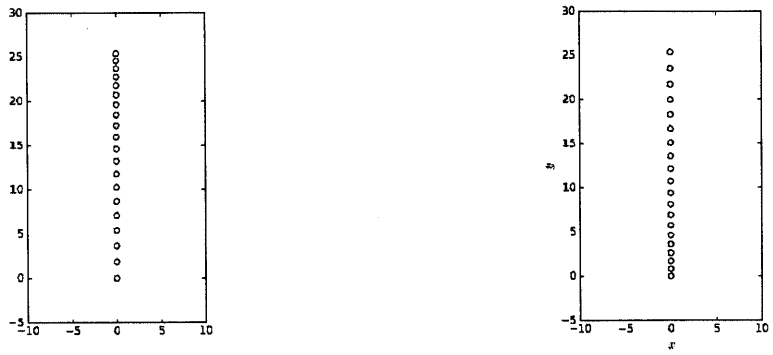

(a) $c_1 = -0.52$ (b) $c_1 = 0.52$

Figure 4.25: Geometry of two 20-body line arrays with linear variation in spacing, for (a) negative and (b) positive value of c_1 ($d = 1.34$ for both).

between any two bodies to prevent bodies from touching each other or being placed too far apart. If we prescribe the minimal spacing d_{min} between the two bodies (center-to-center), the maximal value $c_1^{lim,min}$ that can be used to define array configuration is

$$c_1^{lim,min} = \pm(d - d_{min}) \,. \tag{4.28}$$

Here, the plus or minus sign corresponds to the direction in which the spacings are increasing, c.f. Figure 4.25. Similarly, if we impose the maximal allowable spacing d_{max}, the limiting values of c_1 are

$$c_1^{lim,max} = \pm(d_{max} - d) \,. \tag{4.29}$$

Together, these can be written as

$$|c_1| \leq \min(d - d_{min},\, d_{max} - d) \,, \tag{4.30}$$

which gives the allowable values of c_1 for a given average spacing d. Since the constraints are not on the configuration parameters d and c_1 themselves, but on their combination through (4.30), these constraints are manifested in the d–c_1 plots as lines that reduce the allowable parameter space, Figure 4.26. The feasible parameter space (4.30) is represented by the shaded area between the constraint lines (4.28) and (4.29). The performance of systematically varied array configurations in figures below are all shown in this feasible parameter space.

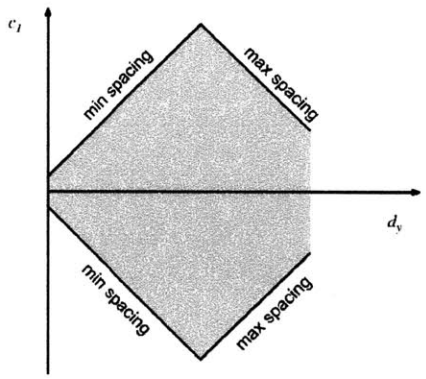

Figure 4.26: The feasible parameter space (gray) for line arrays with linear spacing. The feasible space is constrained by the requirement that the spacing d_i should be between the prescribed minimal and maximal spacing, eq. (4.30). The lines represent the constraints on minimal (4.28) and maximal (4.29) spacing.

The Figure 4.27 shows the total capture width W_a normalized by $N_b = 20$ buoy diameters, which makes the comparison with the single buoy simpler (c.f. $W/D = 0.58$ for the isolated buoy). Comparing the power extraction at three distinct wavenumbers, most of the power is extracted at the resonant wavenumber ka_r, followed by that for super-resonant wavenumber $ka_>$, and then for $ka_<$. This is true for all incoming angles, except those close to the grazing angle for subresonant wavenumbers (see Figure 4.29). The sign of c_1, i.e. the direction of spacing variation, very mildly affects the performance — even for non-zero incoming angles, the performance maps are almost symmetric with respect to $c_1 = 0$ axis.

In general, uniform arrays (or those close to being uniform, $c_1 \approx 0$) exhibit the largest variations in performance — they achieve higher peaks and deeper troughs in performance. This is more clearly visible for array gain q, Figure 4.28. Along the $c_1 = 0$ axis there is a familiar pattern observed in periodic and uniform arrays where the performance is strongly diminished around the Rayleigh points. The maximum performance occurs for arrays that are closer to Rayleigh points from below.

Away from the $c_1 = 0$ axis, i.e. for more spacing-skewed arrays, the performance is pretty independent on the array configuration — array gain q is almost constant. There are, however, linear features in the parameter space along which the performance is aways reduced. These features are emanating from Rayleigh points, running parallel with the spacing constraint lines (4.28) and (4.29), and extend the area of reduced performance into the non-uniform-array region of the parameter space. Interestingly, arrays that resemble the performance of uniform arrays with Rayleigh spacing are not arrays that have the average

spacing equal to the Rayleigh wavelength, i.e. that the distance between middle two bodies in the array is equal to the Rayleigh wavelength. These arrays would have equal d and different c_1 (those would be represented by vertical lines emanating from Rayleigh points). Rather, the continuation seems to be for arrays for which the distance between the the two end bodies, either minimal or maximal, is equal to a Rayleigh wavelength. These arrays are located along the lines that emanate from Rayleigh points and run parallel to the minimal- or maximal-spacing constraint lines. These lines are given by

$$c_1^{R,m} = \pm(d - d_{R,m}) \tag{4.31}$$

where $d_{R,m}$ is spacing equal to the m-th Rayleigh wavelength. (The lines based on (4.31) are shown in Figure 4.16 not to clutter Figure 4.28.) For an array characterized by the parameters constrained by (4.31), the spacing between the bodies is given by

$$d_i^R = d \pm (d - d_{R,m})(2\tau_i - 1) \ , \quad i = 1, \ldots, N_b - 1 \ , \tag{4.32}$$

where the choice of the sign corresponds to the direction of the spacing increase, equivalent to that represented in Figure 4.25. For $\tau_i = 0, 1$, i.e. for spacings at the either end of the array, the spacing is equal to the Rayleigh wavelength. It is not clear as to why the spacings at the edges of an array play a more important role with regards to the similarity to the uniform array performance than would, say, the average spacing.

Similar to line arrays with uniform spacing, $\theta_I = 90°$ is a special case. The for subresonant wavenumber $ka_<$, the array gain q is greater than 1 (with maximal value $q = 1.34$) for almost the entire parameter space (except the Rayleigh points), Figure 4.29. For larger wavenumbers, q is uniformly very low (below 0.8 for ka_r, and below 0.7 for $ka_>$). The attenuator formation, however, leads to the highest dependency on the sign of c_1. For example, for ka_r the arrays with positive c_1 — the spacing increases along the array (in the direction of wave propagation, c.f. Figure 4.254.25b) — are clearly preferred, Figure 4.29b.

Spectral array gain q^S does not offer improvements over the uniformly spaced array, Figure 4.30 (c.f. Figure 4.194.19a). The highest performance is achieved mostly by uniform (or near-uniform) arrays. Notable exceptions occur when uniform arrays perform poorer (e.g. for $d/2a \sim 4$–5, $\theta_I = 0°$), in which case the arrays with the maximal skewness in spacing take the lead (i.e. c_1 as large as possible). The direction of this skewness, however,

is not important, since there is almost no significant dependency on the sign of c_1, in all cases.

Directional spectrum introduces slight changes to the discussion above, Figure 4.31. For a spectrum with the mean incoming direction perpendicular to array axis, the total spectral gain q^{DS} is greatest for closely-spaced uniform arrays. For wider spaced arrays ($d/2a \gtrsim 3$), arrays with high skewness (large $|c_1|$) perform better, although still not outperforming the closely-spaced uniform arrays. The normalized capture width W_a^{DS}/Y is greatest for closely-spaced arrays, and it shows almost no dependency on the spacing skewness. Both q^{DS} and W_a^{DS}/Y are similar in value to that for uniformly spaced arrays.

Overall, the introduction of linear variation in spacing does not significantly improve array performance (q, $W/N_b\,D$) over the uniformly spaced arrays for the wavenumbers in question ($ka_<$, ka_r, $ka_>$). Even though linear variation of spacings introduces other length scales into the problem, there is no significant improvement in spectral performance where one might expect to see some changes. (See additional results on line arrays with linear spacing variation in Appendix D.1.)

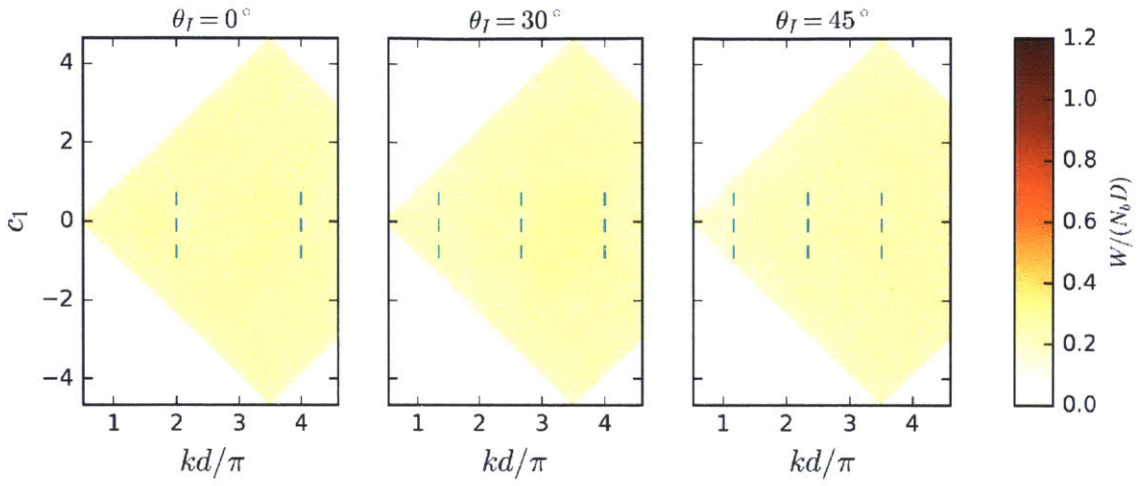

(a) $ka = ka_<$

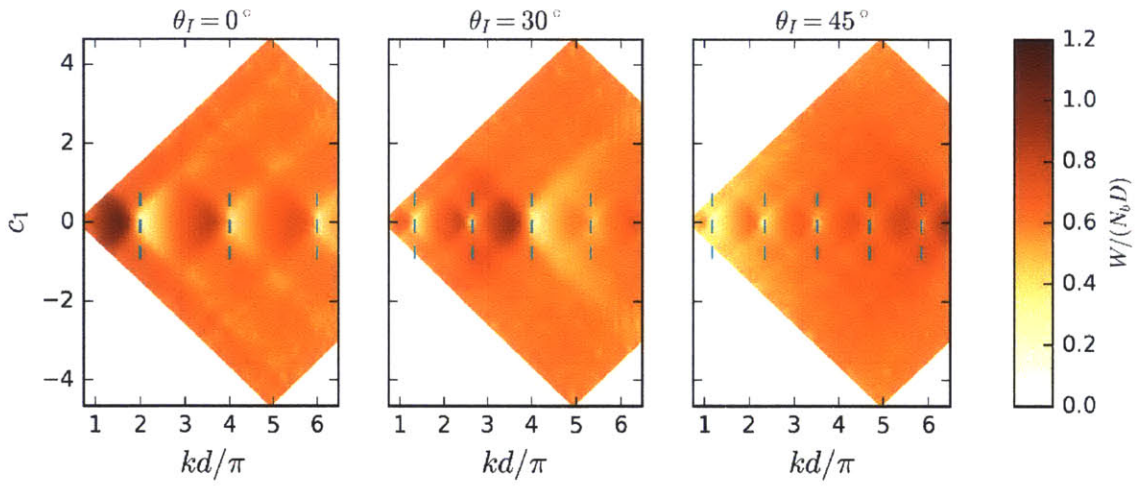

(b) $ka = ka_r$

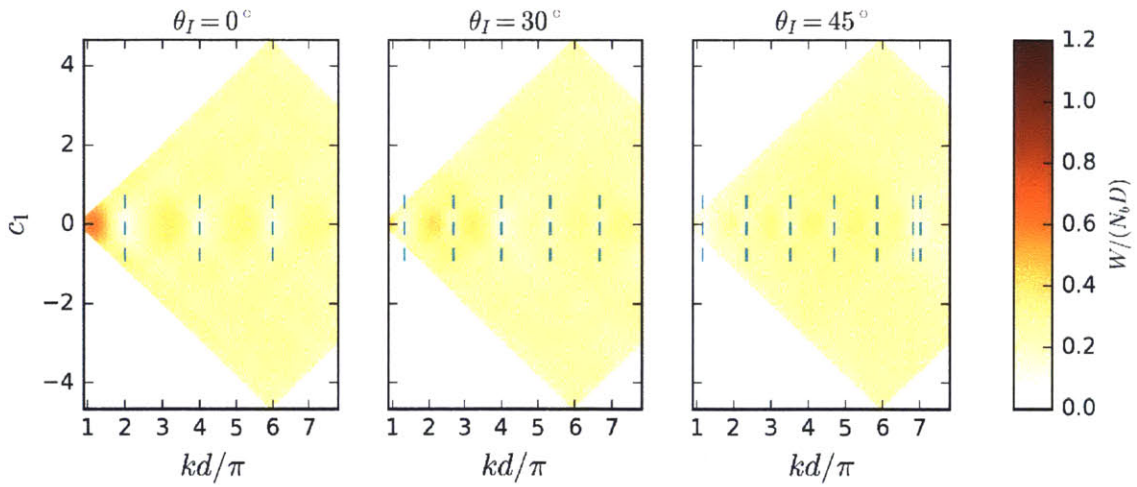

(c) $ka = ka_>$

Figure 4.27: Normalized capture width $W/N_b D$ for 20-body arrays with linear variation in spacing between the bodies. Note that the changes in kd/π correspond to changes in d as the wavenumber is constant for each plot.

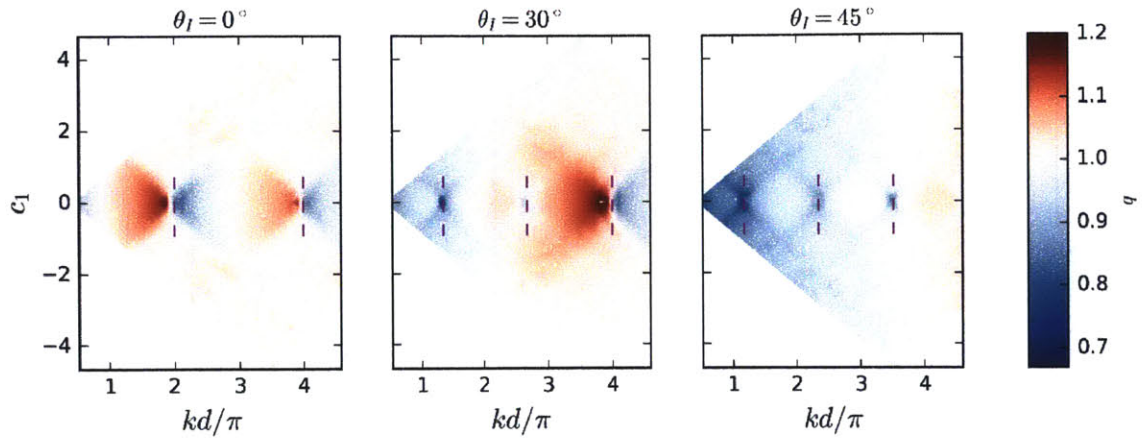

(a) $ka = ka_<$

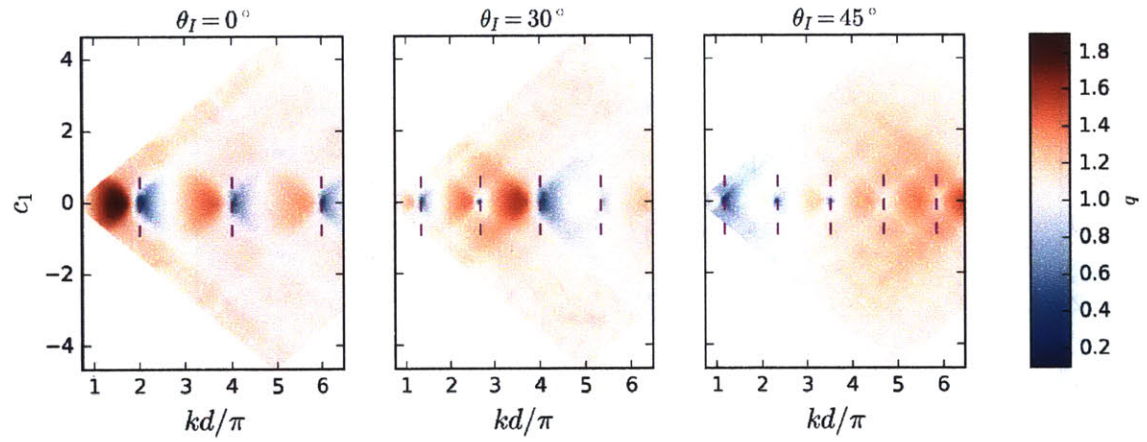

(b) $ka = ka_r$

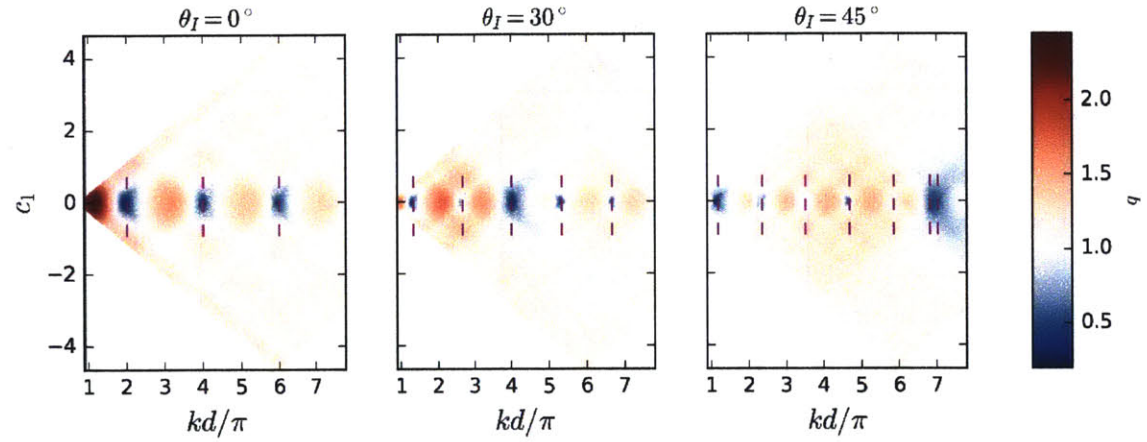

(c) $ka = ka_>$

Figure 4.28: Array gain q for 20-body arrays with linear variation in spacing between the bodies. Note that the changes in kd/π correspond to changes in d as the wavenumber is constant for each plot.

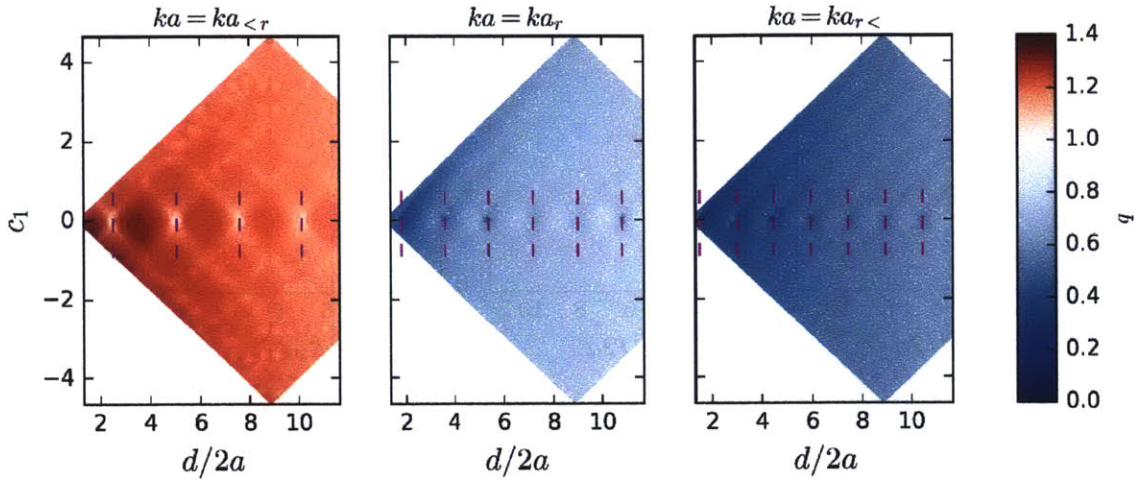

(a)

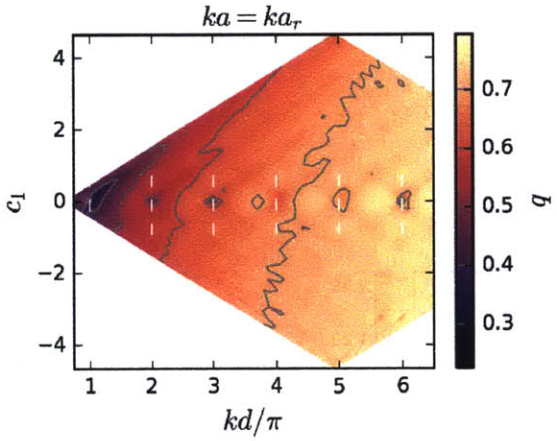

(b) $ka = ka_r$

Figure 4.29: Array gain q for $\theta_I = 90°$. Performance for ka_r is shown in (b) (with a different colormap) to make the asymmetry more visible.

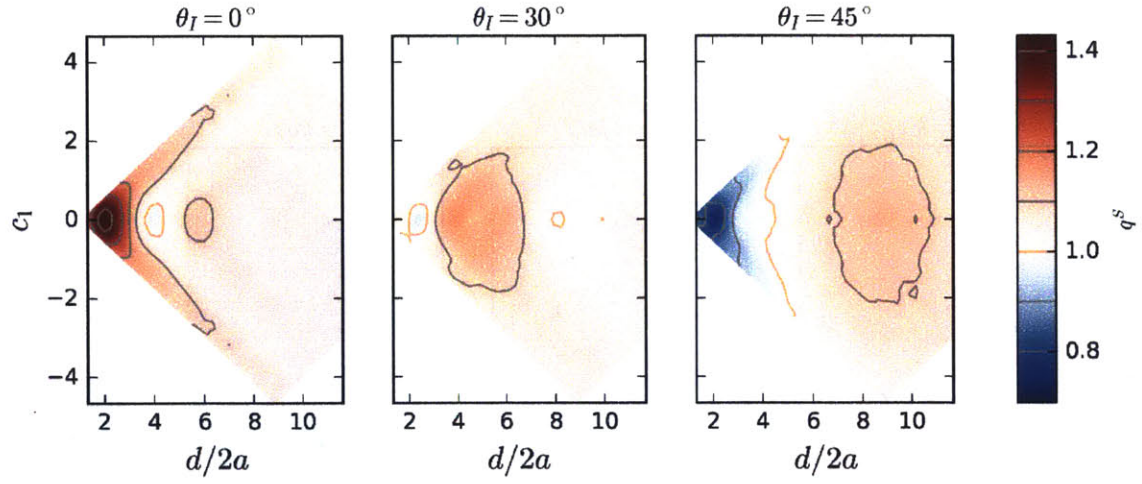

Figure 4.30: Spectral array gain q^S for 20-body arrays with linear variation in spacing between the bodies.

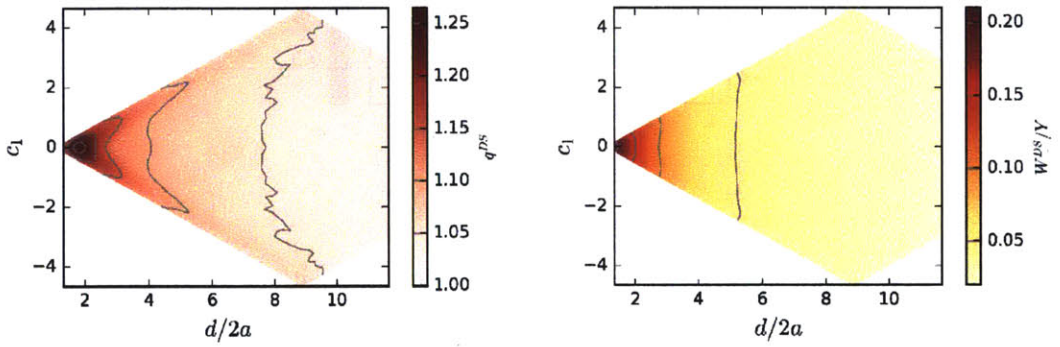

(a) q^{DS} (b) W_a^{DS}/Y

Figure 4.31: Rectangular array performance in directional seas.

4.5.2 Line Arrays with Quadratic Spacing

We again consider a 20-body line array, but here we let the spacing to vary quadratically along the array. The spacing between bodies i and $i+1$ is

$$d_i = d_0 + c_2(8\tau_i^2 - 8\tau_i + 1) \tag{4.33}$$

where d_0 is the constant component of spacing between the bodies, and τ_i is determined according to (4.26). The quadratic function $\psi(x)$ is chosen such that at $\tau_i = 0, 1$ its absolute value is 1, and $\psi(\tau_i = 0.5) = -1$. One can recognize that $8\tau_i^2 - 8\tau_i + 1$ is actually Chebyshev polynomial $T_2(\tau_i)$ on a shifted interval $[0, 1]$. Note that in equation (4.33), d_0 is not the average spacing.

Arrays described by the spacing equation (4.33) are symmetric with respect to the axis that is going through the center of the array, parallel to x-axis. The sign of c_2 determines whether the array is denser in the middle ($c_2 > 0$) or at the ends ($c_2 < 0$), Figure 4.32. Note that the array extent Y depends on the sign of c_2, not only on its absolute value (unlike for linear variation in spacing, c.f. Figure 4.25), where arrays with negative c_2 have larger y-extent than arrays with a positive c_2 (of equal absolute value).

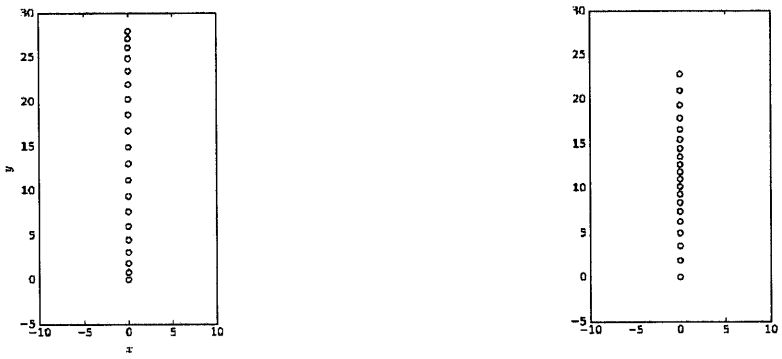

(a) $c_2 = -0.52$ (b) $c_2 = 0.52$

Figure 4.32: Geometry of two 20-body line arrays with quadratic variation in spacing, for (a) negative and (b) positive value of c_2 ($d_0 = 1.34$ for both).

In the analyses below, constraints are imposed on minimal d_{min} and maximal spacing d_{max} between any two bodies, analogously to those in the previous section. The spacing equation (4.33) is linear in c_2, and the spacing function achieves extreme values of 1 and -1 (for $\tau_i = 0$, 1 and $\tau_i = 0.5$, respectively). This results in the same feasible parameter

space as in Figure 4.26 (the only difference is replacing c_1 with c_2).

The analysis closely follows the one presented in the previous section for line arrays with linear variation in spacing. Hence, I will here mostly focus on the more salient aspects of the results. Further results are presented in Appendix D.1.1.

The Figure 4.33 shows the total capture width W_a normalized by $N_b = 20$ buoy diameters for the resonant wavenumber ka_r. The maximal values are identical to those for arrays with linear spacing variations ($W_a/N_bD|_{max} = 1.08$) because the maximum occurs for a uniform array ($c_2 = 0$). However, these arrays with quadratic variation in spacing show more dependency on the "direction" of the variation, i.e. the sign of c_2. This is more visible in array gain plots.

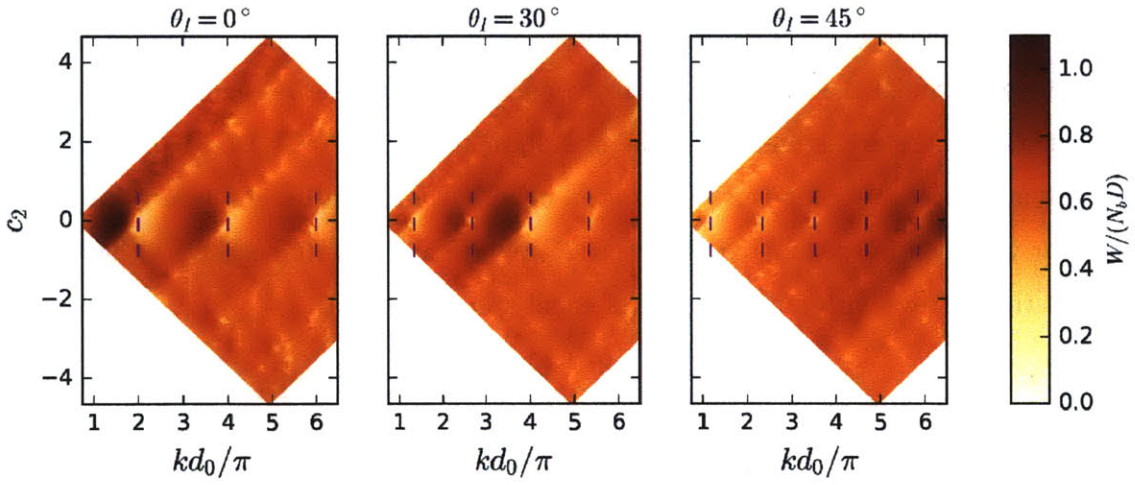

Figure 4.33: Normalized capture width W_a/N_bD for $ka = ka_r$ for 20-body arrays with quadratic variation in spacing between the bodies. Note that the changes in kd_0/π correspond to changes in d_0 as the wavenumber is constant for each plot.

Figure 4.34 shows array gain q for resonant wavenumber ka_r. Identical to the linear-spacing-variation arrays, the performance is dominated by uniform arrays, so the maximal values occur along the $c_2 = 0$ axis. Here, however, the performance shows more prominent features for the $c_2 > 0$ half of the feasible parameter space, i.e. for arrays with bodies more densely packed in the middle of the array. Notably, the region of diminished performance that runs along the lines emanating from Rayleigh points are more pronounced in the $c_2 > 0$ region. This means that the arrays where the spacing between the central bodies equals one of the Rayleigh wavelengths, the performance is diminished.

The spectral array gain q^S makes the preference on the sign of c_2 even more clear, Figure

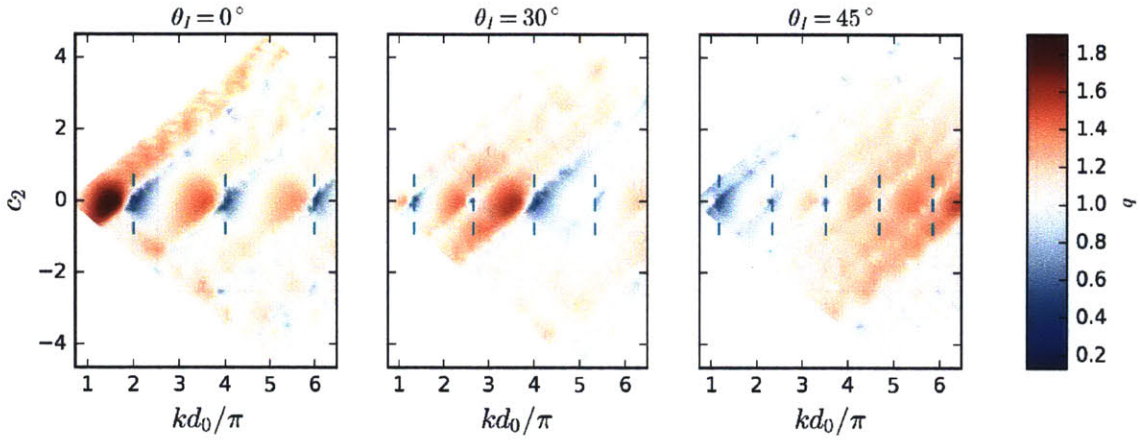

Figure 4.34: Array gain q for $ka = ka_r$. Note that the changes in kd_0/π correspond to changes in d_0 as the wavenumber is constant for each plot.

4.35. For $\theta_I < 45°$ there is a clear preference for arrays with large c_2 values (arrays with dense center), except for very closely spaced arrays ($d_0/2a \lesssim 2.5$) where uniformly spaced arrays is preferred.

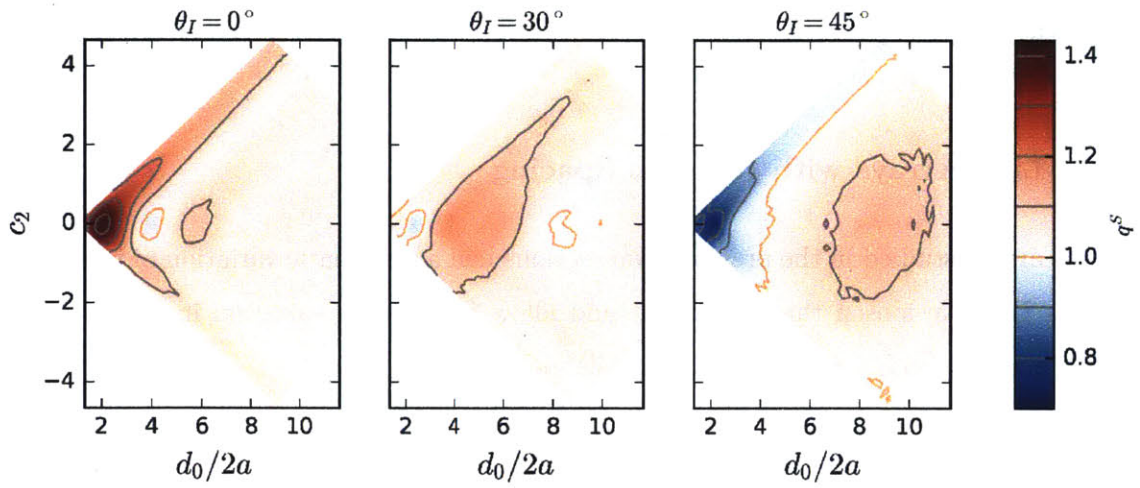

Figure 4.35: Spectral array gain q^S.

The preference for positive values of c_2 (arrays with a denser center) over a large range of incoming angles carries over to the case of directional seas, Figure 4.36. Both in terms of total spectral gain q^{DS} and in terms of extent-normalized spectral capture width W_a^{DS}/Y, arrays with positive (or at least positive-definite) c_2 perform better. Overall, however, maximal values of q^{DS} and W_a^{DS}/Y occur for very closely spaced arrays (small $d_0/2a$) with uniform spacing.

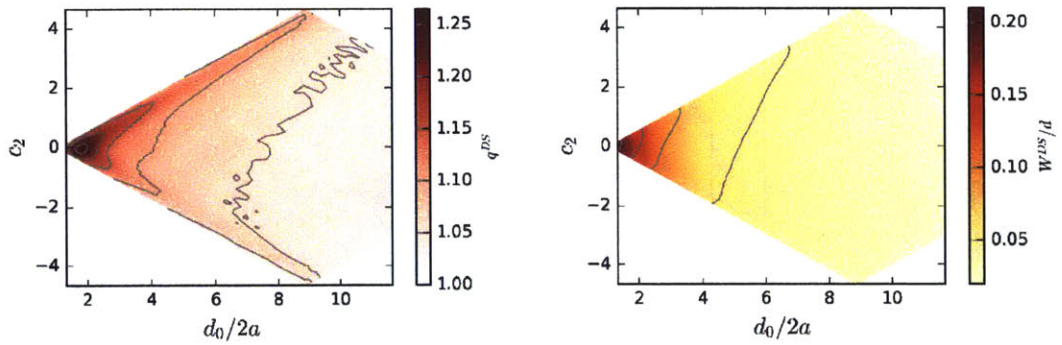

(a) q^{DS} (b) W_a^{DS}/Y

Figure 4.36: Rectangular array performance in directional seas.

In summary, line arrays with quadratic variation in spacing exhibit some similar features to those found in arrays with linear spacing variation. The maximum and minimum performance values are also very similar because both of these array types are dominated by the performance of uniformly spaced arrays. Arrays with quadratic spacing variation exhibit a stronger dependency on the direction of variation, i.e. the sign of c_2, especially for arrays with larger spacing. In those cases, arrays with densely packed center are preferred.

4.5.3 Line Arrays with Random Spacing

The line arrays studied in the previous two sections had a systematic variation of inter-body spacing. Here we loosen that constraint and allow for random variation in spacing. The spacing between bodies i and $i+1$ is now defined

$$d_i = d + \Delta d \tag{4.34}$$

where Δd is the random deviation from the uniform spacing d. The random deviation Δd is drawn from a uniform distribution U

$$\Delta d \sim U(-\epsilon, \epsilon) \ , \tag{4.35}$$

where ϵ denotes the limits of the support of the distribution. The maximum value ϵ is bounded from above by

$$\epsilon < d - 2a \ , \tag{4.36}$$

which prevents cylinders in a perturbed array to touch each other (a is the body radius). Several examples of array configurations are shown in Figure 4.37.

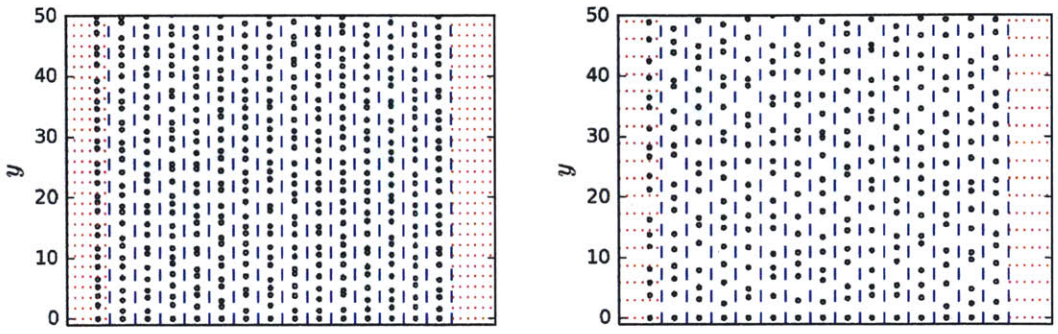

(a) $d/2a = 2.9$, $\epsilon/2a = 1.85$ (b) $d/2a = 4.8$, $\epsilon/2a = 3.75$

Figure 4.37: Examples of 15 configurations of 50-body line array with random spacing perturbation for different average spacings. The random perturbation is close to maximum allowed in both cases. Red lines indicate the average spacing d. Note that these are all line array (i.e. only one column of bodies); multiple realizations of these line arrays are shown together for comparison. Also note that the y-limits have been cropped for clarity, so the entire array extent in y-direction is not captured in this view.

We present here a summary of a number of simulations conducted on 50-body line arrays of different average spacing d and with different random perturbations. For three different amplitudes of perturbation ϵ, we calculate 50 realizations of random array configurations. The results below focus on the means and the standard deviations of the obtained results.

Array gain q for 50-body line arrays for normal incidence is shown in Figure 4.38. As expected, a small amount of position perturbation from a uniform spacing does not alter the performance significantly. As the amount of allowed random perturbation ϵ increases, the performance deviates from the uniform-spacing performance. In particular, the changes in performance act towards ironing out the peaks and troughs in performance. This is effect is amplified for arrays with larger average spacing, especially at larger wavenumbers, Figure 4.38b. As a result, array gain is more uniformly distributed as a function of wavenumber. Note that there is no significant increase of standard deviation of q when increasing ϵ from medium values to maximum, especially for large average spacing and large wavenumbers. The mean, however, is still affected by the increase in ϵ. Performance for different average spacings and incoming angles (smaller than 90°) is very similar, e.g. see Figure 4.29.

When the waves are incoming along the array ($\theta = 90°$), the performance is markedly different than that in Figure 4.38. We still see the usual trait of attenuator arrays — gain

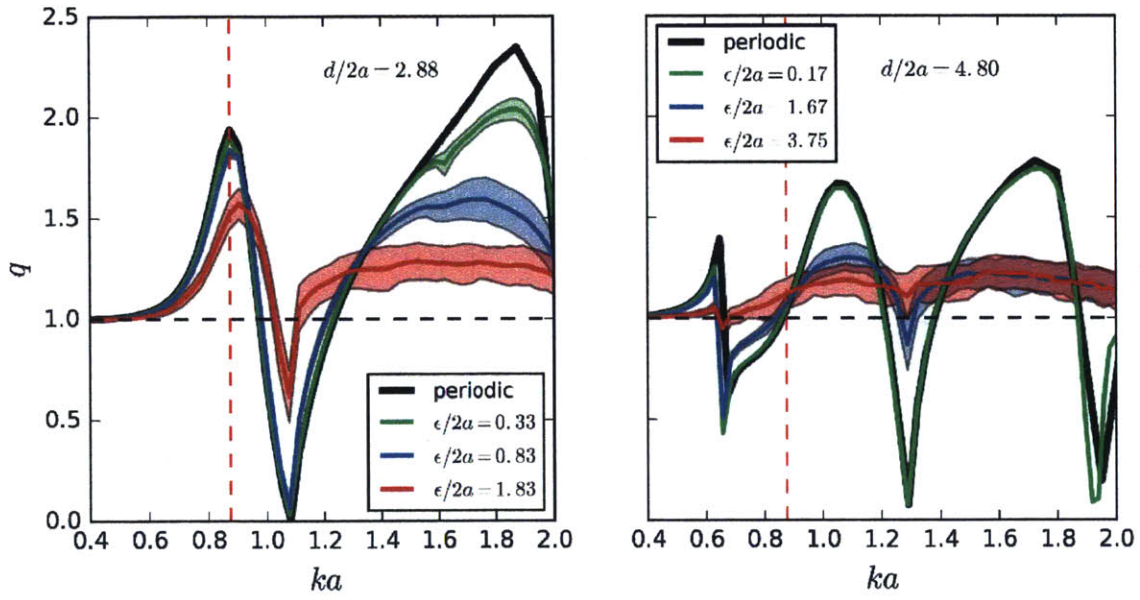

Figure 4.38: Array gain q of 50-body line arrays with different amount of random perturbation, for two different average spacings d; incoming angle $\theta = 0°$. The results show the mean $\pm$ 1 standard deviation for three different perturbation distributions. For both spacings the largest amount of perturbation is very close to the maximal allowed amount based on (4.36). Performance of a periodic array with the periodicity d is shown for comparison.

is larger that 1 for sub-resonant wavenumbers, and much lower than 1 for super-resonant frequencies. The increase of the amplitude of random perturbations slightly affects the mean in that the perturbations iron out the slight jumps in the performance. On the other hand, the standard deviation of q is almost unaffected by the increase of ϵ — it is negligible in all cases. Overall, introducing random irregularities cannot affect the performance of an attenuator arrays.

Increasing the number of bodies in the array to more that 50 has a limited effect on the performance. Figure 4.40 shows the comparison of q for 50- and 100-body arrays with maximum amplitude of random perturbations. For most incoming angles, doubling the number of bodies has almost a negligible effect on the mean q, and its standard deviation is slightly reduced (see also Figure 4.30). For $\theta_I = 90°$, increasing the number of bodies affects the mean in the way that it works to increase the difference in wavenumber-dependent performance — the maximal gain in the sub-resonant region is increased, and the gain in the super-resonant regime is uniformly decreased. The decrease in performance with the increase in N_b for attenuator arrays is similar to the case for uniform spacing, Figure 4.15. There the decrease in q with the increase on N_b is caused by adding bodies "downstream",

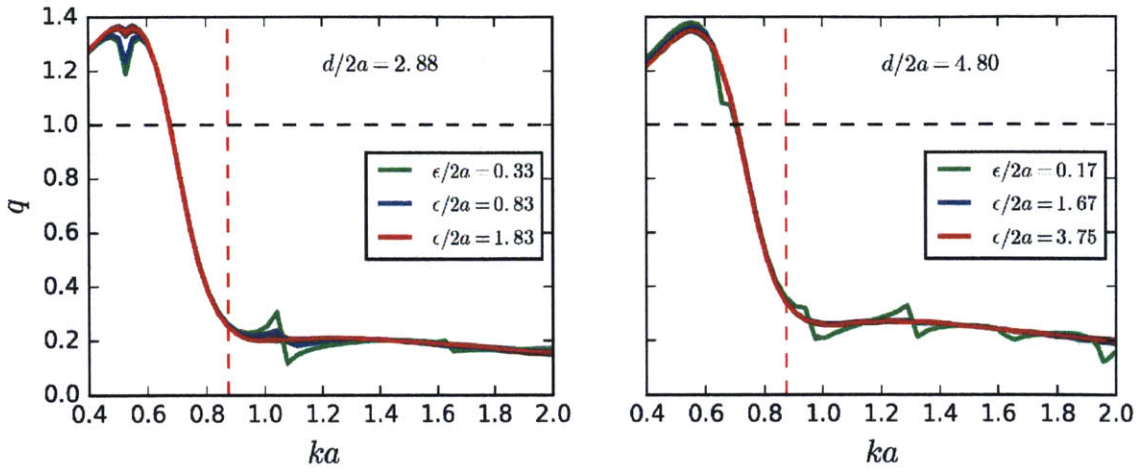

Figure 4.39: Array gain q of 50-body line arrays with different amount of random perturbation, for two different average spacings; incoming angle $\theta = 90°$. The results show the mean $\pm$ 1 standard deviation for three different perturbation distributions. For both spacings the largest amount of perturbation is very close to the maximal allowed amount based on (4.36).

in the shadow of all previous bodies, where they do not contribute significantly to energy extraction (c.f. Figure 4.24). The standard deviation of q is negligible, identical to 50-body arrays.

Spectral gain q^S shows little dependency on the amplitude of random perturbations. For smaller average spacings, there is almost no difference in the mean values of q^S, while the standard deviation is negligible, Figure 4.41. Increasing the spacing only slightly changes that, and mostly for smaller incoming angles θ_I. Choosing a different spectrum could result in larger differences.

Increasing the number of bodies has even smaller effect on q^S than on q, Figure 4.42. The only case where the 100-body array performs differently than a 50-body one is for $\theta_I = 90°$. For $\theta_I = 90°$, q^S of a 100-body array is worse than the 50-body one, similar to that observed for q, and with the same cause.

An alternative approach to the one taken here for studying arrays with random spacing is also possible. Instead of studying random deviations from a uniform spacing, one can draw each spacing d_i from a distribution on a semi-infinite support, e.g. a Gamma distribution

$$d_i \sim \Gamma(\alpha, \beta) + 2a \,, \tag{4.37}$$

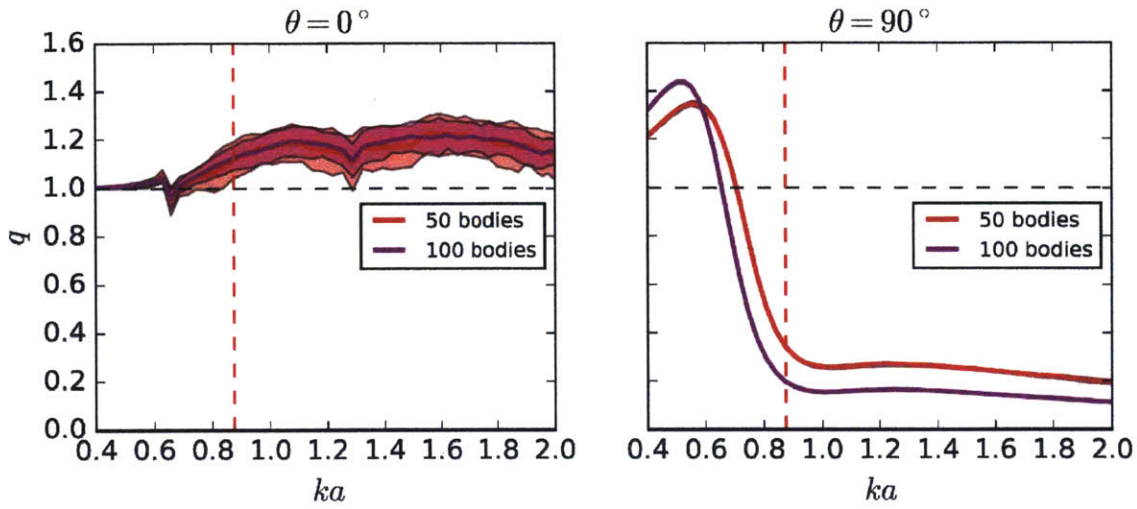

Figure 4.40: Comparison of the mean and standard deviation of array gain q for 50- and 100-body line arrays, for $d/2a = 4.8$. The results show the mean $\pm$ 1 standard deviation for the maximum allowed perturbation.

where α and β are the shape and scaling parameters describing the Gamma distribution (defined on $\{0, \infty\}$)

$$\Gamma(\alpha, \beta) \propto x^{\alpha-1} e^{-\beta x} \, . \tag{4.38}$$

The shape parameter α should be larger than 2 so that the probability of bodies touching is zero (increasing it further would decrease the chances of bodies almost touching). Varying the rate parameter β would then alter the mean spacing of the array (the mean of the Gamma distribution is α/β).

The approach based on (4.34) that is used in this section limits the largest spacing to $d - 2a$. Using a distribution like (4.37) would allow for a much larger range of allowed spacings by removing the maximum spacing constraint. The introduction of large spacings into an array might lead to an improved performance for small wavenumbers. We leave this problem for future studies.

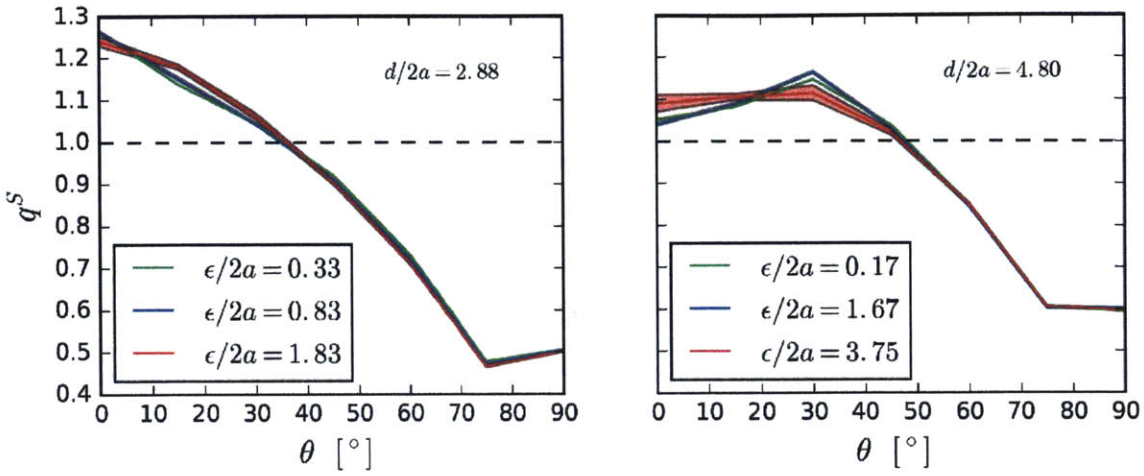

Figure 4.41: Spectral array gain q^S of 50-body line arrays with different amount of random perturbation, for two different average spacings. The results show the mean ± 1 standard deviation for three different perturbation distributions. For both spacings the largest amount of perturbation is very close to the maximal allowed amount based on (4.36).

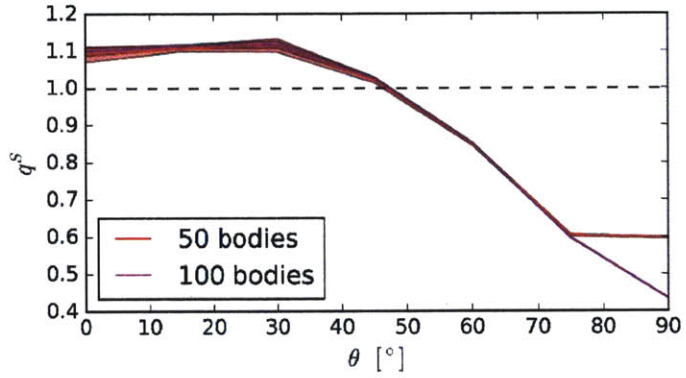

Figure 4.42: Comparison of the mean and standard deviation of the spectral array gain q^S for 50- and 100-body line arrays, for $d/2a = 4.8$. The results show the mean ± 1 standard deviation for the maximum allowed perturbation.

4.6 Performance of Large Regularly Spaced Rectangular Arrays

We now turn our attention from line arrays to rectangular arrays. By a rectangular array we consider an array where bodies are placed in a structured way, on the nodes of a regular, two-dimensional grid. In general, the grid only needs to be topologically identical to a rectangular grid, i.e. such that there exist a bijective mapping between the distorted and the regular grid. For example, uniform rectangular arrays are those for which there is no distortion of the background grid, and the spacings d_x, d_y between bodies along x and y axes (major axes of the grid) are constant. We leave further discussion of different spatial configurations and parameterizations of rectangular arrays for Section 5.3, and focus here on uniform rectangular arrays.

4.6.1 Rectangular Arrays with Uniform Spacing

Consider a rectangular array with uniform spacing between the bodies in each row, and uniform spacing of the rows (leaving aside for a moment the ambiguity in defining a "row"). Without the loss of generality, let us orient the array such that the two major axis of the array grid coincide with x and y axis. We denote the number of bodies in x- and y-direction as N_x and N_y, respectively. Let i and j denote the x- and y-direction body indices. Then the location of body $\mathcal{B}_{ij}$ in an array with uniform spacings d_x and d_y is

$$\begin{aligned} x_{ij} &= (i-1)\, d_x \,, \\ y_{ij} &= (j-1)\, d_y \,, \end{aligned} \tag{4.39}$$

where

$$i = 1, \ldots, N_x \quad j = 1, \ldots, N_y \,. \tag{4.40}$$

We can now define what exactly is meant by a "row". A row of an array in this thesis denotes a collection of bodies that is placed perpendicular to the dominant wave propagation direction. Since we take $\theta_I = 0°$ as the dominant direction, an array row denotes a collection of bodies extending in the y-direction that have the same i-index. Then j index labels a body in the row. This definition is similar to the usual matrix notation where i index denotes a row and j denotes a column, with the difference that in our case the array is

rotated by 90°.

In section we study the performance of uniform rectangular WEC arrays with $N_x = 3$, $N_y = 20$ in regular and irregular seas as a function of spacings d_x and d_y. A part of the geometry of a typical array is given in Figure 4.43.

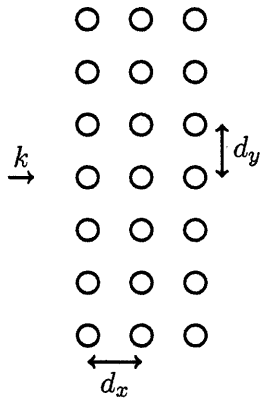

Figure 4.43: Geometry of a rectangular array with uniform spacing.

The effect of spacings d_x and d_y on non-dimensional capture width W_a/N_bD is shown in Figure 4.44, for the resonant wavenumber ka_r and three incoming angles. As is the case for line arrays, the largest portion of energy is extracted at the resonant wavenumber ka_r; off-resonant energy extraction is lagging behind, especially for the sub-resonant wavenumbers (Figure 4.31). A prominent feature is the occurrence of linear features for constant d_x or d_y spacing along which arrays extract far less energy. These features are better visible on the array gain plot, discussed next.

Array gain q for three representative wavenumbers and three incoming angles in shown in Figure 4.46. There is a significant gain for all three wavenumbers, but one has to keep in mind that the absolute amount of extracted energy for off-resonant wavenumbers is still much smaller than for resonant one, Figure 4.31. Compared to the line array configurations, uniform rectangular arrays exhibit larger q values for all wavenumbers in question (c.f. Figure 4.28 for linear-spacing and Figure 4.34 for quadratic-spacing variation arrays, both of which contain the performance of a uniformly spaced line array when the spacing variation is zero). Hence, there is a clear benefit in combining rows of bodies to form rectangular arrays.

There is a lot of structure in the energy extraction response, as can be expected for a structured array. In particular, the linear features of reduced performance resulted from a

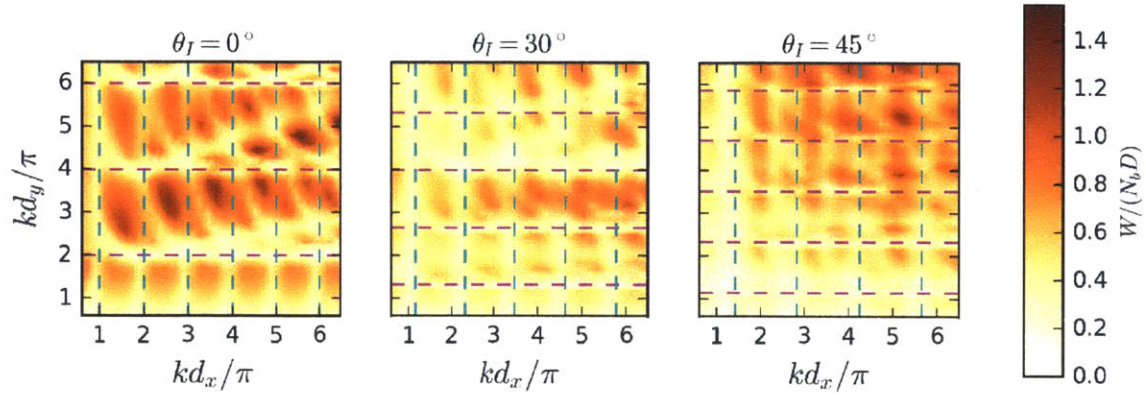

Figure 4.44: Normalized capture width W_a/N_bD for resonant wavenumber ka_r and three different incoming angles θ_I. The dashed lines represent Rayleigh-related spacings (magenta), and Bragg-related (green) spacings. Note that the changes in kd_x/π and kd_y/π correspond to changes in d_x and d_y as the wavenumber is constant for each plot.

well-known physical phenomena. The horizontal lines of decreased extraction performance are due to the new mode creation at Rayleigh wavelengths, i.e. when the spacing d_y equals one of the Rayleigh wavelengths, as given in (4.22). This effect is equivalent to the one occurring in periodic and line arrays with uniform spacings. However, unlike the periodic or uniformly-spaced line arrays where maximal q occurred for kd *below* the first critical point, here the maximal q occurs for higher kd, i.e. for wavenumbers for which there was already some energy redistribution to newly formed scattering modes. The exact location of the maximum and its position relative to the Rayleigh critical points depends on θ_I and d_x, but it is almost always after some new scattering modes have been formed.

The vertical lines along which there is a reduction in extracted energy can be related to Bragg resonance. Bragg resonance occurs when there is a constructive interference from scatterers caused by a favorable relationship between the phases of scattered waves. This occurs when the scatterers are separated by an integer number n of half-wavelengths apart, in the direction of wave propagation. In our notation, that condition reads

$$kd_x \cos\theta_I = n\pi \ . \tag{4.41}$$

Bragg resonance is usually defined when a waves hits a structured medium that occupies semi-infinite space (e.g. a right half-plane), in which case the reflection can be very strong (Li and Mei, 2007a). Here we have an example of a structured array that does not fully

occupy the half-space, so the effects of Bragg scattering are expected to be less prominent. The predictions on the locations of reduced performance based on (4.41) still hold well, Figure 4.44–4.45.

If we compare the array capture width W_a with the array extent Y in the y-direction, Figure 4.46, we see that for the resonant wavenumber $W_a/Y > 1$, i.e. the array extracts all of the energy from an incoming wave crest of length larger than array extent! This is much larger than W_a/Y for line arrays, which was around 0.47 for uniformly-spaced line (and periodic) arrays. These high values occur for smaller d_y values, so that the array operates in the regime before new scattering modes have been created. As seen in Figure 4.45, this is the area with a modest q (still larger than 1), so there is a trade-off between achieving high q and high W_a/Y. For off-resonance wavenumbers, W_a/Y drops below 1, but still remains rather large ($\sim$ 0.6–0.9, Figure 4.32).

For waves incoming at $\theta_I = 90°$, i.e. along the y-axis of the array, we observe the same behavior as for arrays of other configuration types — array gain q is significant only for sub-resonant wavenumbers, Figure 4.47. There are further reductions in q at spacings that correspond to Bragg-resonant spacing due to increased reflection (note that in this case d_y replaces d_x in equation (4.41), and the incoming angle for that equation is measured from 90°). Also, there are two regimes in which an attenuator array at sub-resonant wavenumbers ($ka_<$ in this case) is efficient. The first configuration are arrays with large $d_x/2a$ spacing, and small $d_y/2a$ spacing (d_y below the first Bragg resonance line), corresponding to the high-q area in the lower right corner of Figure 4.47. The second regime is for small $d_x/2a$ and large $d_y/2a$ (upper left region of Figure 4.47a), which can be considered as a line array or closely-spaced groups of bodies. In both cases the behavior should approach that of line arrays (c.f. Figure 4.20), where there is significant gain at sub-resonant wavenumber for any spacing d_y. In the first regime, this should occur when d_x is large enough so that the rows can be considered as isolated line arrays. In the second regime, this occurs for larger d_y values (already visible in Figure 4.47), so that a group of bodies can be approximated by a singe body.

Having the results of Section 4.4 in mind, one might question whether the reductions in q are due to near-trapped waves, rather than Bragg resonance. Both of these phenomena occur (if they exist) around $kd = n\pi$, so they can be hard to differentiate. It is not known whether the array in question supports a trapped wave, and what precisely its effects might

be. However, resonant effects due to trapped waves are usually sharp, asymmetric features Hsu, Zhen, Lee, et al., 2013, while Bragg resonant causes deep, symmetric wells. Since the character of the features in Figure 4.47 is pretty symmetric across the critical value, we believe that the features are predominantly due to Bragg resonance.

Spectral array gain q^S smooths out most of the features in q caused by scattering mode creation and Bragg resonance, Figure 4.48. The maximum value of 1.32 for $\theta_I = 0°$ is smaller than that for uniformly-spaced line arrays and periodic arrays. The maximum q^S occurs for $d_x/2a = 4.28$, $d_y/2a = 5.40$, i.e. for much larger y-direction spacing than for uniform line arrays and periodic arrays. The values of q^S are much more modest for non-zero incoming angles (also see Figure 4.35).

The spectral capture width W_a^S is now much smaller than the array extent Y (maximum value $W_a^S/Y \sim 0.45$ for all incoming angles in question), Figure 4.49, but it is still substantially larger than that for uniformly-spaced line arrays and periodic arrays where the maximum value is ~ 0.24. The maximum values of W_a^S/Y still occur for closely spaced arrays in y-direction, with little dependency on d_x.

The maximal value of the total array gain $q^{DS} = 1.06$ is smaller than for the uniformly-spaced line array ($q^{DS} = 1.28$ in that case), Figure 4.50a. The maximum occurs at $d_y/2a = 6.05$ and $d_x/2a = 2.88$, a much larger y-spacing than for uniformly-spaced arrays. On the other hand, the maximum value of the total capture width $W_a^{DS}/Y = 0.44$ is larger than for line arrays. Smaller d_y is still favored in that case.

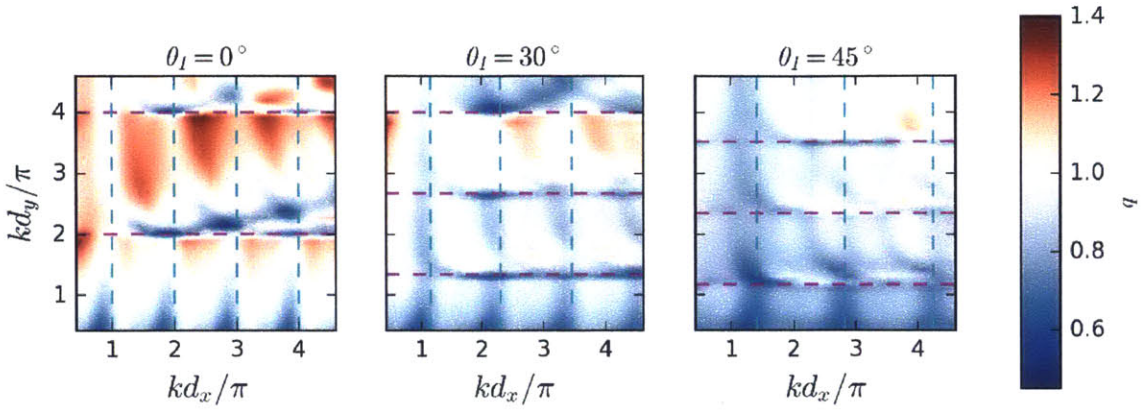

(a) $ka = ka_<$

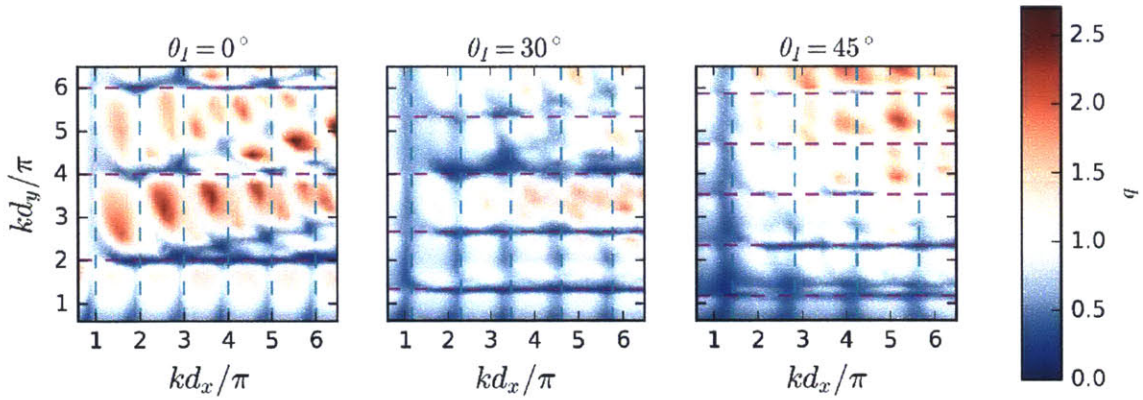

(b) $ka = ka_r$

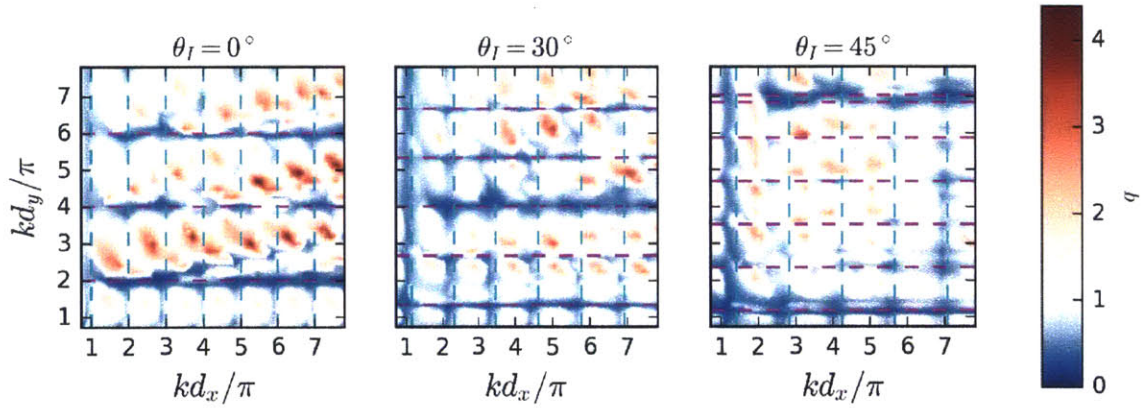

(c) $ka = ka_>$

Figure 4.45: Array gain q for three wavenumbers and three incoming angles. The dashed lines represent Rayleigh-related spacings (magenta), and Bragg-related (green) spacings. Note that the changes in kd_x/π and kd_y/π correspond to changes in d_x and d_y as the wavenumber constant is for each plot.

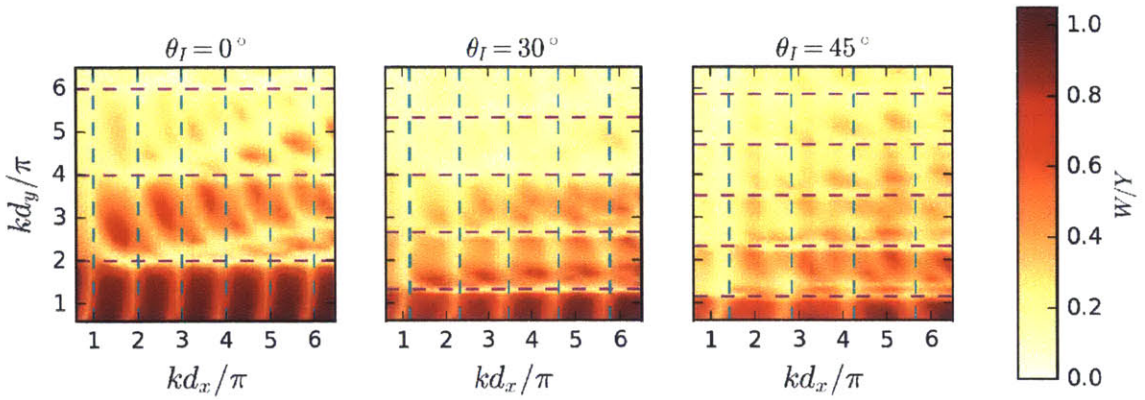

Figure 4.46: Capture width W_a normalized by the array extent Y in y-direction for resonant wavenumber ka_r. The dashed lines represent Rayleigh-related spacings (magenta), and Bragg-related (green) spacings. Note that the changes in kd_x/π and kd_y/π correspond to changes in d_x and d_y as the wavenumber constant is for each plot.

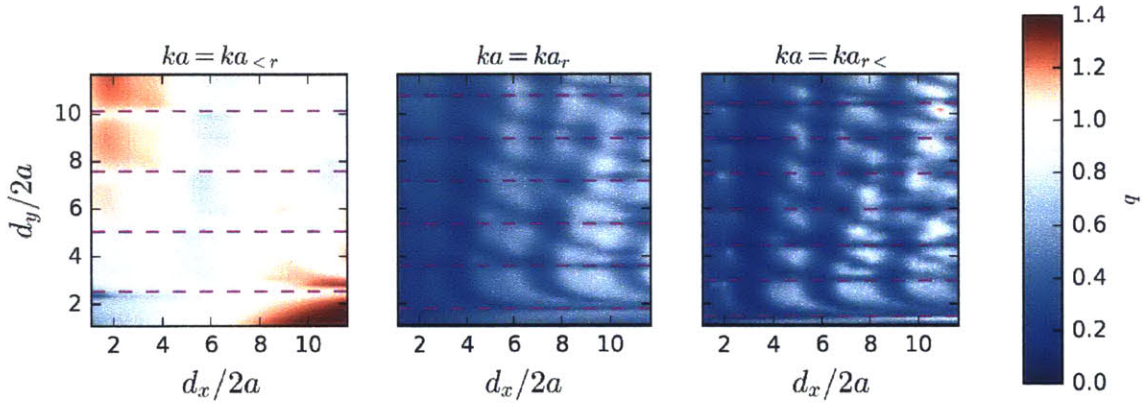

Figure 4.47: Array gain q for $\theta_I = 90°$ for three wavenumbers. The dashed lines represent Bragg-related spacings.

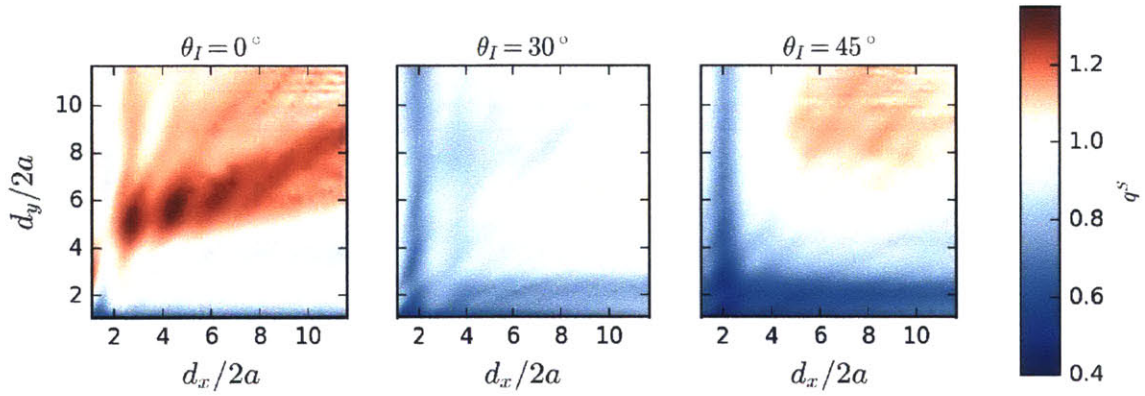

Figure 4.48: Spectral array gain q^S for three incoming angles θ_I as a function of array spacing.

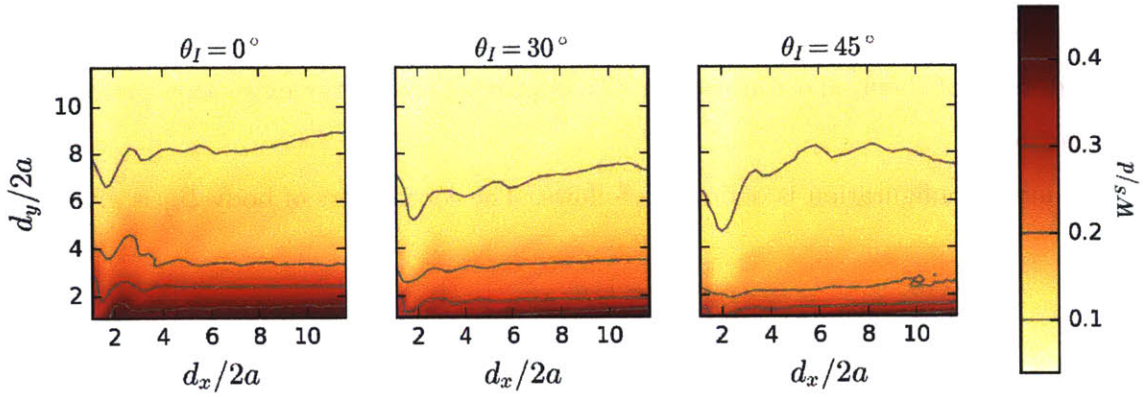

Figure 4.49: Spectral capture width W_a^S normalized by array extent Y in y-direction.

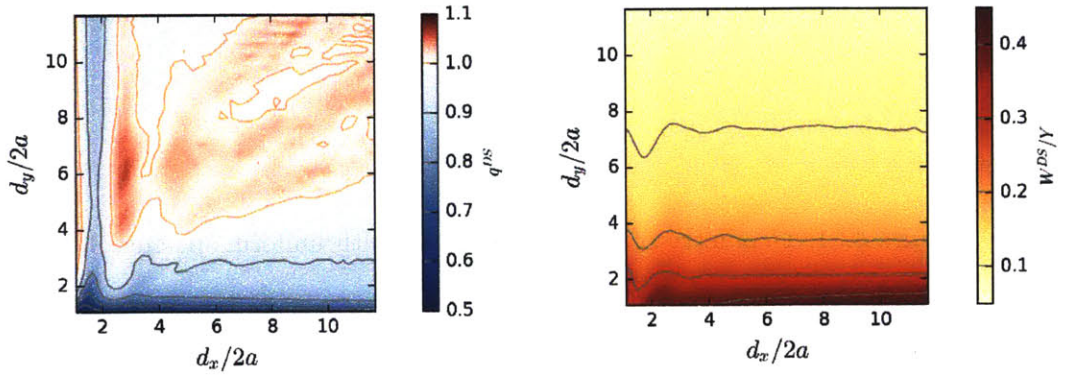

(a) q^{DS} (b) W_a^{DS}/Y

Figure 4.50: Rectangular array performance in directional seas as a function of spacings d_x and d_y.

4.6.2 Rectangular Arrays with Staggered Rows

We study here the effect of row shifts s_y in y-direction on uniformly spaced arrays. We call this configuration an array with staggered rows. A staggered configuration could be beneficial because it allows for the bodies in the back rows to come out of the shadow of the bodies in front of them, and thus potentially improving the energy extraction performance of the array.

The array configuration is defined as follows. The coordinates of body $\mathcal{B}_{ij}$ is given by

$$\begin{aligned} x_{ij} &= (i-1)\, d_x \,, \\ y_{ij} &= (j-1)\, d_y + (i-1) s_y \,, \end{aligned} \tag{4.42}$$

where i and j indices are given in (4.40). In this section, we study a 2×20 ($N_x \times N_y$) staggered rectangular array. We keep d_y spacing fixed ($d_y/2a = 2.8$), and systematically vary spacing d_x and row shift s_y.

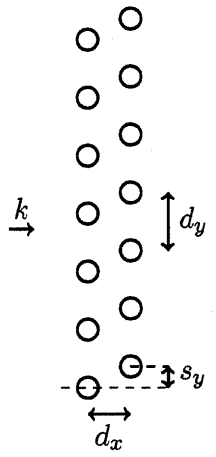

Figure 4.51: Geometry of a staggered array with uniform spacing.

Array gain for staggered arrays in shown in Figure 4.52. The maximum q values for both resonant and off-resonant wavenumbers are larger than for uniformly-spaced line arrays, but still smaller than for the uniform rectangular array studied in the previous section. That could be due to the fact that the arrays studied in the previous section had three 20-body rows, while the arrays in this section have only two. Adding more rows could improve the performance of a staggered arrays, but they are not studied here because they would introduce another parameter that render the presentation of the results very cumbersome. Note that the high q values for the off-resonant wavenumbers are of limited merit because the

overall extracted energy at these wavenumbers is much smaller than that for the resonant wavenumber ka_r, Figure 4.37.

The array capture width W_a normalized by the array extent Y for the resonant wavenumber ka_r is smaller than for the uniformly spaced rectangular array, Figure 4.53, and similar to that of uniform line array. There is only a moderate dependency on the values of d_x and s_y, with many shallow maxima and minima, making it difficult to decide on an optimum. The lack of strong dependency of W_a/Y on d_x is also seen in uniform rectangular arrays (c.f. Figure 4.46). For off-resonant wavenumbers the values of W_a/Y are smaller than for ka_r, but the lack of a strong dependency on d_x and s_y is still present.

Considering again the special case of $\theta_I = 90°$, the familiar picture presents itself again — there is significant gain only for sub-resonant wavenumbers, Figure 4.54. Maximal gain occurs when there is no s_y shift, two rows closely spaced together.

Spectral array gain q^S is shown in Figure 4.52. The maximal values $q^S \sim 1.3$ are comparable to that for uniform rectangular arrays for normal incidence, and outperforming the uniform rectangular arrays for larger incidence angles (see also Figure 4.43). For normal incidence ($\theta_I = 0°$), there are two distinct regions with high q values — one with $s_y = 0$, placing the body in the second row in the direct shadow of the body in the first row, and the other with $s_y = d_y/2$ and d_x as small as allowed. This second case is actually very similar to a 40 body line array with $d'_y = d_y/2$ because the bodies in the second row are located in the middle of the first-row spacing. This is an unconstrained optimum — there is an isolated maximum for non-zero d_x, so the second-row bodies would not end up in the first row if the constraint $d_x > 2a$ were to be removed. For non-normal incidence, non-zero s_y values are strongly favored. The spectral capture width W_a/Y shows only modest values (maximal value ~ 0.12), Figure 4.42. The pattern is very similar to q^S because of the weak dependency of W_a/Y on d_x and s_y.

The total spectral gain q^{DS} and the total capture width W_a^{DS}/Y exhibit the same features as previously discussed, with both achieving lower values than for uniform line arrays. The total array gain q^{DS} achieves maximum in a very similar way to q^S — by either placing the second row body directly behind the first one, or by placing them in between the first row bodies with a small spacing between the rows.

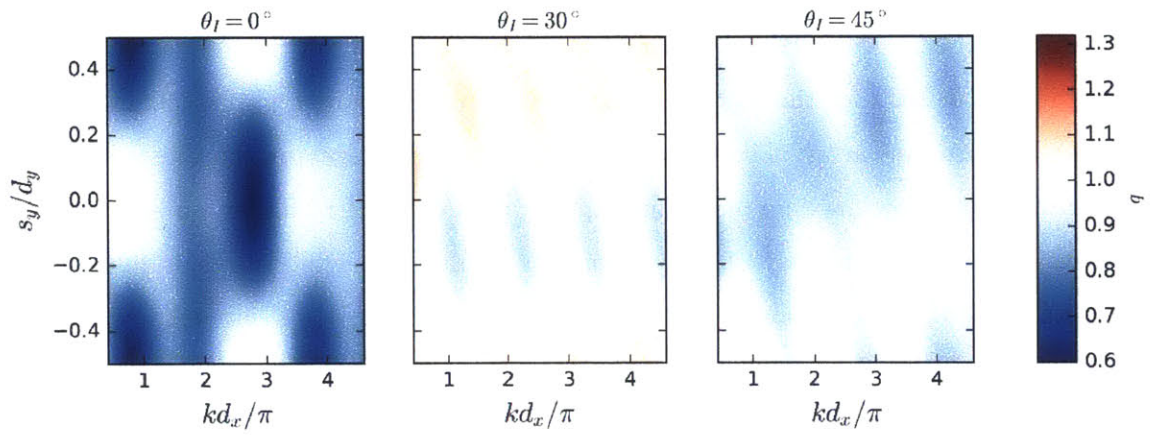

(a) $ka = ka_<$

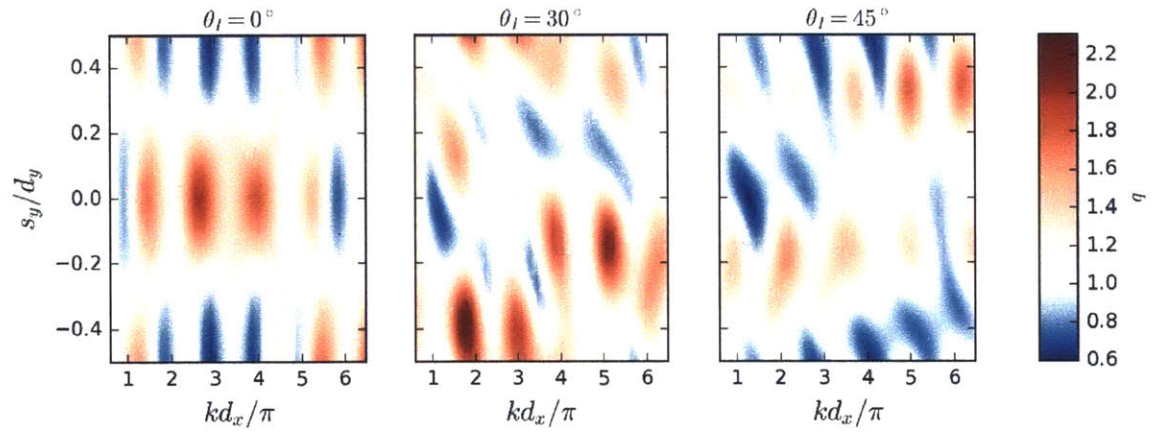

(b) $ka = ka_r$

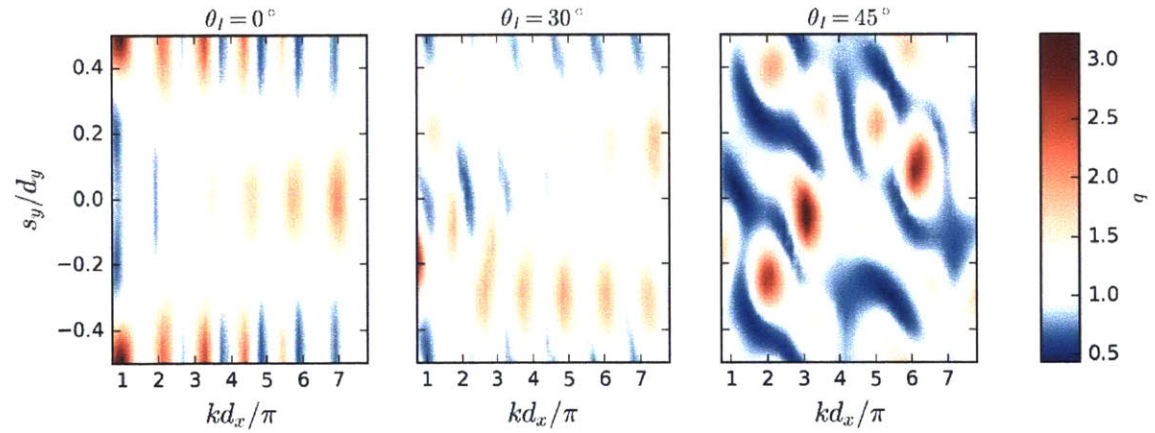

(c) $ka = ka_>$

Figure 4.52: Array gain q. Note that the changes in kd_x/π correspond to changes in d_x as the wavenumber constant is for each plot.

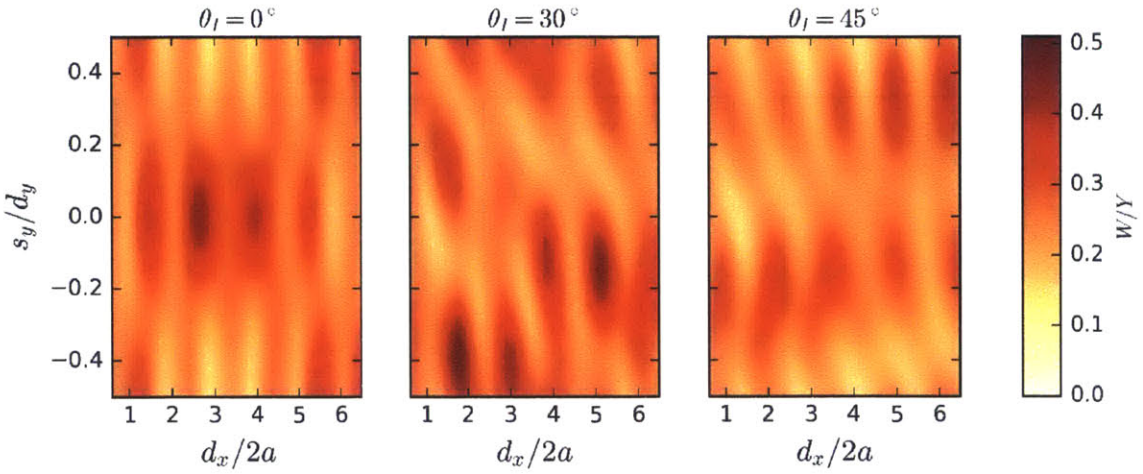

Figure 4.53: Capture width W normalized by the array extent Y in the y-direction for $ka = ka_r$. Note that the changes in kd_x/π correspond to changes in d_x as the wavenumber constant is for each plot.

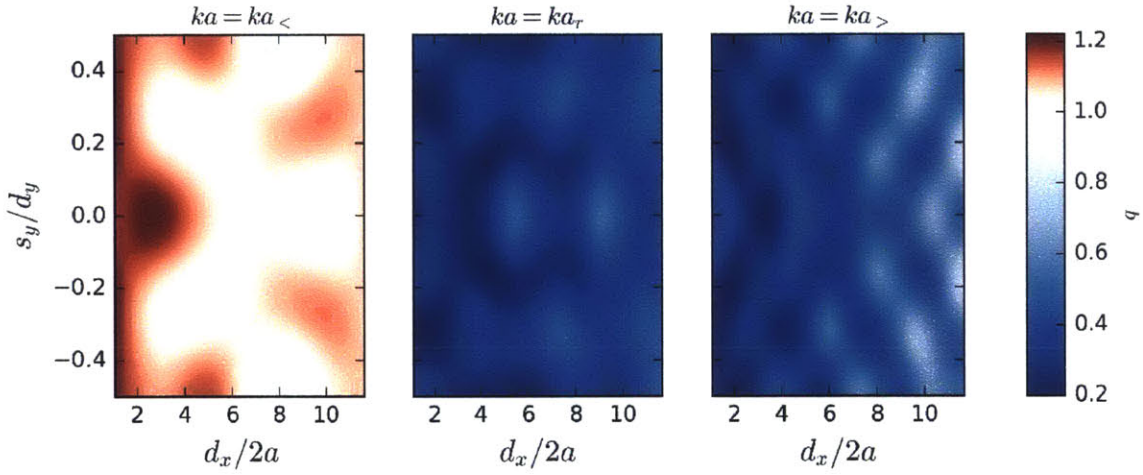

Figure 4.54: Array gain q for $\theta_I = 90°$. Note that the changes in kd_x/π correspond to changes in d_x as the wavenumber is constant for each plot.

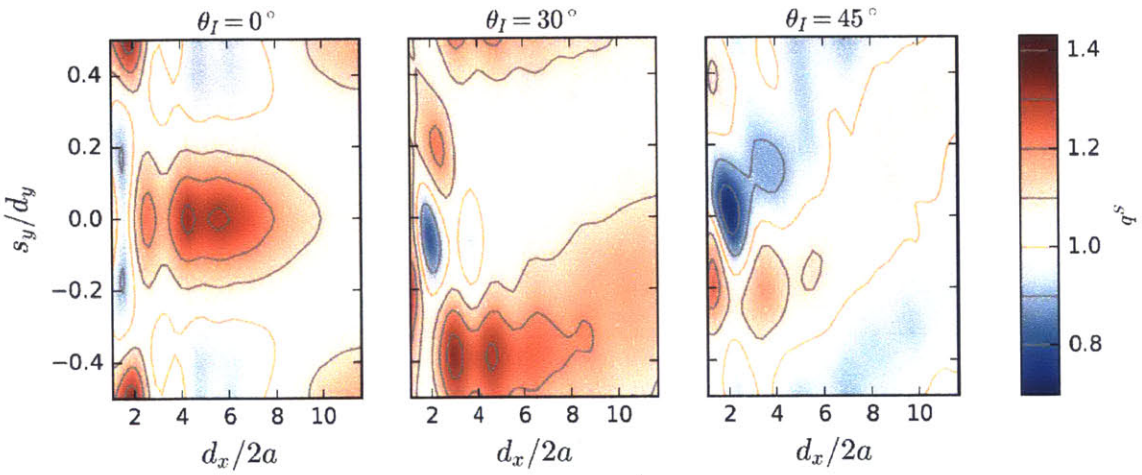

Figure 4.55: Spectral array gain q^S.

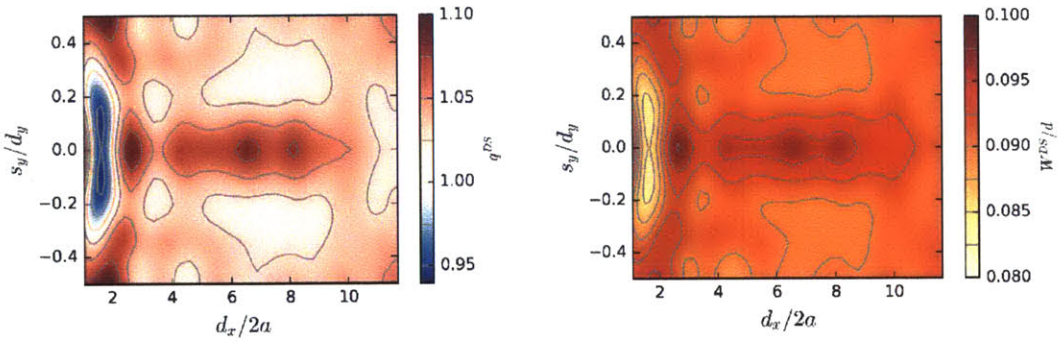

(a) q^{DS}

(b) W_a^{DS}/Y

Figure 4.56: Rectangular array performance in directional seas.

4.6.3 Random Rectangular Arrays

Finally, we present here a computational *tour de force* example — the analysis of 200-body random rectangular arrays. The notation requires some clarifications. The term *rectangular* refers to the fact that every body in the array can be indexed in terms of i, j indices on a grid, in the same way as in (4.40). However, unlike the arrays studied in the previous section where the spacings were either uniform, here every spacing is random — hence the term "random" arrays.

We define the location of body $\mathcal{B}_{ij}$ in a random rectangular array as

$$\begin{aligned} x_{ij} &= \sum_{\hat{\imath}=1}^{i} d_{x;\,\hat{\imath}-1} + s_{x;\,ij} \ , \\ y_{ij} &= \sum_{\hat{\jmath}=1}^{j} d_{y;\,i,\hat{\jmath}-1} + s_{y;\,i} \ , \end{aligned} \tag{4.43}$$

$$i = 1, \ldots, N_x \quad j = 1, \ldots, N_y \ .$$

with the convention that $d_{x,\,0} = d_{y,\,i,0} = d_{y,\,N_x,j} = 0$. The spacings $d_{x,\,i}$, $d_{y,\,ij}$ and the vertical row shift $s_{y,\,i}$ and horizontal body shifts $s_{x,\,ij}$ are all drawn from probability distributions. The spacings $d_{x,\,i}$ and $d_{y,\,ij}$ are drawn from a Gamma distribution

$$\begin{aligned} d_{x\,,i} - 2a &\sim \Gamma(k_x, \theta_x) \ , \\ d_{y\,,ij} - 2a &\sim \Gamma(k_y, \theta_y) \ , \end{aligned} \tag{4.44}$$

Gamma distribution $\Gamma(k, \theta)$ is a two-parameter distribution defined on $[0, \infty\}$, where k is the shape parameter, and θ the scale parameter. The probability density function f of the Gamma distribution is proportional to

$$f(x;\ k, \theta) \propto x^{k-1} e^{-x/\theta} \ . \tag{4.45}$$

The mean of a random variable X distributed according to $X \sim \Gamma(k, \theta)$ is

$$\mathbb{E}[X] = k\theta \ , \tag{4.46}$$

and the variance is

$$Var[X] = k\theta^2 \ . \tag{4.47}$$

The scale parameter θ can be obtained from (4.46) if we provide a desired average spacing $\overline{d}$ and the shape parameter k, e.g. for y-direction

$$\theta_y = \frac{\overline{d_y} - 2a}{k}; . \tag{4.48}$$

Examples of probability density functions of a Gamma-distributed random spacing with different shape parameters k but the same mean $\overline{d_y}/2a$ is given in Figure 4.57.

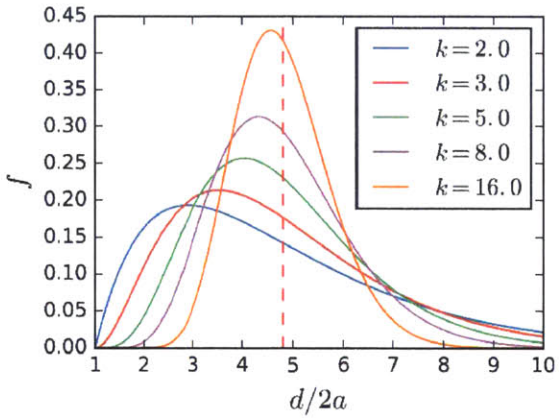

Figure 4.57: Probability density functions of a Gamma-distributed random spacing with different shape parameters k but the same mean $\overline{d_y}/2a$.

The horizontal shift $s_{x,\,ij}$ of a body in row i is drawn form a uniform distribution

$$s_{x,\,ij} \sim U(-\epsilon_{i-1}, \epsilon_i) \ , \tag{4.49}$$

where ϵ_i is the midpoints of spacings $d_{x\,,i}$, adjusted for the body size i.e.

$$\epsilon_i = \frac{d_{x\,,i}}{2} \ . \tag{4.50}$$

The end rows are treated specially, by defining $d_{x\,,0} = d_{x\,,1}$ and $d_{x\,,N_x} = d_{x\,,N_x}$ so that (4.49) holds for all $i = 1, \ldots, N_x$.

Row shifts $s_{y,\,j}$ are designed to be comparable to the uncertainty in array y-extent. According to the Central Limit Theorem, the array extent $Y_i = \sum_{j=1}^{N_y - 1} d_{y\,,ij}$ is a normally

distributed random variable

$$Y_i \sim \mathcal{N}(\mu, \sigma_Y^2) \,, \tag{4.51}$$

where $\mu = (N_x - 1)\overline{d_y}$ is the mean, and σ_Y the standard deviation

$$\sigma_Y = \frac{Var[d_{y,ij}]}{\sqrt{N_y - 1}} = \frac{(\overline{d_y} - 2a)^2}{k\sqrt{N_y - 1}} \,. \tag{4.52}$$

(Note that here the real array extent is $Y = \max_i Y_i$.) We want for the row shifts to be comparable to σ_Y, or to $\overline{d_y}$, which ever is greater. Hence, we draw $s_{y,j}$ from a normal distribution with a zero mean

$$s_{x,ij} \sim \mathcal{N}(0, \sigma^2) \,, \tag{4.53}$$

where the standard deviation σ is defined as

$$\sigma = \max(\overline{d_y}, \sigma_Y) \,. \tag{4.54}$$

The definition (4.43)–(4.54) of array configuration enables a very random-looking arrays, while guaranteeing there will be no overlap between the bodies, regardless of the parameter values or the intricacies of a particular realization.

Here we perform a Monte Simulation on $N_x = 4$, $N_y = 50$ random rectangular arrays, with two different distribution parameters fixed: (i) type-I with $\overline{d_x}/2a = 3.88$, $\overline{d_y}/2a = 3.88$, and (ii) type-II $\overline{d_x}/2a = 3.88$, $\overline{d_y}/2a = 5.8$,both with $k_x = k_y = 3$. The average values $\overline{d_x}$ and $\overline{d_y}$ are selected so that that it matches the high-q^S area for uniform rectangular arrays, Figure 4.48. A few realizations of each array configuration type are shown in Figures 4.58 and 4.59. Calculation is performed on 100 different realizations of array configurations, and a basic statistical analysis is presented next.

The statistical measures of array gain q are shown in Figure 4.60. There is a notable dip in performance at the resonant wavenumber ka_r, and nearly constant gain for super-resonant wavenumbers. The dip in the performance indicates that the optimized performance of an isolated body at resonance is hard to beat with purely random wave interference. No features due to array-resonant behavior like those occurring in arrays with uniform spacing are present any longer. Overall, the maximal values of q (either mean or maximum of all data) are much smaller than for uniform rectangular arrays, c.f. Figure 4.45. On the other hand, there are no regions of strong reduction ($q \approx 0$) in performance caused by uniform-

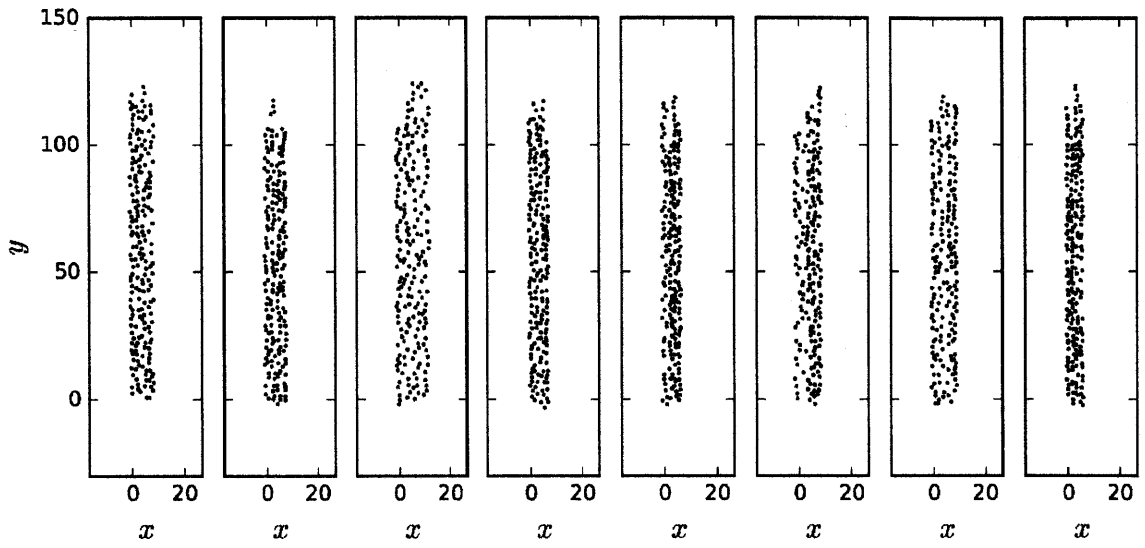

Figure 4.58: Several realizations of random rectangular arrays with $\overline{d_x}/2a = 3.88$, $\overline{d_y}/2a = 3.88$, $k_x = k_y = 3$ (type I).

spacing phenomena as for uniform arrays. The type-II (wider d_y spacing) shows a smaller dip (higher q) at ka_r, but also lower q for super-resonant wavenumbers. This is another example of the trade-off between the achievable maximum values and the broadbandedness in the wavenumber space.

Overall, the performance of the array diminishes with the increase in the incoming angle θ_I. For $\theta_I < 90°$, the performance dip at $ka = ka_r$ is still prominent. Array gain for $\theta_I = 90°$ shows similar features as in all other arrays studied, Figure 4.61, in that there is a significant gain only for low, sub-resonant wavenumbers. Type-I and type-II arrays show almost identical performance. The standard deviation and the extreme values are very close to the mean (a much tighter distribution than for other incoming angles), similar to that for random line arrays (c.f. Figure 4.39). The region of $q > 1$ is pushed to even lower values of ka than for other array configurations studied in this thesis.

Due to the reduced performance at the body resonant wavenumber ka_r for both type-I and type-II arrays, the integration of energy extraction over a spectrum whose peak wavenumber matches ka_r is bound to give low values. This is also borne out in calculation for spectral array gain q^S, Figure 4.62. The maximal values of q^S at $\theta_I = 0°$ barely reach 1, and the performance is monotonically decreasing (with a very tight distribution) with the increase in θ_I. The drop becomes much steeper for $\theta_I \gtrsim 45°$. Given the fact that q is nearly constant for super-resonant wavenumbers, integration over a spectrum that is peaked at

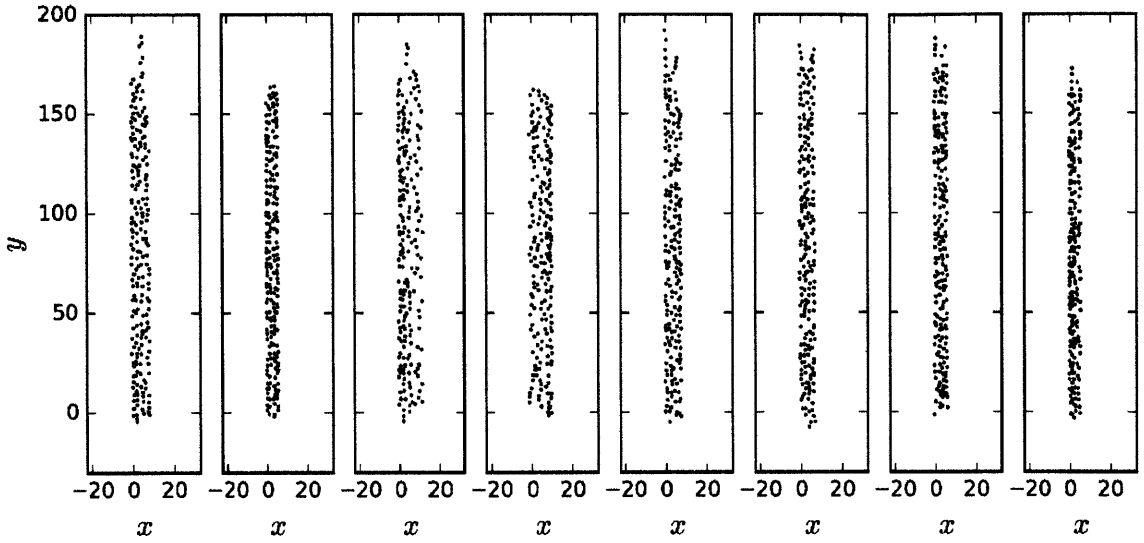

Figure 4.59: Several realizations of random rectangular arrays with $\overline{d_x}/2a = 3.88$, $\overline{d_y}/2a = 5.8$, $k_x = k_y = 3$ (type II).

higher, super-resonant wavenumbers would likely give larger values of q^S. Note, however, that despite having a high gain at super-resonant wavenumbers, the energy extraction is low in that regime so the usefulness of such an approach is questionable.

To further confirm the results on random rectangular arrays, a rectangular array with d_y spacing in between that for type-I and type-II arrays, and with a much tighter distributions ($k_x = k_y = 16$). The results fall in between those presented in this section, with little change in the standard deviation of the results (see Appendix D.1.5).

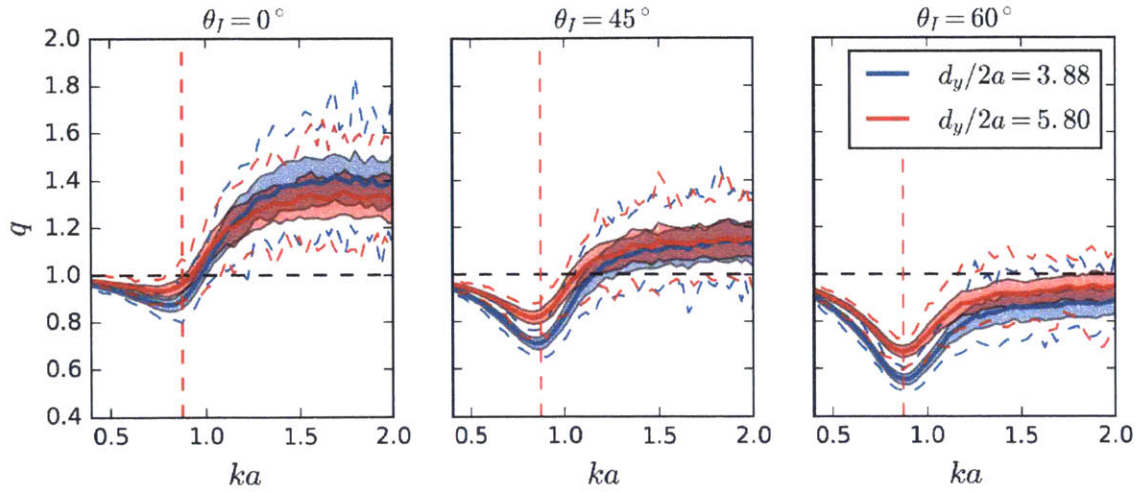

Figure 4.60: Array gain q for random rectangular arrays (type-I and type-II) for three incoming angles θ_I. The results show the mean (solid line) $\pm$ 1 standard deviation (shaded area), and maximal and minimal values (dashed line).

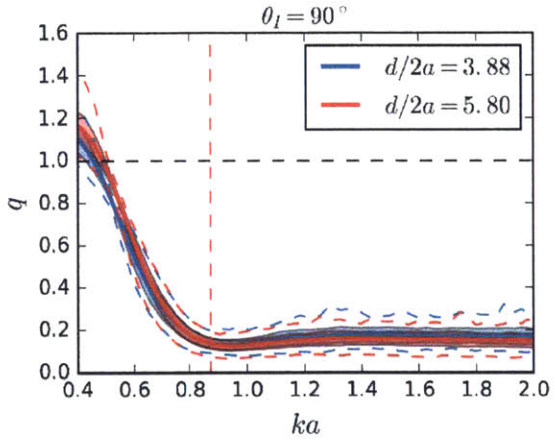

Figure 4.61: Array gain q for random rectangular arrays (type I and type II). The results show the mean (solid line) $\pm$ 1 standard deviation (shaded area), and maximal and minimal values (dashed line).

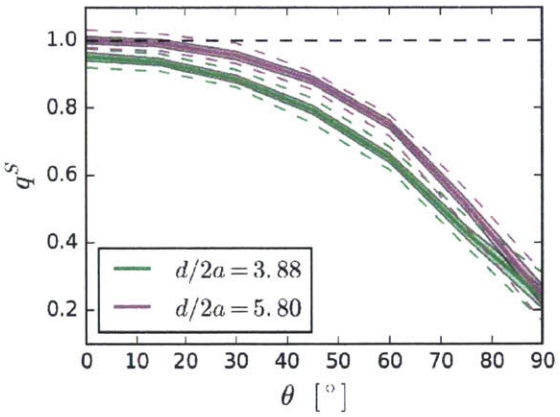

Figure 4.62: Spectral array gain q^S for random rectangular arrays (type-I and type-II). The results show the mean (solid line) $\pm$ 1 standard deviation (shaded area), and maximal and minimal values (dashed line).

4.7 Discussion

What to take away from a slurry of analyses and results presented in this section? Looking at the results presented in this section as a whole, we can make some observation on how WEC arrays behave. Overall, the changes in array configuration parameters affect the wavenumber-dependent quantities much more than the spectrally-averaged ones. This is expected because the physical phenomena that can occur at certain wavenumbers can greatly affect the array performance. This is especially the case for arrays with regular, uniform spacings, where the occurrence of the formation of new scattering modes at Rayleigh points and Bragg scattering all lead to abrupt changes in performance at certain wavenumbers.

The changes in performance are most prominently visible in array gain q. However, one should not be fooled by very high q-values at wavenumbers far away from the resonance because the energy that non-tuned devices (like the ones considered in this thesis) is negligible, so even high amplifications of those small values does not lead to a large absolute gain in extracted energy.

The super-resonant wavenumber $ka_>$ that was specifically considered is in the range where our truncated vertical cylinder still extracts significant amounts of energy. Thus, high gains at that wavenumber do lead to significant improvement in overall energy extraction. This is further confirmed by looking at the array capture width W_a normalized by the array extent along the wave crest Y. We find out that 3×20 uniform rectangular arrays extract almost 90% of the energy at super-resonant wavenumber $ka_>$. At resonant wavenumber ka_r, even higher percentage of energy flux is extracted — $W_a/Y|_{max} = 1.04$, i.e. the array extinction cross-section is greater than its geometrical one!

The presented results show that for uniformly-spaced arrays close spacing results in higher extracted arrays ($d/2a \approx 2.0$ gives best performance based on several criteria for periodic arrays). This gives justification to the choice of the mathematical model — for frequencies and configurations that give maximum power extraction ka, $d/2a$, kd are all $O(1)$, so the scattering and the wave interactions are strong.

Attenuator arrays, i.e. positioning the (long) array axis along the mean wave propagation direction, were shown to have poor performance with $q \sim 0.2$ for all wavenumbers, except for a range of sub-resonant wavenumbers $ka < ka_r$, where q is greater than 1 routinely. This is borne out for both structured and irregular attenuator arryays. One should bear

in mind, however, that despite the perceived gain over the isolated bodies for sub-resonant wavenumbers, the overall energy extracted at these wavenumbers is still minuscule to be used in that regime for practical purposes. This should raise questions on the effectiveness of some attenuator-type devices that are proposed or in use today (Anaconda, Pelamis). Their motion could be approximated as an attenuator array, and we see that, regardless of the array configuration, the extracted energy is much smaller than for a terminator array.

Irregular arrays are less sensitive to the changes in the configuration parameters, especially when the irregularity is already large. The features that emerge in uniformly-spaced arrays are completely absent in irregular arrays, but with the drawback of reduced maximal values in q. We observe a trade-off between high (or low) extreme values of q and the broadbandedness of the response — no high gains, but no very low ones either, and a reduction in performance around the body resonance is balanced by a uniform performance for super-resonant wavenumbers $ka > ka_r$. Somewhat surprisingly, even for spectral gain q^S, where one might expect that there would be benefits of having many different spacings that could correspond to different wavelengths in the spectrum, the uniform spacing rectangular arrays outperform the random ones. In a way, a hydrodynamicist might feel relieved that a random scatter of bodies does not outperform her carefully designed WEC array.

4.7.1 Comparison of WEC Arrays with Optical Structures

Phenomena occurring when an array of bodies placed in a structured manned and exposed to water waves share many similarities with those occurring when photonic crystals and absorbing films are exposed to electro-magnetic (EM) radiation, i.e. light. For one, both are governed by the Helmholtz equation (with a difference that it is the two-dimensional version for water waves (2.2), and three-dimensional for EM waves). Second, photonic crystals and thin-film solar cells are man-made materials, engineered by creating periodic patterns in a dielectric medium. The periodic structure of the material leads to phenomena like band structure, band gaps, mode coupling, etc.

In terms of geometry, our problem is most similar to photonic crystals made out of dielectric rods. The rods are placed in a periodic pattern, and their band structure can possess many interesting features, including embedded localized surface states (Hsu, Zhen, Chua, et al., 2013; Hsu, Zhen, Lee, et al., 2013) and band gaps (Johnson et al., 1999), which can be utilized in practice. For example, band-gap photonic crystals have been

used to design mirrors, wave-guides (Fan et al., 2001), resonant cavities (Joannopoulos, Villeneuve, and Fan, 1997).

Using a two-dimensional periodic array of bodies refracts the incoming wave inside that domain, so the domain effectively becomes as if having a different index of refraction. This way we can remove the change in depth, and just have a region of densely placed bodies. The change of the effective index of refraction has been demonstrated by Hu and Chan (2005) for the incidence of long waves ($kd \ll 1$, $ka \ll 1$) on arrays of bottom-mounted (fixed) cylinders in shallow water. They showed how a densely populated array (small spacing compared to the wavelength and to the cylinder radius) can act as if there is a change in depth (and in gravity for two dimensional arrays). This leads to phenomena like the existence of the Brewster angle (incoming angle at which there is no reflected wave), or the ability to focus the waves to a certain location by organizing the array in a lens-like formation (Hu and Chan, 2005).

Further similarities of densely packed array of cylinders with photonic crystals have been investigated by Hu, Chan, et al. (2011), who found have also looked at energy extraction of if they are not placed in a structured way (Hu, Chan, et al., 2011; Hu and Chan, 2005) These structures resemble photonic crystals the most because they also posses band structure, equivalent to that in photonic crystals.

Solar energy can also be efficiently captured using a thin-film material with a random surface. This material is usually weakly absorbing, if the light were to go through it (in a single pass), it would absorb only a small amount of energy. The idea to improve the absorption is to re-direct the light so that it propagates *along* the film and, thus, absorbs more energy. This field is very well studied in optics, with several established theoretical limits for maximum absorption, especially for thick (slab) cells.

The cell is made out of a material with a higher refractive index n than air (vacuum) so that the light is trapped inside the material by total internal reflection in thick slabs, or by having too slow phase speed to couple with the surrounding wave-field for thin-film cells.

For this concept, however, it is harder to draw parallels with the ocean energy extraction technologies. In case of water waves, there is no difference in the medium (unless we are talking about effective media like discuss by Hu and Chan (2005)). However, the equivalent to changing the medium would be having an abrupt change in water depth h, with the higher refractive index corresponding to the domain with the larger water depth h_H , Figure 4.63.

The refractive index ratio n' would in that case be dependent on the frequency in question because water waves are dispersive, but n' would remain greater than 1.

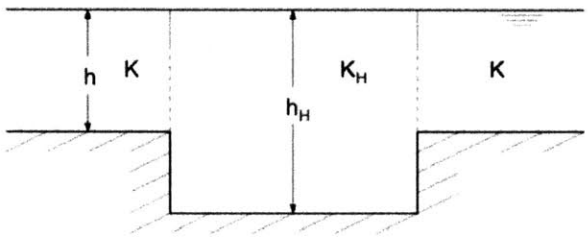

Figure 4.63: An abrupt change in water depth corresponds to a higher refractive index n.

The change of depth still does not resolve the second problem with the analogy — how the energy is extracted. In solar cells, the energy is extracted in the bulk of the material. If we want to use oscillating bodies for energy extraction, they would have to be placed throughout the shallow water region. For thick-slab analogy, these buoys would scatter waves in all directions and a lot of it would leak out without being confined in the high-index area.

Perhaps taking everything into account, the best analogy between the solar cells and water wave energy extraction is to place an energy-extracting membrane on the surface of the fluid. This membrane would change the dispersion relation in that domain, effectively changing the refractive index. Furthermore, if we assume that the membrane is capable of extracting energy over its entire surface (by connecting an elastic membrane to a distributed absorption system, say), this would be equivalent to case when a light penetrates an energy-absorbing material. Ideas for energy extraction by an elastic membrane already exist, although for a membrane placed at the bottom of the sea (WaveCarpet from UC Berkeley). If we stick to the elastic membrane as our energy-extracting system (note that we are leaving the realm of oscillating bodies here), could we apply some of the powerful theorems derived for optical structures?

For thick slabs, i.e. when the material is many wavelengths thick, the fundamental Yablonovitch limit in ray optics states that the intensity of light in is n^2 times larger in a non-absorbing optical slab than in vacuum, provided the surface of the slab is rough enough to achieve isotropic distribution of light rays inside of the slab (the enhancement is $2n^2$ if there is a reflector at the other side of the slab). This results follows from statistical mechanics, and rests on the requirement that the rays internal to the medium behave ergodically. The

energy density of states in the slab in that case is proportional to $k^2 = (n\omega/c)^2$, where c is the speed of light, as if it was in a thermodynamical equilibrium with the black-body radiation from the surrounding vacuum. For weakly absorbing media, this concept leads to large absorption enhancements ($4n^2$), where a single pass would give negligible absorption (Yablonovitch, 1982). For example, for silicon this leads to absorption enhancement of around 50. There are many extension of this limit, e.g. for concentrated light the limit increases to $4n^2/\sin^2\theta$, where θ here is the half-angle of the absorption cone (Campbell and Green, 1986), and further generalized by Yu and Fan (2011) to be $4\pi n^2$ (valid for gratings and roughness with characteristic lengths on the order of a wavelength of light).

For thin-film cells, Stuart and Hall (1997) considered slabs whose thickness is on the order of a single wavelength of light, and provided an absorption enhancement limit that is lower than that of Yablonovich, but with the benefit of having a much thinner slab.

Unfortunately, currently there are no theorems of Yablonovich type for the membrane-type problem. Would such a theorem hold for the case of ocean waves, or be of practical importance? First considering the thick-slab regime, for the ray optics to be valid the characteristic length of the surface roughness has to be large enough so that the wave interaction effects are negligible and ray approximation is valid. Surface roughness in optical slabs would correspond to an irregular front edge of the membrane. The membrane length (equivalent to the slab thickness) should also be at least several wavelengths (in the membrane domain) long to avoid wave interaction effects (Stuart and Hall, 1997). Ocean waves that carry significant amounts of energy have wavelengths of tens to hundreds of meters (see Figure 1.2), so the membrane would have to be several kilometers wide (or more) and hundreds of meters long for the ray approximation to hold. This immediately indicated that the membrane would have to operate in a thin-film regime, where its thickness can be on the order of the wavelength, and the

Taking a step back, however, a bigger problem is that all these theorems are based on the concept of density of states. Density of states (DOS) is a quantum mechanical concept that does not exist for a classical system like water waves. DOS describes the number of states per interval of energy at each energy level that are available to be occupied. In quantum mechanics, energy is directly related to the frequency of a particle

$$E = \hbar\omega \tag{4.55}$$

so that the non-relativistic dispersion relationship

$$\omega = \frac{\hbar k^2}{2m} \tag{4.56}$$

directly connects wavenumber k and its energy E. Such a system does not exist in water waves, where the energy of a wave per unit crest length is not a function of frequency (or wavenumber), it is only a function of amplitude. Without the basic foundation on which these optical theorems are based, it is doubtful that they can be used for water wave problems. Without DOS, some interesting phenomena that occur in quantum systems are not likely to be present in water wave problems. For example, Van Hove singularity (VHS) occurs when group velocity reaches a maximum, i.e. when $\nabla E(k) = 0$. That results in large spikes in DOS, and can potentially have many uses in quantum, thermal, nano and biological systems (Cortes and Jacob, 2013).

Looking into enhancements as the waves propagate into the membrane domain from a classical standpoint, they are constrained by the energy conservation equation. For the case where there is no absorption (equivalent to a non-absorbing optical slab), the energy flux $E \cdot c_g$ is conserved in space, where $E \propto A^2$ is energy of a particular wave of amplitude A at some frequency. Since the extracted power P is proportional to A^2 (cf. 2.24), the enhancement factor e between regions 1 (open water) and 2 (membrane domain), with equivalent water depths h_1 and h_2, would be

$$e \equiv \frac{P_2}{P_1} = \frac{A_2^2}{A_1^2} = \frac{c_{g1}}{c_{g2}} \tag{4.57}$$

For a deep water wave case ($kh \gg 1$), the group velocity is $c_g = \frac{1}{2}\omega/k$, so the enhancement would be

$$e_{\text{deep}} = \frac{k_2}{k_1} = n\,, \tag{4.58}$$

For a shallow water limit $kh \ll 1$, the waves are non-dispersive and $c_g = \sqrt{gh}$, leading to enhancement

$$e_{\text{shallow}} = \sqrt{\frac{h_1}{h_2}} = \sqrt{n}\,, \tag{4.59}$$

For the intermediate depth case, the dispersion relation (2.6) leads to a more complicated expression $c_g = d\omega/dk$, but the enhancement would be between $\sqrt{n}$ and n (leading to a reduction in the required membrane length). In any case, we can see that the enhancement

for water waves is much smaller than that for light, and it rests on different principles than for light waves.

Yu, Raman, and Fan (2010) find that for a thick one-dimensional slab with a periodic grating on the surface the enhancement is $O(n)$ ($2\pi n$ for an asymmetric grating, πn for a symmetric grating). That setup is the closest to the case of an extracting membrane with a periodic front end for water waves, and the result is similar to (4.58). The reduction from $O(n^2)$ to $O(n)$ in optical slabs is due to the reduced number of resonances (not all resonances supported by the film were coupled into). For the water wave case, however, all resonances supported by periodic membrane can be accessed by an incoming wave, so $O(n)$ enhancement is due to the character of energy density, not the inability to couple into resonant channels.

Note also that the character of the absorption enhancement limit for 1D slab with a periodic surface grating (Yu, Raman, and Fan, 2010) is reminiscent of the Srokosz's theoretical limit for optimal gain periodic arrays of point absorbers (equation (4.24)), in that the enhancement(gain) reduces(drops to zero) whenever a new guided channel(scattering order) appears.

Another theoretical similarity is the trade-off between large enhancement and broad angular enhancement. The angular constraint on the light trapping enhancement derived by Yu and Fan (2011) is a direct equivalent of the equation (4.3) for the angular constraint on array gain q. In both cases large gains or enhancements at certain angles must be met by a reduction in performance at others.

One big difference between WEC arrays and solar cells is in the manner of absorption — ocean wave energy converters of the type considered in this thesis extract energy from oscillatory motion and thus further radiate waves, while solar cells absorb energy in the bulk of the material passively, without any addition wave creation. Another significant difference contributing to is that wave energy converters (in isolation) considered in this thesis are not weak absorbers. For example, the truncated vertical cylinder considered in this thesis extracts around 50% of the energy that impinges on its projected area. Truncated vertical cylinders of different radius and draft can extract even more energy than its width, Figure 2.3. For those reasons, in WEC array problems it is not crucial to divert the wave to go along the structure, while still preserving good extraction characteristics (e.g. $W_a/Y \approx 1$).

An area where optical structures and WEC arrays have a lot in common is in practical

design. Optical structures have been designed and optimized to posses the required properties, e.g. light trapping in thin films through periodic and rough interfaces (Sheng et al., n.d.; Kowalczewski, Liscidini, and Andreani, 2012; Ganapati, Miller, and Yablonovitch, 2014) or disordered photonic crystals (Oskooi et al., 2012). In terms of designing a suitable system, this approach is very similar to the one employed in this thesis.

Chapter 5

Optimization of Large WEC Arrays

The results of the previous chapter showed that a careful choice of an array configuration can lead to large amplifications in energy extraction. With the increase in the number of parameters that describe the array configuration, the curse of dimensionality (and our capability to visualize multi-dimensional spaces) prevents us from performing a detailed analysis of array performance as a function of each parameter. Hence, we turn to optimization and look for a arrays that would perform optimally in some sense.

In this chapter, we first introduce optimization objectives and constraints, and then derive gradients of the objective functions to make efficient gradient-based optimization possible. Optimization results on a series of different large WEC array types is shown in the end.

5.1 Optimization Objectives and Constraints

We consider the optimization of WEC arrays with respect to their spatial configuration, i.e. with respect to the positions of individual bodies forming the array. As we have shown in the Chapter 4, the spatial configuration of the bodies in an array is a major factor that determines the amount of the extracted energy. Thus, it is of great interest to find optimal configurations that would lead to maximal power extraction (quantified in a certain manner).

In general, the optimization problem we are studying can be written as follows. Given

a real-valued scalar objective function $f : \mathbb{R}^{N_p} \to \mathbb{R}$ find the solution $\boldsymbol{\chi}^*$ that minimizes $f(\boldsymbol{\chi})$

$$\boldsymbol{\chi}^* = \arg\min_{\boldsymbol{\chi}\in\mathbb{R}^n} f(\boldsymbol{\chi}) \,, \tag{5.1}$$

such that

$$g_l(\boldsymbol{\chi}) \leq 0 \,, \quad l = 1, \ldots, N_g \,, \tag{5.2}$$

and

$$l_i \leq \chi_i \leq u_i \,, \quad i = 1, \ldots, N_p \,. \tag{5.3}$$

Here, $\boldsymbol{\chi}$ is a vector of optimization parameters, consisting of N_p elements that are bounded by (5.3) (for unbounded problems, set l_i or u_i to plus/minus infinity, as needed). In addition to the box-constraints (5.3), there can be an additional number N_g of nonlinear inequality constraints $g_l(\boldsymbol{\chi})$. The optimal value of objective function f^* is then

$$f^* = f(\boldsymbol{\chi}^*) \tag{5.4}$$

The equations (5.1)–(5.4) completely describe our problem in general terms. For the problem of optimal WEC arrays, f is a highly nonlinear and multi-modal function of $\boldsymbol{\chi}$. The specifics of $\boldsymbol{\chi}$, $g_l(\boldsymbol{\chi})$ and $f(\boldsymbol{\chi})$ pertaining to WEC arrays are described next.

Optimization variables. Before defining the optimization variables, some clarification of the terminology regarding array configurations is needed. By *array configuration type* we refer to a parameterization of array configuration that describes it using a particular set of parameters $\boldsymbol{\chi}$. An instance of a parameterization (or of that array configuration type) — a particular point in $\boldsymbol{\chi}$-space — is called an *array configuration.* For example, we can talk about rectangular arrays with Chebyshev-defined spacings as an array configuration type, and proceed to describe an instance of that parameterization/type.

The optimization variables $\boldsymbol{\chi} = (\chi_1, \chi_2, \ldots, \chi_{N_p})$ are the parameters that determine a particular array configuration. In general, they can describe the position of the bodies, individual body shapes, or PTO characteristics. In this thesis, we will only focus on the optimization of spatial configuration (keeping the body shapes and PTO characteristics constant), so $\boldsymbol{\chi}$ describes the spatial configuration alone.

For example, perhaps the simplest parameterization is using the body locations (x_i, y_i)

as optimization parameters. This leads to $N_p = 2N_b - 2$ optimization variables χ_i (one body is held fixed), a number that can slow down convergence rate of optimization algorithms for large arrays. A reduction in the number of variables can be achieved by defining parameterizations that introduce relationships between body positions; e.g. rectangular arrays with uniform spacing along both major axes can be described by only two parameters. Several configuration parameterizations are further described in §5.3.

One aspect of an array configuration that remains constant during the optimization is the number of bodies N_b. Having N_b as an optimization variable introduces various technical difficulties that one is eager to avoid. One difficulty is that N_b is a discrete, integer variable, so having it as an optimization variable so the optimization problem would become one of integer programming. Integer programming is NP-hard, which makes the computational expense of finding the optimum potentially prohibitively expensive computationally. The second difficulty is that the problem is further complicated for some parameterizations (e.g. optimization variables are individual body locations), where a change in N_b would lead to the change in the number of optimization variables during the optimization procedure. However, we can still study the effect of N_b on optimal solutions by running the optimization for a particular parameterization with increasing N_b.

Constraints. We impose two types of constraints on the optimization variables (configuration parameters). The first are box constraints introduced in (5.7), which are imposed on each optimization variable, and they limit the optimization parameter space. If they are imposed arbitrarily (e.g. to limit the search space of an optimization algorithm) and the optimal solution is found on such arbitrary bound, the bound should be increased and the optimization repeated.

The second type of constraint are the non-linear inequality constraints $g_l(\boldsymbol{\chi})$ described by (5.2), and they represent the physical spacing constraints, i.e. the requirement that the bodies do not touch. For bodies $\mathcal{B}_i$ and $\mathcal{B}_j$ with radii a_i and a_j, located at (x_i, y_i) and (x_j, y_j), the spacing between them is

$$r_{ij} = \sqrt{(x_i - x_j)^2 + (y_i - y_j)^2}\,. \tag{5.5}$$

The spacing constraint $g_l(\chi)$ is then

$$g_l(\chi) = r_{ij} - (a_i + a_j) \,, \quad l = 1, \ldots, N_b \times (N_b - 1)/2 \,. \tag{5.6}$$

where each l corresponds to one $i, j, \ , i \neq j$ pair. Note that r_{ij} is a function of $\boldsymbol{\chi}$, which in turn determines the body locations (x_i, y_i). Depending on the configuration parameterization type, the number of the spacing constraints can be reduced, even drastically. For example, for uniformly spaced rectangular arrays of identical bodies of radius a, the spacing constraint (5.2) becomes a simple box-constraint

$$d_x \geq 2a \,, \quad d_y \geq 2a \,. \tag{5.7}$$

Note that in a realistic application, one might need to add additional constraints pertaining to, say, the spatial extend the WEC array is allowed to occupy. These would be added and treated in an analogous manner.

We do not impose any equality constraints.

Objective functions. The choice of the objective function f for our problem is not unique. As described in Section §4.2, there is a number of measures that quantify the "goodness" of energy extraction, and any one of them can be used as an objective function for optimization. For example, we can choose to optimize array gain $q(ka_0, \theta_0)$ for a given wavenumber ka_0 and incoming direction θ_0 to maximize the improvement of energy extraction over the same number of isolated bodies. Similarly, one might optimize spectral array gain $q^S(\theta_0)$, total gain q^{DS}, or normalized capture width $W_a/Y(ka_0, \theta_0)$, to name a few. The final choice might depend on the external requirements a designer of a WEC array might face (e.g. maximal energy extraction over a stretch of shoreline). Since here we have no such requirements, we will illustrate the optimization algorithm and its capabilities mostly on one objective function — array gain q, optimized for different wavenumbers and wave incoming angles. The approach is very similar for the other objective functions, with the caveat that spectral objective functions are computationally more expensive, but still well within the range of the presented algorithm capabilities.

As it is often the case with the shape optimization in physics, the objective function f does not necessarily depend explicitly on the optimization variables $\boldsymbol{\chi}$. Rather, an inter-

mediate physical problem that directly depends on χ needs to be solved, and the objective function depends on the solution of the underlying physical problem. In our case, the underlying physical problem is the one of wave scattering , and the objective function (some version of the extracted power) depends on the obtained wave (and motion) velocities. This distinction — whether the objective function is an explicit function of χ, or only through an underlying physical problem — makes a difference only if gradients of the objective function need to be calculated.

Optimization Algorithm and the Nature of Optima. In general, for non-linear optimization problems one chooses between a certain version of a gradient-based optimization algorithm, and a stochastic evolutionary-type search algorithm that does not require any additional information other than the function value. Both have their advantages and drawbacks.

Gradient-based algorithms for non-linear optimization problems start at a given initial point, and use the objective function gradient information to step towards the optimum. These algorithms are very fast compared to the evolutionary ones, especially if the gradient ∇f is analytically provided. They handle much better the increase in the number of optimization variables. However, once in the vicinity of a local optimum, they will most likely converge to it, regardless of the presence of other (potentially better) local optima, let alone the global optimum. Hence, for multi-modal functions, i.e. those with many local optima, the result highly depends on the initial point because that determines the local optimum the solution will converge to. An additional problem is that the gradient ∇f can be difficult (and/or expensive) to calculate in some cases.

Stochastic evolutionary algorithms, on the other hand, sample a set of randomly selected points from the entire parameter space, and evolve it according to some rule. They do not require any additional information from a function other than its value, so they can handle non-smooth problems. The exploration of the entire parameter space leads to a higher chance of locating the global optimum. The number of function evaluations, however, is much larger than for the gradient-based algorithm to reach an optimum. This is especially true for high-dimensional problems, where an increase in the number of variables can lead to the curse of dimensionality for some algorithms (exponential increase in the required number of samples), making it prohibitively slow for problems with large N_p.

Due to the oscillatory nature of the underlying problem, the objective functions f for WEC arrays are smooth, but usually highly non-linear functions of the spatial configuration parameters, with many local optima (e.g. see any performance plot of array gain q as a function of spatial configuration in Chapter 4). The number of local optima is likely to increase with the increase in the number optimization variables. The multi-modality of the problem makes the finding of a globally optimal configuration a formidable task.

This presents us with a problem of which type of optimization algorithm to use — a gradient-based one that is fast but can get trapped in a local optimum, or a gradient-free algorithm that explores the parameter space and has a greater chance of finding the global optimum, but at a much slower pace. Often the best approach is to combine the two algorithms — first use an evolutionary algorithm for coarse search to determine the region where a global optimum is likely to be found, and then switch to a gradient-based algorithm to find the exact optimum quickly.

In this thesis, however, we will focus only on the gradient-based approach to the problem. As mentioned, In the next section we derive the objective function gradients with respect to the array configuration parameters using the adjoint method, followed by the description of several position parameterizations used.

5.2 Adjoint Method for Gradient Calculation

Adjoint method is especially suited for design optimization problems, where before optimizing an objective function, an underlying physical problem needs to be solved (e.g. solving the wave scattering problem). Considering (potentially) large size of the system (even with limited number of bodies), fast and memory-efficient implementation is needed.

Consider an optimization problem where we want to minimize a real scalar objective function $f(\boldsymbol{\chi}) \in \mathbb{R}$ that depends on N_p optimization variables χ_i

$$\boldsymbol{\chi} = \{\chi_1, \chi_2, \ldots, \chi_{N_p}\} \in \mathbb{R}^{N_p} \,. \tag{5.8}$$

In our case, f is a function that quantifies energy extraction or drift force on an array, and $\boldsymbol{\chi}$ is a certain parameterization of body locations, body sizes and extraction rates.

In a standard optimization problem, f can be directly calculated from χ_i, and the gradients are simply calculated as $\partial f / \partial \boldsymbol{\chi}$. However, if $\boldsymbol{\chi}$ does not appear in the expression

for f, but is actually used as an input to an auxiliary problem from which the objective function f is calculated, then the adjoint method proves to be superior (Johnson, 2012).

Let $f(\boldsymbol{\chi};\, \mathbf{c}(\boldsymbol{\chi}))$ be a (nonlinear) objective function, and $\mathbf{c} \in \mathbb{C}^{M\times 1}$ is $M \times 1$ complex column vector which is the solution to the underlying (linear) physical problem

$$A(\boldsymbol{\chi})\, \mathbf{c} = \mathbf{b} \tag{5.9}$$

Here, the $M \times M$ complex system matrix A and the $M \times 1$ complex vector $\mathbf{b}$ depend on the optimization variables $\boldsymbol{\chi}$.

The total gradient $df/d\boldsymbol{\chi}$ of f with respect to the optimization variables $\boldsymbol{\chi}$ can then be expressed as

$$\begin{aligned} \frac{df}{d\boldsymbol{\chi}} &= \frac{\partial f}{\partial \boldsymbol{\chi}} + \frac{\partial f}{\partial \mathbf{c}}\frac{\partial \mathbf{c}}{\partial \boldsymbol{\chi}} + \frac{\partial \mathbf{c}^{+}}{\partial \boldsymbol{\chi}}\frac{\partial f}{\partial \mathbf{c}^{+}} \\ &= \nabla_{\boldsymbol{\chi}} f + 2\,\mathrm{Re}\left(\nabla_{\mathbf{c}} f \cdot \nabla_{\boldsymbol{\chi}} \mathbf{c}\right) \end{aligned} \tag{5.10}$$

where $\nabla_{\mathbf{a}}\, g$ stands for a gradient of a general (scalar, vector or matrix) function g with respect to vector $\mathbf{a}$. Here, the gradient $\frac{df}{d\boldsymbol{\chi}}$ is $1 \times N_p$ row vector, $\nabla_{\mathbf{c}} f$ a $1 \times M$ vector, and $\nabla_{\boldsymbol{\chi}} \mathbf{c}$ a $M \times N_p$ matrix. While $\nabla_{\mathbf{c}} f$ is usually easily found (the expression is often analytically available), finding $\nabla_{\boldsymbol{\chi}} \mathbf{c}$ can be a very cumbersome process (we would need to solve $M \times M$ linear system N_p times). This is where adjoint method comes to play.

The gradient $\nabla_{\boldsymbol{\chi}} \mathbf{c}$ can be obtained by differentiating the system equation (5.9) with respect to $\boldsymbol{\chi}$

$$(\nabla_{\boldsymbol{\chi}} A)^{\tau} \cdot \mathbf{c} + A\, \nabla_{\boldsymbol{\chi}} \mathbf{c} = \nabla_{\boldsymbol{\chi}} \mathbf{b}\,,$$

giving

$$\nabla_{\boldsymbol{\chi}} \mathbf{c} = A^{-1} \left[\nabla_{\boldsymbol{\chi}} \mathbf{b} - (\nabla_{\boldsymbol{\chi}} A)^{\tau} \cdot \mathbf{c}\right] \tag{5.11}$$

The system matrix gradient $\nabla_{\boldsymbol{\chi}} A$ is a complex three-dimensional matrix of size $M \times M \times N_p$, and the operator $(\cdot)^{\tau}$ represent the transpose with respect to the last two dimensions of a three-dimensional matrix

$$[A^{\tau}]_{ijk} := [A]_{ikj}\,. \tag{5.12}$$

This way the matrix-vector product

$$(\nabla_{\boldsymbol{\chi}} A)^{\tau} \cdot \mathbf{c} = \sum_{j} \frac{\partial A_{ij}}{\partial \chi_k}\, c_j$$

follows the usual rules of summation over the last index for inner products.

Substituting back, we get

$$\begin{aligned}\nabla_{\mathbf{c}} f \cdot \nabla_{\boldsymbol{\chi}} \mathbf{c} &= \nabla_{\mathbf{c}} f \, A^{-1} \left[\nabla_{\boldsymbol{\chi}} \mathbf{b} - (\nabla_{\boldsymbol{\chi}} A)^{\tau} \cdot \mathbf{c}\right] \\ &= \boldsymbol{\lambda}^T \cdot \left[\nabla_{\boldsymbol{\chi}} \mathbf{b} - (\nabla_{\boldsymbol{\chi}} A)^{\tau} \cdot \mathbf{c}\right] \\ &= \boldsymbol{\lambda}^T \cdot \mathbf{B}\end{aligned} \tag{5.13}$$

The entire trick of the adjoint method lies parenthesizing differently the right hand side of the previous expression — instead of calculating and multiplying it term by term, we can group the first two terms together and recognize it is the solution of an adjoint linear system

$$A^T \cdot \boldsymbol{\lambda} = (\nabla_{\mathbf{c}} f)^T \tag{5.14}$$

Here, $\boldsymbol{\lambda}$ is the adjoint, and it is a $M \times 1$ complex vector. This $M \times M$ system is independent of the number of optimization variables N, and has the same complexity and characteristics as the original problem. So by regrouping the product differently, we only need to solve two $M \times M$ systems during the each step of the optimization process, instead of $1 + N$ systems if we had done it in the straight-forward way. The matrix $\mathbf{B}$ in equation (5.13) we term the "adjoint Jacobian"

$$\mathbf{B} = \left[\nabla_{\boldsymbol{\chi}} \mathbf{b} - (\nabla_{\boldsymbol{\chi}} A)^{\tau} \cdot \mathbf{c}\right] . \tag{5.15}$$

We can also further modify the expression to utilize the nature of the problem. The system matrix A is actually a function of the relative positions between the bodies in polar form $\boldsymbol{R} = \{R_{ij} \, : \, i,j = 1,\ldots,N_b;\ i \neq j\}$, $\boldsymbol{\alpha} = \{\alpha_{ij} \, : \, i,j = 1,\ldots,N_b;\ i \neq j\}$, so that the vector of natural variables

$$\widehat{\boldsymbol{\chi}} = \{\boldsymbol{R}, \boldsymbol{\alpha}, \ldots\} \tag{5.16}$$

Using natural variables, the product $(\nabla_{\boldsymbol{\chi}} A)^{\tau} \cdot \mathbf{c}$ can be expressed as

$$\begin{aligned}\sum_j \frac{\partial A_{ij}}{\partial \chi_k} c_j &= \sum_l \frac{\partial \hat{\chi}_l}{\partial \chi_k} \sum_j \frac{\partial A_{ij}}{\partial \hat{\chi}_l} c_j \\ &= \left[(\nabla_{\widehat{\boldsymbol{\chi}}} A)^{\tau} \cdot \mathbf{c}\right] \cdot (\nabla_{\boldsymbol{\chi}} \widehat{\boldsymbol{\chi}})\end{aligned}$$

giving

$$(\nabla_{\boldsymbol{\chi}} A)^{\tau} \cdot \mathbf{c} = \left[(\nabla_{\widehat{\boldsymbol{\chi}}} A)^{\tau} \cdot \mathbf{c}\right] \cdot (\nabla_{\boldsymbol{\chi}} \widehat{\boldsymbol{\chi}}) \tag{5.17}$$

We can now recognize that the first term $\left(\nabla_{\widehat{\boldsymbol{\chi}}} A\right)^{\tau} \cdot \mathbf{c}$ is *independent of parameterization*, while the second term $\nabla_{\boldsymbol{\chi}} \widehat{\boldsymbol{\chi}}$ is *independent of the solution vector* $\mathbf{c}$. We call the matrix $\nabla_{\boldsymbol{\chi}} \widehat{\boldsymbol{\chi}}$ *parameterization Jacobian.*

Similarly, the system forcing vector $\mathbf{b}$ in (5.9) (incoming wave forcing) is also expressed in terms of its own natural coordinates $\widetilde{\boldsymbol{\chi}}$

$$\widetilde{\boldsymbol{\chi}} = \{\mathbf{r}, \boldsymbol{\theta}, \ldots\} \tag{5.18}$$

where $\mathbf{r} = \{r_i \,:\, i = 1, \ldots, N_b;\}$, $\boldsymbol{\theta} = \{\theta_i \,:\, i = 1, \ldots, N_b;\}$ are the distance and the angle from the origin. With that, $\nabla_{\boldsymbol{\chi}} \mathbf{b}$ can be written as

$$\nabla_{\boldsymbol{\chi}} \mathbf{b} = \left(\nabla_{\widetilde{\boldsymbol{\chi}}} \mathbf{b}\right) \cdot \left(\nabla_{\boldsymbol{\chi}} \boldsymbol{\chi}\right) \tag{5.19}$$

Putting it all together, the adjoint Jacobian $\mathbf{B}$ becomes

$$\mathbf{B} = \left(\nabla_{\widetilde{\boldsymbol{\chi}}} \mathbf{b}\right) \cdot \left(\nabla_{\boldsymbol{\chi}} \widetilde{\boldsymbol{\chi}}\right) - \left[\left(\nabla_{\widehat{\boldsymbol{\chi}}} A\right)^{\tau} \cdot \mathbf{c}\right] \cdot \left(\nabla_{\boldsymbol{\chi}} \widehat{\boldsymbol{\chi}}\right) . \tag{5.20}$$

The total gradient of function f is then

$$\frac{df}{d\boldsymbol{\chi}} = \nabla_{\boldsymbol{\chi}} f + 2\,\mathrm{Re}\left(\boldsymbol{\lambda}^{T} \cdot \mathbf{B}\right) . \tag{5.21}$$

This is the formulation we implement in our algorithm for gradient-based formulation. In addition, the system matrix gradient $\nabla_{\boldsymbol{\chi}} A$ is a complex rank-3 tensor of size $M \times M \times N$, so for large problems it would take a lot of memory to store it. However, we have an analytic expression for it, so we apply matrix-free operation when calculating $\left(\nabla_{\boldsymbol{\chi}} A\right)^{\tau} \cdot \mathbf{c}$.

The Application of Adjoint Method to WEC Arrays The application is actually quite simple, and we have all the elements in place. All of the objective functions depend on the extracted power P_a, which is of very simple form

$$P_a = \mathbf{c}^{+} \boldsymbol{\Omega}\, \mathbf{c} \,, \tag{5.22}$$

where $\mathbf{\Omega}$ is a real,symmetric, block-diagonal matrix containing the extraction characteristics

$$\mathbf{\Omega} = \boldsymbol{\varpi} \cdot \mathrm{diag}(b_{\mathrm{PTO}}) \cdot \boldsymbol{\varpi}^{+} \,. \tag{5.23}$$

From here, $\nabla_{\mathbf{c}} P_a = \mathbf{c}^{+}\mathbf{\Omega}$ needed for (5.14) easily follows. This can then be easily adapted to other objective functions. To illustrate, the gradient of the total extracted spectral power by an array with respect to some parameterization $\boldsymbol{\chi}$ is given by

$$\frac{d\,P^S}{d\boldsymbol{\chi}} = \int S(\omega)\left[\nabla_{\boldsymbol{\chi}} P_a + \lambda^T \mathbf{B}\right] d\omega \tag{5.24}$$

If we do not optimize b_{PTO}, $\nabla_{\boldsymbol{\chi}} P_a = 0$ and the expression is even simpler.

5.3 Parameterization of Array Configuration

Spatial configuration of an array can acquire an infinite number of different configurations, both in terms of the number of bodies and their location. With the increase in array size, the number of optimization variables describing the spatial configuration can grow very large as well and make thus pose a significant computational problem. Parameterization of body locations leads to a (significant) reduction in the number of optimization variables, and It can also provide an insight into the physics of certain array configurations.

Although other quantities of interest (body size, PTO extraction rate b_{PTO}) can also be parameterized, here we focus on optimizing body locations alone. Hence, the optimization variables $\boldsymbol{\chi}$ are only related to position parameterization, and the natural variables $\widehat{\boldsymbol{\chi}}$ and $\widetilde{\boldsymbol{\chi}}$ are

$$\begin{aligned}
\boldsymbol{R} &= \{R_{ij} \,:\, i,j = 1,\ldots,N_b;\; i \neq j\} \\
\boldsymbol{\alpha} &= \{\alpha_{ij} \,:\, i,j = 1,\ldots,N_b;\; i \neq j\} \\
\mathbf{r} &= \{r_i \,:\, i = 1,\ldots,N_b\} \\
\boldsymbol{\theta} &= \{\theta_i \,:\, i = 1,\ldots,N_b\} \\
\widehat{\boldsymbol{\chi}} &= \{\boldsymbol{R}, \boldsymbol{\alpha}\}\,, \quad \widetilde{\boldsymbol{\chi}} = \{\mathbf{r}, \boldsymbol{\theta}\}\,.
\end{aligned} \tag{5.25}$$

Because of the translational symmetry of the problem, the location of at least one body in the array needs to be fixed.

5.3.1 Position parameterization in rectangular arrays

Expanding on the concept presented in Chapter 4, we parameterize the spacings in x and y direction in terms of Chebyshev polynomials,

$$d_{x_i} = \sum_{n=0}^{N_{c_x}} c_n^x \, T_n(\tau_i) \; , \tag{5.26}$$

$$d_{y_i} = \sum_{n=0}^{N_{c_y}} c_n^y \, T_n(\tau_i) \; , \tag{5.27}$$

and use the coefficients as optimization variables $\boldsymbol{\chi} = \{c_0^x, c_0^y, \ldots, c_{N_{c_x}}^x, c_{N_{c_y}}^y\}$. Here,

$$\tau_i = (i-1)/(N-2) \; , \quad i = 1, 2, \ldots, N-1 \tag{5.28}$$

with N in the last equation being either N_x or N_y, depending on whether x or y spacings are being parameterized. The maximal orders N_{c_x} and N_{c_x} are set beforehand, and it sets the type of disorder that is permitted in an array. The parameterization Jacobians $\nabla_{\boldsymbol{\chi}} \widetilde{\boldsymbol{\chi}}$ and $\nabla_{\boldsymbol{\chi}} \widehat{\boldsymbol{\chi}}$ follow in a straight-forward manner and are omitted here.

5.4 Optimal Rectangular Arrays with Uniform and Non-Uniform Spacing

We focus on the optimal configuration of a series of rectangular arrays. Each rectangular array is made out of N_x rows of N_y bodies, i.e. of $N_b = N_x \times N_y$ bodies total. Most of the configurations studied in Chapter 4 fall under this category. We study several different spacing parameterizations, each providing a different level of flexibility (or degrees of freedom) to an array configuration.

Given that the optimization of array configuration is a nonlinear optimization problem, an initial configuration needs to be prescribed before starting the optimization. The initial point in the optimization variable space is always the same, and it corresponds to an array with equal uniform spacing in both directions $d_x = d_y$, such that the gap between the bodies is the minimal allowed δ_{min}

$$d_x = d_y = 2a + \delta_{min} \; . \tag{5.29}$$

The array configuration for each (N_x, N_y) rectangular array is then optimized over the spacing parameters, either for maximum array gain q at a given wavenumber (ka_r, $ka_<$ or $ka_>$) or for spectral array gain q^S. We present maps of optimal configuration parameters, optimal performance (e.g. q), or some other performance measure for the optimal array (e.g. W_a/Y) for each (N_x, N_y) rectangular array.

We will often refer to arrays with $N_y \gg N_x$ as *terminator arrays*, and, conversely, those with $N_x \gg N_y$ as *attenuator arrays*.

Note that the number of bodies N_b is not optimized. We approach the problem of the N_b-optimality by running the optimization for an increasingly larger number of bodies, and in that way capture as a function of N_b a possible extreme or an asymptotic value that the objective function might acquire.

5.4.1 Optimization Algorithm

For all the optimization results presented in this section, we use method-of-moving asymptotes (MMA) algorithm from a nonlinear optimization package NLOPT (Johnson, n.d.). MMA algorithm (Svanberg, 2002) is a gradient-based nonlinear optimization algorithm that allows for nonlinear inequality constraints like the ones imposed on this problem.

A note on Local vs. Global optimum. All the results shown in this section are *locally* optimal. There is no guarantee that these are close to global optima, either in terms of the optimal value or of the value of the optimization variables at the optimum. Given the multi-modal nature of the problem, it is very likely that there might be a better solution somewhere in the parameter space.

5.4.2 Optimal Rectangular Arrays with Uniform Spacing

We start by studying optimal rectangular arrays with uniform spacings (i.e. $N_{c_x} = N_{c_y} = 0$). Here there are only two optimization parameters describing a N_x–N_y array — the row spacing d_x, and the spacing between bodies in a row d_y. An analysis of a 3×20 rectangular arrays was conducted in Chapter 4, but here we want to study how the optimal performance might change if we add more rows and more bodies in general and optimize the spacing between them.

Figure 5.1 shows the obtained optimal array gain q for a series of rectangular arrays.

Each (N_x, N_y) pair represents one array that was optimized. We see a clear preference for terminator arrays ($N_x > N_y$) for all wave directions. The maximal obtained values are large, but smaller than the maximal observed in Figure 4.45. That is because of the highly multi-modal character of q, as exemplified in Figure 4.45. For this optimization, the initial array configuration was as tight as possible, so the optimizer found one of the local optima. As mentioned previously, the maximal q for 3×20 array occurs when the spacings are such that the array operates above the first Rayleigh point for the given wavenumber. In this case, the optimizer found a local optimum that is below the first Rayleigh point, where maximal values of q are small than they would be if it was searching in the area beyond the first Rayleigh point. The same argument holds for spacing d_x, where the Bragg resonances locked the optimizer in an area with a smaller local optimum.

Nevertheless, the optimization results reveal interesting results. As for the line arrays, increasing the number of bodies in y-direction beyond 20 bodies does not effect the maximal q. This holds for all incoming angles. The maximal q for all incoming angles $\theta_I \lesssim 30°$ are comparable.

The optimal configurations can be deduced by observing optimal spacings $d_x{}^*$ and $d_y{}^*$ shown in Figures 5.3 and 5.4. It is evident that for terminator arrays with $N_y < 7$ where the optimal gain q^* is significant that the bodies are placed close to each other in x-direction. If we compare this result with the detailed spacing analysis of 3×20 rectangular array, we can understand the reason why q^* is generally smaller than the maximum observer in Figure 4.45 — the optimize is locked in the local maxima with small d_x, while higher q-maxima (and the global maximum) are found for larger $d_x/2a$ spacings.

The spacing $d_y{}^*/2a$ for attenuator arrays is generally larger than $d_x{}^*/2a$ and it asymptotes to a constant value for larger N_y, except in isolated points. The relationship between the asymptotic values of $d_x{}^*/2a$ and Rayleigh critical points is better visible in Figure 5.5, where we plot $d_y{}^*/2a$ as a function of N_y for terminator array with up to four rows. The optimal spacing $d_y{}^*/2a$ is always close to a Rayleigh spacing, and the jumps in the values of $d_y{}^*/2a$ for certain N_y occur when the optimization converged to a different local optimum corresponding to a different Rayleigh point. These jumps in $d_y{}^*/2a$ correspond to jumps in q^* for those same (N_x, N_y) pairs, both being linked to converging to a different local optimum.

The capture width W_a normalized by the y-direction extent of the the q-optimal arrays

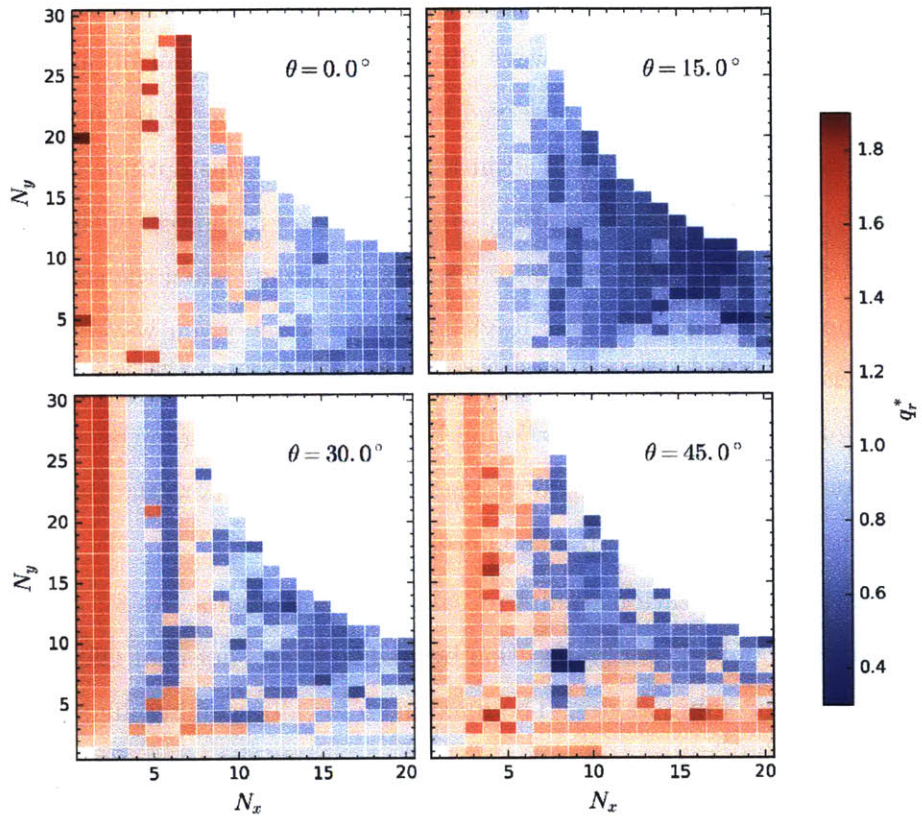

Figure 5.1: Optimal values of gain q^* for rectangular arrays with $N_x \times N_y$ bodies, for resonant frequency $ka = ka_r$.

is shown in Figure 5.6. The large values of W_a/Y do not properly represent the energy extraction potential because the normalizing constant Y in those cases is very small. The low values of gain q^* in those cases confirm that (Figure 5.1). On the other hand, W_a/Y for terminator arrays is a real measure of energy extraction efficacy. The values of W_a/Y are increasing with the increase in the number of rows N_x. For normal incidence, with $N_x = 4$ the array captures all the energy flux incoming on its geometrical extent ($W_a/Y \sim 1$), Figure 5.7; for larger θ it takes more rows to reach values close to 1.

For the 3×20 rectangular array studied in §4.6.1, the configurations that lead to high q-values and high W_a/Y values were different — large d_y was favored in one case, and small d_y in the other. So there is a trade-off when one designs an array. Here however, we can find arrays that achieve high values of both q and W_a/Y at the same time. This is achieved by adding more rows to an array. For example, arrays with $N_x = 7$ and $N_y \gtrsim 13$ all have $q_r^* > 1.7$ and $W_a/Y \sim 1$. The optimal configuration of a 7×25 array for maximal q_r at $\theta = 0°$ is shown in Figure 5.8.

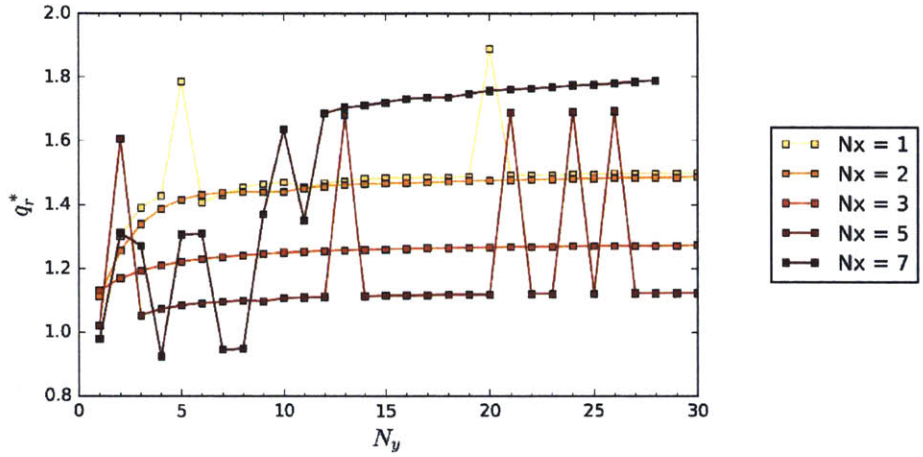

Figure 5.2: Optimal values of gain q^* for rectangular arrays with $N_x \times N_y$ bodies, for resonant frequency $ka = ka_r$ and $\theta = 0°$.

For super-resonant wavenumber, the optimal q^* is even higher, reaching the values of $q^*_> \sim 4.0$ for terminator arrays with $N_x = 3$, Figure 5.9. This is very similar to the 3×20 array at $ka_>$ analyzed in §4.6.1. Relatively high $q^*_>$ is achieved for terminator arrays at all incoming angles θ. For sub-resonant wavenumber $ka_<$, optimal gains reach values of $q^*_< \approx 1.6$. Overall, d_x is smaller for sub-resonant optimal arrays than for super-resonant ones. Further results for super-resonant and sub-resonant wavenumbers are given in Appendix D.2.

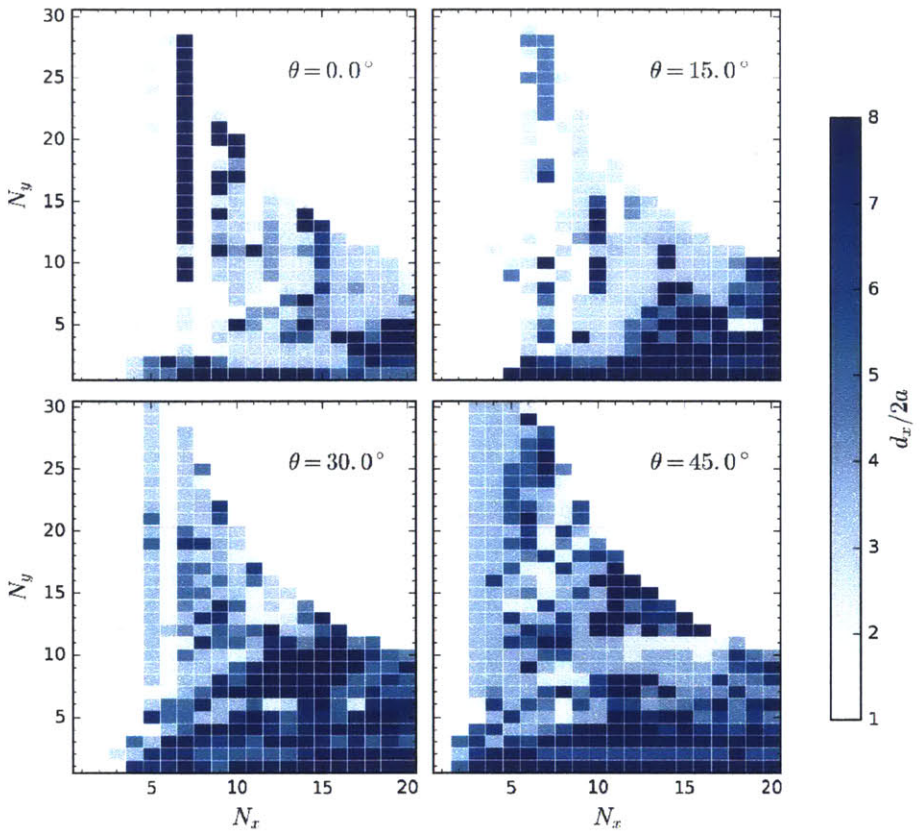

Figure 5.3: Optimal spacing $d_x{}^*/2a$ for rectangular arrays with $N_x \times N_y$ bodies, for resonant frequency $ka = ka_r$.

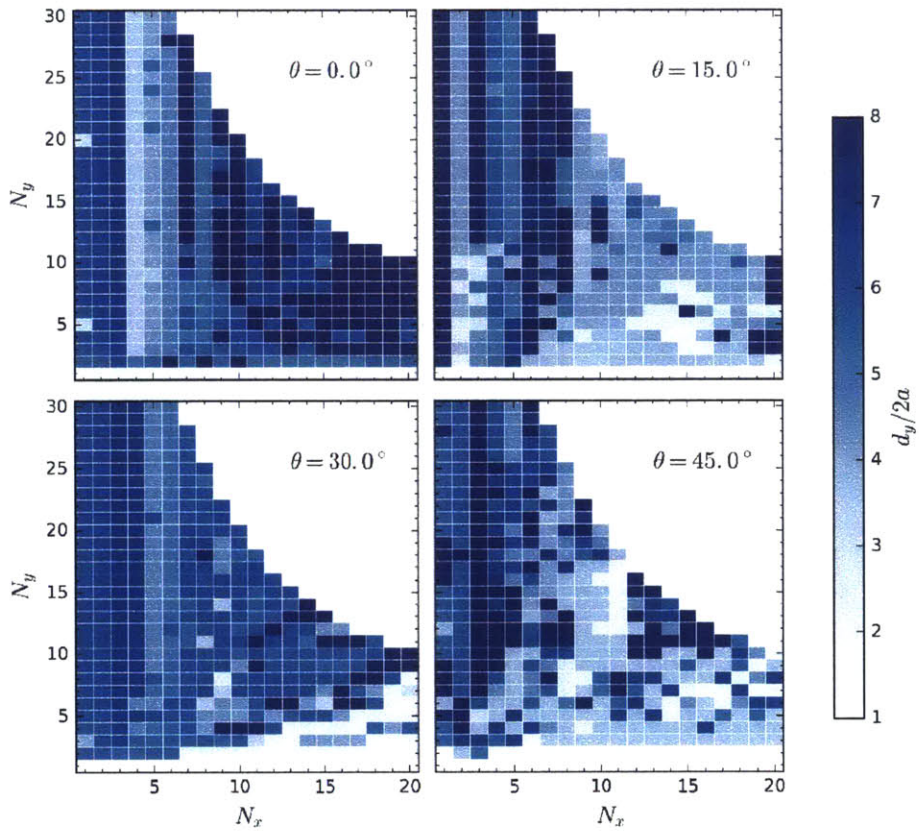

Figure 5.4: Optimal spacing $d_y{}^*/2a$ for rectangular arrays with $N_x \times N_y$ bodies, for resonant frequency $ka = ka_r$.

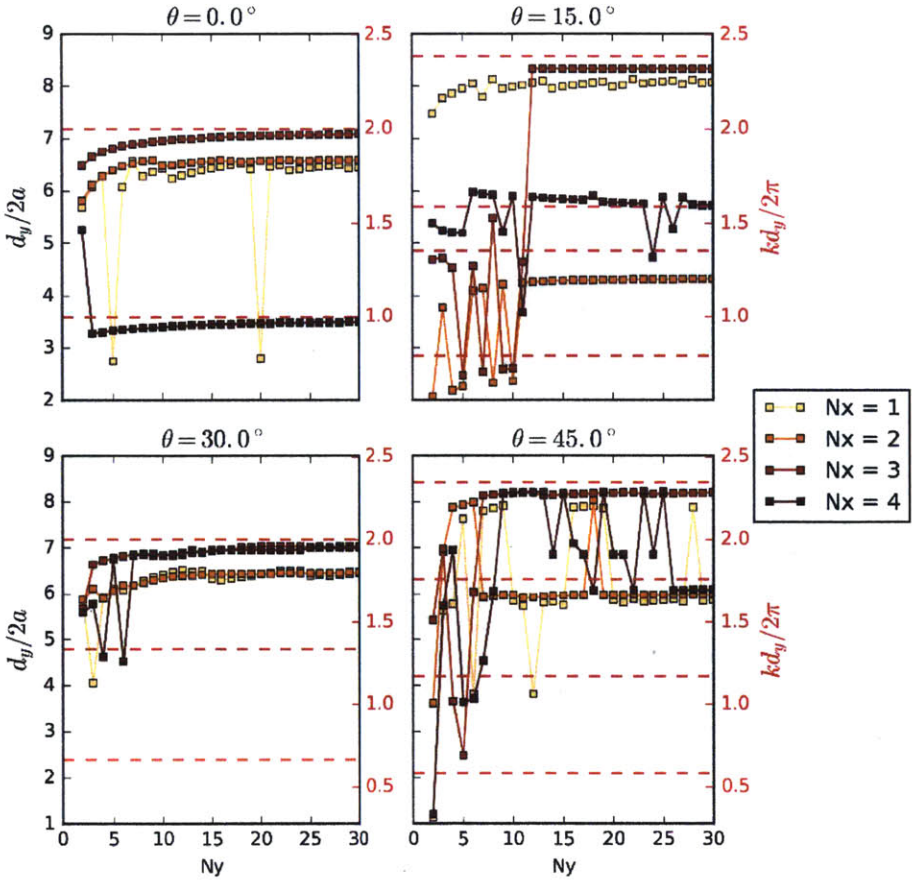

Figure 5.5: Optimal values of $d_y{}^*$ for rectangular arrays with $N_x \times N_y$ bodies, with $N_x = 1, \ldots, 4$, for resonant wavenumber $ka = ka_r$.

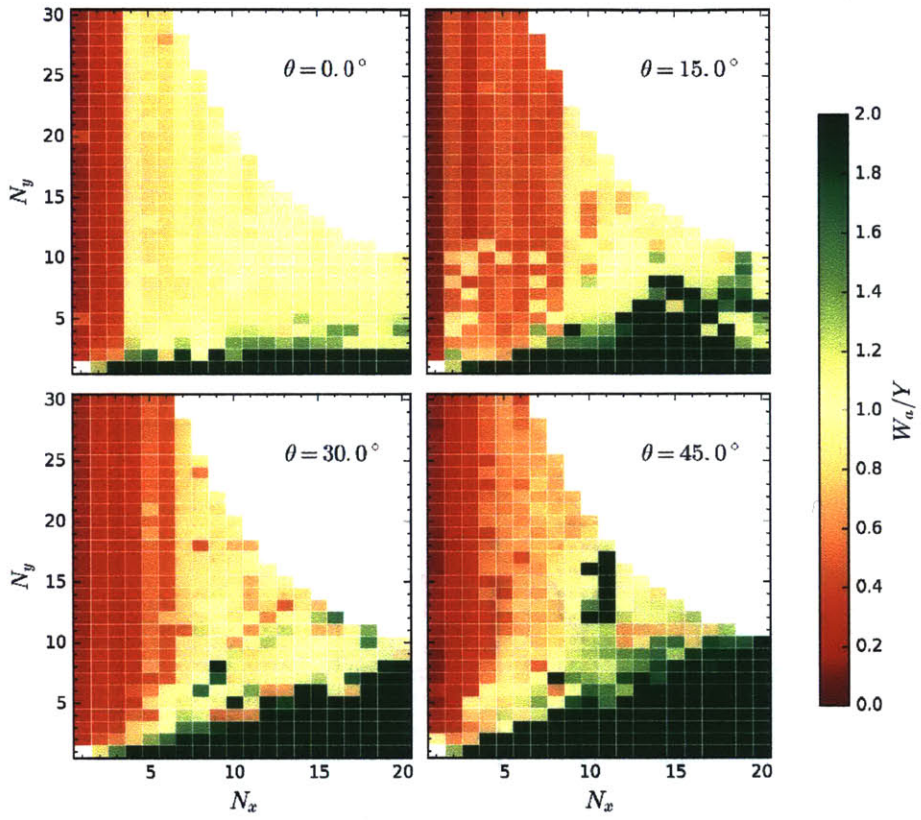

Figure 5.6: Array capture width W_a/Y for q-optimal arrays for rectangular arrays with $N_x \times N_y$ bodies, with $N_x = 1, \ldots, 4$, for resonant wavenumber $ka = ka_r$.

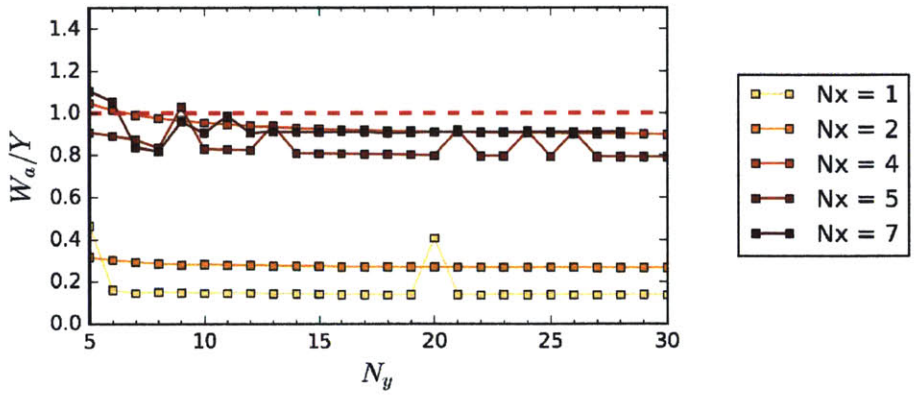

Figure 5.7: Array capture width W_a/Y for q-optimal arrays for rectangular arrays as a function of N_y, with $N_x = 1, 2, 4, 5, 7$, for resonant wavenumber $ka = ka_r$ and $\theta = 0°$.

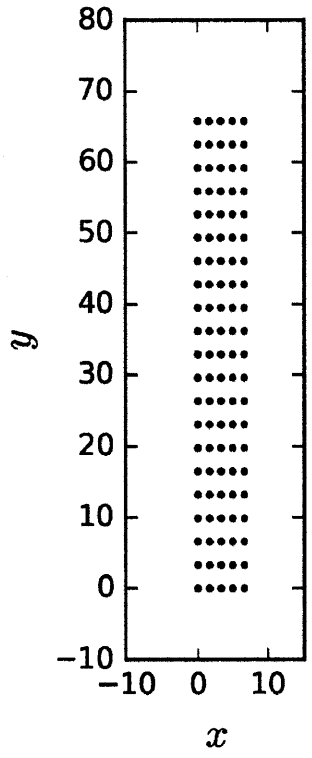

(a) Optimal 5×21 array, achieving $q \approx 1.7$ and $W_a/Y \approx 1.0$.

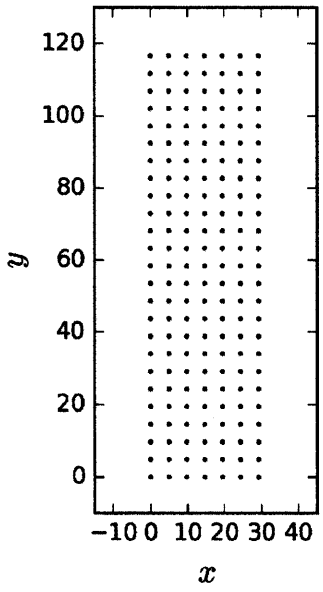

(b) Optimal 7×25 array, achieving $q \approx 1.8$ and $W_a/Y \approx 1.0$.

Figure 5.8: Some optimal array configurations for maximal q_r at $\theta = 0°$.

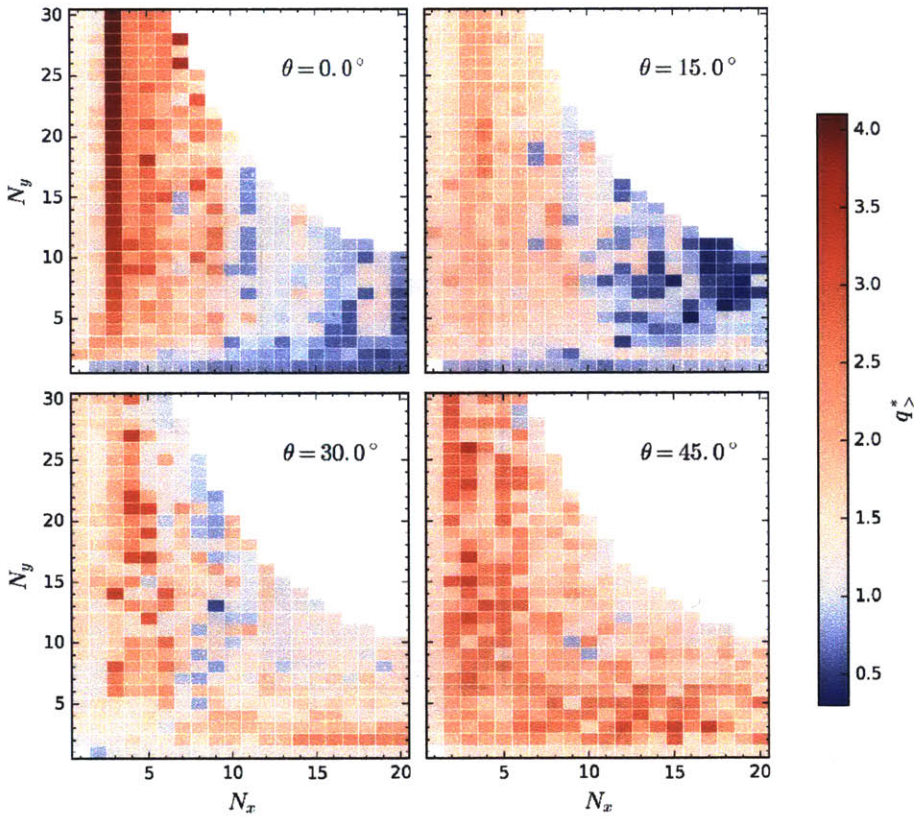

Figure 5.9: Optimal values of gain q for rectangular arrays with $N_x \times N_y$ bodies, for super-resonant frequency $ka = ka_>$.

5.4.3 Optimal Rectangular Arrays with Irregular Spacing

We now allow for the spacing between the bodies to be non-uniform. In particular, we parameterize the y-direction spacing by a quadratic polynomial $N_{c_y} = 2$ from (5.27), and allow that the spacing between the rows d_{x_i} is individually assigned. We will only focus on terminator arrays, so we limit $N_x \leq 7$. We optimize for q for 0° and 15°.

The optimal gain q_r^*, Figure 5.10 is similar to that for uniformly spaced arrays (c.f. Figure 5.1), especially for normal incidence. For the oblique incoming angle $\theta = 15°$, the q-values in this cases are larger than for uniformly spaced arrays.

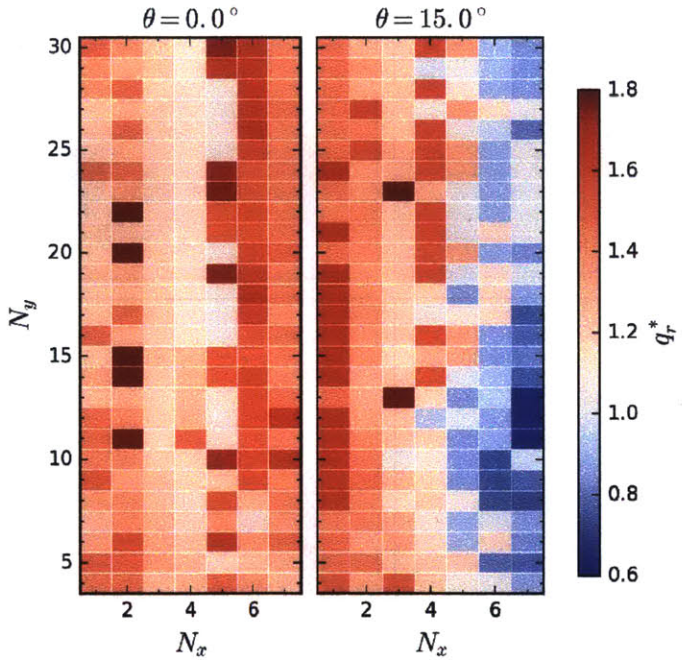

Figure 5.10: Optimal values of gain q for rectangular arrays with $N_x \times N_y$ bodies, with $N_{c_y} = 2$ and d_x individually controlled, for the resonant wavenumber $ka = ka_r$.

To get a better impression of the role of irregularity, we plot the coefficient of a quadratic irregularity $c_2{}^*$ for every array, Figure 5.11. For normal incidence, the highest values of q, whether isolated or as a part of a trend, mostly correspond to cases of uniform arrays ($c_2 \approx 0$). For $\theta = 15°$, that effect is less pronounced, and some high q-values correspond to the areas of high irregularity. Overall if irregularity is present, negative values of c_2 are preferred (c.f. Figure 4.32).

Several optimal array geometries are shown in Figure 5.12. While the y-spacing overall seems to be favored to be uniform, optimal d_x shows more variation. In Figure 5.125.12a we

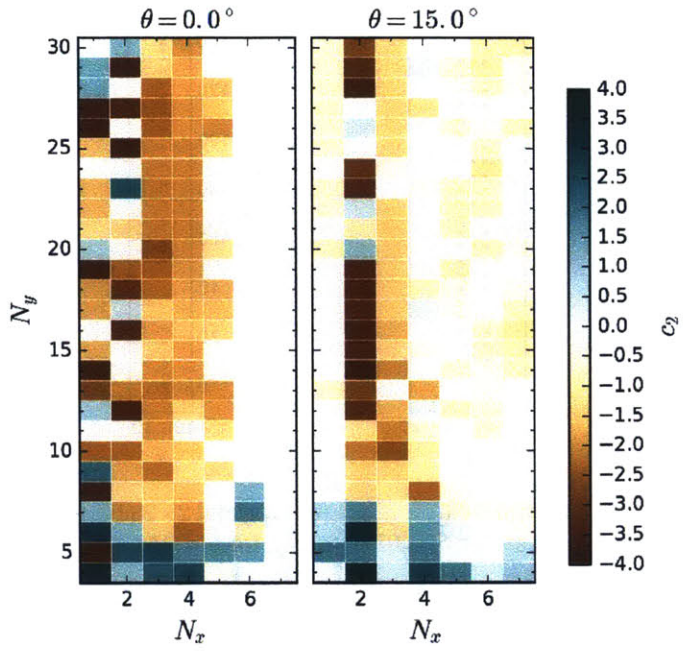

Figure 5.11: Optimal values of quadratic irregularity parameter $c_2{}^*$ for rectangular arrays with $N_x \times N_y$ bodies, with $N_{c_y} = 2$ and d_x individually controlled, for the resonant wavenumber $ka = ka_r$.

see that the rows are placed symmetrically with respect to the central one. For other optimal configurations, such symmetry may not necessarily be present, but the non-uniformity in d_x is always there. For normal incidence, there is a clear preference in some arrays to put the bodies close together. This could indicate that instead of having a circular buoy, a non-axisymmetric device or one with multiple degrees of freedom would be preferred.

Figure 5.13 shows that for terminator arrays with the larger number of rows $N_x \gtrsim 5$ the capture width ratio W_a/Y is close to 1, similar to uniformly spaced arrays. Indeed, those arrays for which $W_a/Y \approx 1$ all have uniform d_y spacing, while arrays with non-zero c_2 have lower W_a/Y. The exact values of W_a/Y are better visible in Figure 5.14.

The results for super-resonant wavenumber $ka_>$ show similar trends and are left for Appendix D.2.

5.4.4 Optimal Rectangular Arrays for Irregular Seas

We move from optimizing q for a single wavenumber to optimizing the array gain over a spectrum $S(\omega)$. We use the same Brentschneider spectrum (with the peak at the resonant frequency) as for the analyses performed in Chapter 4.

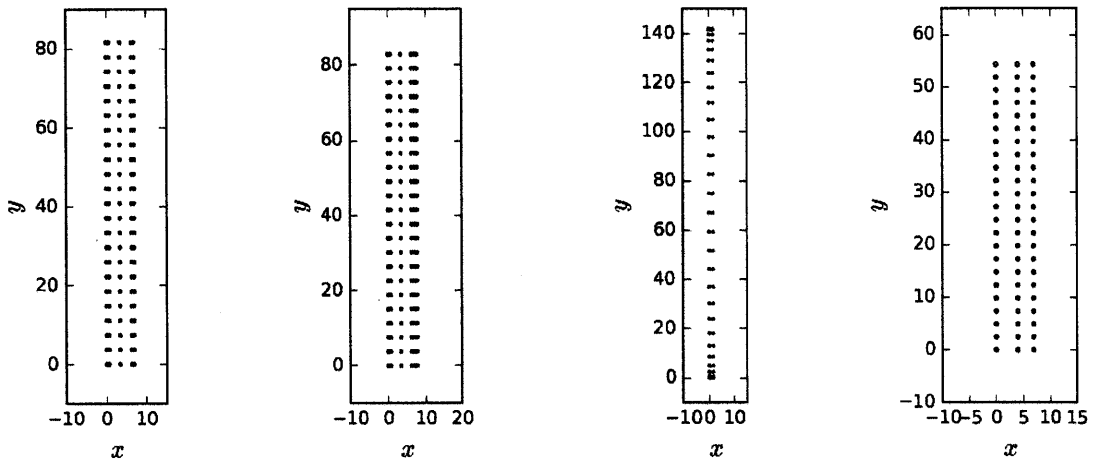

(a) Optimal 5 × 23 body array for $\theta = 0°$

(b) Optimal 6 × 23 body array for $\theta = 0°$

(c) Optimal 2×28 body array for $\theta = 15°$

(d) Optimal 3 × 23 body array for $\theta = 15°$

Figure 5.12: Geometry of four optimal arrays for resonant wavenumber $ka = ka_r$, with $N_{c_y} = 2$ and d_x individually controlled.

The optimal spectral gain q^S for three different array configuration types in unidirectional seas coming from $\theta = 0°$ is shown in Figure 5.15. Interestingly, the highest values of q^S are achieved by uniform spacing arrays ($N_{c_x} = N_{c_y} = 0$). Increasing the allowed degree of irregularity does not lead to higher values of q^S. In fact, the optimized gets stuck in local minima that are of lower value than for the uniformly spaced array, which would be a feasible point to reach for those parameterizations.

The spectral capture width ratio W_a^S/Y is reduced to well below 1, to maximum values of around 0.3, Figure 5.16. This is comparable to W^S/D values of an isolated cylinder, Figure 5.17.

Two examples of optimal uniformly spaced arrays ($N_{c_x} = N_{c_y} = 0$) are given in Figure 5.18.

Optimized total spectral gain q^{DS} for rectangular arrays with quadratic spacing irregularity in y-direction over a directional Brentschneider spectrum with the spreading factor $s = 2.0$ gives modest values, with maximum values barely reaching 1.05, Figure 5.19. The very low values are in part because the optimizer converged to local optima with very large y-direction spacing, which resulted in the fact that there is virtually no gain over the performance of an isolated body. The geometries of two optimal arrays are shown in Figure 5.20. In both cases the spacing in x-direction is much smaller than the y-direction spacing. One can hardly consider these as arrays where the interaction between groups of two bodies

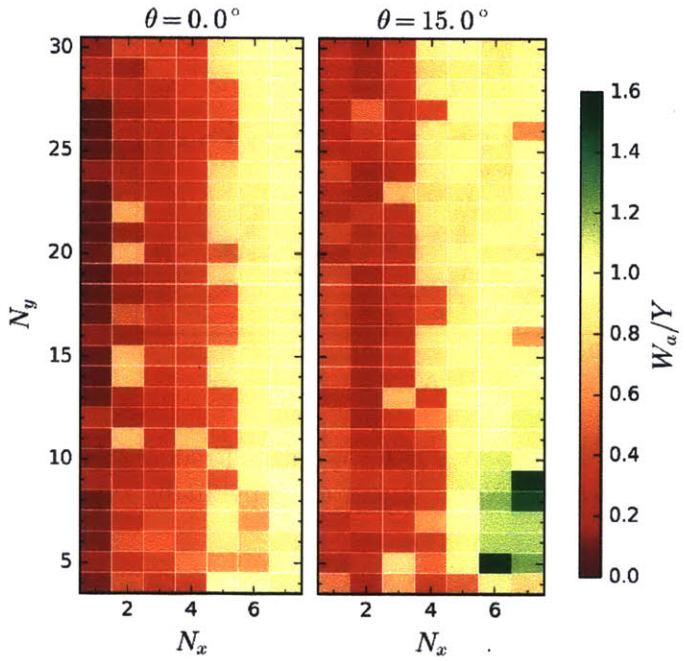

Figure 5.13: Capture width ratio W_a/Y for q-optimal rectangular arrays ($N_x \times N_y$ bodies), with $N_{c_y} = 2$ and d_x individually controlled, for the resonant wavenumber $ka = ka_r$.

is meaningful. A different initial point is clearly required here in order for the optimizer to reach a different, and hopefully better, optimum.

5.5 Discussion

In this chapter, we presented a series of results of the optimization of spatial configuration of WEC arrays of up to 200 bodies. These are by far the largest optimization studies of WEC arrays in literature. Existing studies by Fitzgerald and Thomas (2007) and Child and Venugopal (2010) optimized locations of WEC arrays of optimally tuned 5 bodies, which would be insufficient in size for a realistic practical implementation of WEC arrays as a commercial energy source.

We optimized rectangular arrays of different $N_x \times N_y$ sizes, and employed different parameterizations to study the effects of spacing irregularity. In particular, we studied uniform spacing arrays, and those where a systematic irregularity (quadratic) is allowed in y-direction, with the inter-row spacings $d_{x,i}$ allowed to be set individually. Overall, the number of optimization parameters did not exceed 15. A gradient-based method was used to find the optimum solution, with the gradient calculated by a fast adjoint method

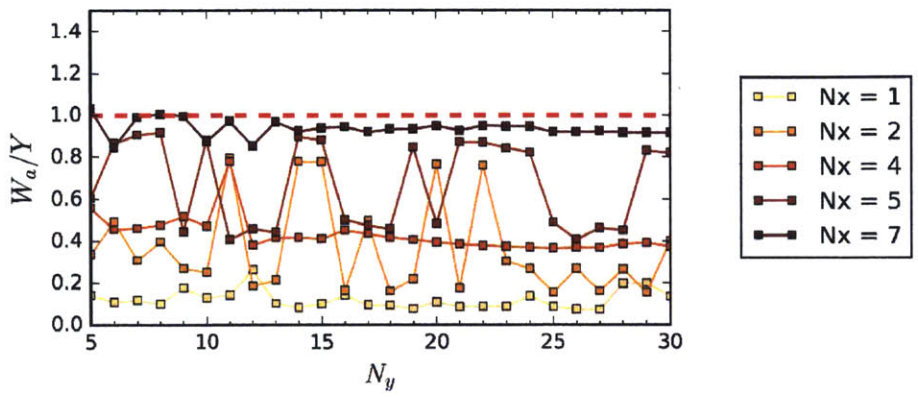

Figure 5.14: Capture width ratio W_a/Y for q-optimal rectangular arrays as a function of N_y for $N_x = 1, 2, 4, 5, 7$ bodies ($N_{c_y} = 2$ and d_x individually controlled), for the resonant wavenumber $ka = ka_r$).

derived in this thesis for the WEC array problem. The arrays were always initialized in a minimum-spacing configuration according to (5.29).

We find that uniformly spaced arrays appear to be favored as optimal solutions, both for regular and irregular seas. The fact that uniformly spaced arrays are favored for a particular wavenumber is expected (especially in the y-direction) because of the array phenomena that boost their performance (around Rayleigh wavelength). A more surprising finding, perhaps, is that non-uniformity does not have a stronger effect on the optimal values for irregular seas. This is probably because the large gains at the tuned wavenumber of uniform rectangular arrays greatly contributes to the overall extracted energy, so that arrays that have a more uniform response due to the irregularity still cannot make up for those large gains (c.f. Figure 4.38).

Optimal uniform spacing in y-direction is again related to the Rayleigh wavelength, although not always to the one of the same order (Figure 5.5). While y-spacing for high-performing arrays was almost always uniform, the optimal row spacing in x-direction was not uniform when such a degree of freedom was allowed. The optimal spacing in x direction resulted in some rows being very close together, indicating that perhaps a body of different shape or more degrees of freedom in place of a simple heaving cylinder would be favored.

Overall, none of the optimal arrays of any size or with any degree of spacing irregularity, optimized for maximal q or maximal q^S, did outperform the maximal performance measures of a 3×20 uniform rectangular array analyzed in Chapter 4. The maximal values of q and W_a/Y are comparable, although sometimes achieved by arrays of different size. The

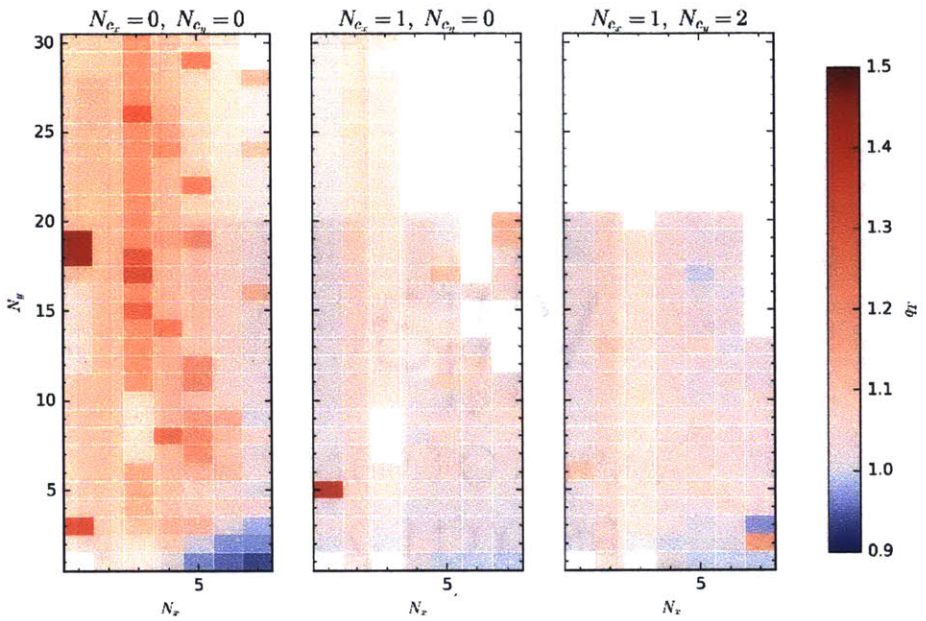

Figure 5.15: Optimal values of spectral gain q^S for rectangular arrays with $N_x \times N_y$ bodies, with varying N_{c_x} and N_{c_y}, for a Brentschneider spectrum with $k_p = k_r$ and $\theta = 0°$.

maximal capture width ratio W_a/Y is around 1 for uniformly spaced arrays in y-direction, indicating that almost all energy is extracted from the incoming wave hitting the array. Falnes and Budal (1982) and Falnes (1984) found that for periodic arrays of point absorbers, all the energy can be extracted if we have 4 optimally placed rows of bodies. Here we show that, indeed, with 4 uniformly spaced rows if is possible to get $W_a/Y \approx 1$, Figure 5.7 The maximal spectral gain q^S found in 3×20 arrays have not been reached in this optimization study. A globally optimal solution would undoubtedly change that claim.

One has to bear in mind, however, that all these are locally optimal solutions, and we can only speculate of whether irregularity would benefit the optimal performance if a globally optimal solution is to be found. In the light of the results on random rectangular arrays from Chapter 4, we can expect that even if some irregularity improves the performance of WEC arrays in, say, irregular seas, this irregularity should not be strong. One could study different parameterizations, and, say, describe the y-spacing according to a NURBS spline whole control points are the optimization variables. This would give more flexibility to the spacing pattern, while still not being completely random. Perhaps a systematically introduced irregular spacing, particularly in x-direction, is the best-case-scenario for irregularities to have a positive impact on the performance.

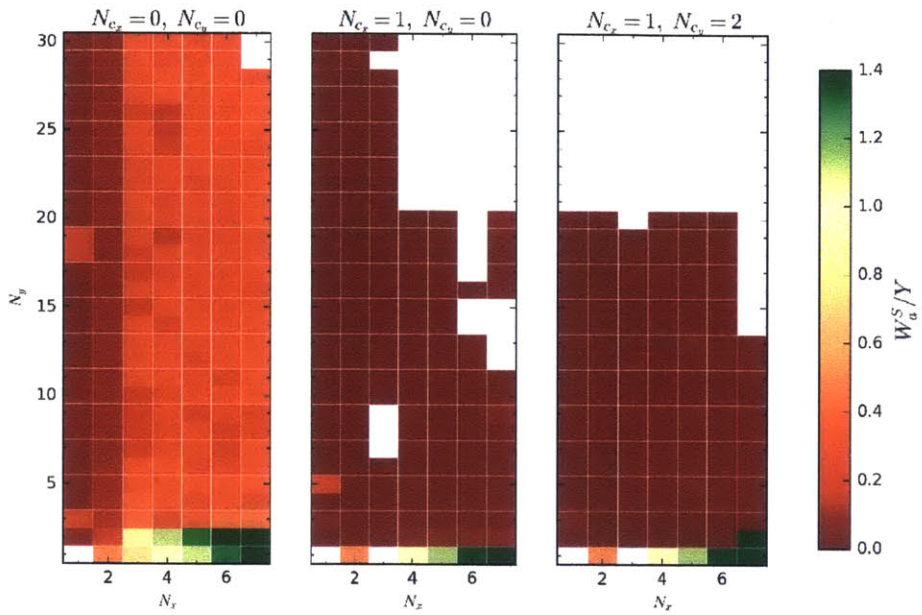

Figure 5.16: Spectral capture width ratio W_a^S/Y for q^S-optimal rectangular arrays with $N_x \times N_y$ bodies, with varying N_{c_x} and N_{c_y}, for a Brentschneider spectrum with $k_p = k_r$ and $\theta = 0°$.

The strong preference for uniform spacing in y-direction gives more weight to the extension of the multiple scattering framework for periodic WEC arrays of groups of closely spaced bodies. We can analyze and optimize the configuration of that group alone, with a great reduction in the computational expense. Before we can conduct a full optimization that also includes periodicity d as an optimization parameter, a convergent expression for the derivative of the lattice sums (3.38) needs to be derived. The lattice sum (Schlömilch series) $\sigma_{n,0}$ as it is is a very slowly convergent series, whose usability was only made possible by a series of accelerations (Kummer transformations). The derivative of $\sigma_{n,0}$

$$\frac{\partial \sigma_{n,m}}{\partial d} = \sum_{B=1}^{\infty} B \left(ik \sin\theta \left[P_B - (-1)^n P_{-B} \right] K_n(B\, k_m d) + k_m \left[P_B + (-1)^n P_{-B} \right] K_n'(B\, k_m d) \right) , \tag{5.30}$$

introduces a growing integer factor B that makes the series (5.30) divergent for $m = 0$. We know that this divergent series has a finite limit (e.g. we can calculate $\partial \sigma_{n,0}/\partial d$ numerically), but an analytical expression that would allow for a fast evaluation of the sum in (5.30) is currently not available.

The high non-linearity and multi-modality of the underlying objective function is the culprit for many issues that might raise questions in the analysis of the results. The most

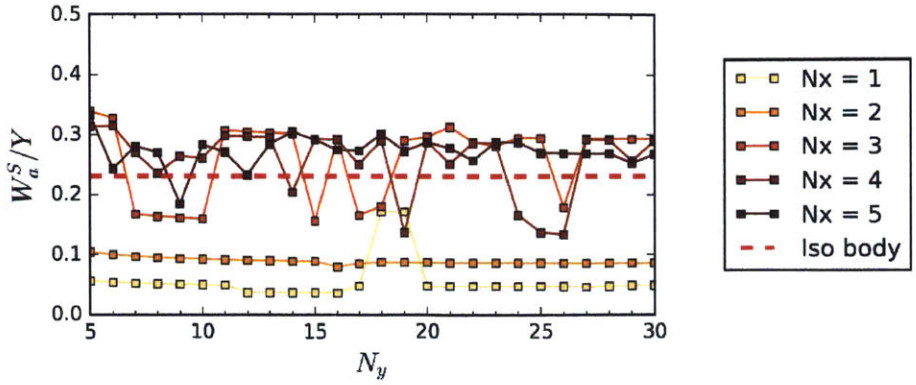

Figure 5.17: Spectral capture width ratio W_a^S/Y for q^S-optimal rectangular arrays as a function of N_y for $N_x = 1, 2, 3, 4, 5$ ($N_{c_x} = N_{c_y} = 0$, Brentschneider spectrum with $k_p = k_r$ and $\theta = 0°$).

immediate consequence of high multi-modality is that the presented results correspond to (different) local optima, and as such are only the lower bounds of the possible performance of optimal WEC arrays. The sometimes checkered result of, say, optimal spacing parameter (e.g. Figure 5.11) is caused by the fact that increasing N_x or N_y by 1 sometimes results in converging to a different local minimum. One would expect that if a true global optimum would be found every time, that changes in array sizes would lead to a gradual change in optimal parameter values and optimal performance with N_x or N_y. We do see such behavior in some cases (e.g. Figure 5.4, especially for $\theta = 30°$), where the change in N_x or N_y does not result in skipping to a different local optimum. However, that still does not mean that the optimum the algorithm keeps converging to is the global optimum.

A different issue, but still related to the convergence to local optima, is the fact that in some cases the optimal results under-perform a trivially available configuration. This is the case for all optimal arrays where the optimal q or q^S is lower than 1 (a trivial configuration better than that is a collection of infinitely spaced bodies with $q = q^S = 1$). This is also the case when an introduction of a degree of freedom in the optimization parameter space results in the decrease in the optimal performance, while the initial configuration is still feasible in the expanded space. For example, increasing the allowed level of spacing irregularity reduced the optimal spectral gain compared to the uniformly spaced array, Figure 5.15, but the uniform spacing results and, thus, equal q^S, were an allowed optimum even in this newly expanded space. These cases all result from the fact that the local optimum closest to the initial point is below some threshold, whether it is the threshold for

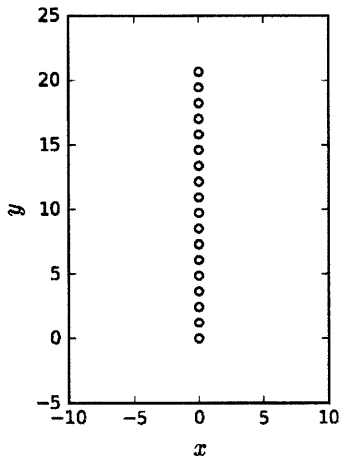

(a) Optimal 1×18 body array

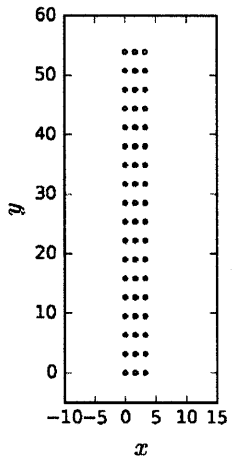

(b) Optimal 3×18 body array

Figure 5.18: Geometry of two optimal arrays for Brentschneider spectrum with $k_p = k_r$ and $\theta = 0°$, with $N_{c_x} = N_{c_y} = 0$.

a collection of isolated bodies ($q = q^S = 1$), or that set by an optimal array with a simpler configuration, a configuration that is attainable with the more complicated parameterization (e.g. a comparison with the uniformly spaced array).

The remedy for most of the issues stated above is, instead of being stuck at different local optima, to find the global optimum. That is, of course, easier said than done, but several things can be done towards that goal. The first approach, if we continue using the same algorithm as described here, would be to start the optimizations at several (drastically) different initial points. The differences should be strong enough such that there is a possibility for the optimization to end up in a different optimum. With enough different tries, one might even feel (falsely) confident that a global optimum has been reached.

A more automated way of testing many initial points is to use a stochastic evolutionary algorithm instead, e.g. Covariance-Matrix Adaptation Evolutionary Strategy (CMA-ES) (Hansen and Ostermeier, 2001; Hansen, 2006). The initial random population would be evolved towards the (global) optimum only to narrow down the region where it might be located. From that as a starting point, the gradient-based optimization algorithms can then be used to speed up the convergence towards the optimum. This way the we would be able to get a better sense of the WEC array performance limits.

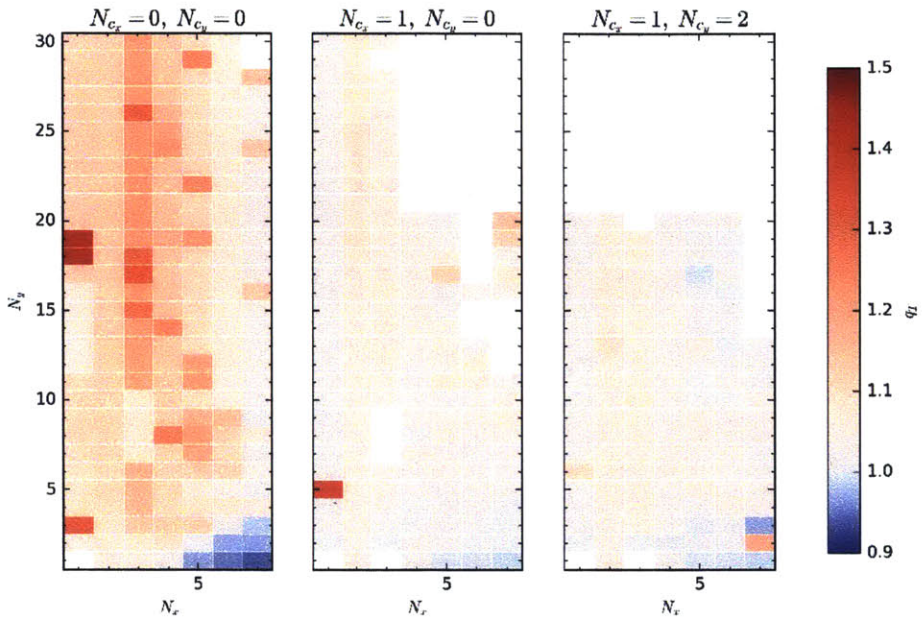

Figure 5.19: Optimal values of spectral gain q^S for rectangular arrays with $N_x \times N_y$ bodies, with $N_{c_x} = 1$ and $N_{c_y} = 2$, for a Brentschneider spectrum with $k_p = k_r$ and directional spreading factor $s = 2.0$.

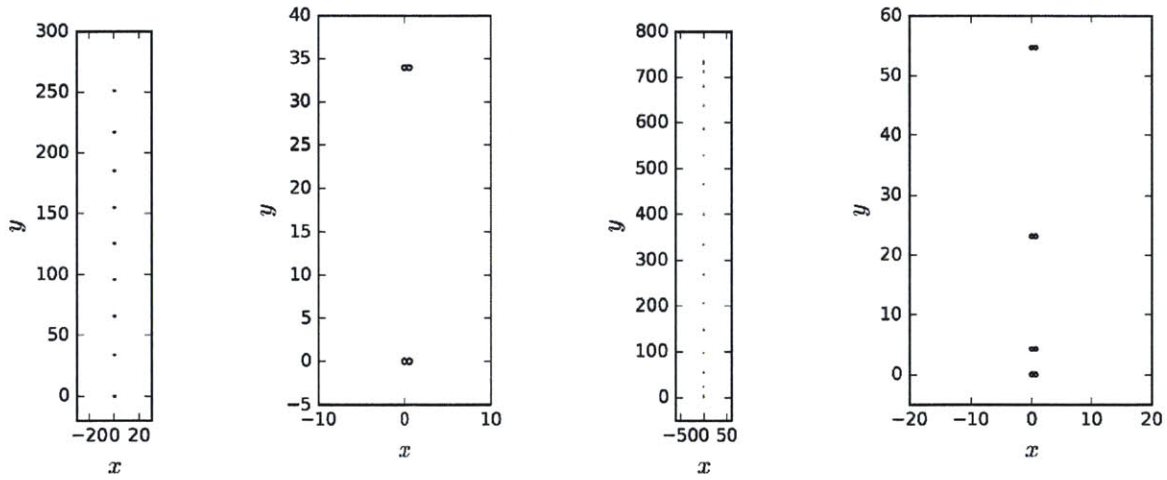

(a) Optimal 2×9-body array

(b) Optimal 6×23-body array, zoomed view

(c) Optimal 2×18-body array

(d) Optimal 2×18-body array, zoomed view.

Figure 5.20: Geometry of two optimal arrays, characterized by $N_{c_x} = 1$ and $N_{c_y} = 2$, for a Brentschneider spectrum with $k_p = k_r$, directional spreading factor $s = 2.0$ and mean incoming direction $\theta_I = 0°$.

Chapter 6

A Novel Formulation for the Mean Drift Force on Arrays

Mean drift force plays a large role in the design of large offshore structures. It is an inviscid, steady force on a structure caused by wave action. While the time-harmonic diffraction forces that were studied in the thesis so far are responsible for body motion and energy extraction, the steady nature of the mean drift force gives headaches to offshore engineers and investors. In order to hold a floating structure in place, large mooring systems need to be devised to counteract the effect of the mean drift force. The price of a mooring system contributes a significant amount to the total cost of a structure, so one has every desire to try to minimize it.

In this chapter, after a brief introduction and a literature review, we introduce a novel formulation of the mean drift force based on multiple scattering framework. The formulation allows for the calculation of the total mean drift force on an array as a sum of the contributions from each body, through the newly introduced drift force transfer matrix. This new formulation enables a simple extension of the optimization framework that we presented in the previous chapter.

6.1 Introduction & Literature review

The mean drift force (MDF) is a steady, non-linear force acting on bodies (or collection of bodies) in arrays. While the diffraction forces F discussed in the previous chapters might have large amplitudes, their mean is always zero. If ships were exposed to diffraction forces

alone, anchors would be superfluous!

MDF is caused by the change in the wave momentum caused by the presence of a structure. Since structures usually reflect the waves, the mean drift force is usually in the direction of wave propagation, especially for simple, compact bodies. However, the mean drift force on an array need not be in the direction of wave propagation. Emmerhoff and Sclavounos (1992) calculated the drift force on a 4-legged structure and noticed that at some wavenumbers the MDF on a structure was directed opposite to the wave propagation direction. Hence, there has to be a wavenumber at which this force is zero, which would minimize the mooring costs.

Since MDF can be calculated entirely from the linear, first-order potential that is the solution to the diffraction (and radiation, if present) problem, one way of calculating the MDF is to integrate the modified potential over the body surface (more on that in the next section).

The other way of calculating the MDF is from the far-field. Since MDF is related to the change of wave momentum, we can evaluate the wave momentum in the far field, and any imbalance in it is cause by the mean force exerted by the structure. This method, however, allows for the calculation of MDF on the structure as a whole only, without being able to calculate the MDF on a body in an array, say.

An interesting trade-off arises when considering the effects of MDF on WEC arrays. Since the entire purpose of WEC arrays is to extract energy from waves, they inescapably alter the wave momentum. The larger the effectiveness of a WEC array in energy extraction, the large change in wave momentum. This means that WEC arrays will almost inevitably experience large MDF, possibly reducing the economical benefits of harvested energy. Depending on the relative costs, one might opt to optimize a multi-objective problem of maximizing energy extraction and minimizing MDF.

In this chapter we will only focus on the MDF aspect alone, with the goal of minimizing it. The proposed framework is completely general so it can also be used for floating offshore structures whose goal is not energy extraction. In fact one of the main objectives of very large floating structure (VFLS) design is how to minimize the MDF. With our purpose clearly set, we proceed with introducing the novel formulation of MDF on arrays.

6.2 Matrix Formulation

The mean drift force $\boldsymbol{D} = (D_x, D_y)$ is caused by the nonlinear hydrodynamic effects on the body. It arises when the pressure from the first-order solution is integrated over the time-dependent wetted surface area. The leading order (second-order) nonlinear mean drift force can be calculated from the linear solution

$$\boldsymbol{D} = \iint_{S_b} \frac{\rho}{4} \nabla\Phi \cdot \nabla\Phi^* \, \mathbf{n} \, dS - \oint_C \frac{\rho\omega^2}{4g} \Phi \cdot \Phi^* \, \mathbf{n} \, dl \tag{6.1}$$

where Φ is the total potential evaluated on the surface of the body, S_b the mean wetted surface of the body, and C the mean waterline. The x and y components of the mean drift force are obtained by taking the inner product.

For a truncated cylinder , this expression can be written in a matrix form as

$$D_x = \mathbf{c}^+ \mathbf{F_x} \, \mathbf{c} \tag{6.2}$$

where $\mathbf{F_x}$ is the drift force transfer matrix (for the x-component of the force) obtained for an isolated body, and c is the vector of coefficients of the scattered waves. This formulation is valid both for isolated bodies and for those in an array. If c represents the scattered wave coefficients for an incoming plane wave, the result will be the isolated body mean drift force. If these coefficients represent the scattered field for a body in an array, it will give the drift force (x and y) for that body.

As an example, consider the mean drift force on a vertical cylinder of radius a. In that case, the surface integral in (6.1) can be separated into depth-dependent and angle-dependent integrals. For the x-direction force, the angle dependent integral gives

$$\int_0^{2\pi} (\cdot) \, e^{in\theta} \cos\theta \, d\theta = \begin{cases} \pi, & n = \pm 1 \\ 0, & \text{otherwise} \end{cases} . \tag{6.3}$$

The y-direction force yields

$$\int_0^{2\pi} (\cdot) \, e^{in\theta} \sin\theta \, d\theta = \begin{cases} i\,n\,\pi, & n = \pm 1 \\ 0, & \text{otherwise} \end{cases} . \tag{6.4}$$

Clearly, the contribution to the mean drift force comes only from the components where

$|n| = 1$.

Let ϕ be the incoming and scattered wave field around the the body

$$\begin{aligned}\phi &= \tilde{A} \sum_{n=-\infty}^{\infty} \sum_{m=0}^{\infty} \psi_m(z)\, e^{in\theta} \left(d_{nm} I_n(k_m r) + c_{nm} K_n(k_m r)\right) \\ &= \tilde{A} \sum_{n=-\infty}^{\infty} \sum_{m=0}^{\infty} \psi_m(z)\, e^{in\theta} \varphi_{nm}(r)\end{aligned} \tag{6.5}$$

where a short-hand notation has been used.

The mean drift force $\boldsymbol{D}$ in x and y directions for a truncated vertical cylinder is

$$\boldsymbol{D}_{\binom{x}{y}} = \int_{-d}^{0} dz \int_{0}^{2\pi} \frac{\rho\, a}{4} \nabla\phi \cdot \nabla\phi^*|_{r=a} \begin{pmatrix}\cos\theta \\ \sin\theta\end{pmatrix} d\theta - \int_{0}^{2\pi} \frac{\rho\, a\, \omega^2}{4g}\, \phi\, \phi^*|_{r=a,z=0} \begin{pmatrix}\cos\theta \\ \sin\theta\end{pmatrix} d\theta \tag{6.6}$$

The required $\nabla\phi \cdot \nabla\phi^*$ and $\phi\,\phi^*$ can be expanded in terms of (6.5) as

$$\phi\,\phi^*|_{r=a} = \left|\tilde{A}\right|^2 \sum_{n=-\infty}^{\infty} \sum_{m=0}^{\infty} \sum_{s=0}^{\infty} \psi_m(z)\psi_s(z) \left(\varphi_{nm}\varphi^*_{n-1,s}\, e^{i\theta} + \varphi^*_{nm}\varphi_{n-1,s}\, e^{-i\theta}\right) \tag{6.7}$$

$$\begin{aligned}\nabla\phi \cdot \nabla\phi^*|_{r=a} = \left|\tilde{A}\right|^2 \sum_{n=-\infty}^{\infty} \sum_{m=0}^{\infty} \sum_{s=0}^{\infty} &\left(\psi'_m(z)\psi'_s(z) k_m k_s^* + \frac{\psi_m(z)\psi_s(z)}{a^2} n(n-1)\right) \cdot \\ &\cdot \left(\varphi_{nm}\varphi^*_{n-1,s}\, e^{i\theta} + \varphi^*_{nm}\varphi_{n-1,s}\, e^{-i\theta}\right)\end{aligned} \tag{6.8}$$

With (6.7) and (6.8) the mean drift force in x direction becomes

$$D_x = |\tilde{A}|^2 \frac{\rho\pi a}{4h} \sum_{n=-\infty}^{\infty} \sum_{m=0}^{\infty} \sum_{s=0}^{\infty} \alpha^n_{ms} \left(\varphi_{nm}\varphi^*_{n-1,s} + \varphi^*_{nm}\varphi_{n-1,s}\right)_{r=a} \tag{6.9}$$

where α^n_{ms} is

$$\alpha^n_{ms} = \int_{-d/h}^{0} \frac{1}{K} \left[\psi'_m(z)\psi'_s(z) + \frac{n(n-1)}{a^2}\psi_m(z)\psi_s(z)\right] dz - K\psi_m(0)\psi_s(0) \tag{6.10}$$

and

$$\begin{aligned}\varphi_{nm}\varphi^*_{n-1,s}\big|_{r=a} = {} & d_{nm} d^*_{n-1,s} I_n(k_m a) I^*_{n-1}(k_s a) + c_{nm} c^*_{n-1,s} K_n(k_m a) K^*_{n-1}(k_s a) + \\ & + d_{nm} c^*_{n-1,s} I_n(k_m a) K^*_{n-1}(k_s a) + c_{nm} d^*_{n-1,s} K_n(k_m a) I^*_{n-1}(k_s a)\,.\end{aligned} \tag{6.11}$$

Note that $I_n(k_m a)$ is real for $m > 0$ and for $k_0 = -i\,\tilde{k}_0$ where $\tilde{k}_0$ is the solution of the dispersion relation for propagating waves (2.6)

$$I_n^*(k_0 a) = I_n(i\,\tilde{k}_0 a)\ .$$

The equation (6.11) can be written in a more compact form by recognizing that we can write each product in terms of vector-matrix-vector product, where the matrices are of the form

$$\begin{bmatrix} 0 & \mathfrak{I}_n & 0 & 0 \\ \mathfrak{I}_n^* & 0 & \mathfrak{I}_{n+1} & \\ 0 & \mathfrak{I}_{n+1}^* & 0 & \mathfrak{I}_{n+2} \\ 0 & 0 & \mathfrak{I}_{n+2}^* & 0 \end{bmatrix} \tag{6.12}$$

Here, $\mathfrak{I}_n$ is a $(M+1)\times(M+1)$ matrix whose (m,s) element is

$$\mathfrak{I}_n^{(m,s)} = \alpha_{ms}^n I_n(k_m a) I_{n-1}^*(k_s a)\ . \tag{6.13}$$

Corresponding to (6.11), we will label there matrices $\mathbf{F_1}$, $\mathbf{F_2}$, $\mathbf{F_3}$, and $\mathbf{F_4}$, respectively. Note that these are all zero-trace matrices.

Putting all together, the drift force can now be written as

$$D_x = |\tilde{A}|^2 \frac{\rho\pi}{4}\left[\mathbf{d}^+\mathbf{F_1}\,\mathbf{d} + \mathbf{c}^+\mathbf{F_2}\,\mathbf{c} + \mathbf{c}^+\mathbf{F_3}\,\mathbf{d} + \mathbf{d}^+\mathbf{F_4}\,\mathbf{c}\right] \tag{6.14}$$

Using the expression between the incoming and scattered coefficients (6.30) (and $\mathbf{d}^+ = \mathbf{c}^+\,\mathbf{T}^{-1^+}$), the upper expression becomes

$$D_x = |\tilde{A}|^2 \frac{\rho\pi}{4}\,\mathbf{c}^+\left[\mathbf{T}^{-1^+}\mathbf{F_1}\mathbf{T}^{-1} + \mathbf{F_2} + \mathbf{F_3}\mathbf{T}^{-1} + \mathbf{T}^{-1^+}\mathbf{F_4}\right]\mathbf{c} \tag{6.15}$$

which is actually the expression (6.2), with

$$\mathbf{F_x} = |\tilde{A}|^2 \frac{\rho\pi}{4}\left[\mathbf{T}^{-1^+}\mathbf{F_1}\mathbf{T}^{-1} + \mathbf{F_2} + \mathbf{F_3}\mathbf{T}^{-1} + \mathbf{T}^{-1^+}\mathbf{F_4}\right] \tag{6.16}$$

For the mean drift force in y direction

$$D_y = |\tilde{A}|^2 \frac{\rho\pi}{4}\sum_{n=-\infty}^{\infty}\sum_{m=0}^{\infty}\sum_{s=0}^{\infty} i\,\alpha_{ms}^n\left(\varphi_{nm}\varphi_{n-1,s}^* - \varphi_{nm}^*\varphi_{n-1,s}\right)_{r=a}\ , \tag{6.17}$$

and the rest follows analogously.

6.3 Low-Scattering Approximation

The low scattering approximation considers that there is only one "bounce" of the wave off any body. The wave after scattering passes through other bodies unaffected. This kind of approximation leads to phasing arguments.

Here we consider only diffraction problem as the bodies are assumed not to be oscillating in waves.

The total potential can be written as

$$\Phi = \Phi^I + \sum_{i=1}^{N_b} \phi_i^S \tag{6.18}$$

Evaluated at body j, this potential can be written as

$$\Phi_j \equiv \Phi^{I,j} + \phi_j^S + \sum_{i=1, i\neq j}^{N_b} \phi_i^S\big|_j \tag{6.19}$$

where $\phi_i^S\big|_j$ is the potential due to body i, evaluated at body j. The notation $|_j$ here implies that the transformation of the coordinate system needs to take place to express the Bessel functions in terms of coordinate system of body j.

The product of potentials required to calculate the drift force on body j from (6.1) gives

$$\begin{aligned}
\Phi_j \Phi_j^* &= \left(\Phi^{I,j} + \phi_j^S + \sum_{i=1, i\neq j}^{N_b} \phi_i^S\big|_j\right) \cdot \left(\Phi^{I,j*} + \phi^{S*}_j + \sum_{i=1, i\neq j}^{N_b} \phi_i^S\big|_j{}^*\right) \\
&= \left(\Phi^{I,j} + \phi_j^S\right)\left(\Phi^{I,j} + \phi_j^S\right)^* \\
&+ \left(\Phi^{I,j} + \phi_j^S\right) \sum_{i=1, i\neq j}^{N_b} \phi_i^S\big|_j{}^* + \left(\Phi^{I,j} + \phi_j^S\right)^* \sum_{i=1, i\neq j}^{N_b} \phi_i^S\big|_j \\
&+ \sum_{i=1, i\neq j}^{N_b} \sum_{l=1, l\neq j}^{N_b} \phi_i^S\big|_j \, \phi_l^S\big|_j
\end{aligned} \tag{6.20}$$

The last term in the previous equation is a higher-order term that can be neglected if $\phi_i^S\big|_j$

is small (i.e. for large spacing). Hence, the product of potentials can be approximated as

$$\Phi_j \Phi_j^* = \Phi_j \Phi_j^* + \sum_{i=1, i\neq j}^{N_b} \tau_{ij} \tag{6.21}$$

where

$$\Phi_j \equiv \Phi^{I,j} + \phi_j^S \tag{6.22}$$

and the interaction factor τ_{ij} is defined as

$$\tau_{ij} \equiv \Phi_j \, \phi_i^S\big|_j^* + \Phi_j^* \, \phi_i^S\big|_j \tag{6.23}$$

Note that τ_{ij} depends only on the locations of bodies i and j, not on the other bodies in the array.

The product of the gradients of potentials $\Phi_j \Phi_j^*$ is derived analogously to (6.20), leading to the gradient of the interaction function τ_{ij}^{∇} defined as

$$\tau_{ij}^{\nabla} \equiv \nabla\Phi_j \nabla \, \phi_i^S\big|_j^* + \nabla\Phi_j^* \nabla \, \phi_i^S\big|_j \tag{6.24}$$

The mean drift force on the body j under the low-scattering approximation can then be written as

$$\begin{aligned} \overline{F_j^D} = \mathcal{F}^D(\Phi_j) &\approx \mathcal{F}^D(\Phi_j) + \sum_{i=1, i\neq j}^{N_b} \left(\frac{\rho}{4} \iint_{S_b} \tau_{ij}^{\nabla} \vec{n} \, dS - \frac{\rho\omega^2}{4g} \int_C \tau_{ij} \vec{n} \, dl \right) \\ &= \overline{F_0^D} + \sum_{i=1, i\neq j}^{N_b} F_{ij}^D(\mathbf{r}_j - \mathbf{r}_i) \end{aligned} \tag{6.25}$$

where $F_{ij}^D(\mathbf{r}_j - \mathbf{r}_i) = (F_{ij,x}^D, F_{ij,y}^D)$ denotes the drift interaction force between bodies i and j, which depends only on their positions relative to the wave direction. For two truncated vertical cylinders, the drift interaction force is given in Section B.3.1.

The drift interaction force $F_{ij}^D(\mathbf{r}_j - \mathbf{r}_i)$ components can be expressed in matrix form in terms of the coefficients of propagating components of scattered and incoming waves c and

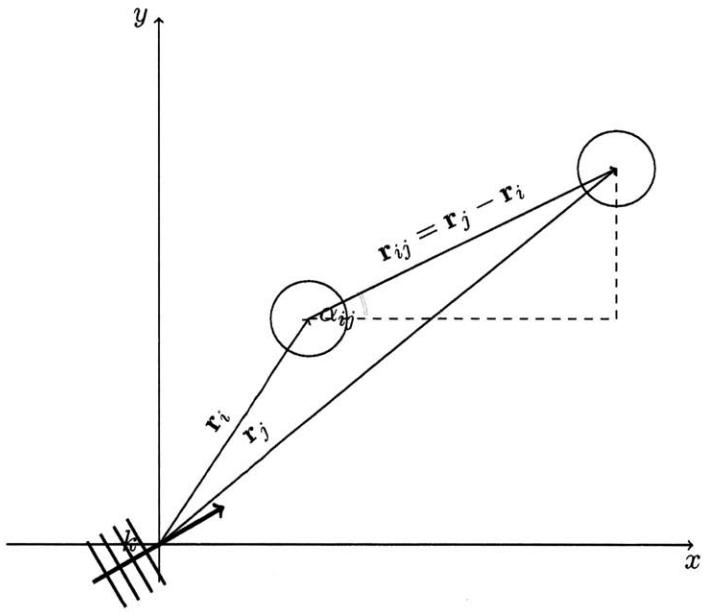

d as:

$$F^D_{ij,x}(\mathbf{r}_j - \mathbf{r}_i) = c^+ \mathbf{F^D}_{ij,x} d + d^+ \mathbf{F^D}_{ij,x}{}^+ c + c^+ \mathbf{C^D}_{ij,x} c = 2\Re(c^+ \mathbf{F^D}_{ij,x} d) + c^+ \mathbf{C^D}_{ij,x} c \tag{6.26}$$

$$F^D_{ij,y}(\mathbf{r}_j - \mathbf{r}_i) = c^+ \mathbf{F^D}_{ij,y} d + d^+ \mathbf{F^D}_{ij,y}{}^+ c + c^+ \mathbf{C^D}_{ij,y} c = 2\Re(c^+ \mathbf{F^D}_{ij,y} d) + c^+ \mathbf{C^D}_{ij,y} c \tag{6.27}$$

where $\mathbf{F^D}_{ij,x}$, $\mathbf{F^D}_{ij,y}$, $\mathbf{C^D}_{ij,x}$ and $\mathbf{C^D}_{ij,y}$ are coefficient matrices obtained from isolated body calculations. These matrices contain the body-dependent information stemming from integrals in (6.25). For a truncated vertical cylinder, the matrices $\mathbf{F^D}_{ij,x}$, $\mathbf{F^D}_{ij,y}$, $\mathbf{C^D}_{ij,x}$ and $\mathbf{C^D}_{ij,y}$ are given by (B.26)in B.3.1.

The scattered and incoming wave coefficients in (6.26) and (6.27) are calculated for an isolated body, and are used for all bodies without the change in phase due to different relative position. All the phase effects due to body positions are contained in the matrices.

The scattering potential $\phi_i^S\big|_j$ can be evaluated using the addition theorem for Bessel

functions (A.5)

$$\phi_i^S\big|_j = \delta_i \hat{A}\psi_0(z) \sum_{n=-\infty}^{\infty} c_n K_n(-ikr_i)e^{in\theta_i} \tag{6.28}$$

$$= \delta_i \hat{A}\psi_0(z) \sum_{n=-\infty}^{\infty} c_n \sum_{l=-\infty}^{\infty} (-1)^l e^{i(n-l)\alpha_{ij}} K_{n-l}(r_{ij}) I_l(r_j) e^{in\theta_j} \tag{6.29}$$

$$= \delta_i \hat{A}\psi_0(z) \sum_{n=-\infty}^{\infty} \sum_{l=-\infty}^{\infty} c_n \kappa_{nl}(\mathbf{r}_j - \mathbf{r}_i) I_l(r_j) e^{in\theta_j} \tag{6.30}$$

where $\kappa_{nl}(\mathbf{r}_j - \mathbf{r}_i)$

$$\kappa_{nl}(\mathbf{r}_j - \mathbf{r}_i) = (-1)^l e^{i(n-l)\alpha_{ij}} K_{n-l}(-ikr_{ij}) \tag{6.31}$$

accounts for the separation effects. If the large spacing approximation is used, far-field expression (A.8) for $K_n(-ikr)$ is substituted into (6.31).

The conditions for neglecting the last term in (6.20) are now clearer—$\phi_i^S\big|_j$ is a small quantity when either the scattering coefficients c_n are small, or when the distance kr_{ij} is large. In both cases, the product $\phi_i^S\big|_j \, \phi_l^S\big|_j$ is an order of magnitude smaller that the other terms.

In the case the scattering is low, the products $\phi_j^S \, \phi_i^S\big|_j{}^*$ and their conjugates can also be neglected.

The interaction factor g_{l0} has to be of smaller order of magnitude ($O(\varepsilon)$) than the leading order interaction. This happens either when the scattering off of a body is small ($ka \ll 1$), or the distance between the bodies is large. Both of these cases are referred here as low-scattering approximation because they do not lead to multiple scatterings to the leading order.

Chapter 7

Conclusion

As a conclusion, we briefly summarize the contributions made in this thesis. We also highlight some topics that, from this vantage point, seem like fruitful directions for future study.

7.1 Thesis Contributions

This thesis made contributions to the mathematical and computational treatment of large wave energy converter (WEC) arrays, to the systematic analysis of the spatial WEC array configuration, and to the understanding of their performance. We first summarize the physical insights we gain from the results presented in the thesis, and then summarize the technical contributions that made such analyses possible.

7.1.1 Summary of Physical Insights into the Energy Extraction by Large WEC Arrays

In this thesis we presented a thorough analysis of the performance of WEC arrays of up to 200 bodies in regular and irregular seas, as a function of the spatial array configuration. The analysis simulations and optimizations conducted in the thesis represent the largest computational analyses of WEC arrays in the literature, both in terms in the number of bodies in the arrays, and the number of array configuration types considered. The results as a whole form the first detailed spacing-dependent performance maps of WEC arrays with uniform spacing (line and rectangular), as well as those with irregular spacing (linear and quadratic). The computations of this scale were made possible by the advances in the

computational algorithm that allowed for a fast and memory-efficient way of calculating wave interactions, without resorting to approximations.

While the underlying hydrodynamic problem is linear — i.e. the wave amplitude is assumed to be small compared to its wavelength, and the body motion is assumed to be on the order of the wave amplitude — the dependency of WEC array performance on its spatial configuration is highly nonlinear and multi-modal (i.e. with many maxima and minima). This multi-modality comes from the complicated nature of wave interactions, which are further amplified in arrays because the slowly decaying outgoing waves couple the responses of all the bodies in an array together. We can talk about short-range interactions, i.e. those that occur between waves scattered and radiated between the bodies in an immediate neighborhood, where the evanescent waves can make a difference and the $\propto 1/\sqrt{r}$ decrease in amplitude of outgoing waves still does not matter. But we can also talk about "long-range" interactions in structured arrays, where the periodicity of the array results in persistent wave features that extend far beyond few spacings between the bodies. The computational algorithm we developed allows us to study all these cases.

We find that by carefully choosing the array configuration, it is possible to achieve very high performance metrics that would bring the real-world utilization of large WEC arrays closer to reality. In particular, uniformly spaced rectangular WEC arrays are shown to have a large gain over the same number of isolated bodies at the resonant wavenumber ($q_r \sim 1.9$), Overall, these high values of q are caused when the incoming wavelength and the array spacing d_y in the direction perpendicular to the wave propagation direction (or its projection) are close to that required for the creation of new scattering modes that would appear in the far field of periodic arrays with periodicity $d = d_y$. The wavelengths at which the new modes appear are called Rayleigh wavelengths λ_R, and the high-q values usually occur when the spacing is slightly smaller than one of the Rayleigh wavelengths $d_y \lesssim \lambda_R$.

The optimized rectangular arrays can also have their capture width equal their geometrical cross-section ($W_a/Y \approx 1$), i.e. they are capable of extracting all the energy flux that is incoming on their geometrical extent. When considering the performance in irregular seas (for a single spectrum considered), the spectral gain reduces to $q^S \approx 1.3$, and the capture width ratio drops down to $W_a^S/Y \approx 0.3$.

Interestingly, uniformly spaced arrays outperform the irregularly spaced arrays even for irregular seas considered here. One might expect that different spacings present in an

irregularly shaped arrays could positively "resonate" with different wave components contained in a spectrum, but that does not appear to be the case. More analysis should be conducted before such a claim can be completely dismissed, but the analyses of purely randomly spaced arrays shows that their performance is lower than that of optimized uniformly spaced rectangular arrays.

The analysis of random arrays points out to an interesting observation that there is a trade-off between extreme values of gain and the bandwidth of high-q performance — a high-q value is not sustained over a large ka interval, while constant q-range comes hand-in-hand with its modest value. While there exists a theoretical constraint on an angular values of q for a given wavenumber (4.3) (Fitzgerald and Thomas, 2007), such a constraint does not appear to exist for wavenumber-dependent values. Nevertheless, we find that carefully tuned arrays (like rectangular ones with uniform spacing) exhibit both very high-q values, as well as those close to zero, while for random arrays such abrupt changes are absent. This is a clear indication why configuration optimization is important if we want to achieve high-q values.

When it comes to array orientation towards the incoming waves, we have shown that attenuator arrays, i.e. arrays whose major dimension is in the direction of wave propagation, behave poorly at body resonant and super-resonant wavenumbers, without exception. Attenuator arrays perform acceptably, i.e. with gain $q > 1$ for sub-resonant wavenumbers. As the number of bodies in along the long dimension of the attenuator array increases, the acceptable range of wavenumbers moves to further lower values. Overall, while still outperforming the isolated bodies, the effectiveness of these arrays at such low wavenumbers is questionable because extractors with passive, non-tuned PTO devices (like all considered in this thesis) extract very small amounts of energy at these wavenumbers, so even a high gain does not bring forth meaningful performance. These results can give some indication on the design of attenuator devices that have been developed in the real world (Pelamis) or are proposed (Anaconda).

The bodies the arrays were made out of were all identical truncated vertical cylinders allowed only to heave, and with a fixed (non-tunable) power take-off device. It is expected that further improvements in WEC array performance if the extractor as a whole is being allowed to change (or optimize) in conjunction with the spatial array configuration. In particular, the body geometry and the number of degrees of freedom can have a large impact

on the bandwidth of efficient energy extraction. In particular, some of our optimization results show that two very closely spaced rows of bodies lead to an improvement in energy extraction, indicating that those might be a surrogate for a single device with multiple degrees of freedom, even an asymmetric device. In periodic arrays (or large arrays with uniform spacing in y-direction), an asymmetry of a device with respect to y-axis might lead to an improved performance. We can also draw similarities with optical structures, where it was shown that asymmetric particles lead to an improved absorption of light (Miller et al., 2014).

7.1.2 Theoretical and Computational Contributions

In addition to the contributions to the understanding of physics behind efficient energy extraction by large arrays that were presented in the previous section, this thesis makes further contributions to the theoretical and computational treatment of wave-body interactions in large arrays.

Main Theoretical Advances. The following theoretical advances have been made to extend the multiple scattering framework:

- Introduced a formulation for scattering by periodic arrays with cells of closely-spaced bodies (Section 3.3). The existing formulation of periodic arrays with a single body in a cell has been extended to include a finite number of closely-spaced bodies. The bodies can be of general shape, spacing, and connection (fixed, free, energy-extracting).

- Introduced velocity transfer matrix (Section 3.2). The new decomposition allows for the added mass and radiation damping for bodies in the array to remain that of an isolated body; the relation between the body velocity and the wave field is now expressed through a velocity transfer matrix. The new formulation is especially advantageous for cases where many different array configurations need to be calculated (e.g. systematic studies of body spacings, or spatial configuration optimization).

- Introduced transfer-matrix-based formulation for second-order mean drift force for arrays (Chapter 6). Introduced drift force transfer matrix that is calculated for an isolated body; the drift force on an array is obtained by calculating the standard multiple scattering system for the array. The new formulation allows efficient minimization

of the mean drift force.

Main Computational Advances. Developed algorithm based on multiple scattering theory capable of analyzing and optimizing large arrays $O(200)$. While current state-of-the-art optimizations or systematic analyses of array configurations have not been made with more than 5 bodies (Child and Venugopal, 2010), the algorithm developed for this thesis was used to produce systematic analyses and optimizations of array of up to 200 bodies. No constraints are imposed on body size, shape or spacing. Some of the advancements that were introduced to enable such performance are:

- Developed a series of array configuration parameterizations for reduced-order optimization and analysis of array performance (Section 5.3).
- Derived and implemented system gradients based on adjoint method.
- Matrix-free algebra for most memory-intensive products.
- Parallelized code.

7.2 Future work

There are several directions in which this thesis can be expanded that are immediately obvious. Some of them we list here.

Couple PTO characteristics optimization with array configuration optimization. All the results in this thesis have been obtained while keeping the extraction rate b_{PTO} constant, and tuned for the maximal power extraction at resonant frequency. As shown in Section 2.3.2, this is not optimal even for an isolated body in irregular seas. One can expect that when bodies operate in an array, the optimal b_{PTO} will be different than for an isolated body, and its optimization (either as constant for the entire array, or individually for each body) would further improve array performance. The framework presented in this thesis can easily tackle this problem (including the already-derived gradients with respect to b_{PTO}). In addition, one could study the effect on energy extraction caused by connecting a spring element (in addition to a PTO device) to every body. For isolated bodies, that shifts the resonant frequency to higher values, but how it might affect the energy extraction capability of an array as a whole is still not known, especially in irregular seas.

Couple body shape optimization with array configuration optimization. Similar to adding b_{PTO} to optimization, optimizing body shape can lead to even higher gains. Coupling shape and configuration optimization, while still preserving the computational efficiency of the multiple scattering framework, is slightly more complex from a technical standpoint. For the multiple scattering formulation presented in this thesis, any change in shape of any body would necessarily lead to a recalculation of all transfer matrices for that body. This could potentially reduce the advantages that this algorithm has over BEM methods. However, a general body shape could be adequately parameterized, and then its hydrodynamic characteristics (including transfer matrices) could be precalculated as a function of these parameters. Depending on the complexity of the shape (i.e. the number of parameters that describe it) and the number of grid points for shape and wavenumber discretization, the resulting matrices could be very large and expensive to calculate. A reduction in size could be achieved by using a course grid determined by the roots of a Chebyshev polynomial, and then approximating the values in between using Chebyshev series.

Energy Extraction from Horizontal Motion.

Implementing iterative solver for the multiple scattering system matrix.

Time-domain formulation and real-time tuning. This thesis has considered the problem of energy extraction in frequency domain only. However, there are aspects of the problem that would be better tackled in time-domain. For example, one simple solution to boosting a performance of an isolated WEC is to use so-called "latching" (Falnes, 2002; Falcão, 2008), i.e. controlling the phase by stopping a body in place until in synchrony with the wave field such that maximal motion velocities are ensured. Instead of a discrete control of that type, one could also tune the b_{PTO} value in a real-time manner, depending on the wave field. However, if the input to the system is the wave elevation at a certain point, this system in time-domain formulation is non-causal (Falnes, 1995), i.e. the response depends not only on the current forcing, but also on the past motion. That is why a fully optimal control to get, say locking phases, is not possible (Falnes, 2002). Whether having the knowledge of the motion of several bodies in the array would improve the causality of the system is not known.

Cloaking for mean drift force. Recently, Newman (2014) and Kashiwagi, Iida, and Miki (2015) have studied how placing bodies around the body we are concerned about can reduce the drag force on the said body. They have used a small number of additional bodies and achieved reductions in mean drift force. It would be interesting to study whether an increase in the number of additional bodies and optimization of their spacing would lead to further reduction (or complete annihilation) of the mean drift force on the object of interest. This could have a large practical use for retro-fitting the existing structures with these cloaking bodies to reduce the mooring costs.

To summarize, in addition to the improvements in WEC array design that have been addressed in this thesis, WEC arrays seem to be brimming with opportunities for further enhancement. Both the prospect of obtaining another reliable method for extracting energy from a dependable source of renewable energy, and the prospect of tackling an interesting and rich scientific problem should excite aspiring researchers, as well as those already practicing in the field. I hope this thesis will provide a small contribution to that endeavor.

Appendix A

Bessel Function Identities

A.1 Bessel Identities

Expressing Hankel function in terms of modified Bessel function of the second kind

$$K_n(-ix) = \frac{1}{2}\pi i^{n+1} H_n^{(1)}(x) \tag{A.1}$$

The Bessel function of the first kind $J_n(x)$ can also be expressed in terms of modified Bessel functions of complex argument.

$$I_n(-ix) = (-i)^n J_n(x) \tag{A.2}$$

The derivatives of Bessel functions of complex argument can be obtained from the well-known expressions for the real-argument ones. For example

$$\begin{aligned} \frac{\partial}{\partial x} J_n(x) &= \frac{1}{2}\left(J_{n-1}(x) - J_{n+1}(x)\right) \\ &= \frac{1}{2} i^{n-1}\left(I_{n-1}(-ix) + I_{n+1}(-ix)\right) \end{aligned} \tag{A.3}$$

where $J_n(x) = i^n I_n(-ix)$ was used. Then it follows

$$i^n \frac{\partial}{\partial x} I_n(-ix) = \frac{1}{2} i^{n-1}\left(I_{n-1}(-ix) + I_{n+1}(-ix)\right)$$

and finally

$$\frac{\partial}{\partial x} I_n(-ix) = -i\frac{1}{2}\left(I_{n-1}(-ix) + I_{n+1}(-ix)\right) . \tag{A.4}$$

A.2 Addition Theorem

Bessel function in one coordinate system can be expressed in terms of another coordinate system using addition theorems (Àbramowitz and Stegun, 1964)

$$K_n(r_i)e^{in\theta_i} = \sum_{l=-\infty}^{\infty} (-1)^l e^{i(n-l)\alpha_{ij}} K_{n-l}(r_{ij}) I_l(r_j) e^{in\theta_j} \tag{A.5}$$

A.3 Far-field Approximation

Hankel function can be expressed in terms of modified Bessel functions of complex argument as

$$K_n(-i\,x) = \frac{1}{2}\,\pi\,i^{n+1}\,H_n^{(1)}(x)\,. \tag{A.6}$$

The far-field (large argument) approximation for the Hankel function is

$$\lim_{kr\to\infty} H_n(kr) = e^{i\,kr}\,e^{-i\,\frac{\pi}{4}-\frac{1}{2}\,i\,n\,\pi}\sqrt{\frac{2}{\pi\,kr}} \tag{A.7}$$

or, in terms of the modified Bessel function

$$\lim_{kr\to\infty} K_n(-i\,kr) = e^{i\,kr+i\,\frac{\pi}{4}}\sqrt{\frac{2}{\pi\,kr}} \tag{A.8}$$

Notice that (A.8) does not depend on the order n. However, with the increase in n, the value of kr for which the approximation is valid increases.

Appendix B

Hydrodynamic Properties of a Truncated Vertical Cylinder

Truncated vertical cylinder is a common body shape considered for energy extraction.

The influence of the cylinder shape can be easily studied due the existence of the analytic solution and due to the small number of the parameters required to describe the shape.

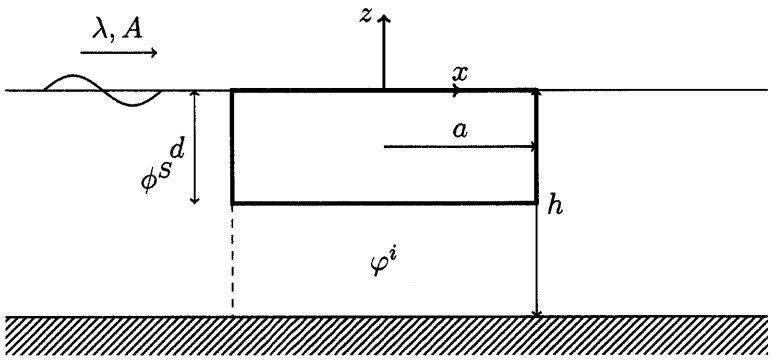

Figure 2.1: Truncated vertical cylinder

B.1 Diffraction Problem

The incoming propagating wave potential can be expanded in terms of Bessel functions. This expansion contains only propagating components since they are the only ones found in a propagating monochromatic wave. However, after scattering from a body evanescent waves are in general present in the wave-field and those modes can reach another body.

Here we describe such general case.

Consider a j-th mode hitting a truncated vertical cylinder, where $j = 0$ represents the propagating wave and $j > 0$ denotes evanescent waves. The incoming potential can be written as

$$\Phi^I = \psi j(z)\, I_n(k_j\, r)\ , \quad k_0 = -i\, \tilde{k}_0\ . \tag{B.1}$$

The scattering potential can in general be written as

$$\phi^S = -\frac{I_n'(k_j a)}{K_n'(k_j a)}\, K_n(k_j r)\, \psi_j(z) + \sum_{l=0}^{\infty} a_{nl}\, \frac{K_n(k_l r)}{K_n'(k_l a)} \psi_l(z)\ ; \quad j = 0, 1, \ldots \tag{B.2}$$

The potential below the cylinder can be expressed as Garrett, 1971

$$\varphi^i = \frac{1}{2}\, c_{n0}^j \left(\frac{r}{a}\right)^{|n|} + \sum_{m=1}^{\infty} c_{nm}^j\, \frac{I_n(k_m r)}{I_n(k_m a)}\, \cos\left(\nu_m(z+h)\right) \tag{B.3}$$

where

$$\nu_m = \frac{m\pi}{h-d}\ .$$

The unknown coefficients a_{nl}^j and c_{nm}^j are determined from the boundary conditions on the body.

For the diffraction problem the body is considered to be fixed in its mean position. The kinematic boundary conditions that needs to be satisfied on the body surface require

$$\frac{\partial \Phi^I}{\partial r} = \frac{\partial \phi^S}{\partial r} \tag{B.4}$$

$$\frac{\partial \varphi^i}{\partial z} = 0 \tag{B.5}$$

Matching of the pressures and the velocities across the artificial boundary that separates the two solutions requires

$$\phi^S + \Phi^I = \varphi^i \tag{B.6}$$

$$\frac{\partial(\phi^S + \Phi^I)}{\partial r} = \frac{\partial \varphi^i}{\partial r} \tag{B.7}$$

These boundary conditions will be satisfied in an integral sense, i.e. matching of pressure

and velocity at $r = a$ leads to

$$\int_{-h}^{-d} \varphi^i\big|_{r=a} \cos\left(\nu_m(z+h)\right)\, dz = \int_{-h}^{-d} \left(\Phi^I + \phi^S\right)\big|_{r=a} \cos\left(\nu_m(z+h)\right)\, dz \tag{B.8}$$

Using the orthogonality of $\cos\left(\nu_m(z+h)\right)$ on the interval $(-h,-d)$, we can get an equation for c_{nm}^j gives the expression

$$c_{nm}^j = 2\left(I_n(k_j a) - \frac{I_n'(k_j a)}{K_n'(k_j a)} K_n(k_j a)\right) g_{mj} + 2\sum_{l=0}^{\infty} a_{nl}^j \frac{K_n(k_l a)}{K_n'(k_l a)} g_{ml}\,, \quad m = 0, 1, \ldots \tag{B.9}$$

where the following expressions were used

$$\frac{1}{h-d}\int_{-h}^{-d} \cos^2\left(\nu_m(z+h)\right)\, dz = \frac{1}{2}\,, \quad m \neq 0$$

and

$$g_{ml} \equiv \frac{1}{h-d}\int_{-h}^{-d} \psi_l(z)\, \cos\left(\nu_m(z+h)\right)\, dz\,. \tag{B.10}$$

Matching of the velocities give the condition

$$\int_{-h}^{0} \psi_l(z) \left[\frac{\partial \Phi^I}{\partial r} + \frac{\partial \phi^S}{\partial r}\right]_{r=a} dz = \int_{-h}^{-d} \left.\frac{\partial \varphi^i}{\partial r}\right|_{r=a} \psi_l(z)\, dz \tag{B.11}$$

where the condition

$$\left.\frac{\partial \varphi^i}{\partial r}\right|_{r=a} \equiv 0, \quad -d \leq z \leq -0$$

that the velocity is only due to external region.

By using the orthogonality of depth eigenfunctions $\psi_l(z)$, the scattering coefficients can be expressed as

$$a_{nl}^j = \frac{1}{k_l h}\left[\frac{|n|}{2}\frac{c_{n0}^j}{a/h}\frac{h-d}{h} g_{0l} + \sum_{m=1}^{\infty} c_{nm}^j \nu_m (h-d) \frac{I_n'(\nu_m a)}{I_n(\nu_m a)} g_{nm}\right] \tag{B.12}$$

The equations (B.9) and (B.12) form a coupled system that can be solved in terms of either internal or scattered coefficients, after it has been truncated to a finite number of evanescent waves M and angular modes N.

In terms of the internal potential coefficients, the obtained system can be written as

$$\sum_{s=0}^{\infty}\left[\delta_{sm}-f_{sm}^{n}\left(\delta_{s0}\,|n|\,\frac{h-d}{h}\frac{1}{a/h}+2(1-\delta_{s0})\mathcal{I}_{ns}\right)\right]c_{ns}^{j}=2\,g_{mj}\left(I_n(k_ja)-\frac{I_n'(k_ja)}{K_n'(k_ja)}K_n(k_ja)\right) \tag{B.13}$$

After the system (B.13) has been solved for all c_{ns}^{j}, the coefficients of scattered waves a_{nl}^{j} can be calculated from (B.12). These coefficients form the T-matrix for the truncated cylinder—every value of a_{nl}^{j} obtained is the amplitude of a partial wave scattered by a unit incoming partial wave j of order n.

The structure of the T-matrix depends on the (arbitrary) arrangement of coefficients of incoming and scattered coefficients. In the case of the truncated vertical cylinder the T-matrix is sparse because the axial symmetry—incoming partial wave of order n scatters waves only of order n.

B.2 Radiation characteristics

The derivation of the added mass and damping coefficients of vertical cylinders follows Yeung, 1981.

B.3 Mean Drift Force

B.3.1 Low-Scattering approximation

$$\begin{aligned}\Phi_j=\Phi^{I,j}+\phi_j^S&=\delta_j\tilde{A}\psi_0(z)\sum_{n=-\infty}^{\infty}e^{in\theta}\left(d_{n0}I_n(-ikr_j)+c_{n0}K_n(-ikr_j)\right)\\&=\delta_j\tilde{A}\psi_0(z)\sum_{n=-\infty}^{\infty}e^{in\theta}\varphi_{n0}(r_j)\end{aligned} \tag{B.14}$$

$$\phi_i^S\big|_j=\delta_i\tilde{A}\psi_0(z)\sum_{l=-\infty}^{\infty}e^{il\theta}I_l(-ikr_j)\,g_{l0}(\vec{r}_j-\vec{r}_i) \tag{B.15}$$

For a circular cylinder, all the contribution to the mean drift force comes from modes

with $|n| = 1$. Using (B.14) and (B.15), the equation (6.23) can be expanded as

$$\tau_{ij} = |\tilde{A}|^2 \sum_{n=-\infty}^{\infty} \left(\mathcal{G}_n^{ij} e^{i\theta} + \mathcal{G}_n^{ij*} e^{-i\theta} \right) \psi_0^2(z) \tag{B.16}$$

$$\tau_{ij}^{\nabla} = |\tilde{A}|^2 \sum_{n=-\infty}^{\infty} \left(\mathcal{G}_n^{ij} e^{i\theta} + \mathcal{G}_n^{ij*} e^{-i\theta} \right) \left(\psi_0^2(z) \frac{n(n-1)}{a^2} + \psi_0'^2(z) |k|^2 \right) \tag{B.17}$$

where

$$\begin{aligned} \mathcal{G}_n^{ij} &\equiv \delta_j \delta_i^* \varphi_n I_{n-1}^* g_{n-1}^*(\mathbf{r}_j - \mathbf{r}_i) + \delta_j^* \delta_i \varphi_{n-1}^* I_n g_n(\mathbf{r}_j - \mathbf{r}_i) \\ &= \delta_j \delta_i^* \left(d_n I_n + c_n K_n \right) I_{n-1}^* \sum_{l=-\infty}^{\infty} c_l^* \, \kappa_{l,n-1}^* + \\ &+ \delta_j^* \delta_i \left(d_{n-1}^* I_{n-1}^* + c_{n-1}^* K_{n-1}^* \right) I_n \sum_{l=-\infty}^{\infty} c_l \, \kappa_{ln} \end{aligned} \tag{B.18}$$

Here for brevity, the arguments of Bessel functions have been omitted; they are to be evaluated at $-ikr_j$, or at ikr_j for conjugated functions ($I_n^* \equiv I_n(ikr_j)$). The spacing factor κ_{ln} is defined in (6.31).

After substituting (B.16) and (B.17) into (6.25), the components of the drift interaction force can be written as

$$F_x = |\tilde{A}|^2 \frac{\rho\pi}{4} \sum_{n=-\infty}^{\infty} \alpha_n \left(\mathcal{G}_n^{ij} + \mathcal{G}_n^{ij*} \right) \tag{B.19}$$

$$F_y = |\tilde{A}|^2 \frac{\rho\pi}{4} \sum_{n=-\infty}^{\infty} i \, \alpha_n \left(\mathcal{G}_n^{ij} - \mathcal{G}_n^{ij*} \right) \tag{B.20}$$

where shorthand notation $\alpha_n \equiv \alpha_{00}^n$ for (6.10) has been used here because there are no evanescent waves. The expressions (B.19) and (B.20) can be expressed in matrix form by expanding the sums $\sum_{n=-\infty}^{\infty} \alpha_n \mathcal{G}_n^{ij}$.

$$\begin{aligned} \sum_{n=-\infty}^{\infty} \alpha_n \mathcal{G}_n^{ij} = \sum_{n=-\infty}^{\infty} \sum_{l=-\infty}^{\infty} & \delta_j \delta_i^* d_n \alpha_n I_n I_{n-1}^* \kappa_{l,n-1}^* c_l^* + \\ & + \delta_j^* \delta_i d_{n-1}^* \alpha_n I_{n-1}^* I_n \kappa_{ln} c_l + \\ & + \delta_j \delta_i^* c_n K_n I_{n-1}^* \kappa_{l,n-1}^* c_l^* + \\ & + \delta_j^* \delta_i c_{n-1}^* K_{n-1}^* I_n \kappa_{ln} c_l \end{aligned} \tag{B.21}$$

After the truncation to a finite number of N_p angular modes, the sum in (B.21) can be

expressed in matrix form as

$$\sum_{n=-N_p}^{N_p} \alpha_n \mathcal{G}_n^{ij} = c^+ \mathbf{F_1} d + d^+ \mathbf{F_2} c + c^+ \mathbf{F_3} c \,, \tag{B.22}$$

where the (l, n) element of matrices $\mathbf{F_1}$, $\mathbf{F_2}$ and $\mathbf{F_3}$ are, respectively:

$$\begin{aligned} F_1^{(l,n)} &= \delta_j \delta_i^* \alpha_n I_n I_{n-1}^* \kappa_{l,n-1}^* \\ F_2^{(l,n)} &= \delta_j^* \delta_i \alpha_{00}^{l+1} I_l^* I_{l+1} \kappa_{n,l+1} \\ F_3^{(l,n)} &= \delta_j \delta_i^* \alpha_n K_n I_{n-1}^* \kappa_{l,n-1}^* + \delta_j^* \delta_i \alpha_n K_{n-1}^* I_n \kappa_{ln} \end{aligned} \tag{B.23}$$

Using (B.19) and (B.22), it follows

$$\begin{aligned} &c^+ \mathbf{F_1} d + d^+ \mathbf{F_2} c + c^+ \mathbf{F_3} c + (c^+ \mathbf{F_1} d)^* + (d^+ \mathbf{F_2} c)^* + (c^+ \mathbf{F_3} c)^* = \\ =&c^+ (\mathbf{F_1} + \mathbf{F_2}^+) d + d^+ (\mathbf{F_1}^+ + \mathbf{F_2}) c + c^+ (\mathbf{F_3} + \mathbf{F_3}^+) c \end{aligned} \tag{B.24}$$

where transpose of a scalar has been used to get the products in the right form. Similarly, for (B.20) and (B.22) we get

$$\begin{aligned} &i \left[c^+ \mathbf{F_1} d + d^+ \mathbf{F_2} c + c^+ \mathbf{F_3} c - (c^+ \mathbf{F_1} d)^* - (d^+ \mathbf{F_2} c)^* - (c^+ \mathbf{F_3} c)^* \right] = \\ =&c^+ \left[i \left(\mathbf{F_1} - \mathbf{F_2}^+ \right) \right] d + d^+ \left[i \left(\mathbf{F_2} - \mathbf{F_1}^+ \right) \right] c + c^+ (i \, \mathbf{F_3} - i \, \mathbf{F_3}^+) c \,. \end{aligned} \tag{B.25}$$

With (B.24) and (B.25), the matrices are

$$\begin{aligned} \mathbf{F^D}_{ij,x} &= |\tilde{A}|^2 \frac{\rho\pi}{4} (\mathbf{F_1} + \mathbf{F_2}^+) \\ \mathbf{F^D}_{ij,y} &= |\tilde{A}|^2 \frac{\rho\pi}{4} \left[i \left(\mathbf{F_1} - \mathbf{F_2}^+ \right) \right] \\ \mathbf{C^D}_{ij,x} &= |\tilde{A}|^2 \frac{\rho\pi}{4} (\mathbf{F_3} + \mathbf{F_3}^+) \\ \mathbf{C^D}_{ij,y} &= |\tilde{A}|^2 \frac{\rho\pi}{4} (i \, \mathbf{F_3} - i \, \mathbf{F_3}^+) \end{aligned} \tag{B.26}$$

Note that $\mathbf{C^D}_{ij,x}$ and $\mathbf{C^D}_{ij,y}$ are Hermitian matrices, and that the sum of first two terms is Hermitian as well, so the overall sum is always real.

Appendix C

Validations

In this chapter, the computer code developed for this thesis is validated against the published results for multiple interactions in array, both with energy extraction and without.

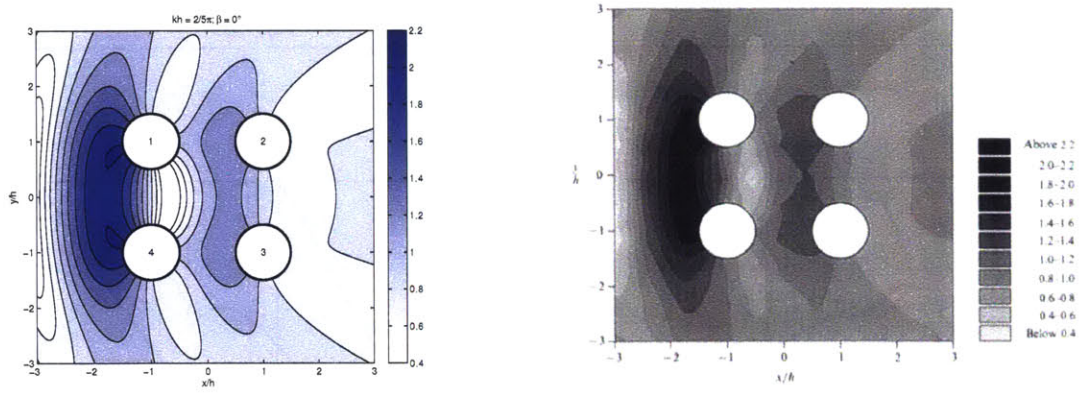

Figure 3.1: Comparison of free surface amplitudes with Linton and Evans (1990), $ka = \pi/5$.

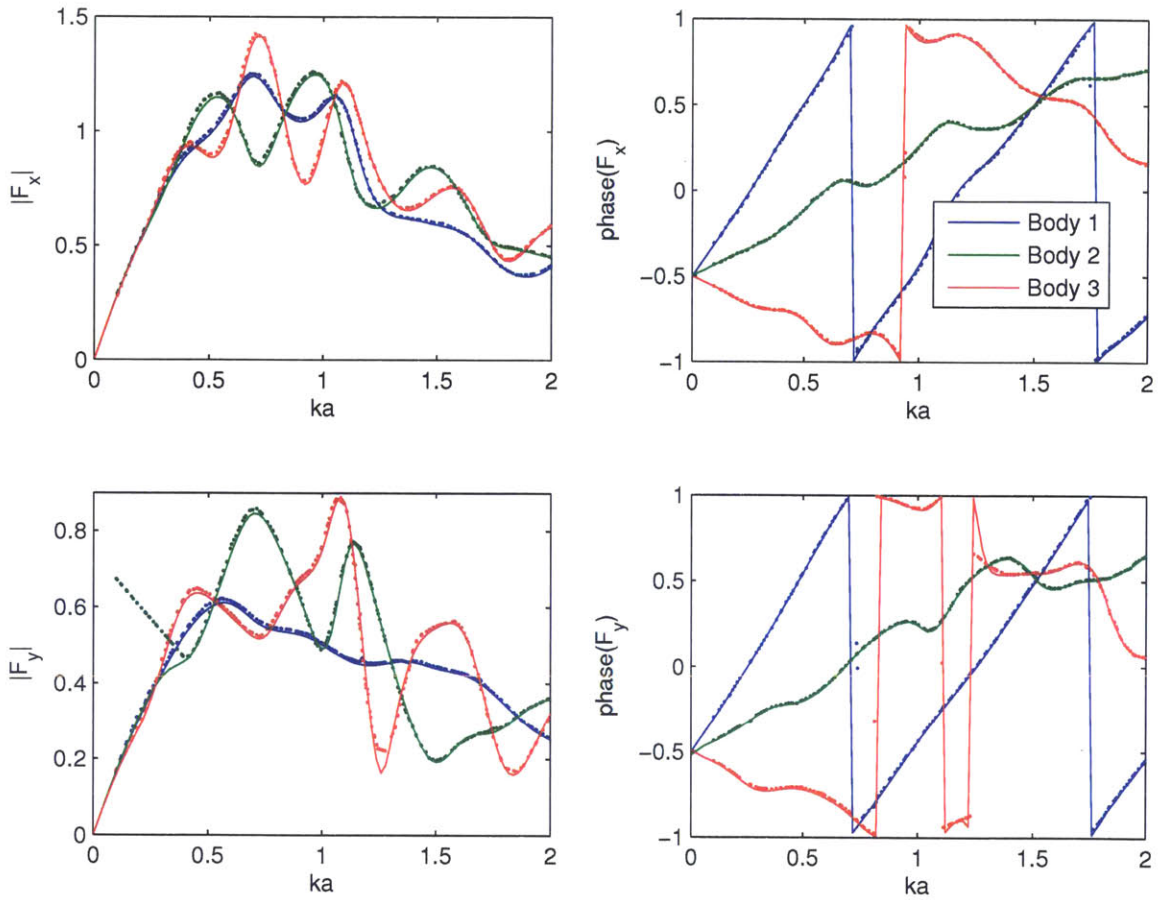

Figure 3.2: Comparison of force amplitudes and phases on a 3-body array calculated by the present algorithm (lines) with Mavrakos and Koumoutsakos (1987) (points).

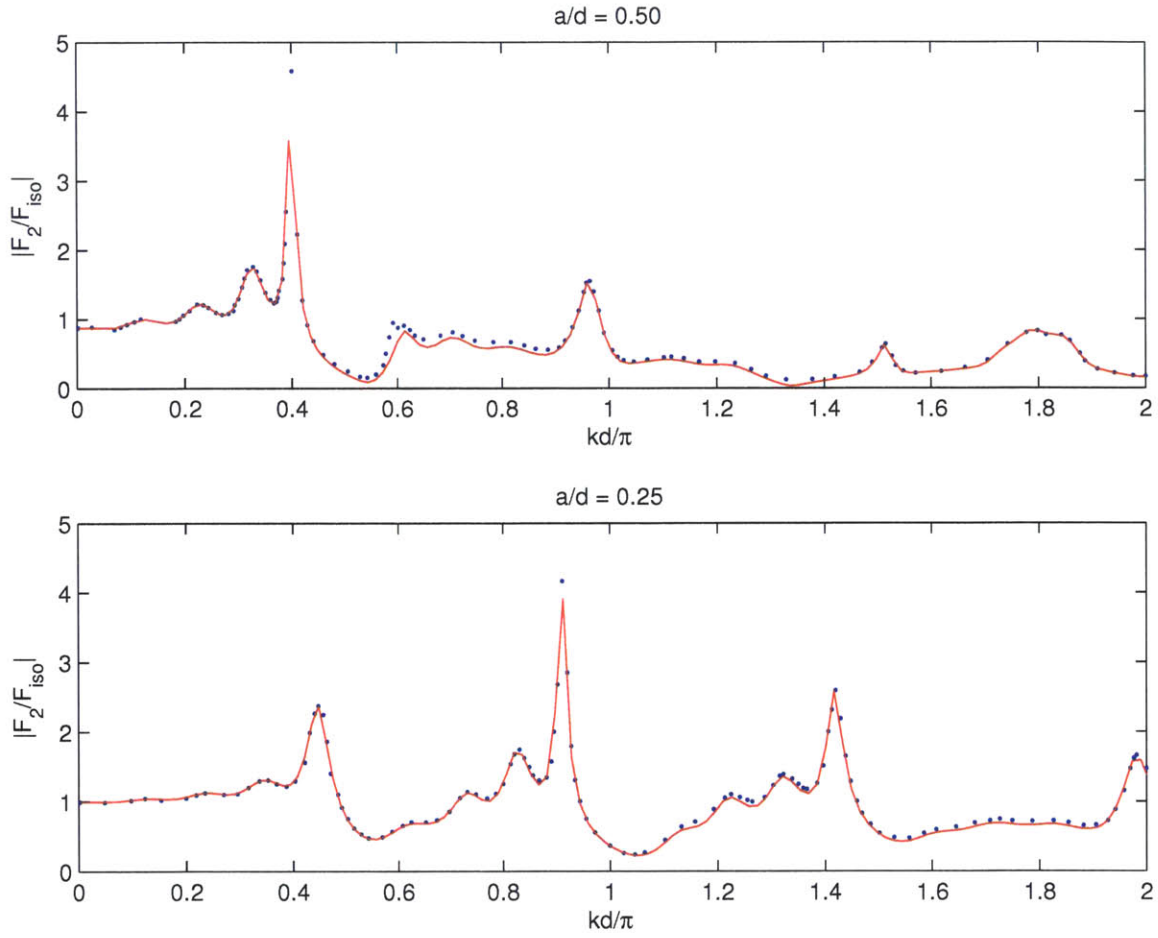

Figure 3.3: Surge force amplification in a 2×9 array, comparison of the present model (lines) with Evans and Porter (1999) (points).

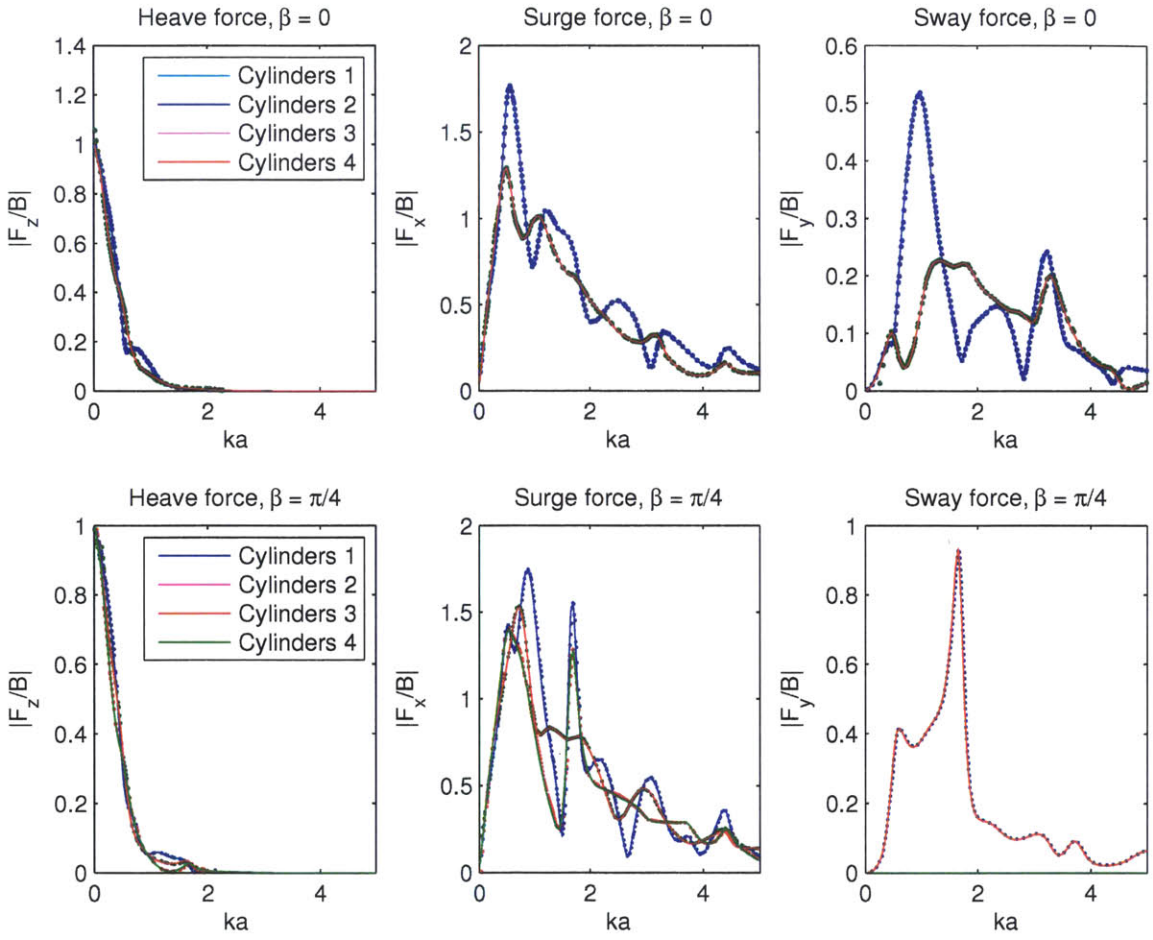

Figure 3.4: Comparison of force amplitudes on a rectangular 4-body array calculated by the present algorithm (lines) with Siddorn and Eatock Taylor (2008) (points).

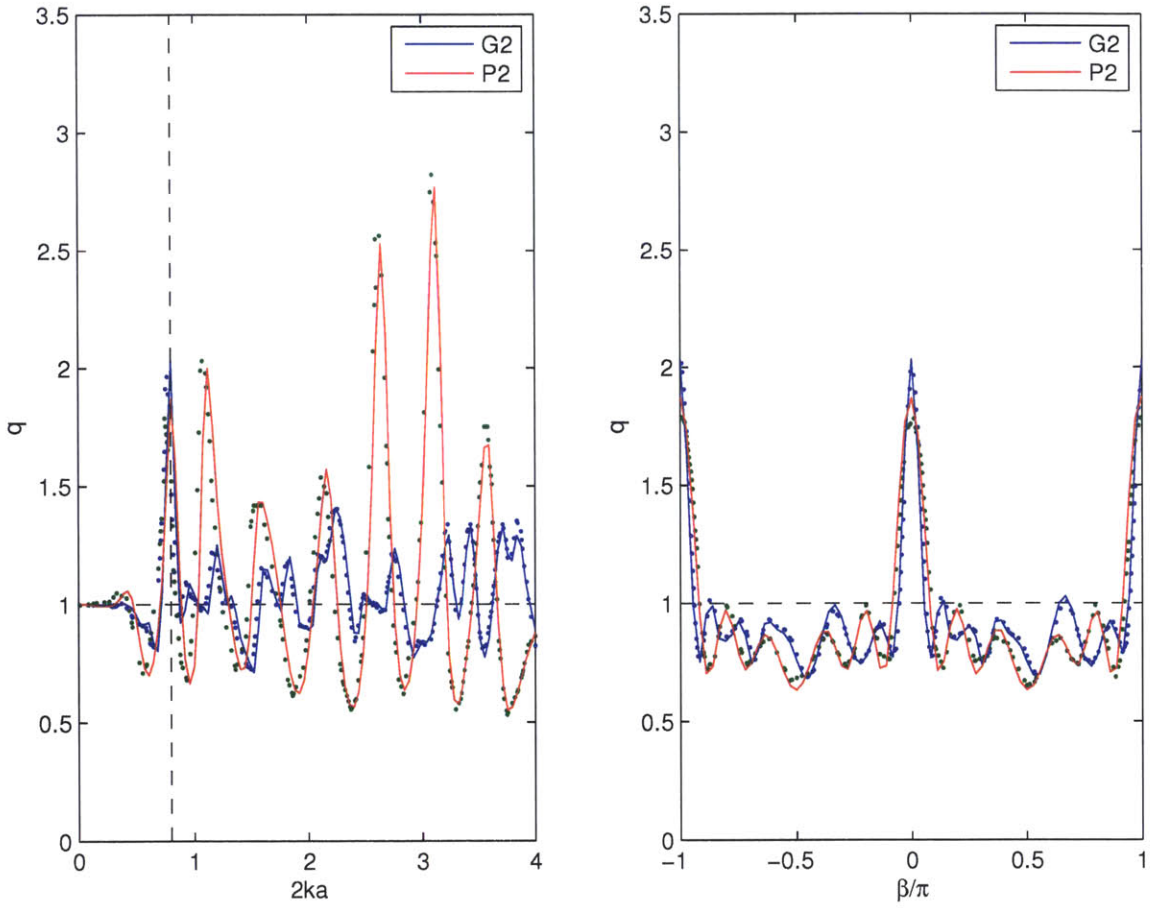

Figure 3.5: Comparison of array gain q of a 5-body array with calculated by the present algorithm (lines) Child and Venugopal (2010) (points).

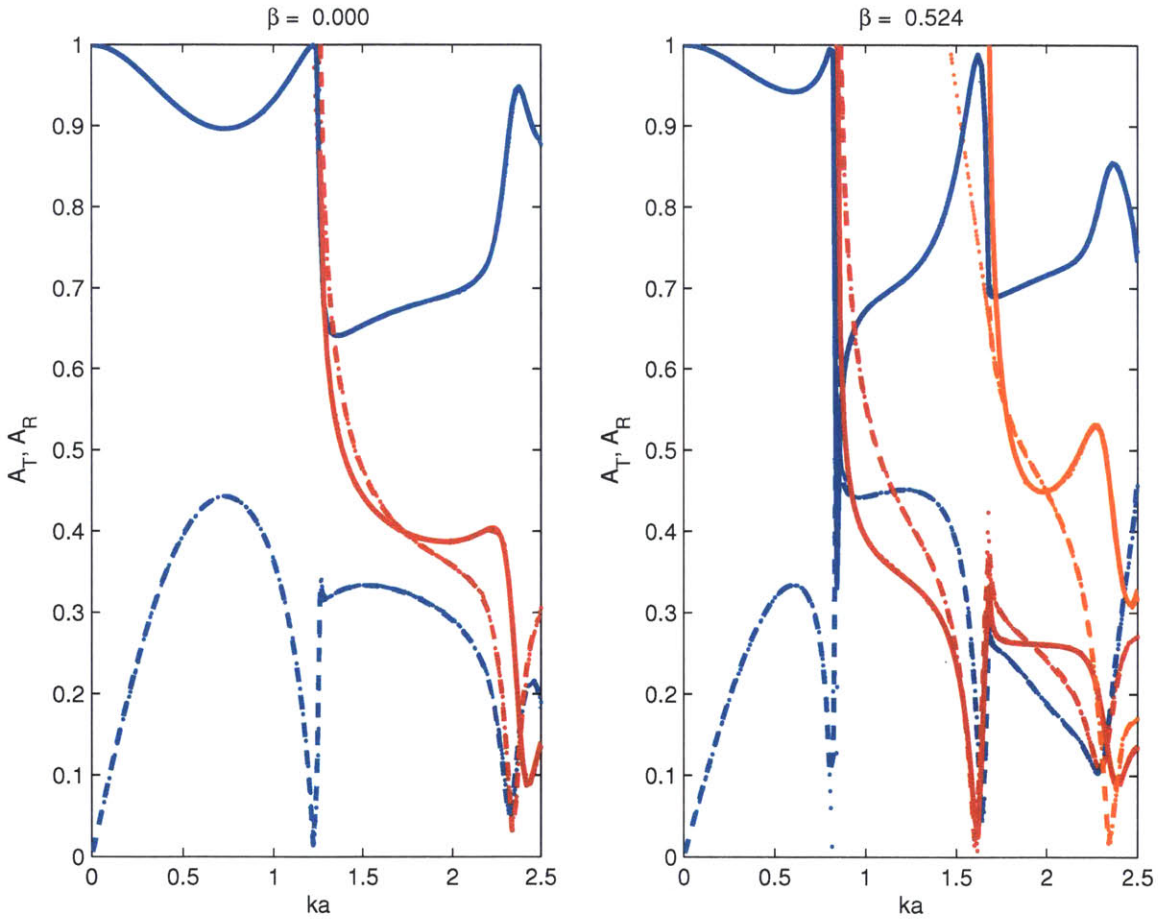

Figure 3.6: Comparison of transmission and reflection coefficients calculated by the present algorithm (lines) with Peter, Meylan, and Linton (2006) (points), for a periodic array made of bottom-mounted cylinders (single row) for incoming angles 0° and 30°. Note that the data points almost perfectly match, so the difference between the two data sets is at some places difficult to discern.

Appendix D

Supplementary Results

D.1 Array Performance Analysis

Analysis of Line Arrays with Uniform Spacing

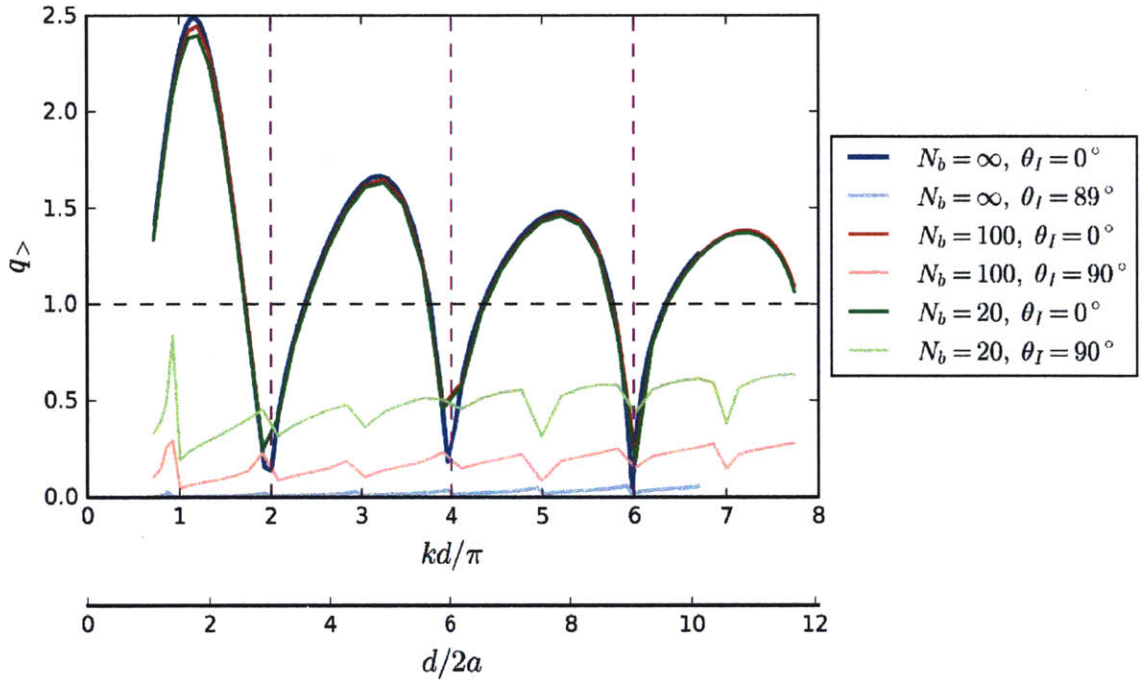

Figure 4.1: Comparison of the array gain q between arrays of different size as a function of body spacing for super-resonant wavenumber $ka_>$ for $\theta_I = 0°$, $90°$.

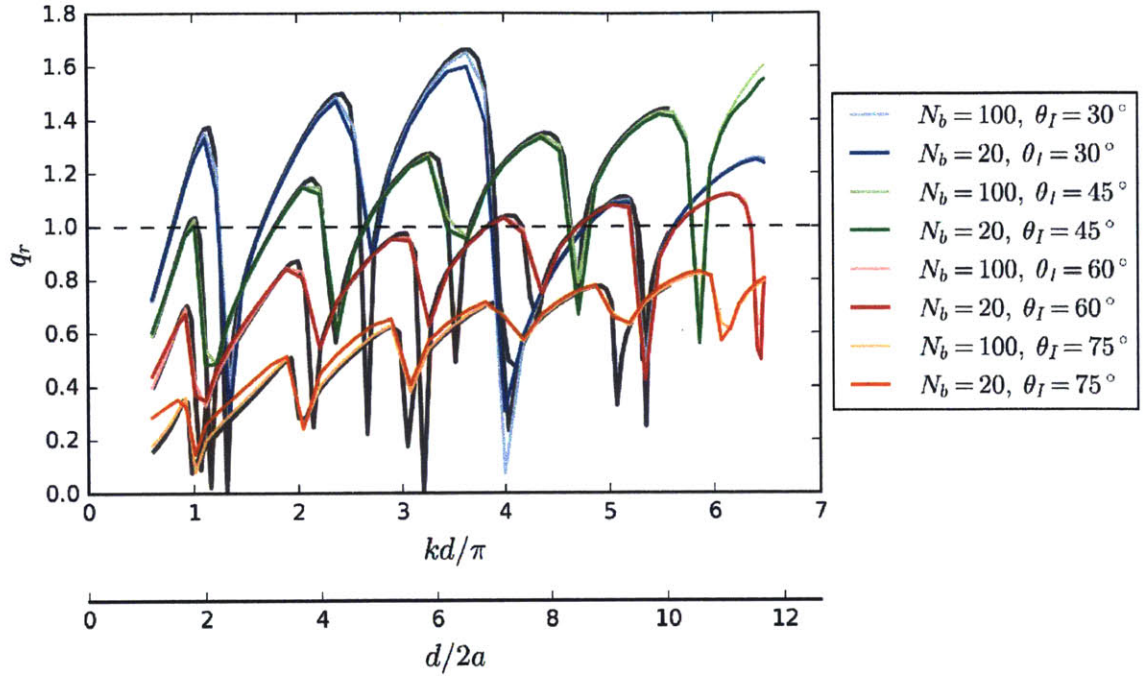

Figure 4.2: Comparison of the array gain q between arrays of different size as a function of body spacing for resonant wavenumber ka_r for $\theta_I = 30°, 45°, 60°, 75°$.

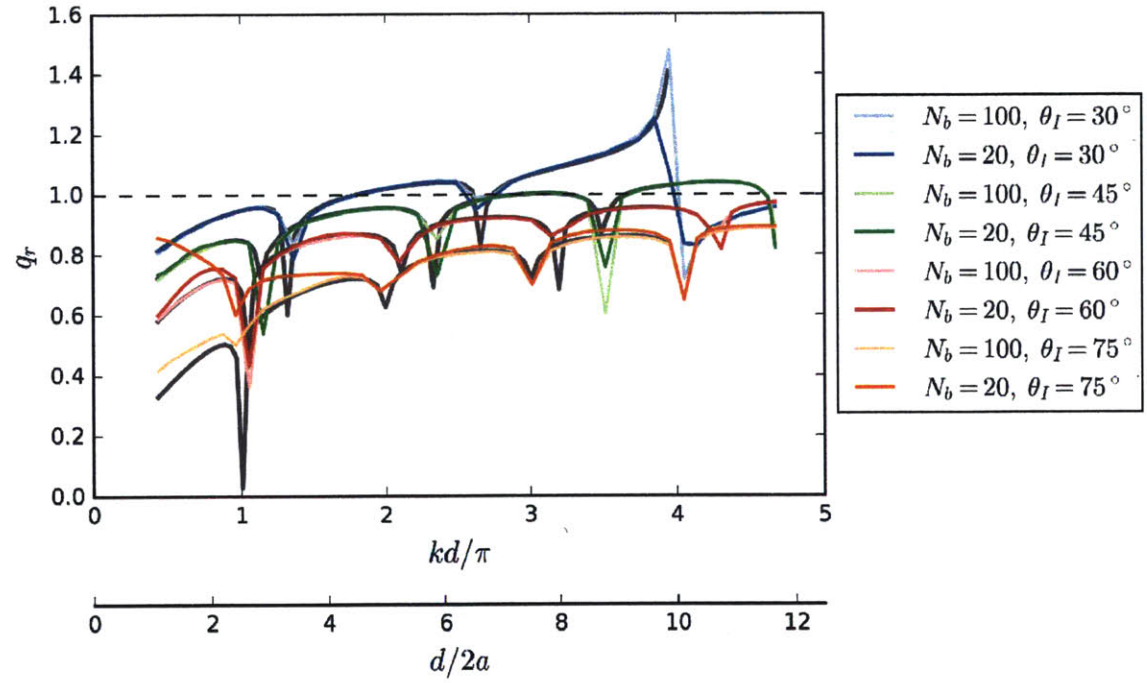

Figure 4.3: Comparison of the array gain q between arrays of different size as a function of body spacing for sub-resonant wavenumber $ka_<$ for $\theta_I = 30°, 45°, 60°, 75°$.

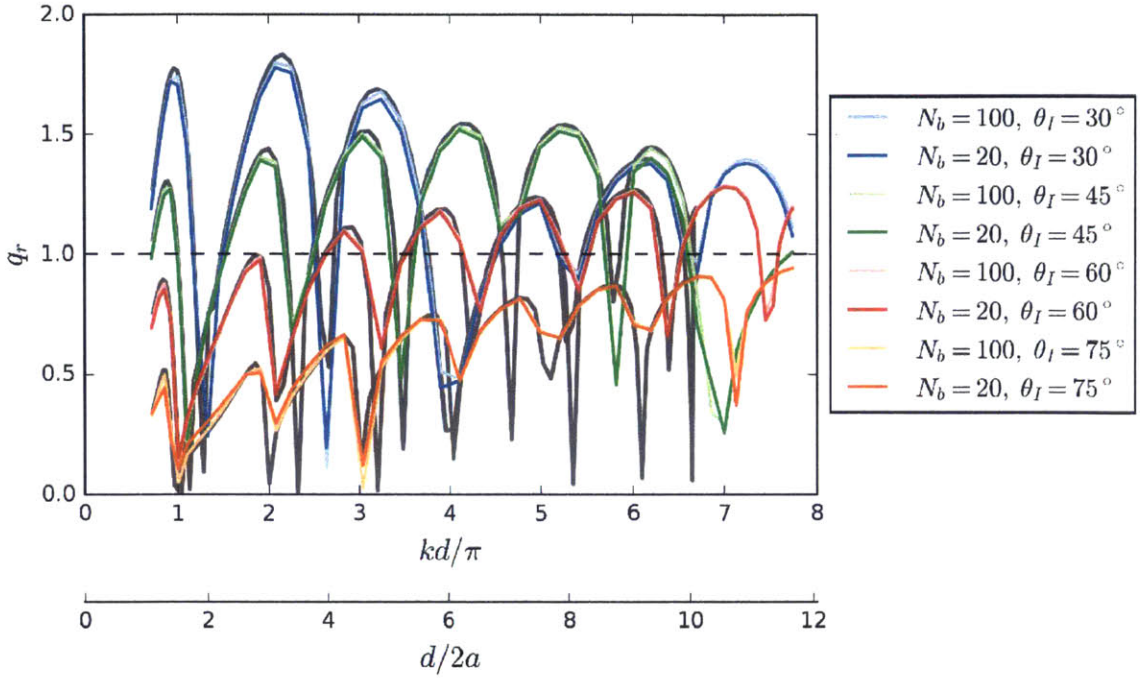

Figure 4.4: Comparison of the array gain q between arrays of different size as a function of body spacing for sup-resonant wavenumber $ka_>$ for $\theta_I = 30°, 45°, 60°, 75°$.

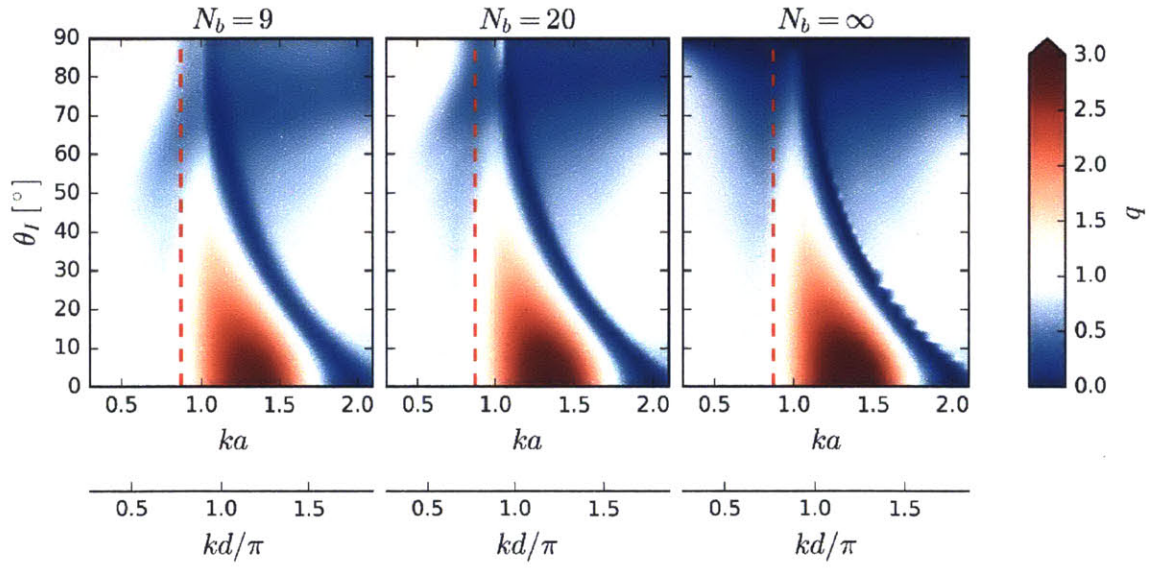

Figure 4.5: The contours of array gain q as a function of wavenumber ka and incoming angle θ_I for arrays with (a) $N_b = 9$ bodies, (b) $N_b = 20$ bodies, and (c) periodic array, all with spacing $d/2a = 1.40$.

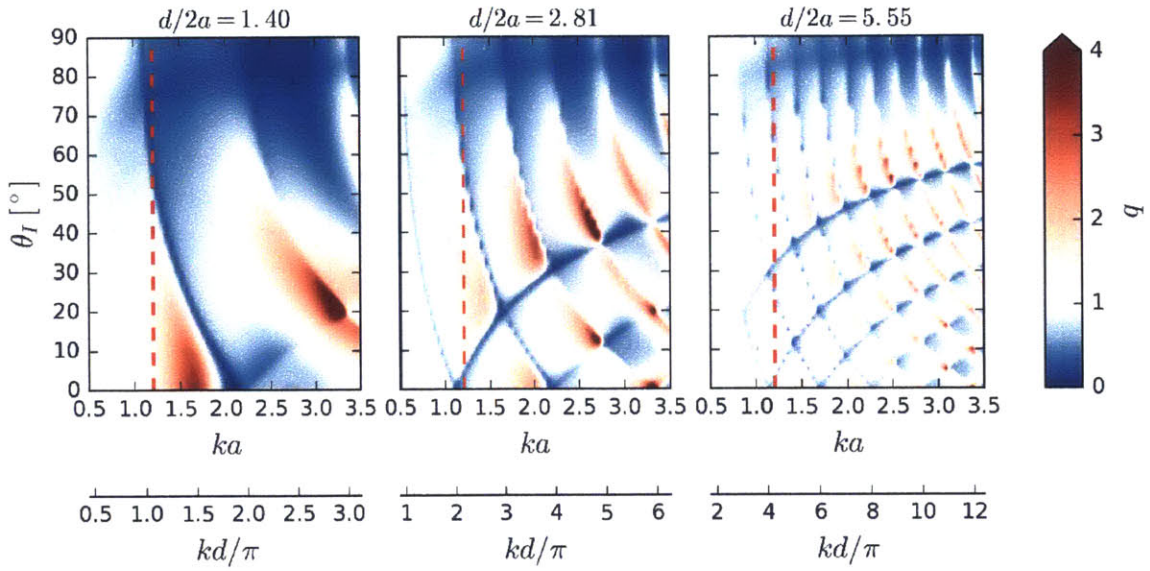

Figure 4.6: The contours of array gain q as a function of wavenumber ka and incoming angle θ_I for 20-body line array with uniform spacing (a) $d/2a = 5.55$, (b) $d/2a = 5.55$, and (c) $d/2a = 5.55$. The array is composed of larger truncated vertical cylinders ($a/h = 0.5$, $H/h = 0.2$)

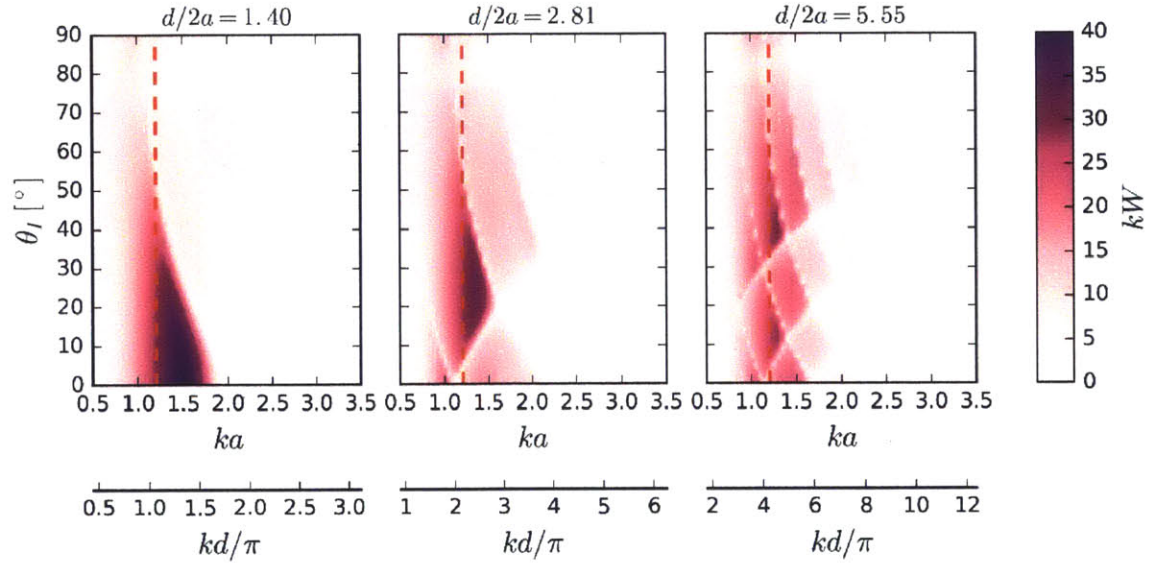

Figure 4.7: The contours of capture width kW as a function of wavenumber ka and incoming angle θ_I for 20-body line array with uniform spacing (a) $d/2a = 5.55$, (b) $d/2a = 5.55$, and (c) $d/2a = 5.55$. The array is composed of larger truncated vertical cylinders ($a/h = 0.5$, $H/h = 0.2$). Note that there is energy extraction below the resonant frequency, but at the same rate as for an isolated body.

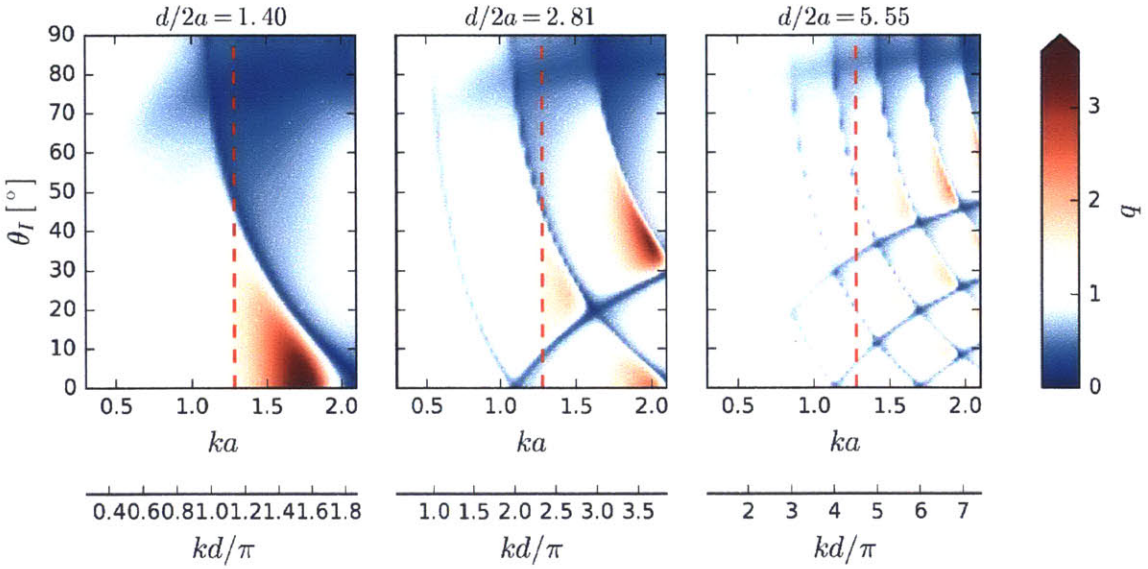

Figure 4.8: The contours of array gain q as a function of wavenumber ka and incoming angle θ_I for 20-body line array with uniform spacing (a) $d/2a = 5.55$, (b) $d/2a = 5.55$, and (c) $d/2a = 5.55$. The array is composed of truncated vertical cylinders with a smaller draft ($a/h = 0.3$, $H/h = 0.1$)

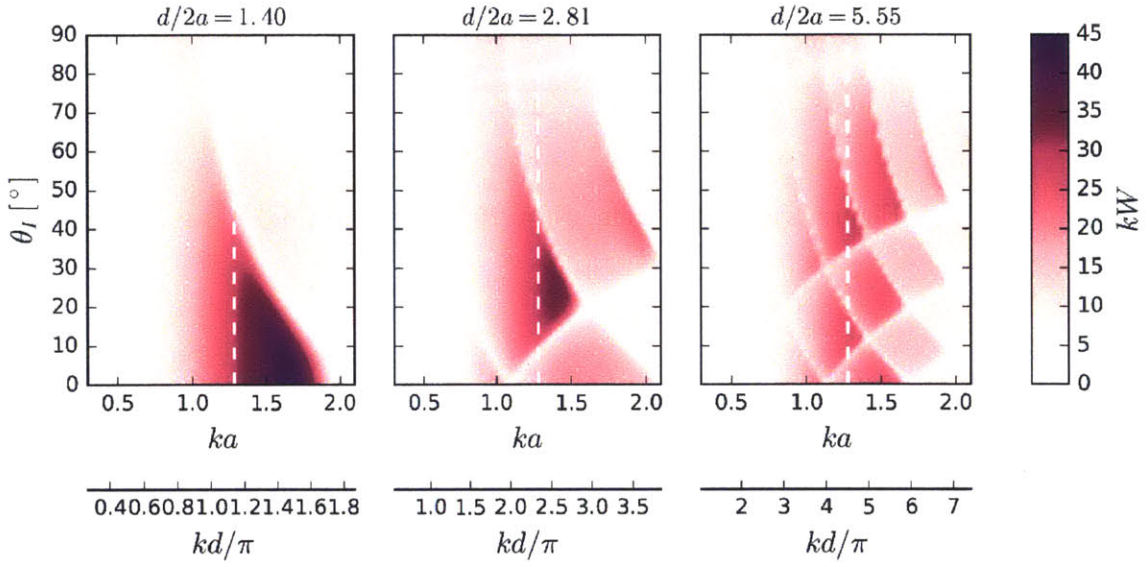

Figure 4.9: The contours of capture width kW as a function of wavenumber ka and incoming angle θ_I for 20-body line array with uniform spacing (a) $d/2a = 5.55$, (b) $d/2a = 5.55$, and (c) $d/2a = 5.55$. The array is composed of truncated vertical cylinders with a smaller draft ($a/h = 0.3$, $H/h = 0.1$). Note that there is energy extraction below the resonant frequency, but at the same rate as for an isolated body.

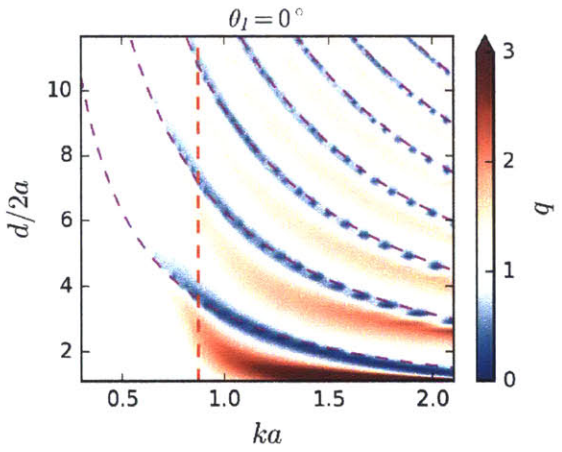

Figure 4.10: Array gain, $N_b = 25$ (cf. Figure 4.6a)

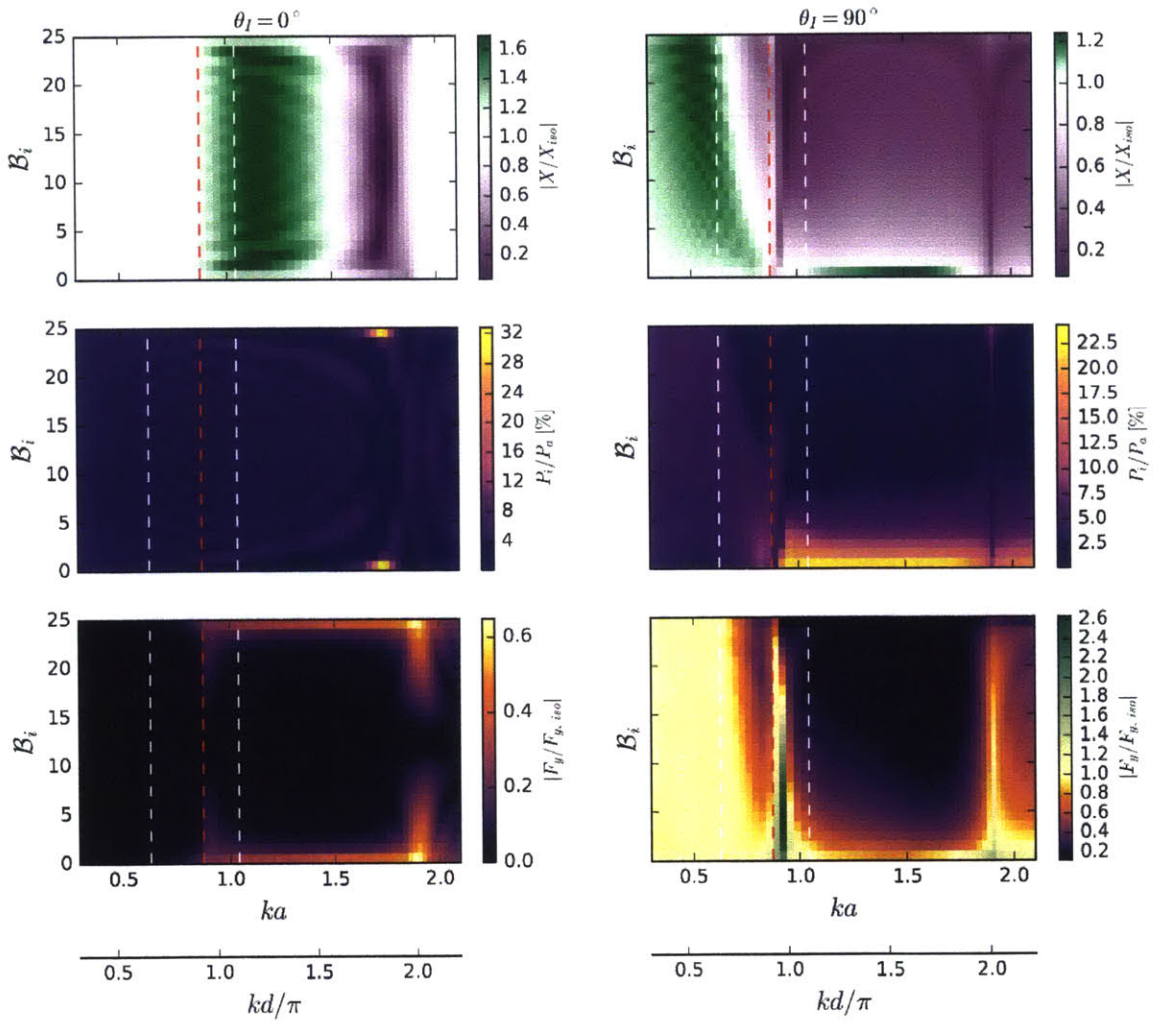

Figure 4.11: Detailed body performance plot for a 25-body array with $d/2a = 1.66$ for $\theta_I = 0°$ (left column) and $\theta_I = 90°$ (right column). For any wavenumber ka, the performance of body $\mathcal{B}_i$ is plotted along the y-axis in color patches according to the corresponding performance colorbar. The first row shows the amplification factor of the body motion amplitude, the second the percentage of the extracted power by a body, and the third row the amplification factor of the inline force. Red dashed line corresponds to the resonant wavenumber ka_r, and the white dashed side-lines to $ka_<$ and $ka_>$.

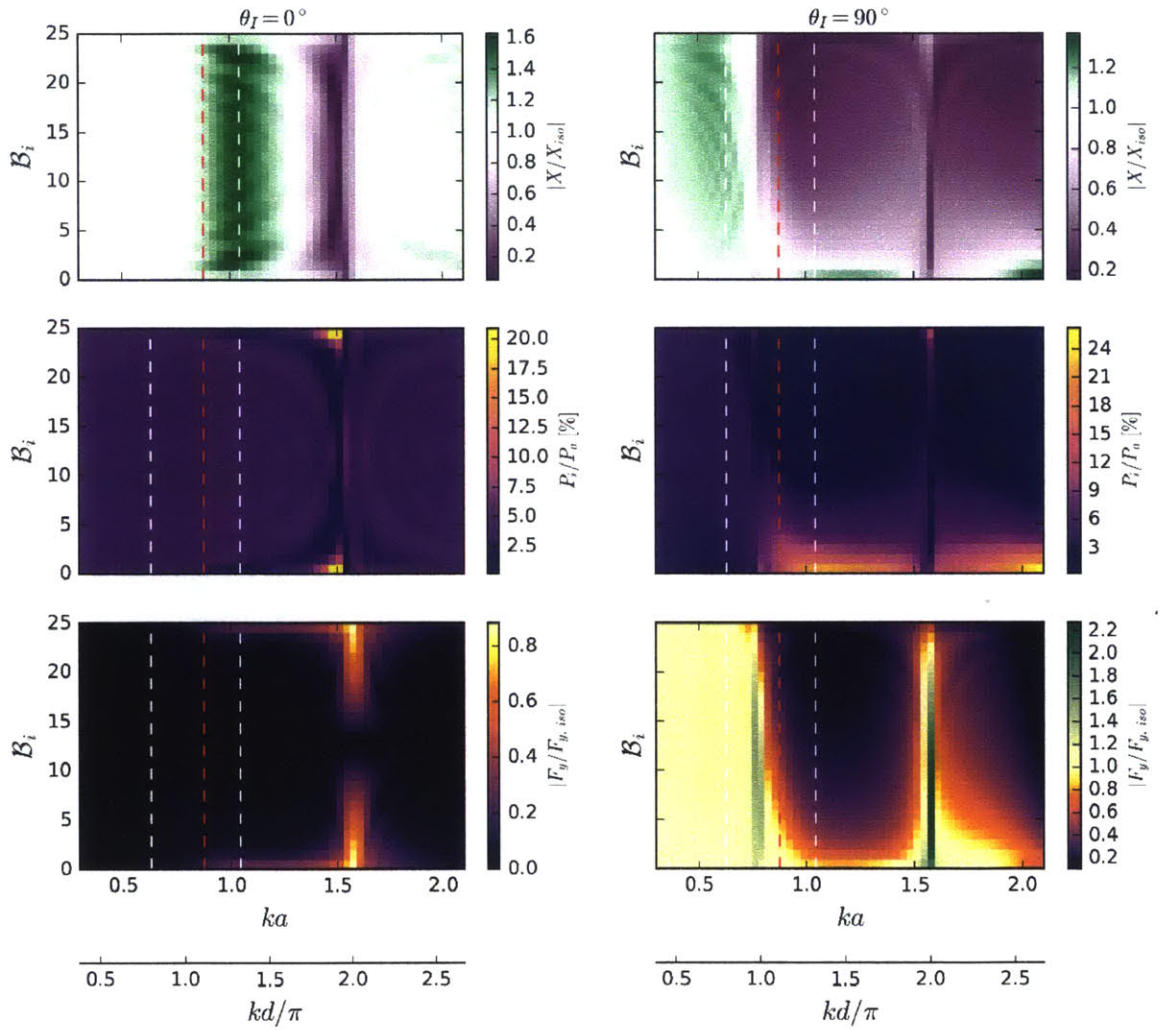

Figure 4.12: Detailed body performance plot for a 25-body array with $d/2a = 2.0$ for $\theta_I = 0°$ (left column) and $\theta_I = 90°$ (right column). See Figure 4.11 for the description of the plots.

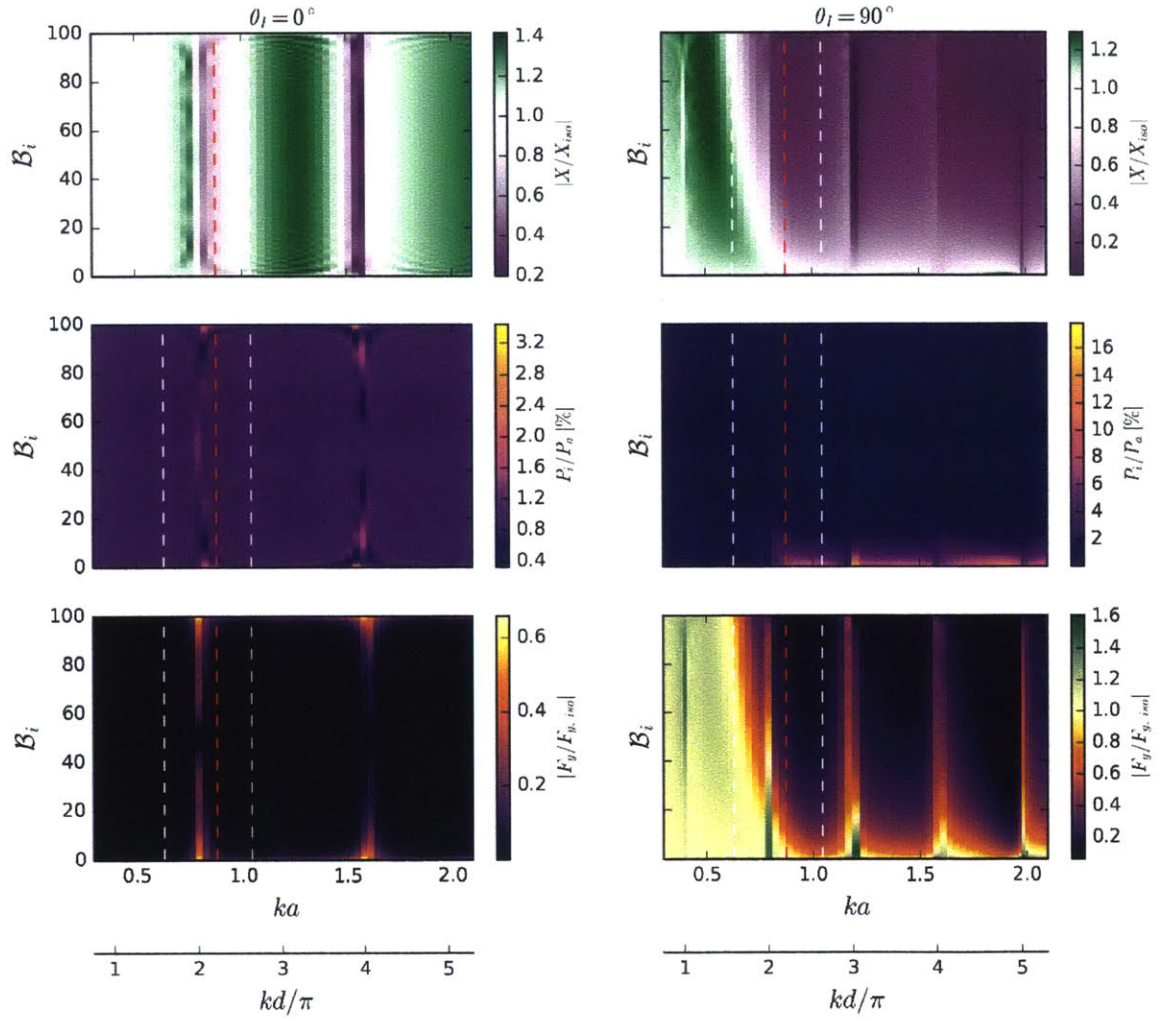

Figure 4.13: Detailed body performance plot for a 100-body array with $d/2a = 4.0$ for $\theta_I = 0°$ (left column) and $\theta_I = 90°$ (right column). See Figure 4.11 for the description of the plots.

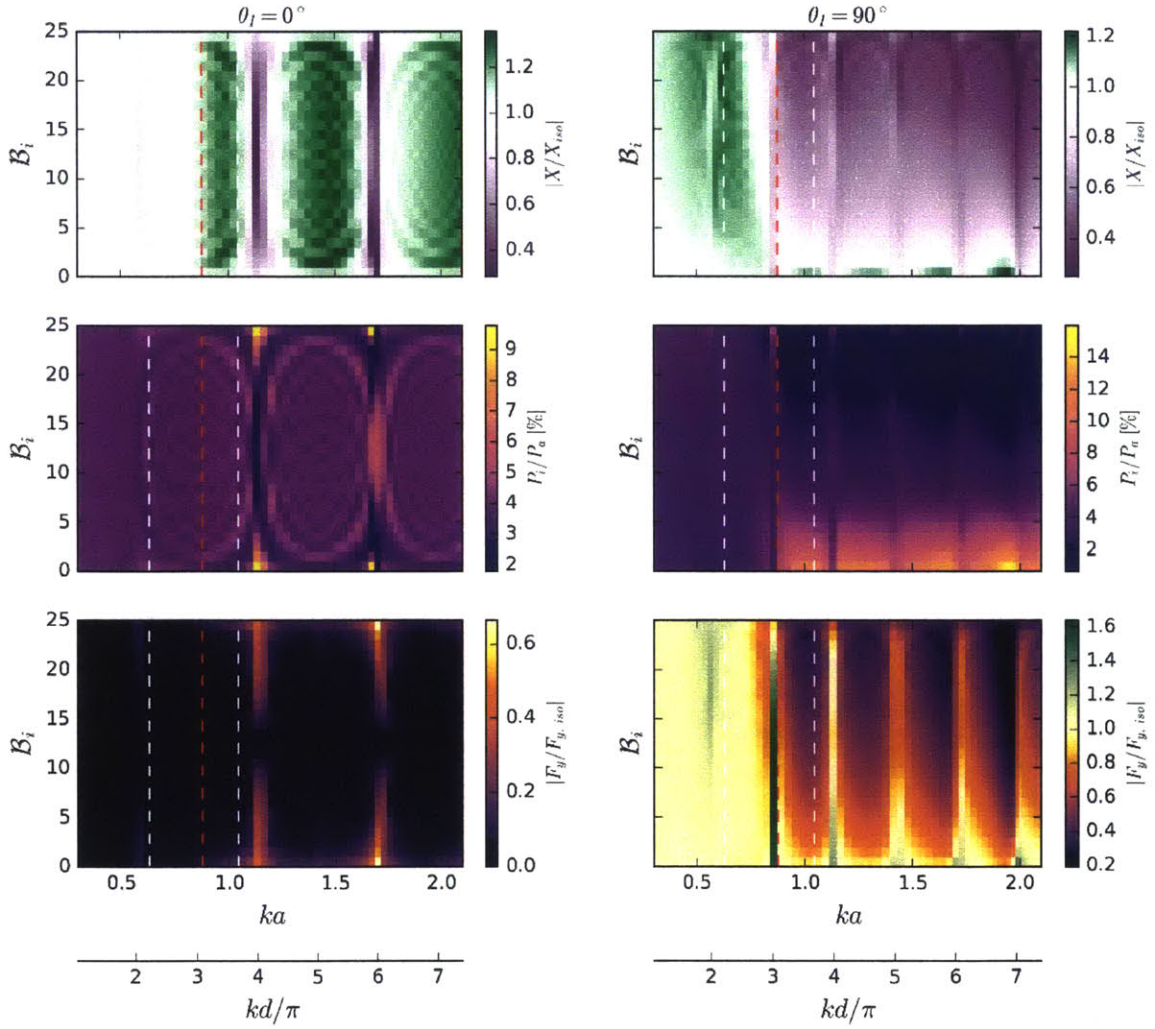

Figure 4.14: Detailed body performance plot for a 25-body array with $d/2a = 5.55$ for $\theta_I = 0°$ (left column) and $\theta_I = 90°$ (right column). See Figure 4.11 for the description of the plots.

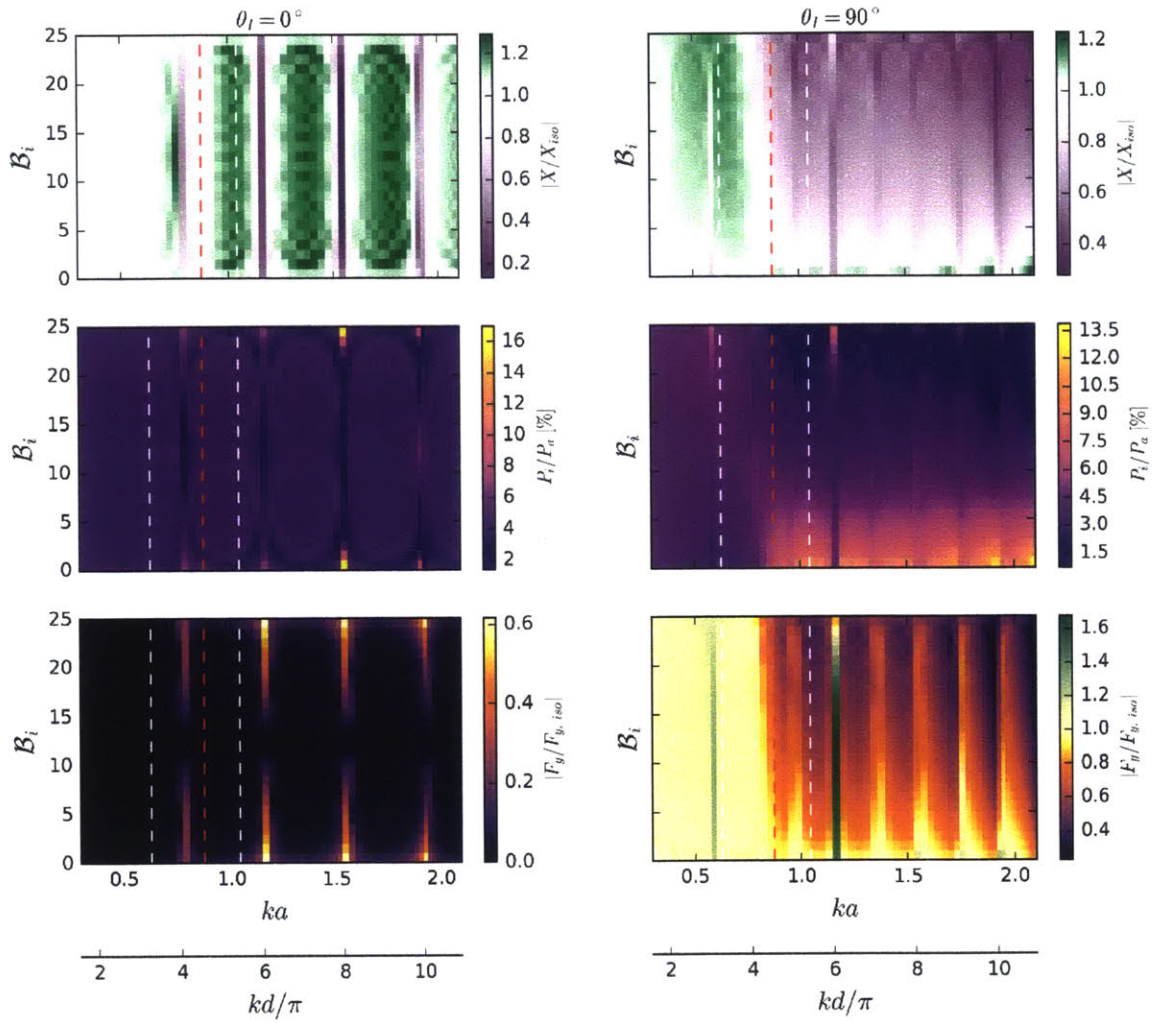

Figure 4.15: Detailed body performance plot for a 25-body array with $d/2a = 8.2$ for $\theta_I = 0°$ (left column) and $\theta_I = 90°$ (right column). See Figure 4.11 for the description of the plots.

Analysis of Line Arrays with Linearly Varying Spacing

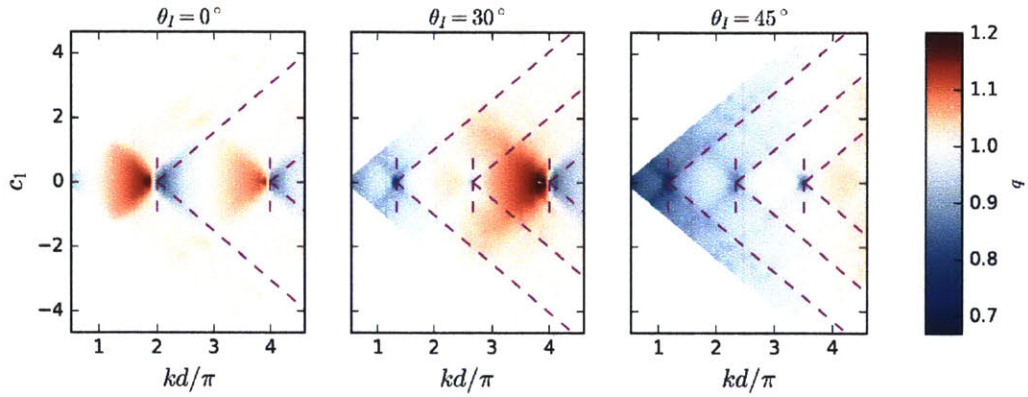

(a) $ka = ka_<$

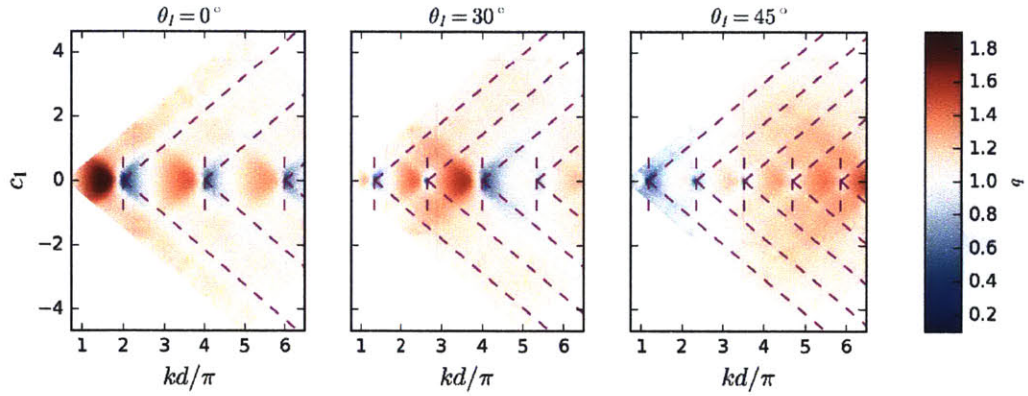

(b) $ka = ka_r$

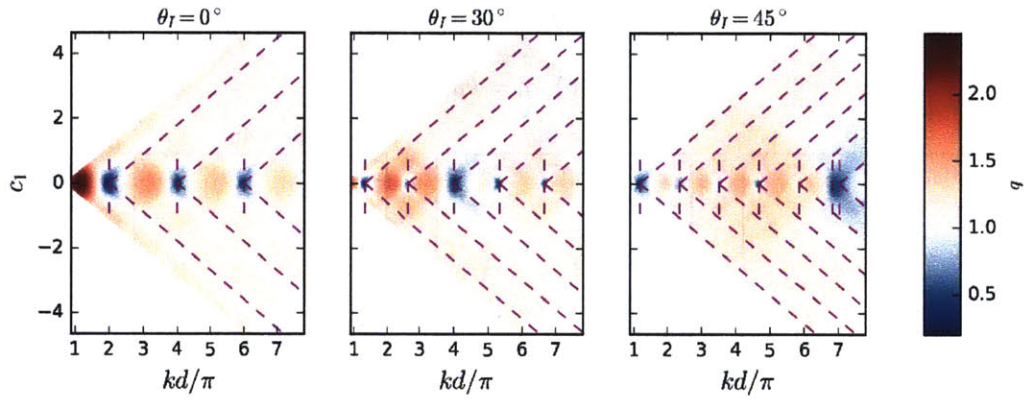

(c) $ka = ka_>$

Figure 4.16: Array gain q for 20-body arrays with linear variation in spacing between the bodies. The rays emanating from Rayleigh points correspond to arrays where the minimal spacing between the end two bodies is equal to the Rayleigh wavelength. Note that the changes in kd/π correspond to changes in d as the wavenumber is constant for each plot.

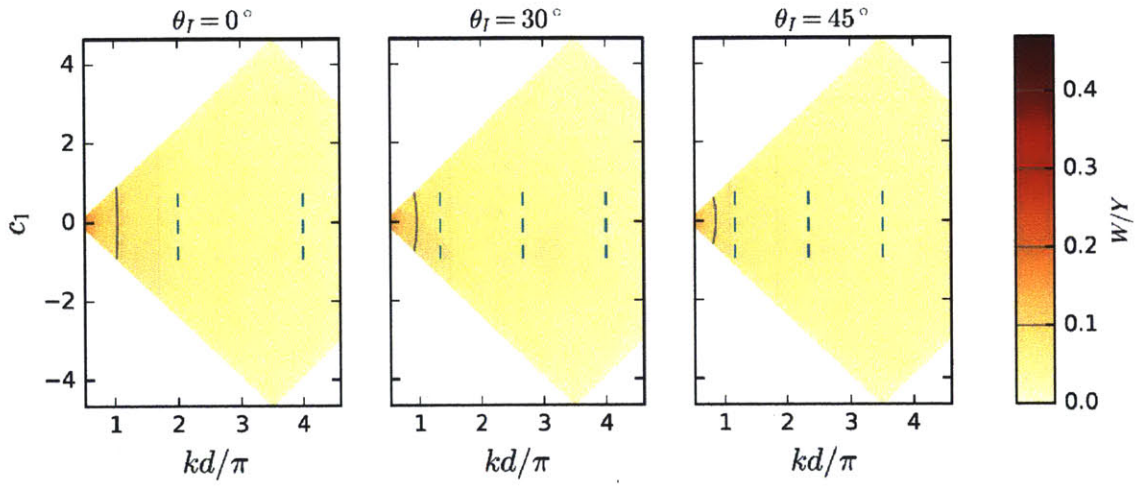

(a) $ka = ka_<$

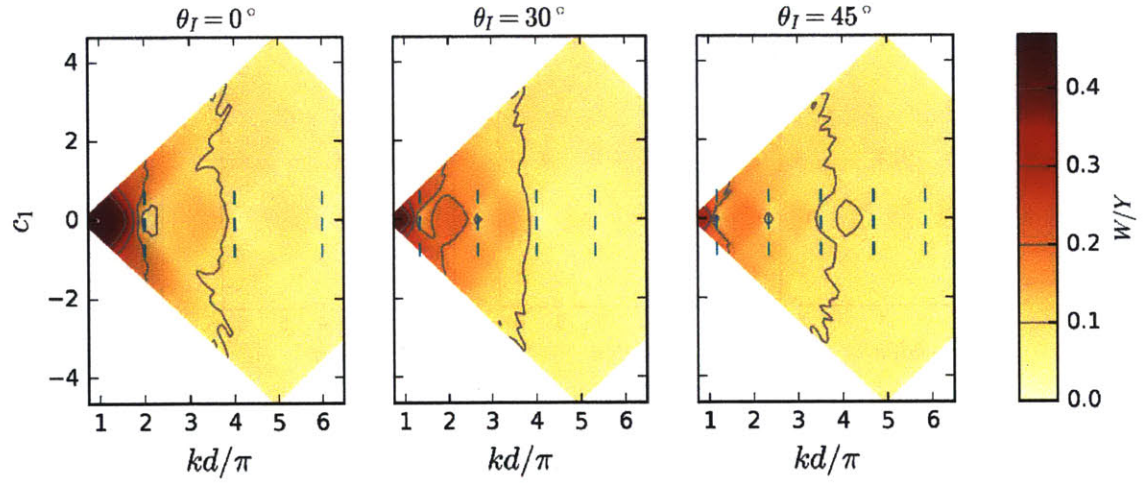

(b) $ka = ka_r$

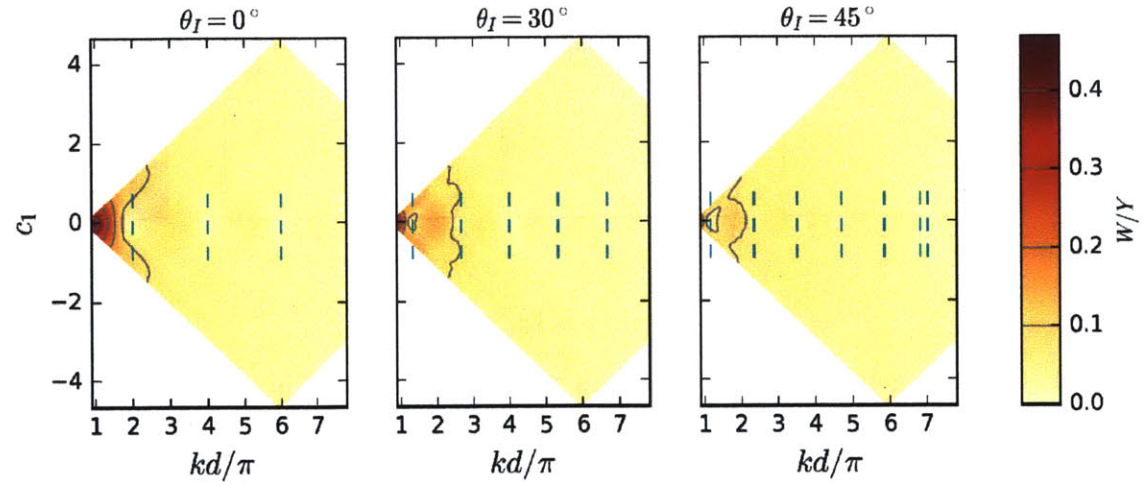

(c) $ka = ka_>$

Figure 4.17: Capture width W_a normalized by the array extent Y in the y-direction. The values are very similar to that for uniform and periodic arrays, closer spaced arrays are preferred in terms of W_a/Y, and there is very little dependency on the sign of c_1. Note that the changes in kd/π correspond to changes in d as the wavenumber is constant for each plot.

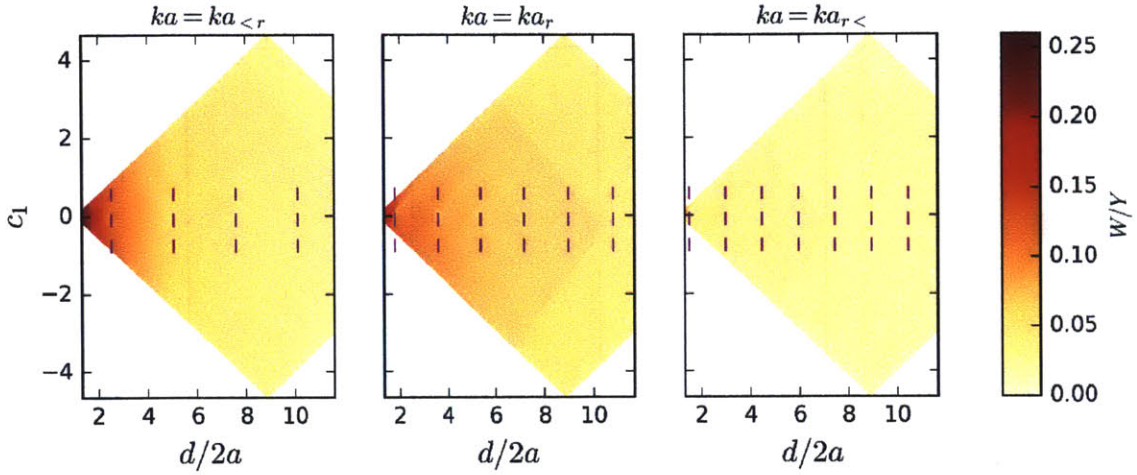

Figure 4.18: Capture width W normalized by array extent Y for $\theta_I = 90°$. Note that the changes in kd/π correspond to changes in d as the wavenumber is constant for each plot.

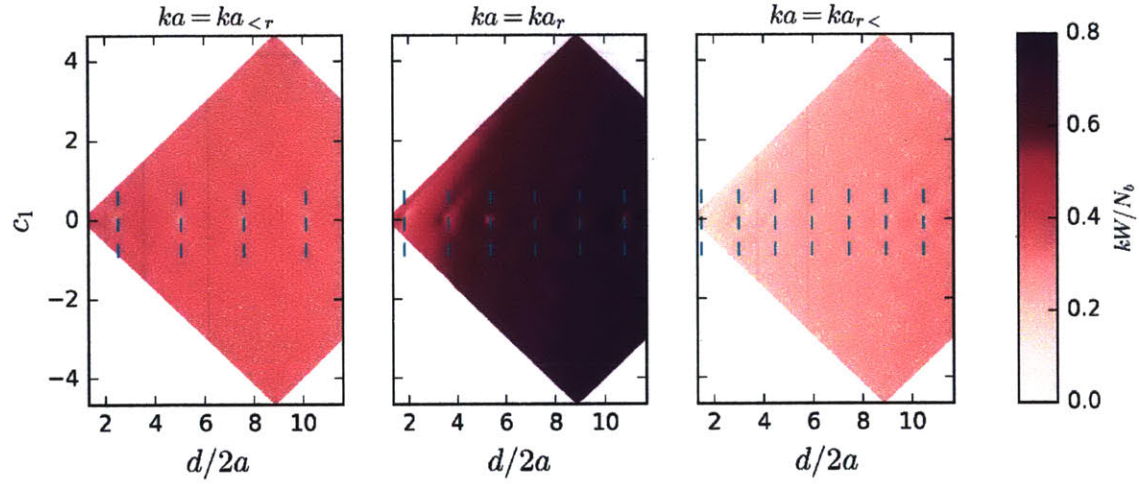

Figure 4.19: Nondimensional capture width kW/N_b for $\theta_I = 90°$ for 20-body arrays with linear variation in spacing between the bodies.

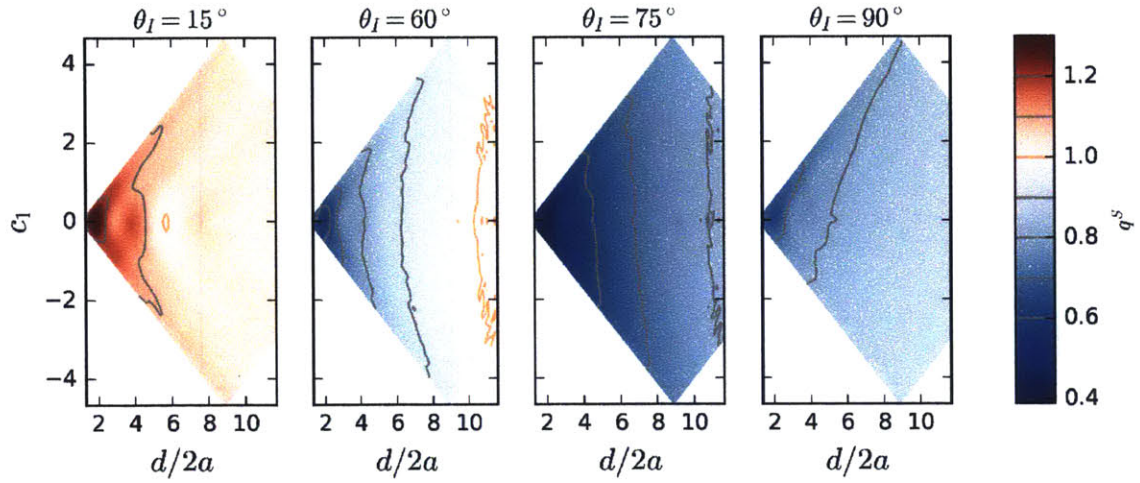

Figure 4.20: Spectral array gain q^S for 20-body arrays with linear variation in spacing between the bodies.

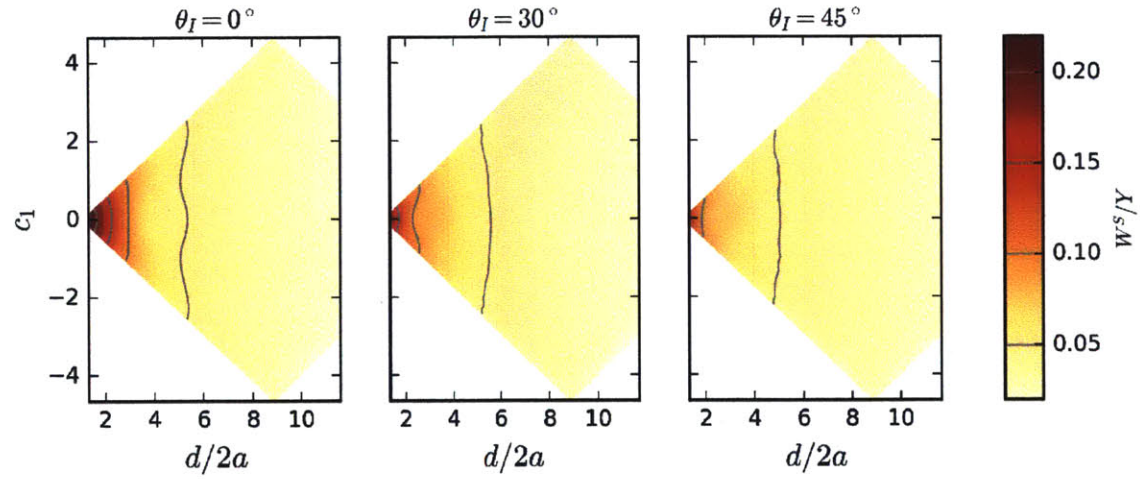

Figure 4.21: Spectral array gain W_a^S normalized by array extent in y-direction for 20-body arrays with linear variation in spacing between the bodies.

D.1.1 Analysis of Line Arrays with Quadratically Varying Spacing

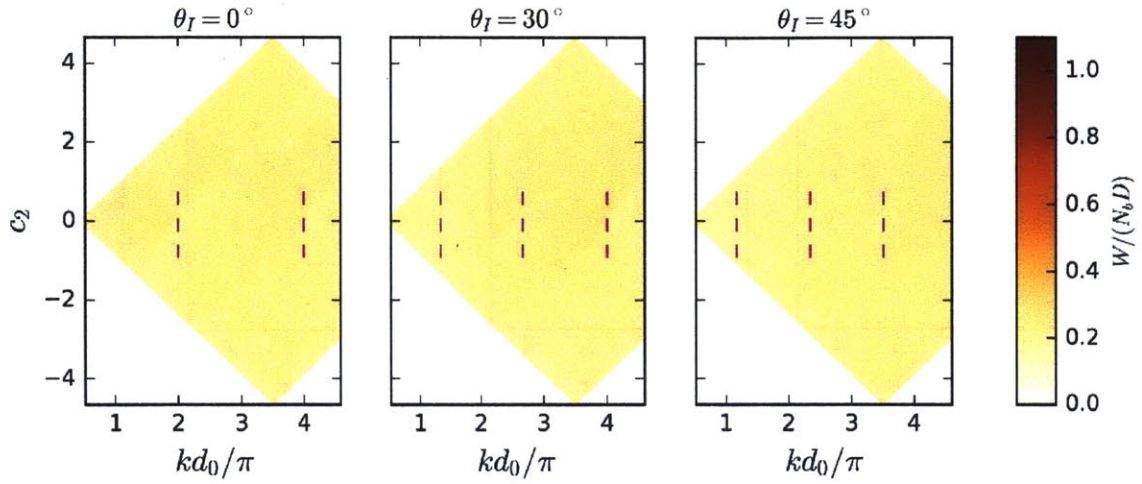

(a) $ka = ka_<$

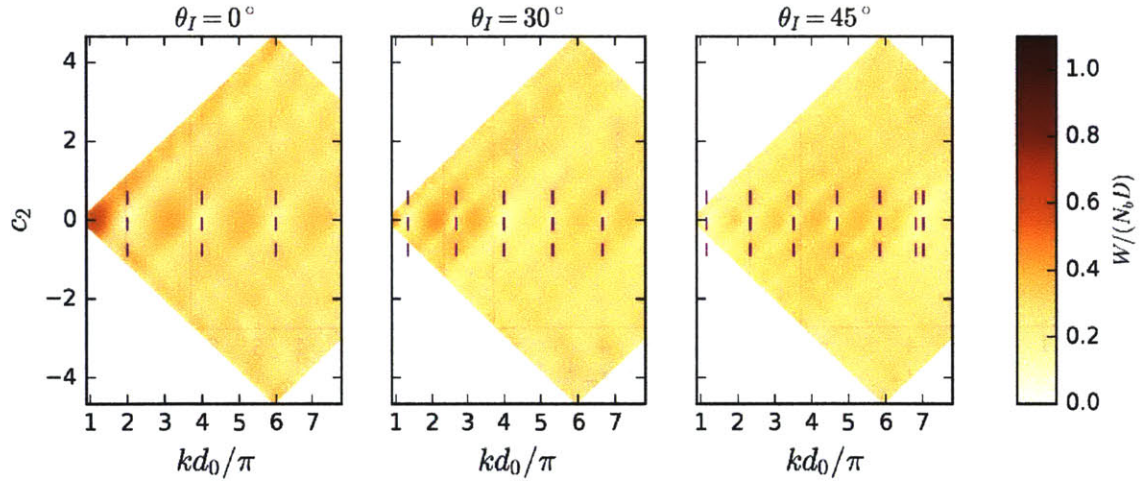

(b) $ka = ka_>$

Figure 4.22: Normalized capture width $W/N_b D$. Note that the changes in kd_0/π correspond to changes in d_0 as the wavenumber is constant for each plot.

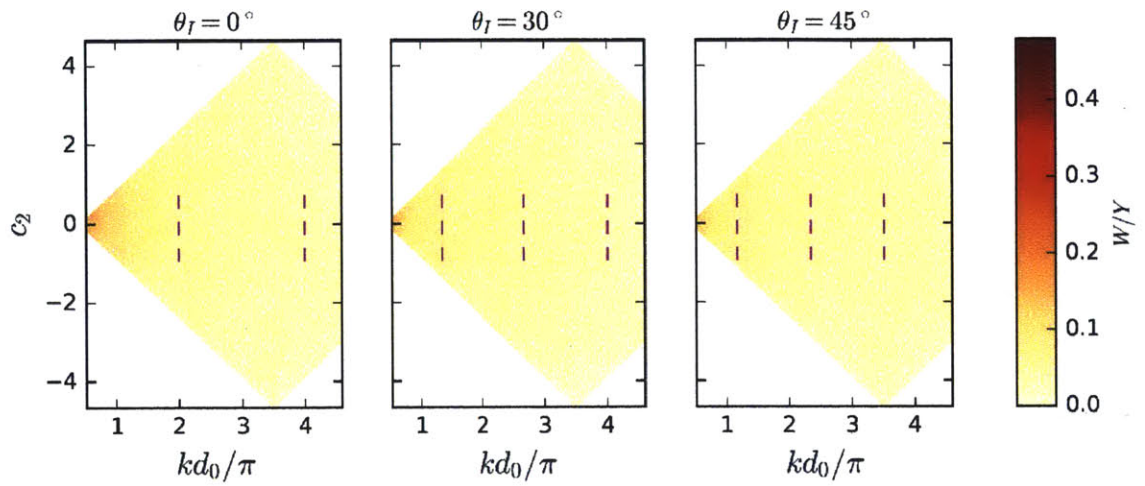

(a) $ka = ka_<$

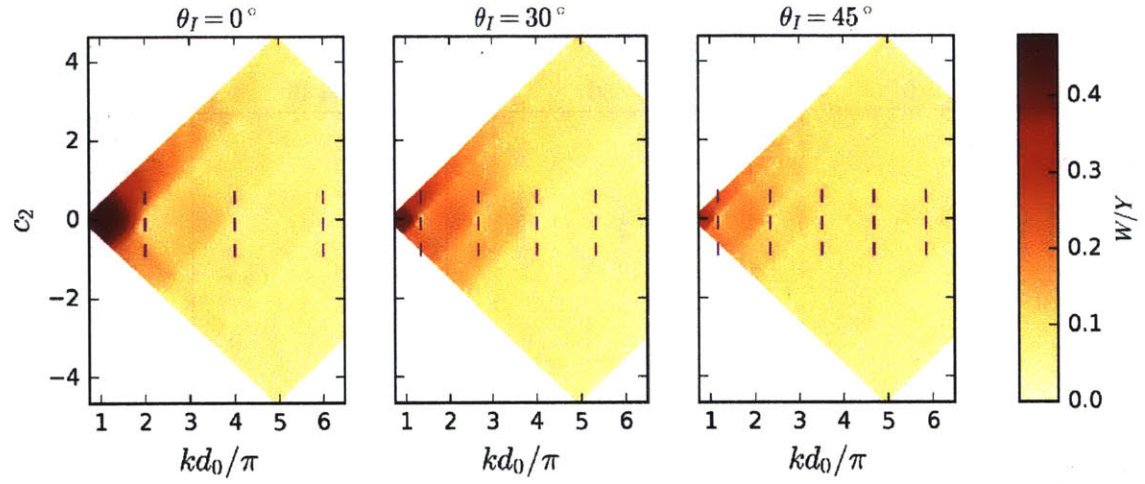

(b) $ka = ka_r$

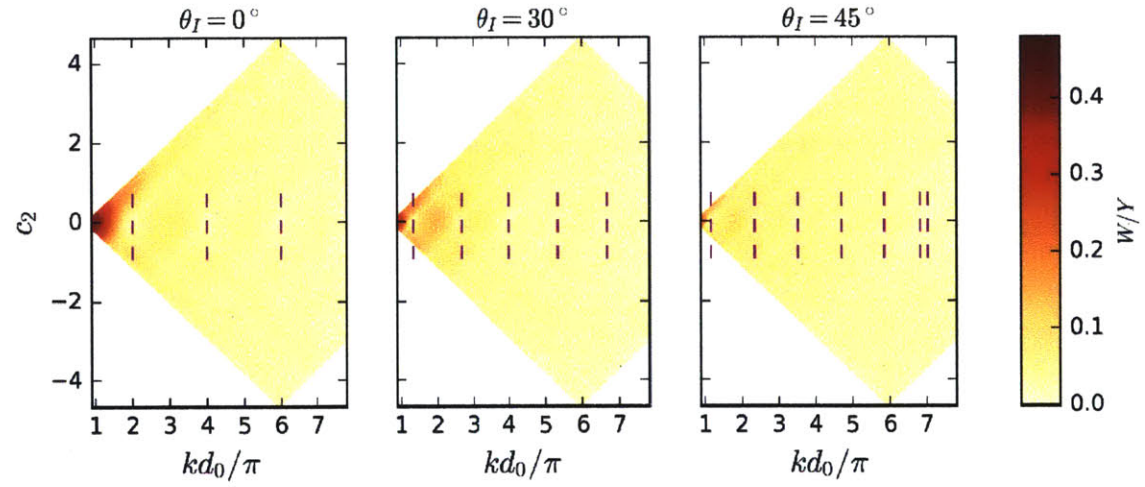

(c) $ka = ka_>$

Figure 4.23: Capture width W normalized by the array extent Y. Note that the changes in kd_0/π correspond to changes in d_0 as the wavenumber is constant for each plot.

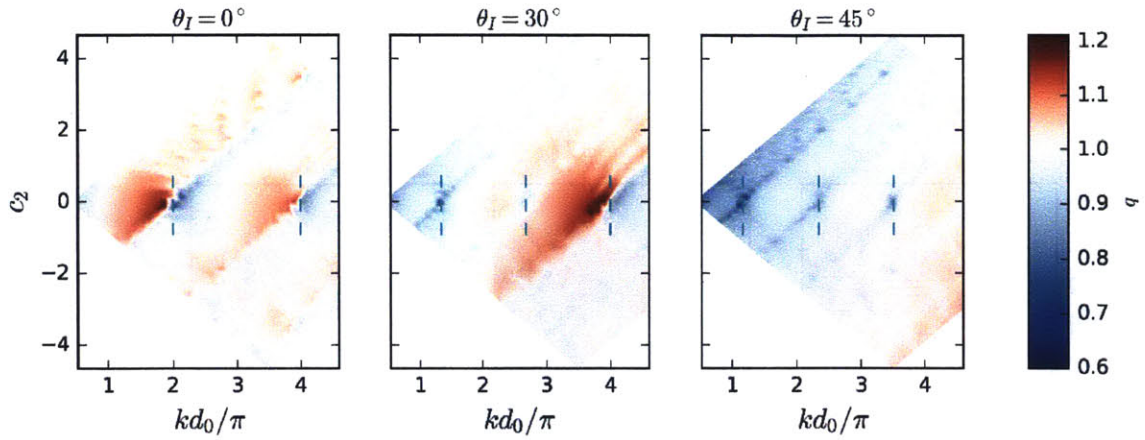

(a) $ka = ka_<$

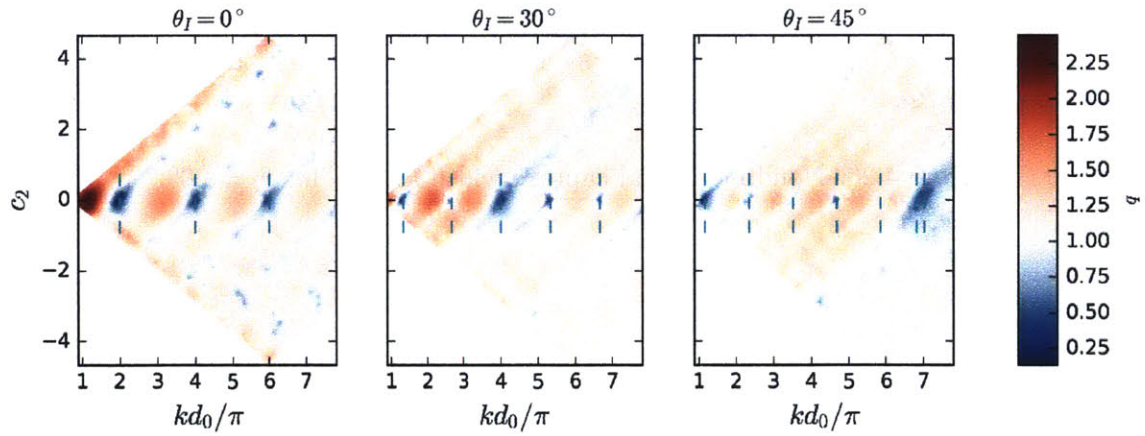

(b) $ka = ka_>$

Figure 4.24: Array gain q. Note that the changes in kd_0/π correspond to changes in d_0 as the wavenumber is constant for each plot.

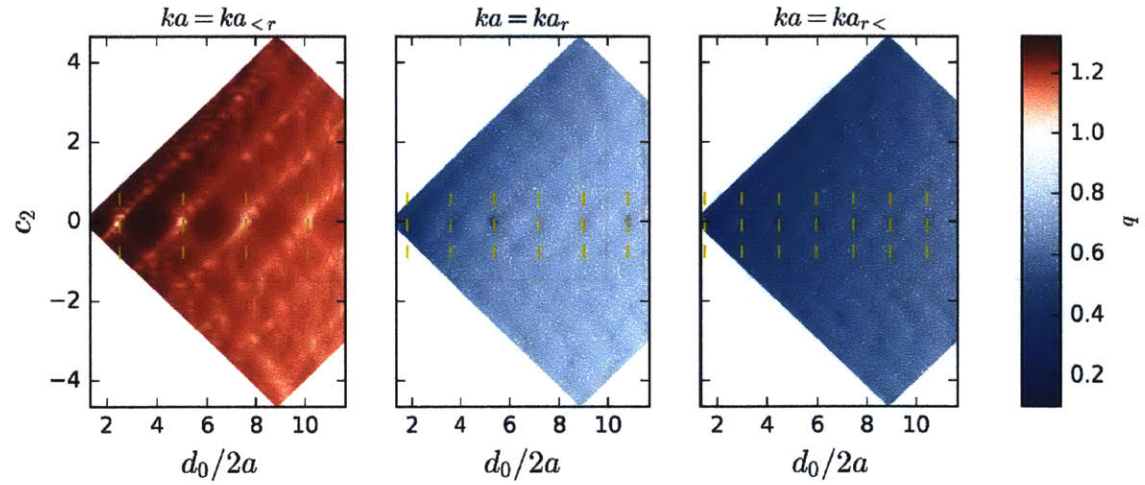

Figure 4.25: Array gain q for $\theta_I = 90°$.

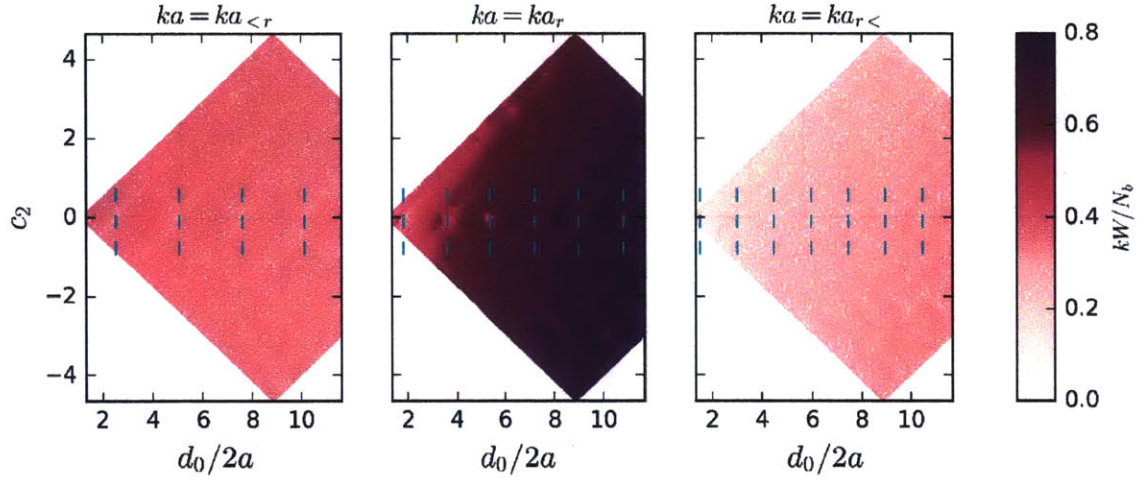

Figure 4.26: Nondimensional capture width kW/N_b for $\theta_I = 90°$.

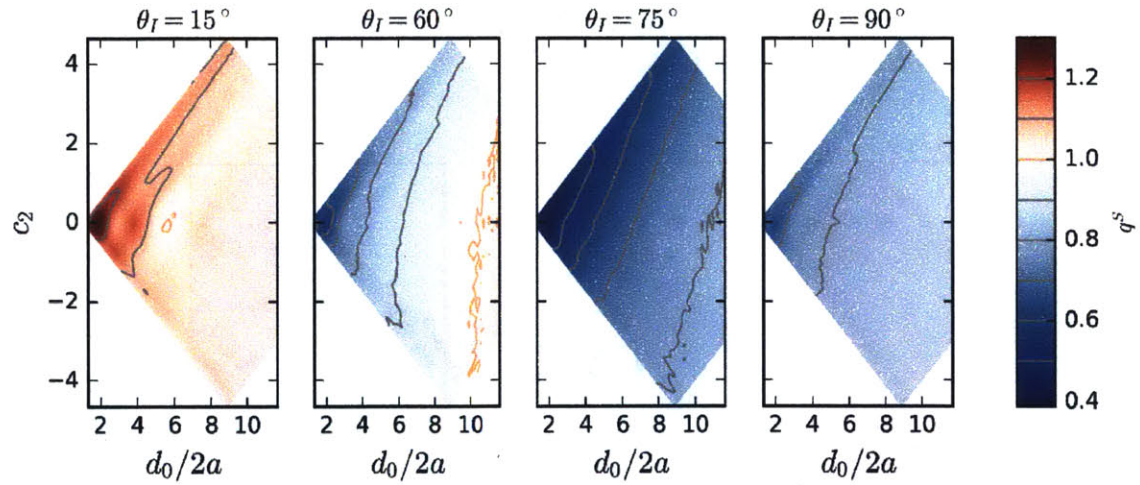

Figure 4.27: Spectral array gain q^S.

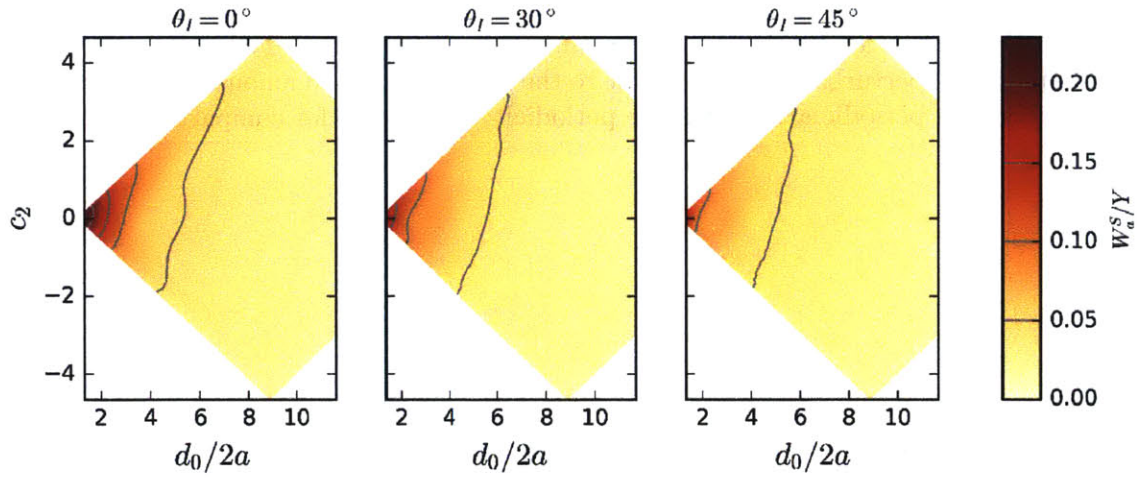

Figure 4.28: Spectral array gain W_a^S normalized by array extent in y-direction.

D.1.2 Analysis of Line Arrays with Random Spacing

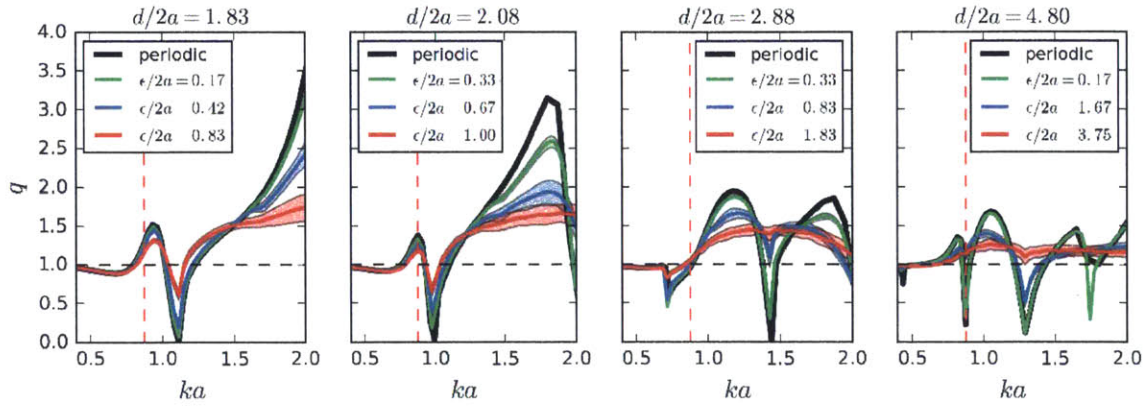

Figure 4.29: Array gain q of line arrays with different amount of random perturbation, for two different average spacings d; incoming angle $\theta = 30°$. The results show the mean $\pm$ 1 standard deviation for three different perturbation distributions. For both spacings the largest amount of perturbation is very close to the maximal allowed amount based on (4.36). Performance of a periodic array with the periodicity d is shown for comparison.

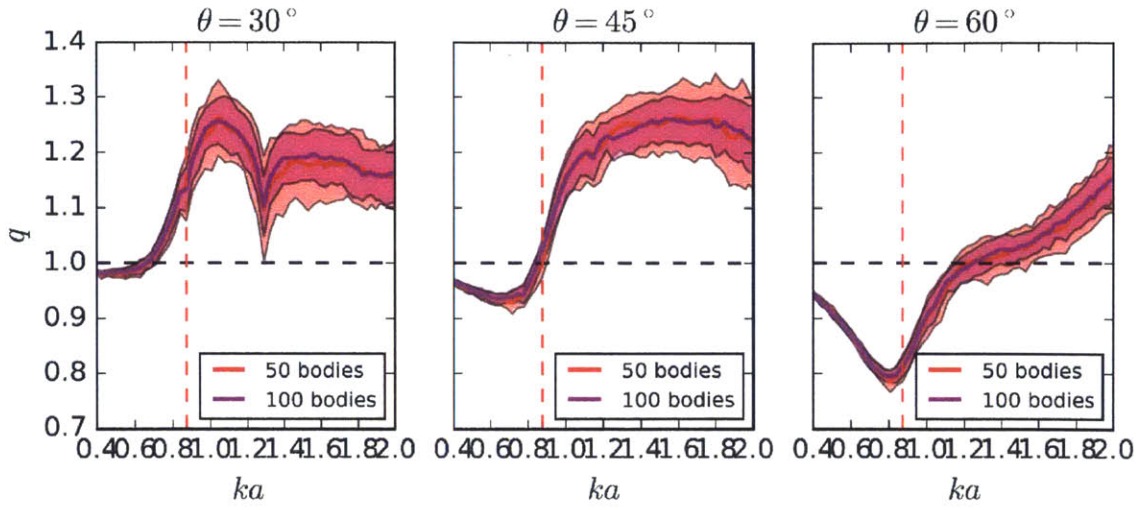

Figure 4.30: Comparison of the mean and standard deviation of array gain q for 50- and 100-body line arrays, for $d/2a = 4.8$. The results show the mean $\pm$ 1 standard deviation for the maximum allowed perturbation.

D.1.3 Analysis of Rectangular Arrays with Uniform Spacing

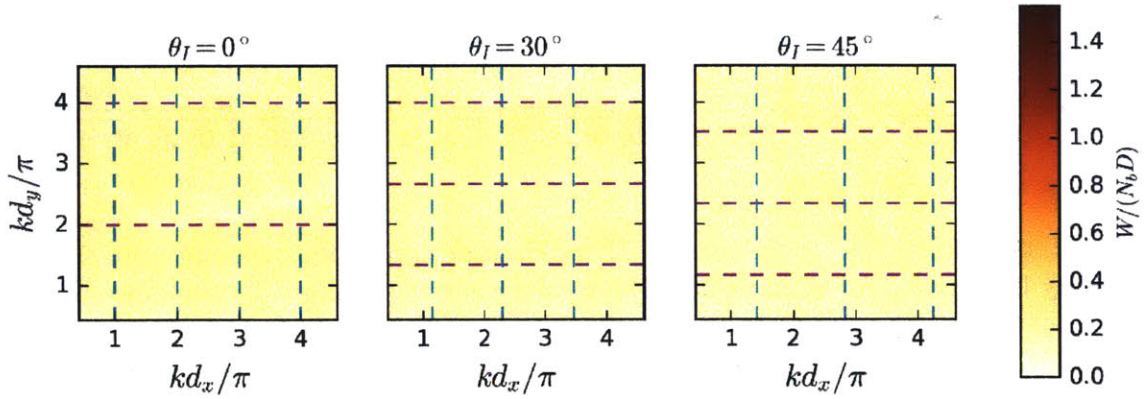

(a) $ka = ka_<$

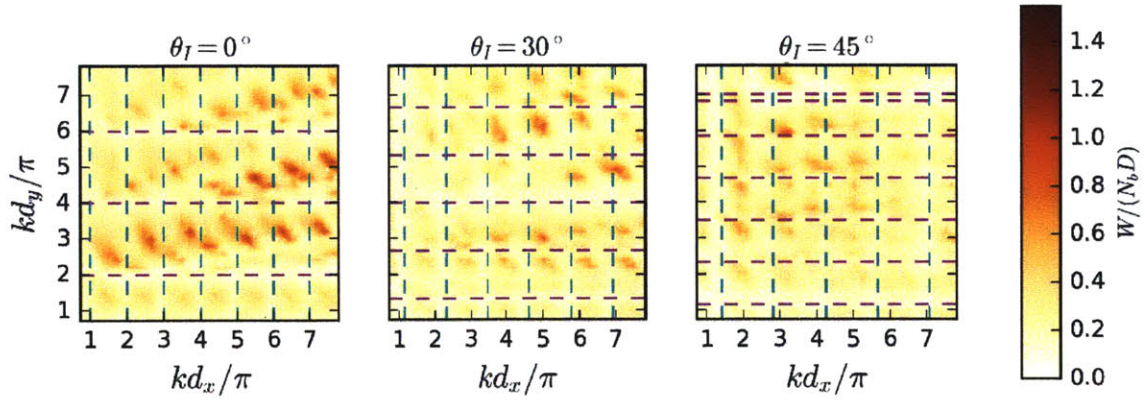

(b) $ka = ka_>$

Figure 4.31: Normalized capture width W_a/N_bD for off-resonant wavenumbers and different incoming angles θ_I. The colorbar is matched to the W_a/N_bD at resonant wavenumber ka_r, Figure 4.44. Note that the changes in kd_x/π and kd_y/π correspond to changes in d_x and d_y as the wavenumber is constant for each plot.

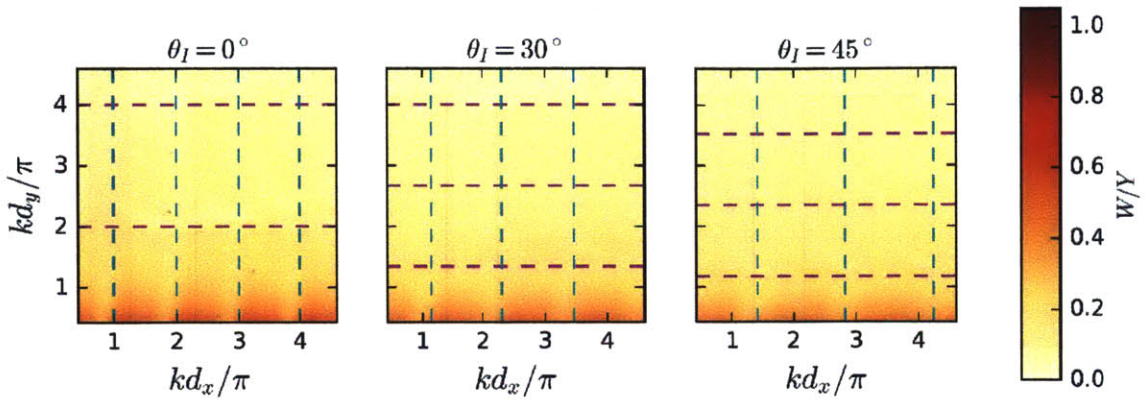

(a) $ka = ka_<$

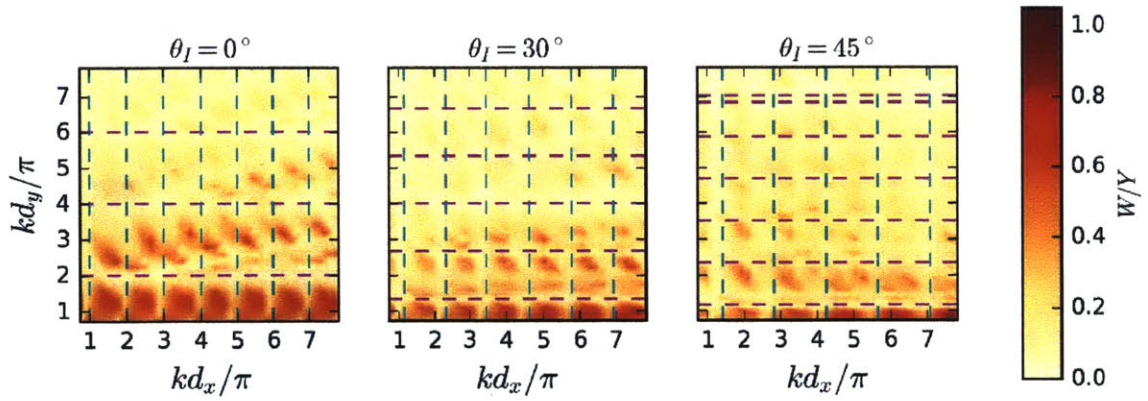

(b) $ka = ka_>$

Figure 4.32: Capture width W_a normalized by the array extent Y in y-direction for off-resonant wavenumbers and three incoming angles. The dashed lines represent Rayleigh-related spacings (magenta), and Bragg-related (green) spacings. Note that the changes in kd_x/π and kd_y/π correspond to changes in d_x and d_y as the wavenumber constant is for each plot.

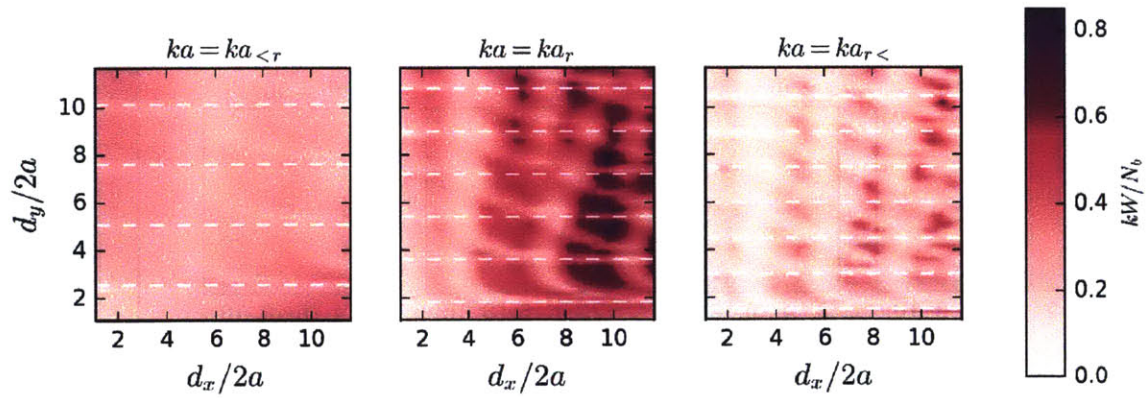

Figure 4.33: Nondimensional capture width kW/N_b for $\theta_I = 90°$ for three wavenumbers.

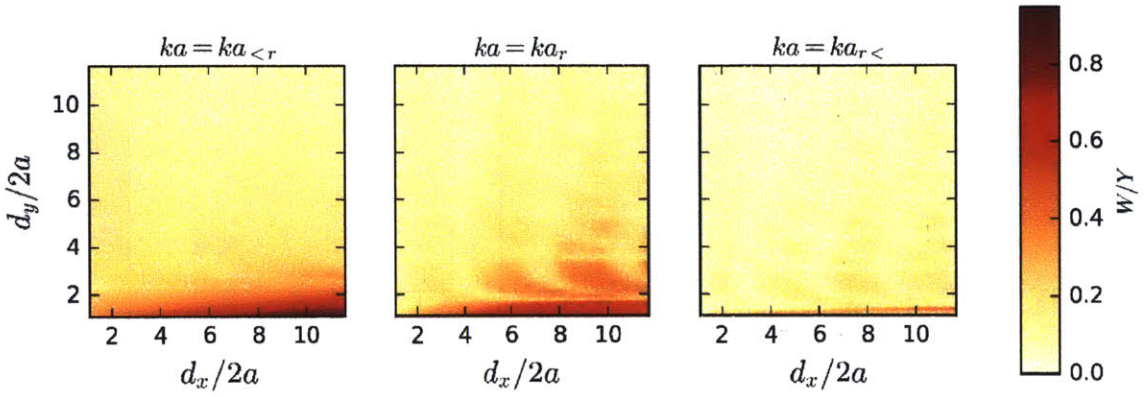

Figure 4.34: Capture width W_a normalized by array extent Y for $\theta_I = 90°$ for three wavenumbers.

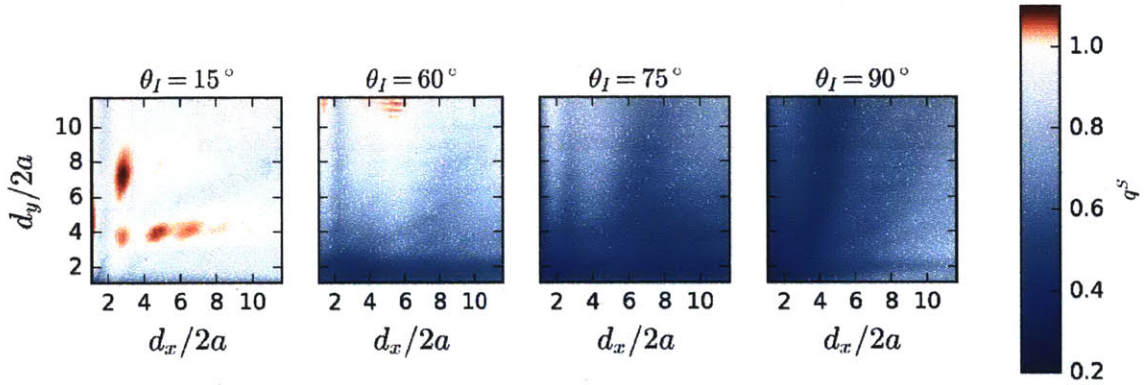

Figure 4.35: Spectral array gain q^S.

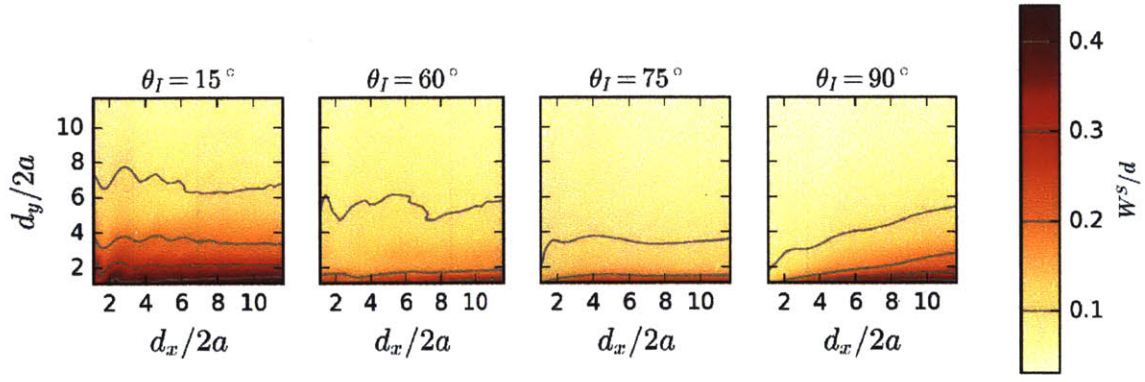

Figure 4.36: Spectral array gain q^S.

D.1.4 Analysis of Rectangular Arrays with Staggered Rows

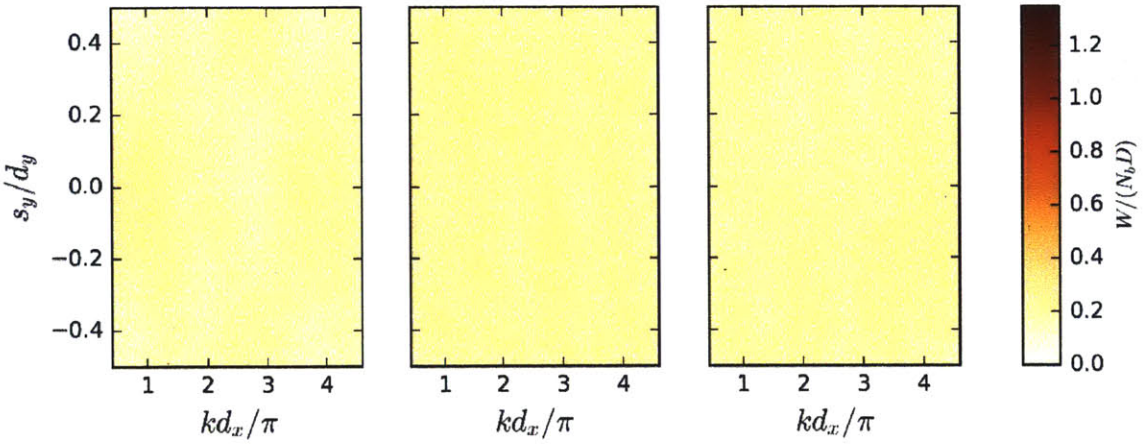

(a) $ka = ka_<$

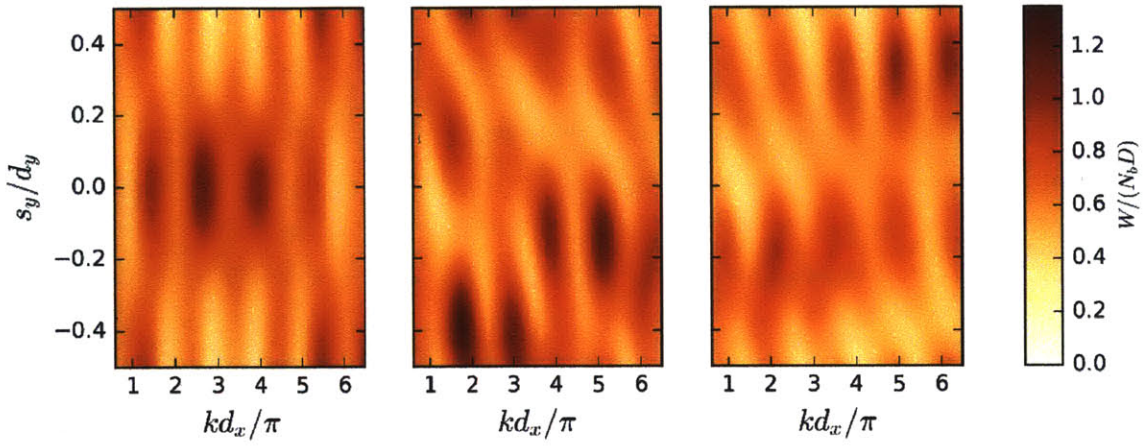

(b) $ka = ka_r$

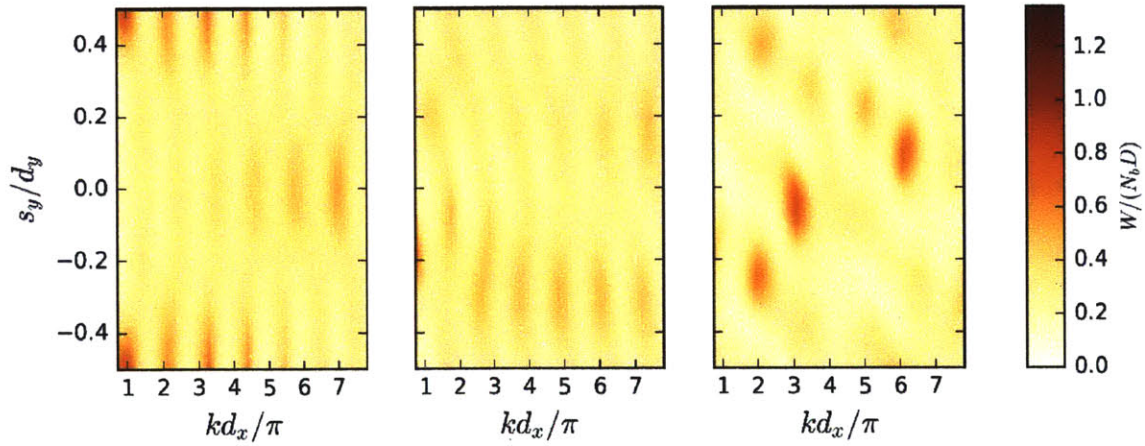

(c) $ka = ka_>$

Figure 4.37: Normalized capture width W_a/N_bD for three characteristic wavenumbers and different incoming angles θ_I. Note that the changes in kd_x/π corresponds to changes in d_x as the wavenumber is constant for each plot.

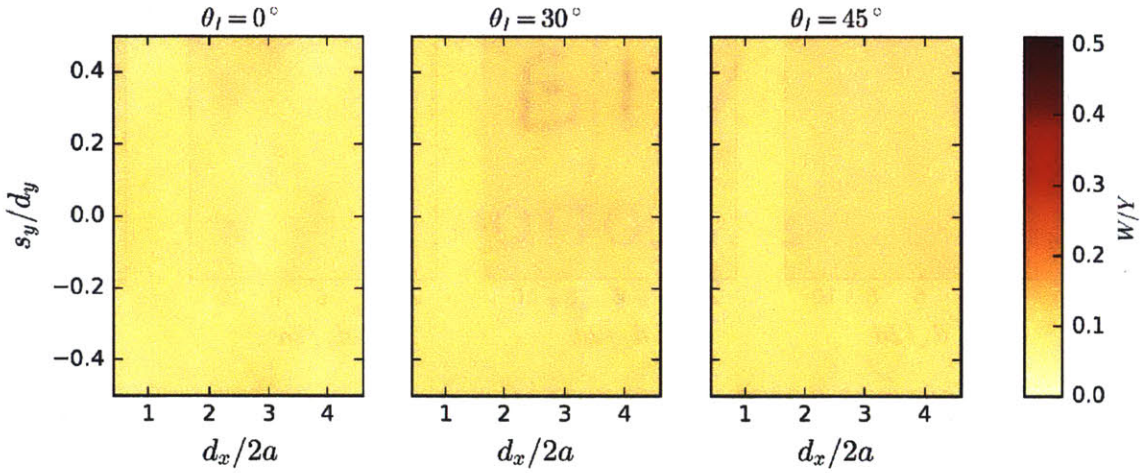

(a) $ka = ka_<$

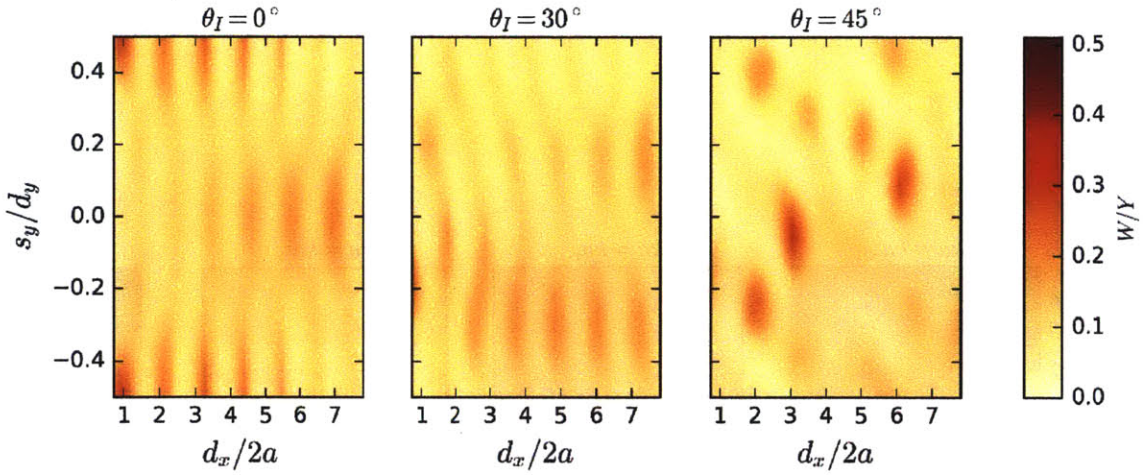

(b) $ka = ka_>$

Figure 4.38: Capture width W_a normalized by the array extent Y in the y-direction for off-resonant wavenumbers and different incoming angles θ_I. Note that the changes in kd_x/π correspond to changes in d_x as the wavenumber constant is for each plot.

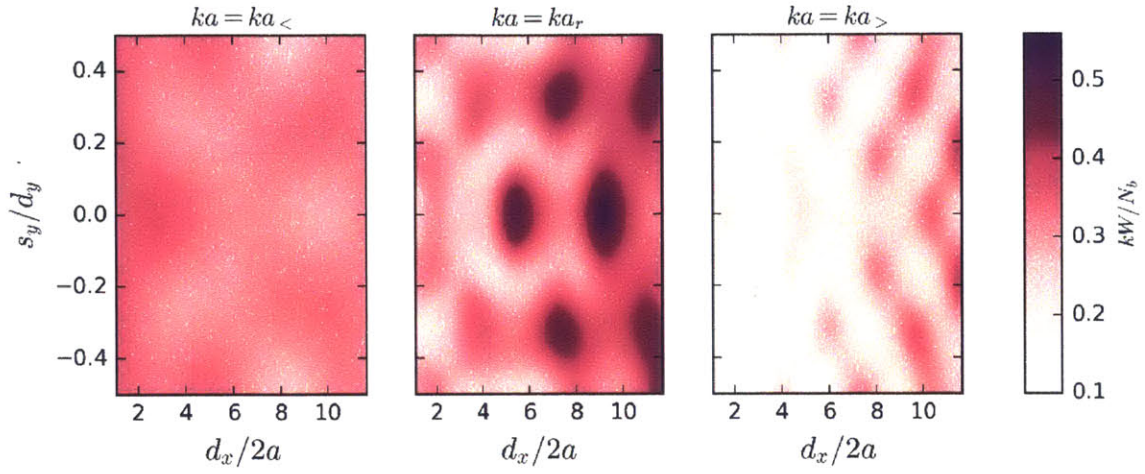

Figure 4.39: Nondimensional capture width kW/N_b for $\theta_I = 90°$. Note that the changes in kd_x/π and kd_y/π correspond to changes in d_x and d_y as the wavenumber is constant for each plot.

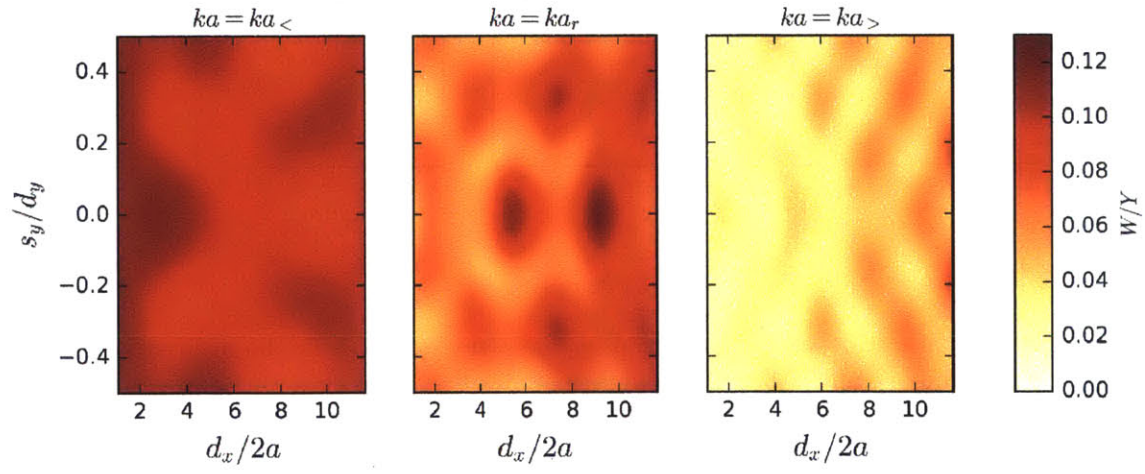

Figure 4.40: Array capture width W_a/Y for $\theta_I = 90°$. Note that the changes in kd_x/π and kd_y/π correspond to changes in d_x and d_y as the wavenumber is constant for each plot.

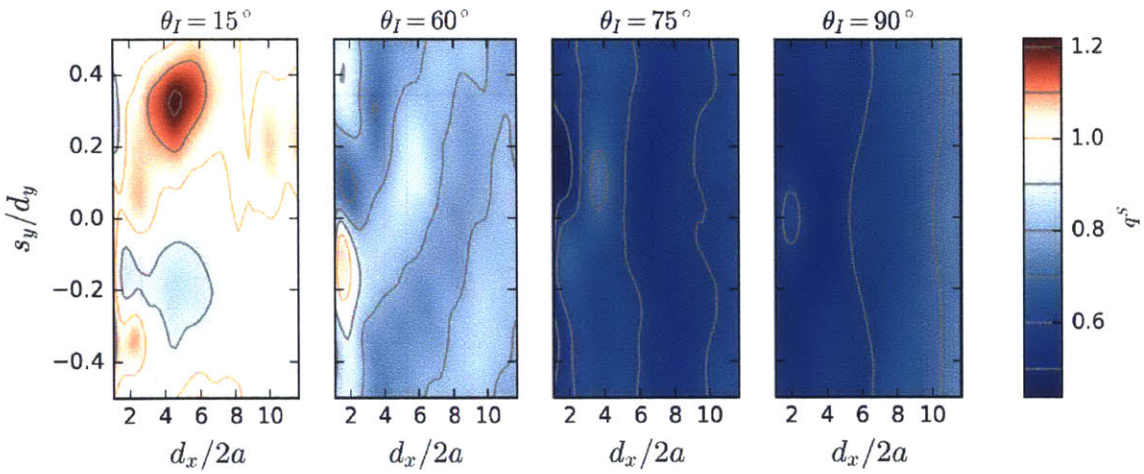

Figure 4.41: Spectral array gain q^S.

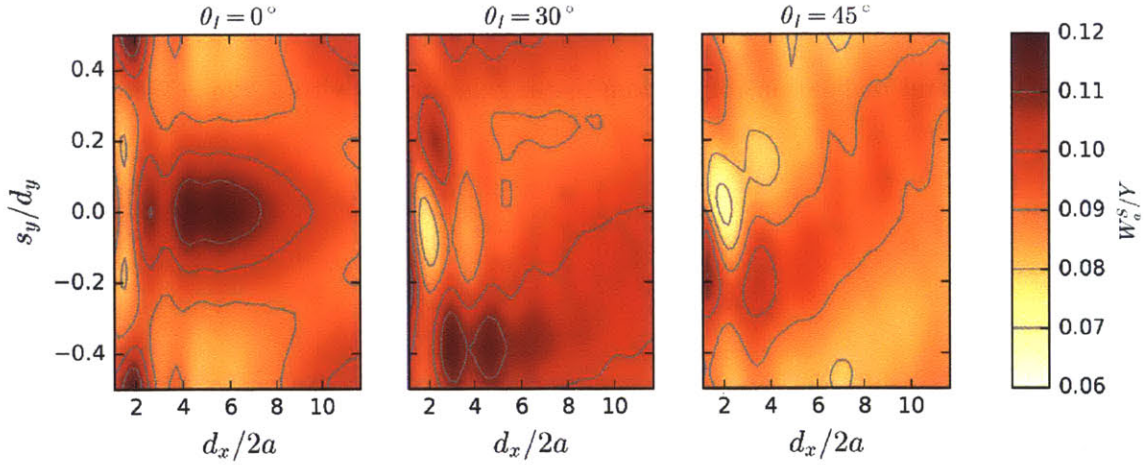

Figure 4.42: Spectral capture width W_a^S normalized by array extent in y-direction.

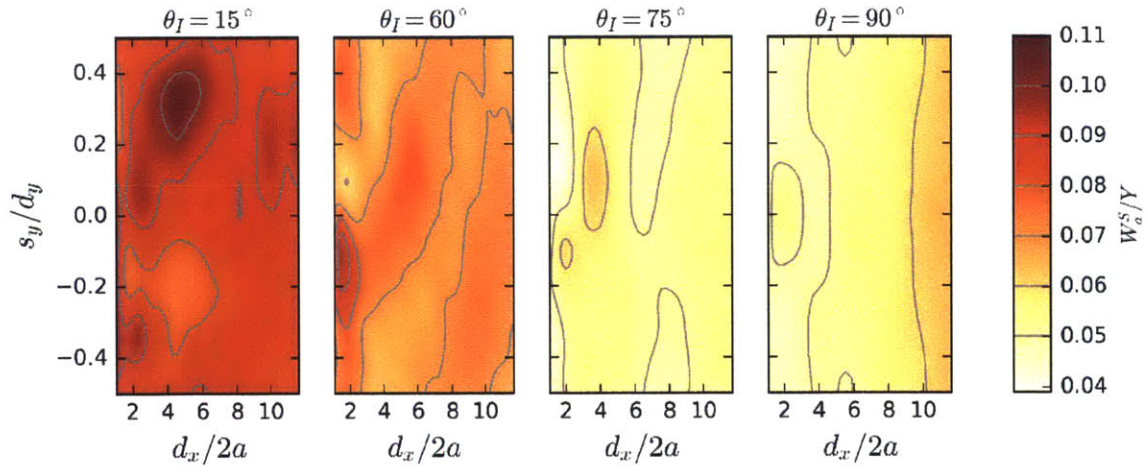

Figure 4.43: Spectral capture width W_a^S normalized by array extent in y-direction.

D.1.5 Analysis of Random Rectangular Arrays

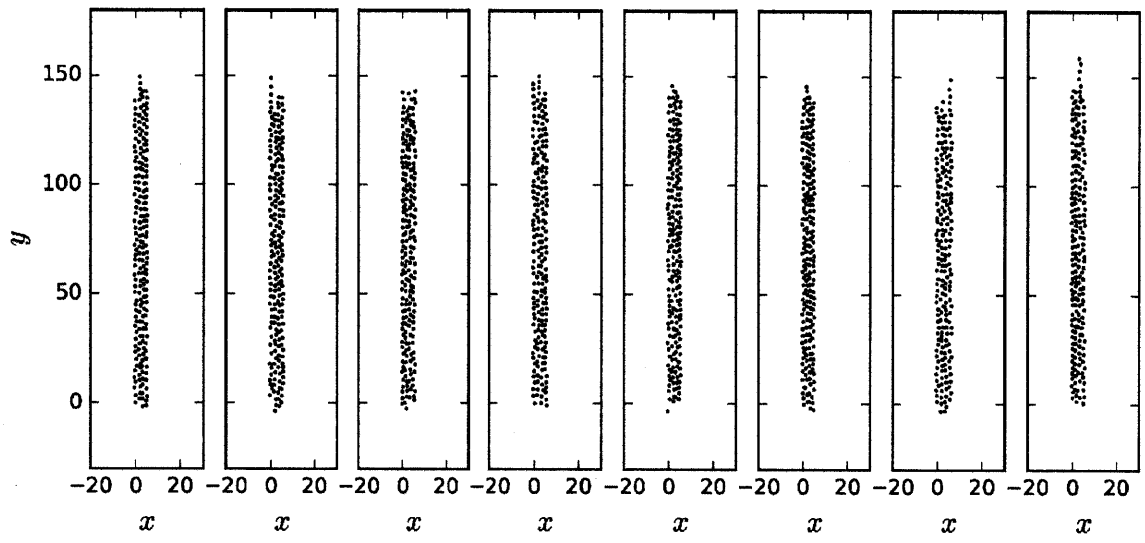

Figure 4.44: Several realizations of random rectangular arrays with $\overline{d_x}/2a = 2.88$, $\overline{d_y}/2a = 4.8$, $k_x = k_y = 16$.

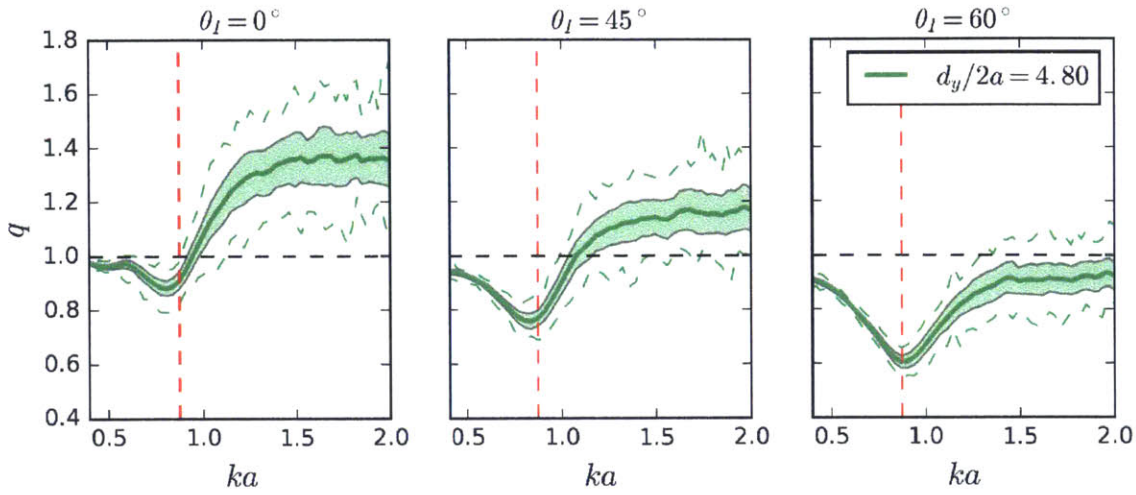

Figure 4.45: Array gain q for random rectangular arrays ($\overline{d_x}/2a = 2.88$, $\overline{d_y}/2a = 4.8$, $k_x = k_y = 16$) for three incoming angles θ_I. The results show the mean (solid line) $\pm$ 1 standard deviation (shaded area), and maximal and minimal values (dashed line).

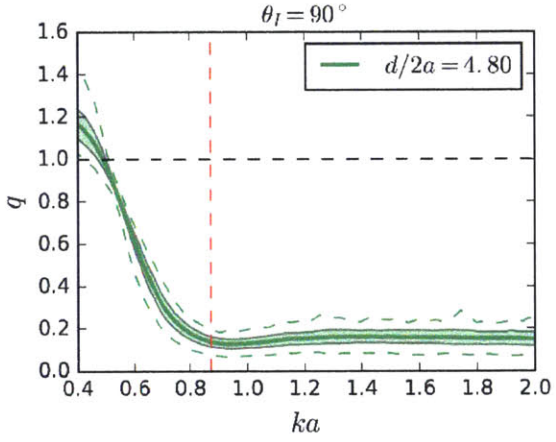

Figure 4.46: Array gain q for random rectangular arrays ($\overline{d_x}/2a = 2.88$, $\overline{d_y}/2a = 4.8$, $k_x = k_y = 16$). The results show the mean (solid line) $\pm$ 1 standard deviation (shaded area), and maximal and minimal values (dashed line).

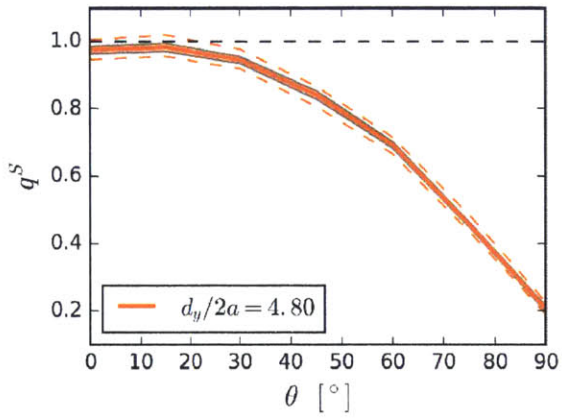

Figure 4.47: Spectral array gain q^S for random rectangular arrays ($\overline{d_x}/2a = 2.88$, $\overline{d_y}/2a = 4.8$, $k_x = k_y = 16$). The results show the mean (solid line) $\pm$ 1 standard deviation (shaded area), and maximal and minimal values (dashed line).

D.2 Optimal Arrays

D.2.1 Optimal Rectangular Arrays with Uniform Spacing

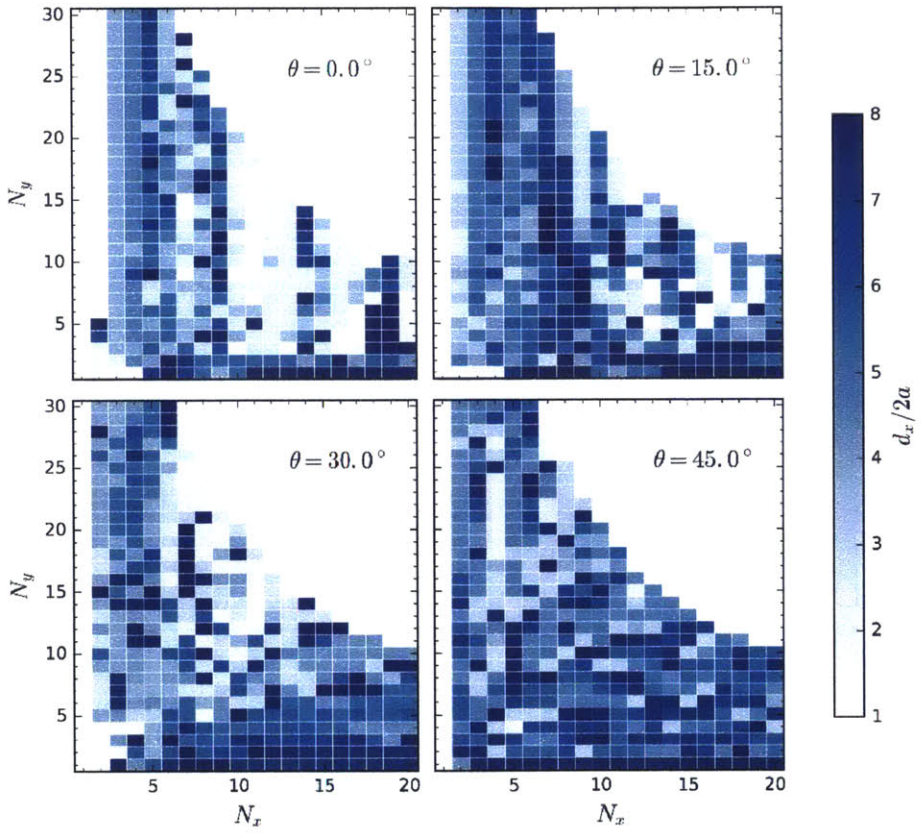

Figure 4.48: Optimal values of spacing $d_x/2a$ for rectangular arrays with $N_x \times N_y$ bodies, for super-resonant frequency $ka = ka_>$.

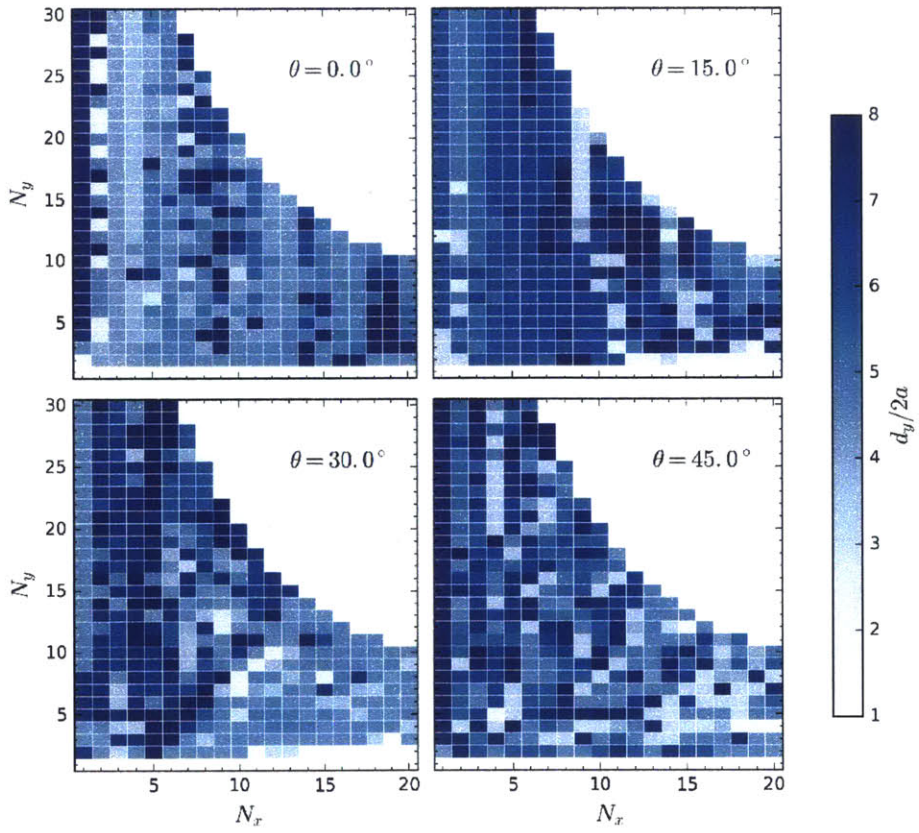

Figure 4.49: Optimal values of spacing $d_y/2a$ for rectangular arrays with $N_x \times N_y$ bodies, for super-resonant frequency $ka = ka_>$.

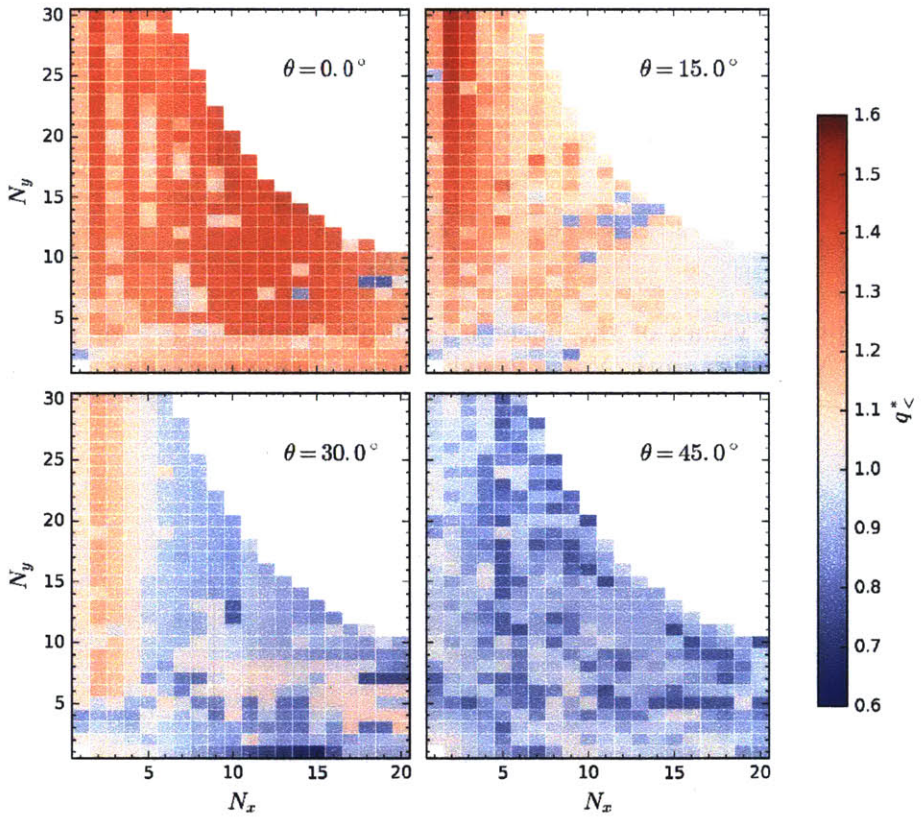

Figure 4.50: Optimal values of gain q for rectangular arrays with $N_x \times N_y$ bodies, for sub-resonant frequency $ka = ka_<$.

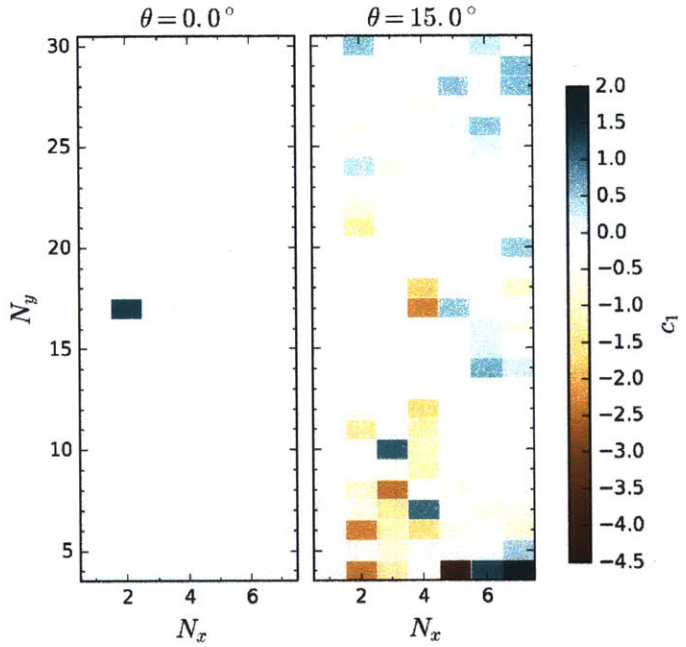

Figure 4.51: Optimal values of the linear irregularity parameter $c_1{}^*$ for rectangular arrays with $N_x \times N_y$ bodies, with $N_{c_y} = 2$ and d_x individually controlled, for the resonant wavenumber $ka = ka_r$.

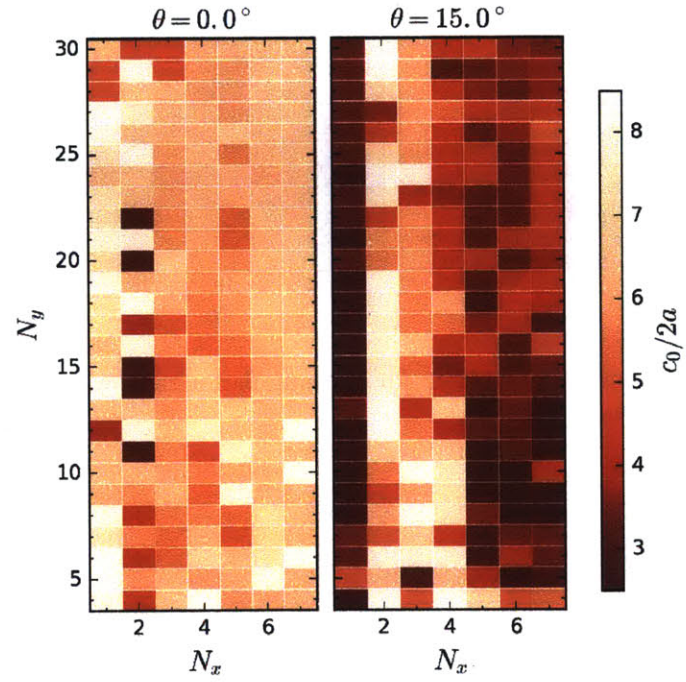

Figure 4.52: Optimal values of the constant spacing parameter $c_0{}^*$ for rectangular arrays with $N_x \times N_y$ bodies, with $N_{c_y} = 2$ and d_x individually controlled, for the resonant wavenumber $ka = ka_r$.

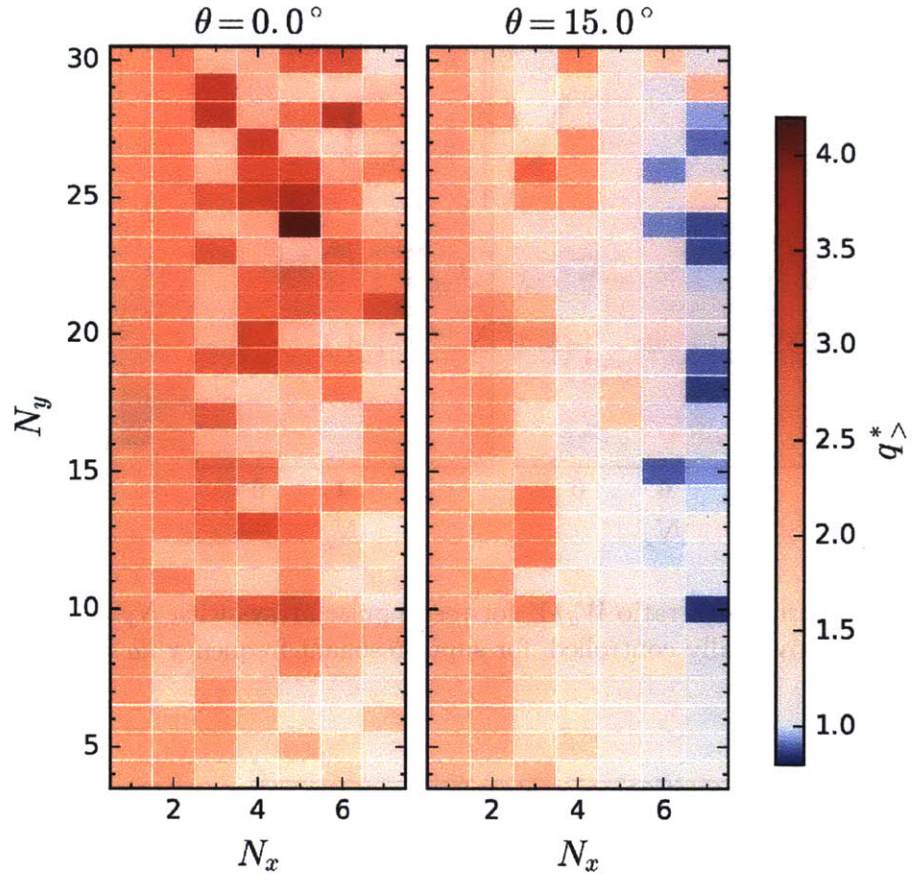

Figure 4.53: Optimal values of gain q for rectangular arrays with $N_x \times N_y$ bodies, with $N_{c_y} = 2$ and d_x individually controlled, for super-resonant frequency $ka = ka_<$.

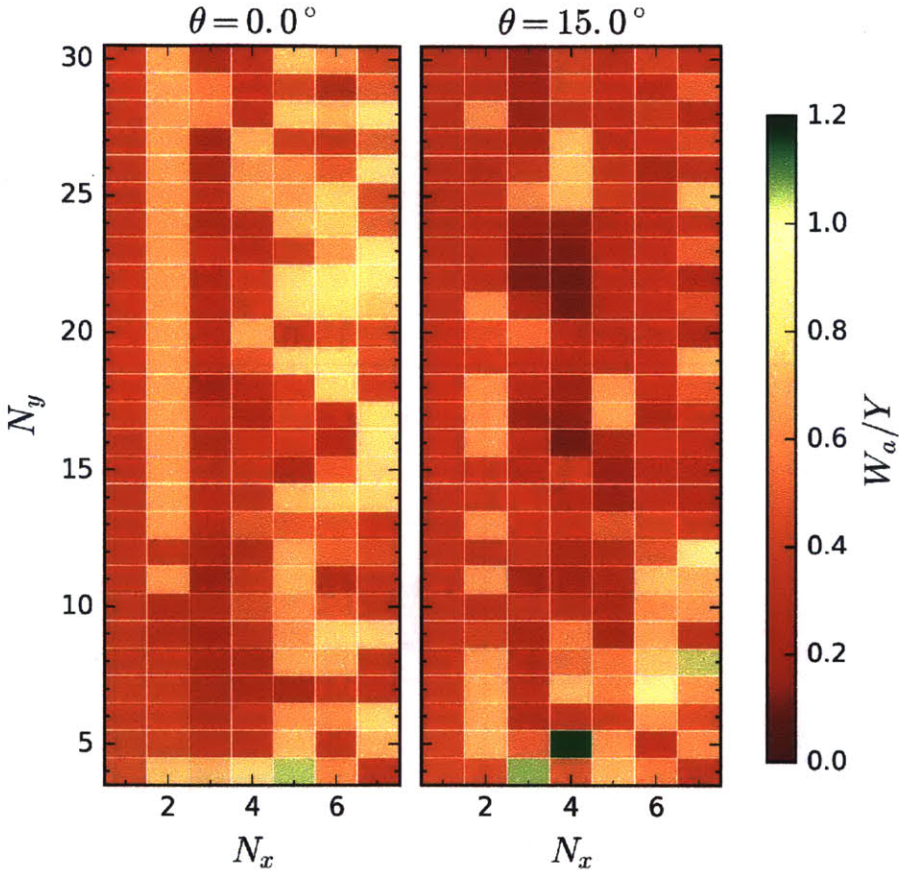

Figure 4.54: Capture width ratio W_a/Y for rectangular arrays with $N_x \times N_y$ bodies, with $N_{c_y} = 2$ and d_x individually controlled, for super-resonant frequency $ka = ka_<$.

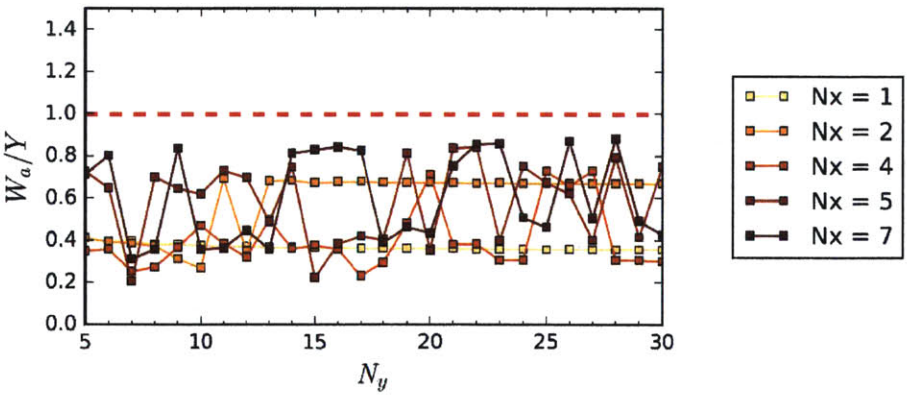

Figure 4.55: Capture width ratio W_a/Y for q-optimal rectangular arrays as a function of N_y for $N_x = 1, 2, 4, 5, 7$ bodies ($N_{c_y} = 2$ and d_x individually controlled), for the super-resonant wavenumber $ka = ka_>$).

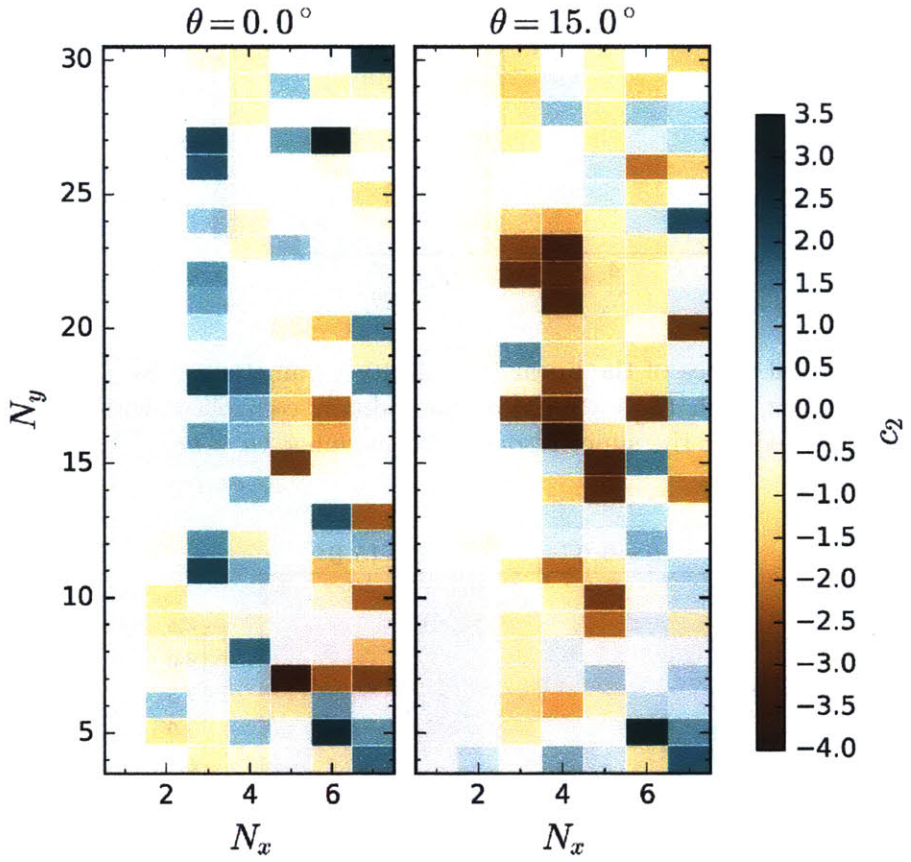

Figure 4.56: Optimal values of the quadratic irregularity parameter $c_2{}^*$ for rectangular arrays with $N_x \times N_y$ bodies, with $N_{c_y} = 2$ and d_x individually controlled, for super-resonant frequency $ka = ka_>$.

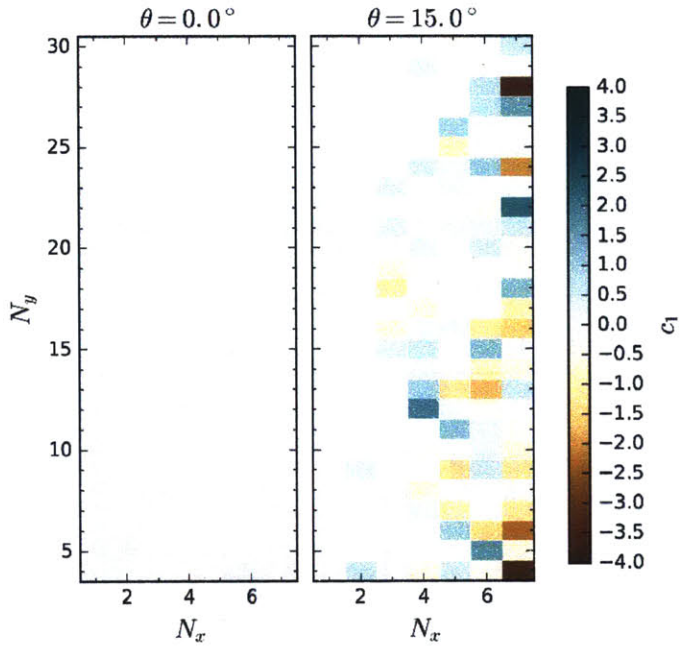

Figure 4.57: Optimal values of the linear irregularity parameter $c_1{}^*$ for rectangular arrays with $N_x \times N_y$ bodies, with $N_{c_y} = 2$ and d_x individually controlled, with $N_{c_y} = 2$ and d_x individually controlled, for the super-resonant wavenumber $ka = ka_>$.

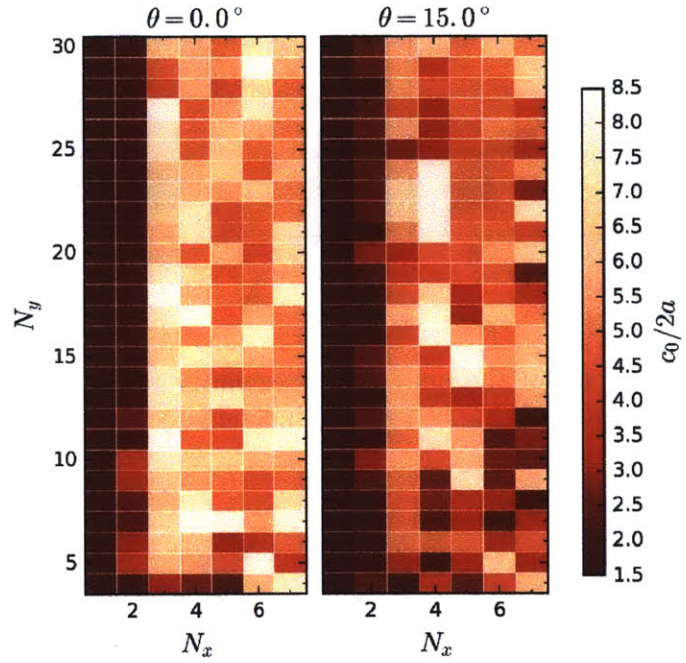

Figure 4.58: Optimal values of the constant spacing parameter $c_0{}^*$ for rectangular arrays with $N_x \times N_y$ bodies, with $N_{c_y} = 2$ and d_x individually controlled, for the super-resonant wavenumber $ka = ka_>$.

Bibliography

Abramowitz, M. and Stegun, I. A. (1964). *Handbook of mathematical functions: with formulas, graphs, and mathematical tables.* Vol. 55. Courier Corporation.

Babarit, A. (2015). "A database of capture width ratio of wave energy converters". In: *Renewable Energy* 80, pp. 610–628.

Budal, K. (1977). "Theory for absorption of wave power by a system of interacting bodies". In: *Journal of Ship Research* 21 (4), pp. 248–253.

Budal, K. and Falnes, J. (1975). "A resonant point absorber of ocean-wave power". In: *Nature* 256, pp. 478–479.

Campbell, P. and Green, M. A. (1986). "The limiting efficiency of silicon solar cells under concentrated sunlight". In: *IEEE Transactions on Electron Devices* 33 (2), pp. 234–239.

Child, B. F. M. and Venugopal, V. (2007). "Interaction of waves with an array of floating wave energy devices". In: *7th European Wave and Tidal Energy Conference.* Porto, Portugal.

— (2010). "Optimal configurations of wave energy device arrays". In: *Ocean Engineering* 37 (16), pp. 1402–1417.

Cortes, C. L. and Jacob, Z. (2013). "Photonic analog of a van Hove singularity in metamaterials". In: *Phys. Rev. B* 88, pp. 045407+.

Cruz, J., Sykes, R., Siddorn, P., and Eatock Taylor, R. (2009). "Wave Farm Design: Preliminary Studies on the Influences of Wave Climate, Array Layout and Farm Control". In: *Proceedings of the 8th European Wave and Tidal Energy Conference.* Uppsala, Sweden, pp. 736–745.

Cruz, J., Sykes, R., Siddorn, P., and Taylor, R. E. (2010). "Estimating the loads and energy yield of arrays of wave energy converters under realistic seas". In: *Renewable Power Generation, IET* 4 (6), pp. 488–497.

Cruz, J. (2008). *Ocean Wave Energy*. Ed. by J. Cruz. Green Energy and Technology. Berlin: Springer.

Dalrymple, R. A., Seo, S. N., and Martin, P. A. (1988). "Water Wave Scattering By Rows of Circular Cylinders". In: *Coastal Engineering Proceedings* 1 (21), pp. 2216–2228.

De Backer, G. et al. (2010). "Power absorption by closely spaced point absorbers in constrained conditions". In: *Renewable Power Generation, IET* 4 (6), pp. 579–591.

Drew, B., Plummer, A. R., and Sahinkaya, M. N. (2009). "A review of wave energy converter technology". In: *Proceedings of the Institution of Mechanical Engineers, Part A: Journal of Power and Energy* 223 (8), pp. 887–902.

Duclos, G. and Clément, A. H. (2004). "Wave propagation through arrays of unevenly spaced vertical piles". In: *Ocean Engineering* 31 (13), pp. 1655–1668.

Emmerhoff, O. J. and Sclavounos, P. D. (1992). "The slow-drift motion of arrays of vertical cylinders". In: *Journal of Fluid Mechanics* 242, pp. 31–50.

Evans, D. V. (1976). "A theory for wave-power absorption by oscillating bodies". In: *Journal of Fluid Mechanics* 77 (01), pp. 1–25.

— (1980). "Some Analytic Results for Two and Three Dimensional Wave-Energy Absorbers". In: *Power from Sea Waves*. Ed. by B. M. Count. The Institute of Mathematics and its Application. University of Edinburgh: Academic Press, pp. 213–249.

— (1981a). "Maximum wave-power absorption under motion constraints". In: *Applied Ocean Research* 3 (4), pp. 200–203.

— (1981b). "Power From Water Waves". In: *Annual Review of Fluid Mechanics* 13, pp. 157–187.

Evans, D. V., Jeffrey, D. C., et al. (1979). "Submerged cylinder wave energy device: theory and experiment". In: *Applied Ocean Research* 1 (1), pp. 3–12.

Evans, D. V. and Porter, R. (1997). "Near-trapping of waves by circular arrays of vertical cylinders". In: *Applied Ocean Research* 19 (2), pp. 83–99.

— (1999). "Trapping and Near-Trapping by Arrays of Cylinders in Waves". In: *Journal of Engineering Mathematics* 35 (1), pp. 149-179–179.

Falcão, A. F. (2008). "Phase control through load control of oscillating-body wave energy converters with hydraulic PTO system". In: *Ocean Engineering* 35 (3-4), pp. 358–366.

Falnes, J. (1980). "Radiation impedance matrix and optimum power absorption for interacting oscillators in surface waves". In: *Applied Ocean Research* 2 (2), pp. 75–80.

— (1984). "Wave-power absorption by an array of attenuators oscillating with unconstrained amplitudes". In: *Applied Ocean Research* 6 (1), pp. 16–22.

— (1995). "On non-causal impulse response functions related to propagating water waves". In: *Applied Ocean Research* 17 (6), pp. 379–389.

— (2002). "Optimum control of oscillation of wave-energy converters". In: *International Journal of Offshore and Polar Engineering* 12 (2), pp. 147–154.

Falnes, J. and Budal, K. (1982). "Wave-power absorption by parallel rows of interacting oscillating bodies". In: *Applied Ocean Research* 4 (4), pp. 194–207.

Faltinsen, O. (1993). *Sea loads on ships and offshore structures*. Vol. 1. Cambridge university press.

Fan, S. et al. (2001). "Waveguide branches in photonic crystals". In: *Journal of the Optical Society of America B* 18 (2), pp. 162–165.

Fitzgerald, C. and Thomas, G. (2007). "A preliminary study on the optimal formation of an array of wave power devices". In: *7th European Wave and Tidal Energy Conference*. Porto, Portugal.

Ganapati, V., Miller, O. D., and Yablonovitch, E. (2014). "Light Trapping Textures Designed by Electromagnetic Optimization for Subwavelength Thick Solar Cells". In: *IEEE Journal of Photovoltaics* 4 (1), pp. 175–182.

Garnaud, X. and Mei, C. C. (2009). "Wave-power extraction by a compact array of buoys". In: *Journal of Fluid Mechanics* 635 (-1), pp. 389–413.

— (2010). "Bragg scattering and wave-power extraction by an array of small buoys". In: *Proceedings of the Royal Society A: Mathematical, Physical and Engineering Science* 466 (2113), pp. 79–106.

Garrett, C. J. R. (1971). "Wave forces on a circular dock". In: *Journal of Fluid Mechanics* 46 (01), pp. 129–139.

Hansen, N. (2006). "The CMA Evolution Strategy: A Comparing Review". In: *Towards a New Evolutionary Computation*. Ed. by J. Lozano et al. Vol. 192. Studies in Fuzziness and Soft Computing. Berlin, Heidelberg: Springer Berlin Heidelberg. Chap. 4, pp. 75–102.

Hansen, N. and Ostermeier, A. (2001). "Completely Derandomized Self-Adaptation in Evolution Strategies". In: *Evolutionary Computation* 9 (2), pp. 159–195.

Hessel, A. and Oliner, A. A. (1965). "A New Theory of Wood's Anomalies on Optical Gratings". In: *Applied Optics* 4 (10), pp. 1275–1297.

Hsu, C. W., Zhen, B., Chua, S.-L., et al. (2013). "Bloch surface eigenstates within the radiation continuum". In: *Light Sci Appl* 2, e84+.

Hsu, C. W., Zhen, B., Lee, J., et al. (2013). "Observation of trapped light within the radiation continuum". In: *Nature* 499 (7457), pp. 188–191.

Hu, X. and Chan, C. T. (2005). "Refraction of Water Waves by Periodic Cylinder Arrays". In: *Physical Review Letters* 95 (15), pp. 154501+.

Hu, X., Chan, C. T., et al. (2011). "Negative Effective Gravity in Water Waves by Periodic Resonator Arrays". In: *Physical Review Letters* 106, pp. 174501+.

Hu, X., Shen, Y., et al. (2004). "Superlensing effect in liquid surface waves". In: *Physical Review E* 69 (3), 030201(R)+.

Joannopoulos, J. D., Villeneuve, P. R., and Fan, S. (1997). "Photonic crystals: putting a new twist on light". In: *Nature* 386 (6621), pp. 143–149.

Johnson, S. G. *The NLopt nonlinear-optimization package.*

— (2012). "Notes on Adjoint Methods for 18.335".

Johnson, S. G. et al. (1999). "Guided modes in photonic crystal slabs". In: *Physical Review B* 60, pp. 5751+.

Kagemoto, H. and Yue, D. K. P. (1986). "Interactions among multiple three-dimensional bodies in water waves: an exact algebraic method". In: *Journal of Fluid Mechanics* 166, pp. 189–209.

Kashiwagi, M. (2002). "Wave-induced Local Steady Forces On a Column-Supported Very Large Floating Structure". In: *International Journal of Offshore and Polar Engineering* 12 (2), pp. 98–104.

Kashiwagi, M., Iida, T., and Miki, M. (2015). "Wave Drift Force on Floating Bodies of Cloaking Configuration and Associated Wave Patterns". In: *The 30th International Workshop on Water Waves and Floating Bodies.* Bristol, UK.

Kowalczewski, P., Liscidini, M., and Andreani, L. C. (2012). "Engineering Gaussian disorder at rough interfaces for light trapping in thin-film solar cells". In: *Optics Letters* 37 (23), pp. 4868–4870.

Kyllingstad, A. (1984). "A low-scattering approximation for the hydrodynamic interactions of small wave-power devices". In: *Applied Ocean Research* 6 (3), pp. 132–139.

Li, Y. and Mei, C. C. (2007a). "Bragg scattering by a line array of small cylinders in a waveguide. Part 1. Linear aspects". In: *Journal of Fluid Mechanics* 583 (-1), pp. 161–187.

— (2007b). "Multiple resonant scattering of water waves by a two-dimensional array of vertical cylinders: Linear aspects". In: *Physical Review E* 76 (1), pp. 016302+.

Linton, C. M. (1998). "The Green's Function for the Two-Dimensional Helmholtz Equation in Periodic Domains". In: *Journal of Engineering Mathematics* 33 (4), pp. 377–401.

Linton, C. M. and Evans, D. V. (1990). "The interaction of waves with arrays of vertical circular cylinders". In: *Journal of Fluid Mechanics* 215 (-1), pp. 549–569.

— (1992). "The Radiation and Scattering of Surface Waves by a Vertical Circular Cylinder in a Channel". In: *Philosophical Transactions of the Royal Society of London. Series A: Physical and Engineering Sciences* 338 (1650), pp. 325–357.

Linton, C. M. and McIver, P. (1996). "The scattering of water waves by an array of circular cylinders in a channel". In: *Journal of Engineering Mathematics* 30 (6), pp. 661-682–682.

Maniar, H. D. and Newman, J. N. (1997). "Wave diffraction by a long array of cylinders". In: *Journal of Fluid Mechanics* 339 (-1), pp. 309–330.

Martin, P. A. (2006). *Multiple Scattering.* Encylopedia of Mathematics and its Applications. Cambridge: Cambridge University Press.

Mavrakos, S. (1997). "Comparison of methods for computing hydrodynamic characteristics of arrays of wave power devices". In: *Applied Ocean Research* 19 (5-6), pp. 283–291.

Mavrakos, S. and Koumoutsakos, P. (1987). "Hydrodynamic interaction among vertical axisymmetric bodies restrained in waves". In: *Applied Ocean Research* 9 (3), pp. 128–140.

McIver, P. and Evans, D. V. (1984). "Approximation of wave forces on cylinder arrays". In: *Applied Ocean Research* 6 (2), pp. 101–107.

McNatt, J. C., Venugopal, V., and Forehand, D. (2015). "A novel method for deriving the diffraction transfer matrix and its application to multi-body interactions in water waves". In: *Ocean Engineering* 94, pp. 173–185.

Mei, C. C. (1976). "Power extraction from water waves". In: *Journal of Ship Research* 20, pp. 63–66.

Mei, C. C., Stiassnie, M. S., and Yue, D. K. P. (2005). *Theory and Applications of Ocean Surface Waves.* Advanced Series on Ocean Engineering. Singapore: World Scientific.

Miller, O. D. et al. (2014). "Fundamental Limits to Extinction by Metallic Nanoparticles". In: *Phys. Rev. Lett.* 112, pp. 123903+.

Newman, J. N. (1983). "The low-frequency limit for wave-power systems". In: *Applied Ocean Research* 5 (1), pp. 38–44.

— (2014). "Cloaking a circular cylinder in water waves". In: *European Journal of Mechanics - B/Fluids* 47, pp. 145–150.

Oskooi, A. et al. (2012). "Partially disordered photonic-crystal thin films for enhanced and robust photovoltaics". In: *Applied Physics Letters* 100 (18), pp. 181110+.

Peter, M. A. and Meylan, M. H. (2009). "Water-Wave Scattering by Vast Fields of Bodies". In: *SIAM Journal on Applied Mathematics* 70 (5), pp. 1567–1586.

Peter, M. A., Meylan, M. H., and Linton, C. M. (2006). "Water-wave scattering by a periodic array of arbitrary bodies". In: *Journal of Fluid Mechanics* 548, pp. 237–256.

Salter, S. H. (1974). "Wave power". In: *Nature* 249 (5459), pp. 720–724.

Shen, Y. et al. (2014). "Optical Broadband Angular Selectivity". In: *Science* 343 (6178), pp. 1499–1501.

Sheng, X. et al. "Optimization-based design of surface textures for thin-film Si solar cells". In: *Optics Express* 19 (S4), A841–A850.

Siddorn, P. and Eatock Taylor, R. (2008). "Diffraction and independent radiation by an array of floating cylinders". In: *Ocean Engineering* 35 (13), pp. 1289–1303.

Simon, M. J. (1982). "Multiple scattering in arrays of axisymmetric wave-energy devices. Part 1. A matrix method using a plane-wave approximation". In: *Journal of Fluid Mechanics* 120 (-1), pp. 1–25.

Sommerfeld, A. (1949). *Partial differential equation in physics.* Vol. 1.

Spring, B. H. and Monkmeyer, P. L. (1974). "Interaction of Plane Waves with Vertical Cylinders". In: *Proceedings of the 14th Coastal Engineering Conference*, pp. 1828–1847.

Srokosz, M. A. (1980). "Some relations for bodies in a canal, with an application to wave-power absorption". In: *Journal of Fluid Mechanics* 99, pp. 145–162.

Stratigaki, V. et al. (2014). "Wave Basin Experiments with Large Wave Energy Converter Arrays to Study Interactions between the Converters and Effects on Other Users in the Sea and the Coastal Area". In: *Energies* 7 (2), pp. 701–734.

Stuart, H. R. and Hall, D. G. (1997). "Thermodynamic limit to light trapping in thin planar structures". In: *J. Opt. Soc. Am. A* 14 (11), pp. 3001–3008.

Svanberg, K. (2002). "A class of globally convergent optimization methods based on conservative convex separable approximations". In: *SIAM Journal on Optimization* 12 (2), pp. 555–573.

Taghipour, R. and Moan, T. (2008). "Efficient Frequency-Domain Analysis of Dynamic Response for the Multi-Body Wave Energy Converter in Multi-Directional Waves". In: *Proceedings of the 18th International Offshore and Polar Engineering Conference*. Vancouver, Canada, pp. 357–365.

Twersky, V. (1952). "Multiple Scattering of Radiation by an Arbitrary Configuration of Parallel Cylinders". In: 24 (1), pp. 42+.

Twersky, V. (1962). "On scattering of waves by the infinite grating of circular cylinders". In: *IRE Transactions on Antennas and Propagation* 10 (6), pp. 737–765.

Wang, C. M. and Tay, Z. Y. (2011). "Very Large Floating Structures: Applications, Research and Development". In: *Procedia Engineering* 14, pp. 62–72.

Wolgamot, H. et al. (2011). "The interaction factor for wave power in arrays". In: *International Workshop on Water Waves and Floating Bodies*. Athens, Greece.

Wood, R. W. (1902). "On a remarkable case of uneven distribution of light in a diffraction grating spectrum". In: *Philosophical Magazine Series 6* 4 (21), pp. 396–402.

Yablonovitch, E. (1982). "Statistical ray optics". In: *J. Opt. Soc. Am.* 72 (7), pp. 899–907.

Yeung, R. W. (1981). "Added mass and damping of a vertical cylinder in finite-depth waters". In: *Applied Ocean Research* 3 (3), pp. 119–133.

Yu, Z. and Fan, S. (2011). "Angular constraint on light-trapping absorption enhancement in solar cells". In: *Applied Physics Letters* 98 (1), pp. 011106+.

Yu, Z., Raman, A., and Fan, S. (2010). "Fundamental limit of nanophotonic light trapping in solar cells". In: *Proceedings of the National Academy of Sciences* 107 (41), pp. 17491–17496.